5-2018

Investigating the likelihood of pediatric femur fracture due to falls through finite element analysis.

Keyonna McKinsey
University of Louisville

INVESTIGATING THE LIKELIHOOD OF PEDIATRIC FEMUR FRACTURE DUE
TO FALLS THROUGH FINITE ELEMENT ANALYSIS

By

Keyonna Mckinsey
Bioengineering B.S., University of Louisville, 2015

A Thesis
Submitted to the Faculty of the
University of Louisville
J.B. Speed School of Engineering
As Partial Fulfillment of the Requirements
For the Professional Degree

MASTER OF ENGINEERING

Department of Bioengineering

INVESTIGATING THE LIKELIHOOD OF PEDIATRIC FEMUR FRACTURE DUE
TO FALLS THROUGH FINITE ELEMENT ANALYSIS

Submitted by: _____

Keyonna Mckinsey

A Thesis Approved On

_____

(Date)

by the Following Reading and Examination Committee:

_____

Gina Bertocci, Thesis Director

_____

Angela Thompson, Thesis Director

_____

Hermann Frieboes

_____

Michael Voor

iii

ACKNOWLEDGEMENTS

I would like to thank both of my advisors Dr. Gina Bertocci and Dr. Angela Thompson for their support, and guidance over the course of completing this thesis. I'd also like to thank my other committee members, Dr. Hermann Frieboes and Dr. Michael Voor, for their time and contributions especially questions and potential aspects of the project that could be pursued in future work.

I would also like to thank the members of the iRAP lab, Dr. Nathan Brown, Dr. Raymond D'Souza, and Craig Smalley, for aiding me with any testing or additional help throughout my research.

ABSTRACT

Bone fracture is the second most common injury of child abuse. Studies have generally

reported that femur fractures are more likely due to abuse than accidental causes in cases where

the child is non-ambulatory. They have also found that household falls are commonly offered as

the cause of injury in cases of abuse. In this study, a finite element (FE) pediatric femur model

will be developed and used to evaluate likelihood of fracture in common household fall scenarios

(bed falls and feet first falls). This will provide greater biomechanical evidence as to the

likelihood of femur fracture due to common fall scenarios which may serve to better inform

clinicians when assessing compatibility between stated cause and injury when household falls are

reported. *The purpose of this study is to determine the likelihood of fracture of a 12-month-old*

child's femur due to commonly reported accidental fall scenarios using finite element analysis.

Loading conditions in the FE model were derived from femur loads reported in a previously

study measured using a 12-month old anthropomorphic test device (ATD) in experimentally

simulated household falls. A FE femur model was derived from a CT scan performed on an 11-

month old child. Validation of the FE model was conducted through mechanical testing of a bone

v

surrogate printed using selective laser sintering of glass-fiber reinforced nylon. The finite element model used simple support for the constraints and the loads from the ATD study were applied at the corresponding location of the load cells, which bounded the diaphysis of the femur. The FE predicted outcomes including maximum principal stress and strain values were used to evaluate the likelihood of fracture by comparing to three different thresholds: (1) tensile yield strain, (2) ultimate tensile strength, and (3) ultimate flexural strength. Fifty-percent of bed falls exceeded the yield strain and ultimate tensile strength fracture threshold whereas only two (of 12) exceeded the flexural strength fracture threshold. Different bed fall dynamics considered resulted in a significant difference in peak strains while impact surface did not. Peak strains in bed falls were associated with the peak bending moment. No feet-first falls exceeded fracture thresholds. Fall height resulted in a significant difference in peak strains while the impact surface did not. Peak strains in feet-first falls were associated with the peak bending moment or torsional loads.

TABLE OF CONTENTS

NOMENCLATURE

ATD = anthropomorphic test device

AUC = area under the curve

BMD = Bone mineral density

CRABI = Child Restraint Air Bag Interaction

CT = computed tomography

DXA = Dual Energy X-Ray

FE = finite element

GF = glass fiber

HIC = head injury criteria

HU = Hounsfield Unit

ML = Medial-lateral

AP = anterior-posterior

OI = osteogenesis imperfecta

QCT = quantitative computed tomography

UNM = University of New Mexico

$\rho_{qct},$ = QCT calculated density

$\rho_{app},$ = apparent density

ρ_{ash} = ash density

LIST OF TABLES

LIST OF FIGURES

xiii

xiv

I. SPECIFIC AIMS

In 2014, the National Child Abuse and Neglect Data System estimated that over 700,000 children had either been abused or neglected in the United States (Children's Bureau, 2016). Bone fractures are the second most common presentation of abuse (Clarke, Shelton, Taylor, Khan, & Needhirajan, 2012). For clinicians who encounter these injuries, it is important for them to be able to distinguish between fractures that are potentially abusive or truly accidental so that further investigation of suspected abuse can be pursued if necessary. The likelihood of bone fracture in children due to either accidental or non-accidental causes has been evaluated through retrospective case studies, in-depth investigations, and biomechanical testing. Clinical studies have generally reported that femur fractures are more likely to be due to abuse in cases where the child is non-ambulatory and that falls from a height are commonly offered as the cause of injury in cases of abuse (Dalton et al., 1990; Pandya et al., 2009). Biomechanical research has been used to evaluate aspects of findings from these clinical studies. Tools, such as finite element analysis and anthropomorphic test devices (ATDs), have been used to simulate commonly reported causes of injury and evaluate the resulting likelihood of injury. Finite element models of the femur have successfully been used to evaluate the likelihood of fracture due to various loading conditions such as those seen in sideway falls in elderly populations (Bessho et al., 2009; Bryan, Nair, & Taylor, 2009). To the best of our knowledge, only one study has developed a pediatric, *in silico* femur model and only considered bending loads in their analysis (Li et al., 2015).

The purpose of this study is to determine the likelihood of fracture of a 12-month-old child's femur due to commonly reported accidental fall scenarios using finite element analysis. The fall scenarios being evaluated are feet-first falls, which will consider two different heights, and falls from a horizontal surface such as a bed. Both falls will include two different impact surfaces, carpet and linoleum. A pediatric femur model that addresses these scenarios commonly encountered in the clinical environments can provide further biomechanical evidence for clinicians as to whether specific accidental falls are likely to result in a fracture of the femur.

The *in-silico* femur model for this study was developed from computed tomography (CT) scans of an 11-month-old child. The loading conditions for the finite element analysis will be based on previous studies which used an instrumented ATD to simulate the falls mentioned previously. The ATD was developed to be representative of a 12-month-old child and has an improved biofidelic femur based on the same 11-month-old CT scans being used in this study. Physical replicas of the femur were developed from the 3D model and printed using selective laser sintering of a glass fiber and nylon blend. Mechanical testing, which included bending and compression, of these bone surrogates was conducted to validate the finite element models through a comparison of strain time history using strain rosettes and comparison of force-displacement curves. The likelihood of fracture of the femur will be evaluated by using the maximum principal strain theory and the use of two stress-based thresholds based on ultimate strength values found in the literature to assess the likelihood of a fracture occurring. The influence of fall height and impact surface on the likelihood of fracture was also evaluated. The

results from this study will provide further insight into the likelihood of femur fractures for a 12-month-old child due to these accidental falls.

Specific Aims:

1. Develop a finite element model of a 12-month old healthy femur to evaluate the stress and strain distributions across the femur due to loading conditions representative of short distance falls.

    a. Segmentation from CT scan

    b. Application of material properties.

    c. Development of boundary conditions and constraints.

    d. Validation of model geometry through use of bone surrogate.

2. Evaluate the likelihood of femur fracture for a healthy 12-month old child in two short distance fall scenarios using finite element modeling.

    a. Selection of factors to consider (e.g., fall height, impact surface, and fall dynamics).

3. Determine the influence of impact surface on the resulting stress and strain distributions and the likelihood of femur fracture using finite element modeling.

    H01 - Linoleum surface will result in an increased likelihood of fracture compared to carpet surface.

4. Determine the influence of fall height on the resulting stress and strain distributions and the likelihood of femur fracture using finite element modeling.

    H02 – Falls from a higher height will result in an increased likelihood of fracture.

II. BACKGROUND AND SIGNIFICANCE

In 2014, the National Child Abuse and Neglect Data System estimated that over

700,000 children had either been abused or neglected in the United States. Approximately

17% of those children had been physically abused (Children's Bureau, 2016). In order to

better identify potential cases of abuse, clinicians need to be able to identify injuries that

do not appear to correspond with the stated of injury. Studies such as one by Taitz et al.

(2004) have evaluated cases with long bone fractures. A general pediatrician and child

protection specialist evaluated each case by identifying indicators of abuse that have been

found in the literature, whether there were any further investigations into potential abuse,

and if there were any future incidents of abuse of the cases evaluated. Of the 100 cases

evaluated, 31 were found to have indicators of abuse where only one had been referred

for further evaluation. While it is possible that the injuries observed in the remaining 30

of these cases may not have been abusive, further investigation and better documentation

in their chart of the injury, especially if it and future injuries appear suspicious, could

help prevent future incidences of abuse. A study by O'Neill et al. (1973) examined 110

verified abuse cases where 8 patients died due to abuse also had previous injuries that

were most likely non-accidental in nature as well. Research in this field through

retrospective clinical case studies and biomechanical studies can provide evidence to help

distinguish between accidental and abusive injuries based on the risk of injury, such as a

bone fracture due to a stated cause. Studies in this field can provide guidance as to the

indicators that would benefit from suspicion of abuse leading to further investigation

which would begin the process of potentially removing a child from a harmful situation and prevent further incidences of abuse or even death.

A. Retrospective Clinical Studies of Pediatric Injury

1. General Patterns of Injury

Retrospective clinical studies can be used to evaluate cases, where typically a child has been admitted into an emergency room department due to an injury, over a specific period. Through the results found in the retrospective clinical studies, relationships between the associated injury due to the reported incidence and whether these injuries were abusive can be made. While the data collected in clinical studies do not necessarily provide biomechanical evidence or data as to the likelihood of a fracture occurring, the patterns found could be used to further the knowledge of the likelihood of an injury being accidental or abusive in nature.

The objective of a study conducted by Pandya et al. was to determine if there was a distinct difference in fracture type between abuse and accidental cases (Pandya et al., 2009). Pandya investigated the patterns of fracture due to accidental and nonaccidental trauma for cases collected from 1998-2007 at an urban level I pediatric trauma center. Children up to the age of 4 years old were included in the study. Child abuse cases were obtained from the hospital's database for child abuse. Control, or accidental cases, were taken from those initially admitted to the emergency room and not included in the child abuse database. A total of 500 abuse and 985 accidental cases were evaluated. Cases were also separated into two groups based on age where 18 months was the boundary for these groups. The occurrence of fractures and non-bony head injuries were examined using

statistical analysis. The most prevalent injury for both abuse and accidental cases was non-bony head injuries. For the child abuse cases, the next most prevalent injuries were skull fractures (21.2%), rib fractures (18.8%), and femur fractures (14.6%). For the accidental cases, skull fractures (21.9%), femur fractures (14.2%), and humerus fractures (10.3%) were also prevalent injuries. The child abuse group had a significantly greater proportion of non-bony head injuries, ribs, and other bone fractures excluding femur fractures when compared to the accidental group. The researchers also calculated the odds ratios using binary logistic regression. Femur fractures for the under 18-month age group were 1.8 times more likely to occur in cases of abuse than accidents. The odds ratio was 3.3 for the over 18-month age group where the incidence of femur fracture was higher in accidental cases. The researchers concluded that long bone fractures were more prevalent for cases of abuse especially when the child is non-ambulatory.

Leventhal et al. have aimed to distinguish child abuse from unintentional injuries (Leventhal, Thomas, Rosenfield, & Markowitz, 1993). The x-rays and medical records of children less than 3 years of age that were treated for fracture between 1979 and 1983 and were listed either in the hospital's Child Abuse Registry or the emergency department log were evaluated. To include a higher sample of cases with child abuse, 14 cases from the Child Abuse Registry in 1984 were added for analysis. A 7-point scale was developed to categorize the likelihood of abuse which included 3 levels for certainty of abuse, 3 levels for unintentional injury, and a central rating of unknown cause. A combination of clinicians and radiologists provided opinions on the likelihood of abuse in each case where a final score on the 7-point scale was decided. If a consensus was unable to be achieved as to whether the injury was due to abuse or was accidental, then it was

assigned an unknown rating. 215 cases with confirmed fractures were considered. In 27 of these cases, more than one fracture was present. 24% of these cases were categorized as abuse. 67% were categorized into one of the accidental categories. Long bone fractures were generally categorized under unintentional where 9 out of the 11 were due to abuse for children younger than a year old. For femoral fractures, the age of the child had the best correlation with whether abuse had occurred. Falls were among the most common occurrence of the histories that were reported with it being the cause of 60% of the cases. Falls such as a short fall from a bed were also a commonly reported (11%) history for cases of abuse. The researchers observed that even minor falls such as a fall less than 120cm could result in complicated fractures.

Stewart et al. evaluated patterns of injury in infants (Stewart, Meert, & Rosenberg, 1993). The two main objectives of this study were to describe the characteristics of traumatic injury in infants less than three months of age and to determine whether abused infants had an increased risk for subsequent trauma. Patients were identified for this study through the emergency department over a one-year period where children less than three months of age that presented with a traumatic injury were included and infants that were identified to have birth related trauma were excluded. Each patient's age, sex, birth weight, encounter date, number of previous emergency visits, mechanisms and type of injury, suspicion of abuse or neglect, radiographic studies, social or protective service involvement, and disposition were recorded. The medical records were also reviewed one year after the initial presentation to determine if there were any further emergency visits or hospitalizations. In 2% of the total number of identified cases (5500), a traumatic injury occurred. 28% of these cases of traumatic injury involved

either abuse or neglect. The researchers also observed that the cases of non-accidental

trauma occurred more frequently between July and September. Two-thirds of the

accidental trauma cases were due to falls where 29% were from a bed or couch and 26%

from a caretaker's arms. Reported causes in the nonaccidental trauma cases included

when the infant was left in the presence of another child, deliberate abuse, or unrestrained

in a motor vehicle accident. Non-accidental trauma tended to present with a greater

frequency of skull fractures, diastatic and multiple skull fractures, and intracranial

hemorrhages than accidental trauma cases. Extremity fractures were more frequent in the

cases of non-accidental trauma and multiple extremity fractures were only present in

those with non-accidental trauma. The majority of non-accidental extremity injuries were

long bone fractures except for one acromion fracture.

Other studies may look at specific causes of injuries such as one conducted by

Wang et al. (2001). The study aimed to describe the constellation of injuries and

outcomes resulting from pediatric falls. The cases were identified from a seven-year

period at level 1 trauma center where a total of 784 patients, where the injuries sustained

were due to a fall, were identified. Cases where abuse had been identified were excluded

from the study. The cases were split into either falls from a low level (<15 feet) or a high

level (>15 feet). Other data that was collected and reviewed included ICD-9 codes, the

injury severity score (ISS), Glasgow coma score (GCS), radiographic imaging results,

disposition, hospital length of stay, and outcome. ISS is a scoring system that takes the

top three scores from the highest Abbreviated Injury Scale (AIS) scores, which are a

measure of the severity of the injury, for regions of the body with the highest AIS score

from that region (e.g. face, chest, abdomen, extremity, etc.) to produce the final ISS

score. The GCS is predominantly used to assess the level of consciousness of a person usually following a head injury. The incidence of injuries from falls rose around the ages of one to two years old where there is an increased mobility of the child. Low level fall cases comprised 53% of the patients. The most common sites of falls in decreasing order were from a window, a balcony, or stairs. Twelve cases resulted in death; 8 of them were from high level falls. Less than 1% of cases with fall height less than 25 feet experienced a severe injury (ISS>35). GCS scores were not significantly different between low and high-level falls. Low level falls had an increased rate of intracranial bleeding compared to high level falls. Two-third of the cases that had either upper extremity long bone fractures or lower extremity long bone fractures, which comprised 6.2% and 5.6% of the total number of cases respectively, were from high level falls. The researchers concluded that there is a range of injuries that can occur at most levels but there is an increased likelihood for serious abdominal or head injury due to high level falls.

Generalized clinical case studies aiming to differentiate the patterns of both accidental and abusive injuries have demonstrated common patterns. Household falls are a common accidental injury mechanism that can result in fractures. A study by Pomerantz (2012) evaluated injuries as a result of falls leading to hospitalization in children up to five years old. Falls observed in this study were mostly from furniture where 21.7% of these falls resulted in femoral injuries. But as seen in the study by Leventhal et al., a fall can also be a common falsely reported injury mechanism in cases of abuse. Femur fractures are consistently shown to be more frequently due to with abuse in cases involving non-ambulatory children.

9

2. Femur-Specific Injury Evaluation

Clinical case studies have also looked at a specific type of injuries such as long bone fractures or more specifically femur fractures between accidental and definitively non-accidental cases to determine any difference in injury patterns. Skellern et al. found the femur being one of the most prevalent sites of fracture in both accidental and abusive cases (Skellern, Wood, Murphy, & Crawford, 2000). Other clinical studies have also looked at specifically the occurrence of lower extremity injuries in cases of abuse.

Coffey et al. aimed to characterize the incidence of child abuse in children with lower extremity trauma (Coffey, Haley, Hayes, & Groner, 2005). Children who were admitted to the trauma center over a period of 5 years and had lower extremity injuries were the focus of this case study. Two age groups were identified to be those younger or older than 18 months of age. Other characteristics such as ethnicity, injury location and description, injury severity score, and revised trauma score were also reviewed. Cases were identified if a lower extremity injury was noted in their patient history or a lower extremity fracture if the fracture was also documented with radiographic findings. If the case was noted as abuse or suspected abuse, the case was placed in the abuse category. The researchers in this study assumed that, following a full clinical evaluation, if the child has not been removed from the suspected abuse category, that case most likely would be classified as abuse from suspected abuse upon further investigation. Due to this assumption, the suspected abuse cases were categorized as abuse for the purposes of this study. Of the 5497 cases considered during this period, 90% were 18 months or older and 2% of these cases involved child abuse. Only 23% of the cases collected had lower extremity injuries noted in their files. This subset was evaluated for further analysis. The

incidence of child abuse in the subset with lower extremity injuries was 1%. For the

under 18-month age group, there was an incidence of 32% of child abuse. Only 12% of

the cases in the under 18-month group had lower extremity injuries where 67% of those

were associated with child abuse. 74% of the lower extremity fractures of the younger

age group were linked to abuse compared to 27% of cases with any injury that was not a

lower extremity fracture within the younger age group. Femur fractures were the most

common lower extremity fracture in both the abuse and accidental categories. The

researchers observed a lower incidence in lower extremity fractures in the older age

group that had an association with abuse. Based on survival analysis calculations, the

researchers concluded that 90% of the children with lower extremity injuries due to abuse

were younger than 3 years of age and over 50% less than 6 months. It is important to note

that even in cases where abuse was only suspected, these cases were still categorized as

abuse which could lead to a false overestimate of abuse observed.

Dalton et al. conducted a retrospective analysis of 138 cases of children younger

than 3 years of age with a femoral fracture when admitted to one of three hospitals

between 1979 and 1983 (Dalton et al., 1990). In conjunction with obtaining the patient's

histories and whether there was social services intervention or police involvement, the

researchers also coordinated with the Michigan State Child Abuse Registry to determine

if the child had been described as abused by March of 1985. The cases were then

assigned to one of four categories which were accidental, bone pathologic condition,

abusive, or uncertain cause. The abuse category included cases where there was an

admission of abuse or common evidence associated with physical abuse such as burns,

bruises, welts, bite marks, or multiple fractures. The researchers observed that most of the

11

injuries had occurred in children less than one-year of age. Of the cases considered, sixty percent were categorized as due to uncertain causes and ten percent as abuse. The researchers could make no specific correlation between the type of fracture and the cause of the injury based upon the predefined categories. The amount of spiral fractures increased with age. Of the uncertain cases that were reported to state protective services, 76% were determined to be caused by abuse. Of the total number of fractures considered in this study, 26% were initially categorized as abuse with an additional seven cases identified as abuse at a later point in time. A higher proportion of children under the age of one were represented in the abused category. Only in children under 15 months old, there was a higher association of abuse and spiral fractures. The researchers concluded that due to the higher incidence of abuse in children younger than three years old, it is important to admit those with femur fractures and under 3 years of age into the hospital and pursue further investigation as to whether abuse had occurred.

While these case studies illustrate that femur fractures, especially in non-ambulatory children are more likely to be due to abuse, there is no specific pattern of injury to be able to distinguish an accidental versus an abusive femur fracture. Although diaphyseal femur fractures have often been found to be the predominant location of femur fractures in accidental mechanisms, there is a lack of studies that have evaluated specific injury mechanisms beyond the initial reports of a fall such as falls from a height or furniture. There still needs to be more investigation as to how to distinguish these injuries especially by considering other factors such as bone health and biomechanics of bone.

<u>3, Bone Pathologies and Likelihood of Injury</u>

Other clinical studies have evaluated the association of clinical measures such as bone pathology and bone mineral density with the likelihood of injury. These studies can further a clinician's understanding of how bone fragility disorders can affect a child's risk of fracture.

A study conducted by Cook et al. evaluated the bone mineral densities of the lumbar spine and femoral neck in children with recent fractures where fractures of the fingers, skull, teeth, or ribs were excluded (Cook et al., 1987). They compared various factors of these cases such as age, height, weight, and sex. Dual phantom absorptiometry (DPA) was used to measure the bone mineral density. This method was more accurate than most available methods of measuring densitometry at the time of this study. 17 children, who were 3-14 years old, were considered. They were scanned with DPA within 4 weeks of the fracture. The cases considered did not present with any metabolic bone disease; malnutrition; or growth impairment. Data collected for each of these cases included history of bone disease, medications, and dietary habits. These fractured cases were compared to a normal control group of children (n=17) of a similar sex, age, height, and weight. In comparison to the normal control group, the cases with fractures had no significant reduction in lumbar bone mineral density. There were differences in the femoral neck densities but there were negligible differences for the greater trochanter region of the femur. None of these differences were statistically significant for the femur between the fractured cases and the control group. While the average of the fractured group had a consistently lower bone mineral density compared to the average of the control group across all measures, the statistical analysis indicated that none of these

differences were statistically significant. The researchers concluded that the reduced bone

mass averages of the fractured group were most likely not a factor in the children

sustaining a fracture. A main limitation of this study is that the researchers did not control

for location or cause of fracture. The researchers also acknowledged that it is unknown

whether any reduction in bone mineral density that was observed had existed prior to the

fracture occurring as well.

The focus of a study conducted by Chan et al. was to evaluate the bone mineral

and calcium status of children less than 12 years old that have experienced an accidental

limb fracture (Chan, Hess, Hollis, & Book, 1984). There were 17 subjects where each

subject was evaluated approximately 16 months following their injury. Control subjects

were chosen such that they matched the subject in sex, race, and age that is within a six-

month range. The subjects ranged from 2 to 12 years of age with an average

immobilization time of six weeks. A history of each subject's diet for the prior 48 hours

had been recorded. A blood sample was used to determine the levels of calcium,

phosphorus, magnesium, alkaline phosphate, albumin, and calcidiol. Bone mineral

content was determined by a bone mineral analyzer with the radius of the subject that was

either not fractured or not dominant. The blood levels measured were determined to be

within normal range and were not significantly different between the two groups of

subjects. There was an observed difference in the bone mineral content of the fractured

and control group where the fractured group had lower values than their corresponding

control subject. Based on the evaluation of the dietary intake of the previous 48 hours,

four of the fractured subjects had less than 60% of the recommended daily allowance for

calcium and phosphorus while all the controls had at least 60% of the recommended

amount. There was no observed difference between the levels of calcium and phosphorus and bone mineral density.

The purpose of a cohort study conducted by Clark et al. was to determine if there was an association between bone mass and fracture risk in childhood through an evaluation of 6213 children at an average age of 9.9 years old who were followed for 24 months (Clark, Ness, Bishop, & Tobias, 2006). The population of children were determined from those born in 1991-1992, of which there are fourteen thousand children, and invited to join the study at an overall mean age of 9.9 years old. If there were any associations that were found between the bone mass and fracture risk, the study would also consider the influence of volumetric bone mineral density, and bone size on fracture risk. The total area and density of the body excluding the head were measured through dual-energy x-ray absorptiometry (DXA). Over the two-year period of analysis, 549 children with reported fractures and an additional 836 subjects, randomly selected, were measured using the DXA of the right humerus. Other measures such as the sex, ethnicity, education level of the mother, paternal social class, and pubertal measurements based on the Tanner staging of puberty were recorded. Of the children with useable DXA scans at 9.9 years of age, 8.9% were confirmed to have one fracture over the period of observation and 1.5% of those had reported multiple fractures. The most common fracture site was the forearm for 44.6% of the fractures that had occurred. The total bone mineral density that was measured was correlated with an increase in fracture risk once the researchers had adjusted for factors such as age, sex, ethnicity, and socio-economic status. Per standard deviation decrease in bone mineral content, there was an 89% increased risk of fracture that was observed after accounting for other measurements such as height,

weight, and bone area. A similar inverse association for areal bone mineral density of the humerus and fracture risk were seen in the analysis of the humerus in the patients that experienced a fracture from a subset of 1317 children. The researchers concluded that this data suggests a lower volumetric bone mineral density is associated with a higher risk of fracture.

Bone disorders such as rickets and osteogenesis imperfecta are also diseases which may affect the fragility or structure of the bone. The most common bone fragility disorder in children is osteogenesis imperfecta (OI) which is typically caused by mutations in genes which code for type 1 collagen. This disorder can result in bone deformities and increased fragility of the bone (Caouette et al., 2014). Rickets is the result of a deficiency or insufficient supply of a mineral. For rickets, calcium and phosphate are both important minerals but phosphorus is considered to be the critical mineral in the development of the disease (Rauch & Schoenau, 2002). Rickets is also generally due to a true vitamin D deficiency and abnormal vitamin D metabolism. In bone that has been affected by rickets, there have been observed fractures such as metaphyseal fractures and transverse long bone fractures. Children younger than three years old may be 100 times for those with rickets or 20 for those with osteopenia times more likely to sustain a fracture than those without bone fragility diseases (Servaes et al., 2016).

Since the research testing pediatric, or even infant, bone is scarce, many studies may not have studied the biomechanics of the pediatric femur. It is important to understand how factors such as bone mineral density can affect fracture risk even when lacking a biomechanical analysis. Some studies have also considered how bone diseases,

such as rickets, can led to an increased risk of fracture. In the context of child abuse, it is important to realize that some of these studies have illustrated that those with bone fragility diseases or lower bone mineral density may be more susceptible to fractures in the injury mechanisms studied. While this study will focus on healthy bone, the resulting observations on fracture risk may result in an increased risk for other populations.

B. Biomechanical Testing Using Anthropomorphic Test Devices

Anthropomorphic test devices (ATDs) have allowed for reported injury mechanisms to be experimentally simulated. Combined with the use of instrumentation such as strain gauges and load cells, these experiments provide biomechanical outcomes which can be compared to injury threshold values or act as inputs to a finite element analysis. In the context of research related to child abuse, ATDs have been used to evaluate the injury risk due to common fall scenarios. The risk of injury due to these accidental fall scenarios can provide clinicians with further biomechanical evidence as to whether to suspect an injury as abusive due to a fall.

Many studies have used ATDs to evaluate the likelihood of head injuries in simulated falls. The injury risk measure commonly used is the HIC (Head Injury Criteria) which is a measure of the initial impact of the head and accounts for the duration of the impact as well as the acceleration of the head on impact. These studies also incorporate other factors when evaluating these mechanisms such as common impact surfaces that may be encountered and different fall heights. A study conducted by Bertocci et al. used a Hybrid II three-year-old test dummy to investigate the effect of impact surface (which includes playground foam, carpet, linoleum, and wood) on injury risk (G. E. Bertocci et

al., 2003). This study used 3 uniaxial accelerometers and videography to be able to capture the motion and impact of the head. The procedure for this study began with an initial position of the ATD lying on a horizontal surface which was 0.68m above the impact surface. The ATD was pushed at the midpoint of the body. The legs of the ATD impacted the surface floor. The study found that there were significant differences in HIC values when comparing across different impact surfaces with an alpha value of 0.05. This study had only used HIC values to evaluate head injury and did not consider other rotational acceleration of the head which is another measure used in evaluating head injury risk.

Another study conducted by Thompson et al. also simulated falls using ATDs (A. K. Thompson, Bertocci, & Pierce, 2009). The ATD used in this study was a 12-month old Child Restraint Air Bag Interaction (CRABI) dummy. This ATD was suspended and dropped from heights of 18, 27, and 47 inches onto different impact surfaces which included linoleum over concrete, linoleum over wood, playground foam, carpet, and wood. The ATD had 4 accelerometers which would allow for linear acceleration in each axis and the anterior-posterior rotational acceleration of the head to be measured. The results compared a few different head injury outcome measures which included linear head acceleration, angular head acceleration, and the impact duration. The fall dynamics were also evaluated. At the lowest height (18 inches), the feet would then fall rearward. At increasing heights, the researchers observed that the fall after the initial impact may also be onto the ATD's side as well as its back. The impact surface had also affected the fall dynamics for the 27 inches and 47 inches fall heights where the feet upon initial impact would tend to slide for the wood and linoleum tiled concrete and stick for the

other impact surfaces study demonstrated that at increasing heights the child was much less likely to fall rearward. This study acknowledged that the initial position before the fall could contribute to different fall dynamics.

One of the ways in which potential fracture evaluation is limited is the extent of the biofidelity of the ATD. Over time, researchers have incrementally improved ATDs to be more biofidelic. These modified ATDs may incorporate more accurate anatomical representation and/or more accurate materials to better model the behavior of a child while falling. A study conducted by Ibrahim et al compared the results from a six-week-old infant ATD which was tested in a previous study to that of an 18-month-old child ATD (Ibrahim & Margulies, 2010). The heights of these falls ranged from one to three feet. The impact surfaces were carpet pads and concrete. This researchers in this study modified a Hybrid II ATD. These modifications incorporated features of the skull that were assumed to better represent it. The skull was modified to be thicker and have a similar modulus to that of an infant skull that the researchers had evaluated previously. Another modification included adjusting the neck stiffness of the cervical spine where the target stiffness of this design was determined based on scaled data from adults and pediatric caprine data. The ATD had a nine-unit accelerometer to measure the triaxial linear and rotational acceleration of the head. An angular velocity transducer was also used. The modified ATD was used in free fall drop tests with the heights and impact surfaces mentioned previously. The free falls consisted of a fall where the limbs were restrained to prevent interference during the fall and where the initial position of the ATD was a supine position with the head at 15-20 degrees lower than the feet which ensured that the occiput would impact the floor first. The researchers had found that most of the

head motion occurred in the sagittal and horizontal directions. Comparison of the outcome measures such as impact forces, peak to peak change in angular velocity, and time duration of the impact were made across the different heights and impact surfaces. Compared to the researchers' infant ATD study that was previously conducted, the toddler model had doubled the head accelerations of the infant which appears to correspond to the increased occurrence of concussions reported in other literature. The researchers had observed different dynamics of the head impact for the infant and toddler ATDs. These differences could be attributed to factors such as the neck stiffness which was stiffer both in flexion in tension for the toddler compared to that of the infant. While the design of the necks and the neck stiffness chosen for the ATDs used was not determined based on pediatric human data, it does show that the neck properties could play more of a role in the motion of the head following the initial impact.
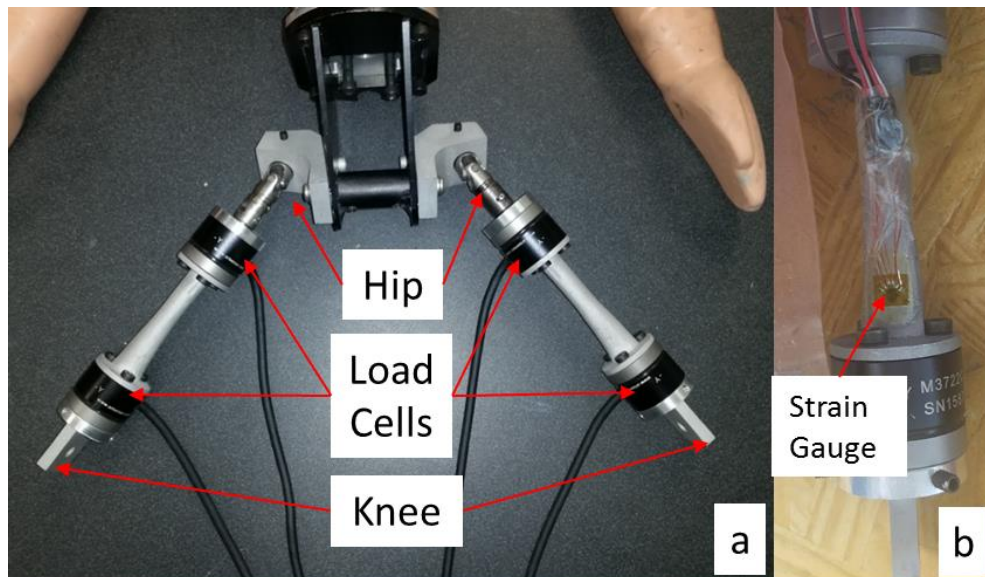
FIGURE 1. ATD Femur Model Setup (a). The strain gauge can be seen in (b) where it is on the posterior side of the femur located near the knee. The strain gauge is located 7.14mm above the bracket.

The previously described studies illustrate that ATDs can be used to experimentally simulate injury mechanisms accounting for factors such as type of impact

surface and the height of the fall. By improving the biofidelity of the ATD, the researchers can simulate a fall and assess injury potential more accurately. Thompson et al. (2018) developed a modified femur for use with a 12-month-old CRABI (Child Restraint Air Bag Interaction) ATD. The modified femur (Figure 1) included a shaft that was modeled based on CT scans of an 11-month-old infant. Biomechanical instrumentation for the femur included the use of 4 load cells measuring the tri-axial forces and moments at the proximal and distal ends of the femur shaft and strain rosettes located at the distal end of the diaphysis as seen in b. The proximal portion, which is towards the hip, of the femur used a universal joint. The range of motion allowed was 90° of flexion, 40° of extension, 90° of abduction, and 6° of adduction. This ATD was used to experimentally simulate two common household falls: bed falls and feet-first falls. Carpet and linoleum were the impact surfaces evaluated in each fall. The feet-first falls evaluated two different heights, 27 and 47 inches. The bed fall was only conducted from a height of 24 inches. For non-ambulatory children, of which a 12-month-old may be on the boundary, femur fractures are more likely to be due to abuse. By being able to further evaluate the loading conditions of the femur observed in these simulated falls through a finite element analysis, more insight may be given as the likelihood of fracture due to these household falls.

C. Mechanical Properties of the Femur

In the previous section, ATD studies have used biomechanical outcomes obtained through the instrumentation of the dummy to be able to compare to injury outcome measures developed for injuries such as head injuries. While comparison to these injury

outcome measures can be made, these criteria may not be specific to children or as relevant to children due to various anatomical differences (such as the skull not being fully formed in infants) that may result in injury criteria that may not be able to be scaled from adult data. With respect to the pediatric femur, there are no specific criteria for the risk of injury. This is in part due to the lack of studies that have evaluated the mechanical properties of the pediatric femur which are fairly rare compared to adult specimens. The mechanical properties of bones have been evaluated for other populations, such as the elderly, which may be used to extend these properties to infants. Animal studies of immature animal bone, such as porcine or bovine, have also been used to evaluate fracture risk of the femur.

1. Mechanical Properties of Adult Bones

Many studies have evaluated the relationship between bone mineral density and mechanical properties such as the elastic modulus and yield strain for cortical and trabecular adult bone. The ability to be able to make this relationship offers a few advantages. For the elderly population who may be more prone to lower bone mineral density and have osteoporosis, physicians are better able to understand who is at risk for injury due to their low bone mineral density and be able to make the appropriate recommendations to their patients to be able to address it. Another aspect is to be able to develop finite element models based on CT scans where one can scale the intensity of the CT scan (Hounsfield Unit value) to the bone mineral density which would then be translated to the mechanical properties of the bone based on the relationships defined in

these studies. A few studies have evaluated biomechanical properties of the bone especially with respect to the femur.

A study conducted by Morgan et al. focused on the yield strain properties of bone (Morgan & Keaveny, 2001). The study aimed to quantify the on-axis (with respect to the direction of the osteon) compressive and tensile yield strains for various anatomic sites, determine the dependence of these values on site, and determine the dependence of the yield stress-apparent density relationship on anatomic site. Cylindrical on-axis specimens from the tibia, vertebral bodies, greater trochanter of the femur, and femoral neck were evaluated. The femoral sites (greater trochanteric region and femoral neck) were treated as separate sites due to the large differences in density between the two regions. Specimens were tested using either uniaxial tensile or compressive tests. Strains were measured with an extensometer. The modulus from these tests was defined as the slope at zero strain of a quadratic curve fit to the portion of the curve from 0-0.2% strain. The yield point was determined using the 0.2% offset technique. Yield stress nor yield strain appeared to have a significant dependence on apparent tissue density. The yield strain did have a dependence on anatomic site in both compression and tension. The mean yield strain was 0.85 and 0.7 for the femoral neck and the greater trochanter of the femur, respectively. The variation within anatomical sites of the yield strain varied between 5% and 12% while there was up to a 20% variation between anatomic sites. The researchers also observed a dependency on anatomic site for the relationship between yield stress and apparent density.

The objectives of another study conducted by Morgan et al. were to compare the on-axis modulus-density regressions for human trabecular bone from multiple anatomical

sites such as the vertebra and femur, to determine the effect of using a pooled regression from all of the sites on the precision of the regression's predictions, and to apply the relationships with high resolution finite element analysis to investigate the roles of tissue modulus and architecture in the site specificity of apparent modulus-density relationships (Morgan, Bayraktar, & Keaveny, 2003). Human bone tissue was obtained from 61 donors with no history of metabolic bone disease or cancer. The tissue was frozen within 24 hours post-mortem. Specimens were collected as an 8mm diameter and 25mm length (nominal) on-axis specimen from each anatomical site of interest (vertebra, proximal tibia, and proximal femur. For each site, the specimens were randomized to either be tested using compression or tension. The protocols for uniaxial testing were conducted based on a previous protocol that was designed to minimize end artifacts. Four strain measurements from which the modulus was defined were averaged to give the modulus for the specimen. The modulus was defined as the slope of the quadratic fit between 0% and 0.2% strain. Apparent density was also measured. Using a general linear regression model, loading mode was found to be not a significant variable. A pooled and site-specific regressions were developed for the modulus-density relationship. The modulus-density relationship was then evaluated through analysis of covariance across the anatomic sites where the apparent density was the covariate. Using high resolution µCT scans of the specimens, FE models were created. A modulus of 1.0GPa for all elements and two different moduli applications which were calculated based on previously defined relationships, where one was dependent upon specimen-specific architecture and the other was not, were used to evaluate the application of the materials. Results indicated that accounting for the site-specific architecture for trabecular bone is necessary to

determine the modulus-density relationship. The results also indicated that the different sites had different modulus-density relationships. For the accuracy of the finite element models, the tissue moduli calculated from them were consistently and significantly higher than the calculated values. The researchers suggest that this could be due errors in the alignment of the axis of the trabecular specimen.

A study conducted by Bayraktar et al. aimed to determine the effective tissue-level elastic modulus and both the tensile and compressive yield strains for femoral neck trabecular bone (Bayraktar et al., 2004). Another objective was to compare these properties to that of cortical tissue derived from tension testing. Similar testing outlined from the team's previous studies described above were used to complete the compressive and tensile testing. 74 femoral neck specimens were 8mm in diameter and 32mm long where the principal trabecular orientation was determined using contact radiographs. The modulus, apparent density, and yield stress were obtained similar to the studies mentioned previously. A finite element model of each specimen was once again created. To evaluate the yield strain, the trabecular tissue was modeled as a bilinear elastic material and a principal strain failure criterion was used. The effective trabecular modulus averaged 18GPa which did not have a significant dependence on measured volume fraction, apparent modulus, or apparent density based on a linear regression analysis. The same lack of significant dependence was found for the tensile and compressive yield strains which were 0.62% and 1.04% respectively. The tensile yield strain for cortical was found to be 0.73%. The cortical bone was negatively correlated with porosity for the elastic modulus and the yield stresses. The cortical bone was

consistently higher for both elastic modulus and tensile yield strain by 10% and 15%, respectively when adjusting for zero-porosity.

Other considerations for bone properties have evaluated the orientation dependence of the loading, Dong et al. evaluated the orientation dependence (longitudinal, circumferential, and radial directions) of the mechanical properties using cadaveric cortical samples of the femur (Dong, Acuna, Luo, & Wang, 2012). This study only had eight subjects who were middle aged males. They evaluated the differences in mechanical properties which included the elastic modulus, yield stress, and energy dissipation between the orientations. There were no significant differences in the yield strain and plastic strain in response to the increasing applied strain in the three directions.

Another aspect to these type of studies is to be able to determine predictors, such as bone mineral density, that influence mechanical properties. A study conducted by Ohman et al. had aimed to do this while also considering subjects that were as young as four years old (Ohman et al., 2011). While four years old is not as young as the subjects evaluated in our study, it does aid in examining if the properties considered in adults can be extended to pediatrics. Ohman et al. evaluated the correlations between tissue density and compressive mechanical properties when applying these properties to children and whether or not the yield strain is an invariant in human cortical bone tissue. Due to the limited availability of healthy pediatric bone tissue, tissue samples were obtained from pediatric cancer patients where bone samples were already being excised. The healthy portion of these bone segments were used for analysis. Samples were harvested from twelve pediatric patients whose ages ranged from four to 15 years old. The adult samples were obtained from 12 healthy adults whose ages ranged from 22 to 61 years of age. The

samples were obtained from the shaft of either the femur (n=5) or tibia (n=7).

Cylindrical bone slices were used in the mechanical testing with a total of 120 total

samples created from the 24 subjects. Each specimen had undergone compression testing

using a uniaxial testing machine where the bottom end was fixed in

polymethylmethacrylate (PMMA). An extensometer, which was attached to the center of

the specimen, was used to measure the strain. The compressive Young's modulus was

calculated. The yield strain and stress were calculated based on the 0.2% strain offset

method. The compressive ultimate stress and the corresponding strain were identified by

the first point on the stress-strain graph where the slope was zero. A general linear model

was used to investigate the correlation between the observed properties with the subject's

age and specimen ash density. The most notable result that there was no significant

difference found in the yield strain between the adult and pediatric group while there was

a significant difference for the young's modulus, yield stress, and the ultimate

compressive stress and strain. High correlations through regression analysis were found

for the predictor ash density with young's modulus, ultimate compressive stress, and

yield stress. The researchers concluded that the properties related to ash density of adult

cortical tissue can be extended to children and the compressive yield strain is an invariant

with respect to ash density.

2. Mechanical Studies Evaluating Pediatric Specimens

While the youngest subject in the study conducted by Ohman et al. was four years

old, other bone mineral density evaluation studies have illustrated a correlation in bone

mineral density values with respect to age (Boot et al., 2010) as seen in Figure 2. While

there are few studies that have evaluated pediatric bones, these studies tend to focus on specimens that have various bone pathologies such as osteogenesis imperfecta or rickets. These studies also tend to focus more on the ribs or vertebrae although femur specimens have been tested as well.
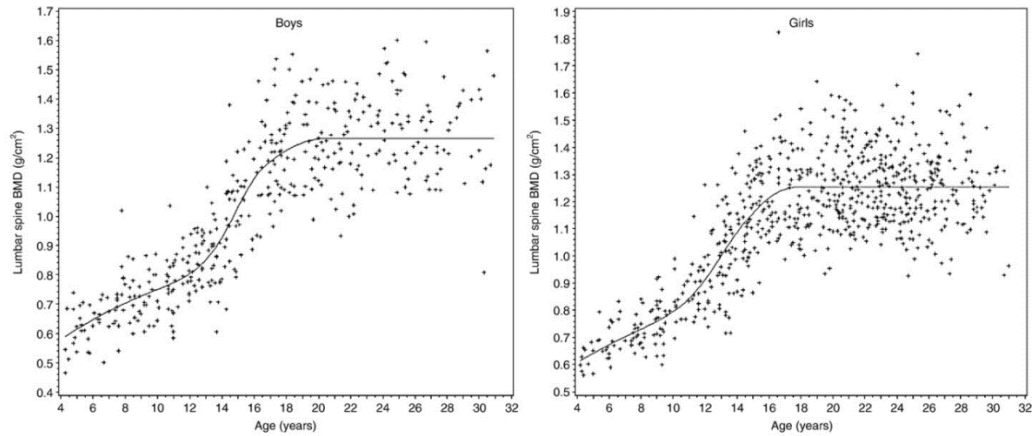
FIGURE 2. From Figure 1 of (Boot et al., 2010). The graphs show the lumbar spine bone mineral density with respect to age for both boys (left) and girls (right). The lines are of the fitted curves of the non-linear models.

Mechanical property studies were conducted on pediatric bone from the 1960s to 1980s. While these studies have their limitations, the trends in data appear to be like those seen in studies evaluating pediatric specimens compared to adult specimens in other studies. Two sets of femoral specimens were evaluated by Hirsh et al. using tensile testing where one set was from 7 infants, who were six months of age and younger, and the other was from one 14-year-old male (Hirsch & Evans, 1965). If possible, multiple specimens from each subject were obtained where the maximum number of specimens was four from the 14-year-old. The ultimate tensile stress, tensile strain, and tangent elastic modulus were compared for the two sets. The ultimate tensile stress and average tensile strain were higher for the infant specimens. The modulus was less than that of adult specimens. The test methodology had many potential factors that could output less

reliable results such as: (1) the heat of the machining and other procedures used to procure the test specimens, (2) not all specimens were composed entirely of compact bone due to the size of the femurs, and (3) influences of the setup such as the epoxy of the strain gauge and the grips on the bone specimens used during testing.

Currey and Butler evaluated 18 femoral cortical specimens from subjects ranging between two and 48 years old (Currey & Butler, 1975). The bone specimens were not obtained from the same site of the bone which may not allow for a reliable comparison between samples. Three-point bending testing was conducted with a 5mm/min rate of loading until fracture occurred. Bending strength was evaluated based on the outcomes of this testing where the mean strength of the children was lower than that of adults. The elastic modulus had also increased with age. The work absorbed for the children was consistently higher than that of the adult bone specimens.

A couple of different studies evaluated cortical specimens and their flexural bone material properties for those who have osteogenesis imperfecta. A study conducted by Albert et al. evaluated cortical bone of the humeral diaphysis and femoral diaphysis from specimens that had osteogenesis imperfecta using a three-point bending test (C. I. Albert, Jameson, & Harris, 2012). To evaluate the test setup, the researchers first used bovine and acrylic specimens. The validated test method, which was found to be able to be used on specimens as small as 5mm in length, was then conducted on two pediatric specimens with osteogenesis imperfecta. The mean elastic modulus was 4.5GPa and 5.1GPa for the two specimens. The yield strain was 1.66% and 1.43%. The flexural strength was 94MPa and 74MPa for each specimen. The study was able to characterize the flexural properties of two pediatric specimens with osteogenesis imperfecta.

Another study conducted by Imbert et al. compared the mechanical properties and the microstructural properties between healthy subjects and those with osteogenesis imperfecta (OI) treated with bisphosphonates (Imbert, Aurégan, Pernelle, & Hoc, 2015). They also aimed to establish correlations between mechanical and microstructural properties within the osteogenesis imperfecta population to determine the major factors involved in the bone fragility because of the disease. The specimens were scanned using a high-resolution X-ray computed topography with two calibration phantom inserts ($0.25g/cm^3$ and $0.75g/cm^3$ of hydroxyapatite). Uniaxial compression testing was conducted with a 10N pre-load and a displacement rate of 0.7µm/s. The specimen was first loaded to 100N, unloaded, and then loaded to fracture. Loads and displacements were measured with the use of a 2.5kN load cell and extensometer, respectively. The Young's modulus was calculated. A scanning electron microscope was used to determine the number of osteocyte lacunae. Mechanical properties were found to be significantly lower in bones with osteogenesis imperfecta. The average Young's modulus was 4.0GPa for OI subjects and 1.9GPa for healthy subjects. The specimens from the subjects with osteogenesis imperfecta were also found to have a much higher porosity and a higher osteocyte lacunar density. Mechanical properties appeared to have a negative correlation with porosity but no significant correlation with the osteocyte lacunar density.

There are also studies which have evaluated pediatric specimens of other anatomical sites such as the ribs. Agnew et al aimed to characterize the difference in the structural properties of the ribs in a dynamic loading pattern which simulates a frontal impact across a wide range of ages spanning from pediatric to elderly specimens (Agnew, Schafman, Moorhouse, White, & Kang, 2015). The ages included in this study were six

years old to 99 years old. There were 140 specimens from 70 subjects. A bending test was conducted using a 54.4kg pendulum to impact the ribs at a rate of either 1 or 2 m/s. Data such as fracture location, displacement, force at fracture, and linear structural stiffness were recorded. Displacement in the x-direction which was defined as the primary loading axis and the structural stiffness both significantly decreased with age. The force at fracture appeared to have peaked around 25-40 years old.

3. Animal Studies Evaluating Immature Femurs

Since there is a scarcity of pediatric femoral specimens, especially infant specimens, immature animal bone has been used to evaluate mechanical properties. Animal studies allow for an initial investigation of these properties to be able to better understand how fractures may occur in infants.

A study conducted by Koo et al. used an immature porcine model to determine if there is a relationship between noninvasive bone mass measurements and bone strength of the femur and humerus (Koo, Yang, Begeman, Hammami, & Koo, 2001). Twelve piglets, who were between 6 and 68 days old, were scanned using a fan beam densitometer to obtain the areal bone mineral density, bone mineral content, and the bone area. The femora and humeri were then dissected from the sacrificed piglets. Three-point bending tests were conducted to evaluate the strength. The femora rested on their anterior surface. A displacement rate of 1mm/sec and 0.1mm/sec was used to apply the loads to the femora and humeri, respectively. The loads and displacements were recorded throughout the trial until it had fractured where the point of fracture is where the maximum force and displacement values were recorded. The energy to bone failure, fracture moment, and

31

flexural rigidity were calculated from the load-displacement curves. Pearson correlation analysis and the Bland and Altman method were used to determine the relationship and agreement of the left and right side of the humeri and femora. This was also done to evaluate each of the bone strength measurements calculated previously. Regression analysis was used to evaluate whether the bone mass measurements could be used as predictors for the bone strength measurements for each set of bones. The left and right sides had correlated well for both the bone mass and strength measurements. The bone mineral content and density had a higher correlation with the bone strength measurements than the bone area. The bone mass measurements had a stronger correlation with the fracture moment than energy or flexural rigidity measurements. The researchers demonstrated that there was a positive correlation with bone mass measurements (bone mineral density and content) with bone strength measurements. These bone mass measurements were predictive of the bone strength with r^2 values greater than 0.90.

Another study conducted by Pierce et al. had also used an immature porcine model to evaluate the ability to predict fracture loads using Dual-Energy X-Ray Absorptiometry (DXA) (Pierce, Valdevit, Anderson, Inoue, & Hauser, 2000). Three-point bending and torsional loading conditions were used to cause transverse and spiral fractures, respectively. Twenty-two porcine femora where the donor age range was from three to twelve months, were tested. The bones were first DXA scanned to obtain both anteroposterior and lateral views. The geometric dimensions, bone mineral content, and bone mineral density were obtained from these scans. 15 femora were tested using three-point bending where the force was applied at a displacement rate of 1mm/s to the lateral aspect of the mid-diaphysis. The maximum force was defined as the point of fracture during

the testing. The torsional testing was conducted for the remining femora where the force was applied at a rate of one degree per second. Of the first five femora tested, only one resulted in a spiral fracture while the others resulted in a fracture at the growth plate. The test setup was adjusted so that only half the area between the growth plates of the bone were exposed where only one of the two remaining specimens tested had resulted in a spiral fracture. Linear regression was used to identify correlations between the bone mineral content, bone mineral density, geometry, and failure load for the three-point bending group. Due to the different type of resulting fractures in the torsional loading group, a regression was not performed. The failure load ranged from 530N to 1024N and from 1.383Nm and 3.559Nm for the three-point bending and torsional loading conditions, respectively. The total bone mineral density ranged from 0.288 to 0.369. The strongest correlation with an r^2-value of 0.92 for the bending parameter was with the observed failure load moment. An empirically derived formula resulted in a strong linear correlation with the mechanical bone strength where the bone mineral content and bone mineral density were directly correlated and the geometric measures (the outer and inner width of the femoral shaft) were inversely correlated. The researchers demonstrated a relationship between the bone mass measurements and the bone strength for the bending loads while the torsional test setup would need future additional investigation to be able to consistently achieve spiral fractures.

Other studies have also looked at how specific types of fractures can be generated. A study conducted by Thompson et al. had used an immature porcine model to investigate classic metaphyseal lesion which commonly occur at the distal femur for abused children (A. Thompson, Bertocci, Kaczor, Smalley, & Pierce, 2015). A classic metaphyseal lesion

is a fracture through the immature metaphyseal bone near the growth plate. The 26 porcine pelvic limb specimens, obtained from three- and seven-day old piglets, were tested in lateral varus and valgus bending conditions. The limbs were removed from the body and the ankles were also removed so that only the femur, tibia, and knee joint remained. The skin was removed, and the soft tissue was kept intact for testing. Holes were drilled in the proximal femur, distal tibia, and the knee was fully extended. The holes were used to insert pins which were then potted. A four-point bending configuration was then used. The direction of loading was adjusted to induce either a varus or valgus bending moment. Preliminary testing conducted at a rate of 42.3mm/s until fracture was used to estimate the magnitude of failure and associated fracture type. These preliminary tests resulted in failures at the growth plate. Since the intended classic metaphyseal lesion were expected to occur before this failure at the growth plate, the peak loads were set to be at 50-85% of the loads determined in the preliminary testing. Testing was conducted on the remaining specimens were conducted at the same loading rate with varying peak loads determined from the range above until the peak load was reached. A micro-computed tomography scan was used to verify if a classic metaphyseal lesion occurred. These lesions were identified in 12 specimens where five were from the 7-days old specimens. This occurred in both loading directions with peak applied bending moments of 3.2Nm-5.4Nm and 5.4-6.8Nm in the 3-day old and 7-day old specimens, respectively. Most of the fractures occurred at the medial aspect of the bone regardless of the loading condition (varus or valgus). The researchers demonstrated that the metaphyseal lesion or fracture could be induced by the varus or valgus loading condition where future work would investigate other loading conditions that may be able to produce this fracture as well.

Another study conducted by Theobald et al. had investigated spiral fractures using torsional loading of immature ovine long bone of 7-day old calves (Theobald, Qureshi, & Jones, 2012). Thirty-two specimens were separated into eight groups for testing different applied rotational velocities to failure. A hole was drilled at the epiphyseal center of rotation to place in the housing to be used in a torsional servo-hydraulic testing machine. The rotational velocities applied ranged from 0.5 to 90 degrees per second and the specimens were loaded to failure. All bones resulted in a spiral fracture, but six specimens were excluded due to potting material failure. The highest rate of fracture (90 degrees per second) resulted in three pieces after fracture instead of two for all the other loading rates. Normalized fracture angles of the fractures were calculated, where the normalization was with respect to the narrowest diaphyseal diameter and resulted in a linear relationship with the rotational rate applied ($R^2= 0.78$). While the loads to fracture were not reported, the researchers were able to create a relationship between the resulting fracture angle and the rotational velocity applied.

D. *In-Silico* Femur Models and Risk of Fracture Assessment

Finite element analysis has been used to effectively evaluate the risk of femur fracture. The relationships and properties discussed in previous sections can be used in finite element analysis to define the material properties of a femur. Finite element analysis allows for evaluation of the loading conditions observed in ATD studies without the need for bone specimens by developing models based on CT scans.

1. Development of *In-Silico* Models and Application of Material Properties

To develop a relevant *in silico* model, it is important to be able to accurately derive the material properties. The first step in doing so requires calibration of the CT scan to be able to use the appropriate Hounsfield Unit values for determination of material properties such as the Young's modulus of the bone. This can typically be accomplished by using a calibration phantom in the scans. For our study, the reference scan did not include a calibration phantom. Therefore, it was important to find alternative methods. Other considerations to develop this model would need to be made since the reference CT scan was not a high-resolution scan as is typically considered for use in finite element analysis.

A phantom-less calibration method used by clinicians to be able to evaluate bone mineral density levels in scans where a calibration phantom may not have been available. One study conducted by Budoff et al. used phantom-less calibration methods for coronary artery calcium (CAC) CT scans (Budoff et al., 2013). By applying this only to CAC CT scans, the researchers could use a larger range of scans that used the same scanning protocol. The purpose of this study was to determine the accuracy and precision of using calibration factors to determine the bone mineral density measurements. These scans were completed across 14 commercially available CT scanners with one of two phantoms that contained either three (0, 75, and 150 mg/cc) or four (0, 50, 100, and 200 mg/cc) inserts of calcium hydroxyapatite. There were three subgroups of data that were analyzed for this study. The first subgroup (n=1536) was used to calculate the general calibration factor for each scanner. The general calibration factor is defined as the ratio of the bone mineral density (BMD) of the specimen, which may be determined by using the

calibration phantom to find this value, to the measured CT Hounsfield value. In the

second subgroup (n=1587) was the application of the phantom-less method was used to

calculate the BMD for three vertebrae and these values were averaged. The phantom-less

BMD value was calculated by multiplying the general calibration factor by the CT

Hounsfield value for the region of interest comprising the vertebrae. The third subgroup

was used to analyze factors such as sex, spinal site, section thickness, and image

acquisition protocol. The third group was then scanned on the same scanner and had an

additional typical helical CT scan of the chest, abdomen, and pelvis. The individual

calibration factor which is the true density of the 150 mg/cc insert of calcium

hydroxyapatite divided by the CT Hounsfield unit was calculated for each scan to

compare the differences due to sex and the location of the calibration along the vertebrae.

A comparison between the calibration factors for phantom-less BMD and the quantitative

CT BMD across the scanners and between groups were conducted. It was found that both

the individual and general calibration factors had a statistically significantly variation

across and within CT scanner models. Between the phantom-less and CT BMD values,

there was no significant difference and a significant positive correlation as well. There

was also no significant difference for the individual calibration factors calculated for

group three between the sexes and between the location of the calibration. The

researchers had concluded that the calibration factors derived could be applied to

determine the phantom-less BMD values for a CAC CT scan.

The accuracy of applying the material properties of the bones to a finite element

model of the femur has been evaluated by multiple teams. The application of the material

properties generally follows the conversion of the HU of the CT scan to the respective

modulus value. This pathway usually compromises of converting from HU to bone mineral density to ash density to apparent density and finally, to the calculated modulus value. There are different approaches researchers have taken to reduce the number of material properties so that there are not a unique number of modulus values for each corresponding HU value. Further evaluation may consider different failure theories and how the mechanical properties and relationships defined, as seen in the previous section for properties such as the yield strain, can be applied to analyze fracture risk. The following studies considered various parameters of the process to be able to effectively evaluate the loading of an anthropomorphic femur.

The aim of a study conducted by Schileo et al. was to evaluate which of three density-elasticity relationships, which were previously defined in the literature, results in the most accurate strain predictions when applied to an automated subject specific finite element model (Schileo, Taddei, Malandrino, Cristofolini, & Viceconti, 2007). The specimens, which were of the entire femur, came from four pairs of harvested femurs. The specimens were determined to be in the range of osteopenia to osteoporotic as determined by DXA (Dual energy X-ray Absorptiometry). Fifteen strain gauges were placed on each specimen in the metaphyseal and epiphyseal regions of the femur to be used to compare against the finite element results. Six different loading scenarios were applied to generate bending in different planes, axial loading, and torsion. The maximum load applied was 75% of the donor's body weight. The data collection lasted 30 seconds after the load application. The maximum value collected from each strain gauge for each loading scenario was used for validation of the FE models. The FE models were derived from CT datasets of the specimens to create a 10-noded tetrahedral meshed model where

38

a node was placed at each strain gauge center. The model was constrained at the same level constrained for the mechanical testing. The CT scans were calibrated using the European Spine Phantom (a density calibration phantom). The average HU of each element of the mesh was used in the application of material properties. Three different equations from other studies were used for material property definition which related the elastic modulus to the HU value. These equations were:

$$E = 3.790\rho_{app}^{3} \quad \text{(DR Carter \& Hayes, 1977)} \tag{1}$$
$$E = 10.500\rho_{ash}^{2.29} \quad \text{(Keller, 1994)} \tag{2}$$
$$E = 6.950\rho_{app}^{1.49} \quad \text{(Morgan et al., 2003)} \tag{3}$$

where E is in GPa, ρ_{ash} is ash density in g/cm^3 and ρ_{app} is apparent density in g/cm^3. An assumed ratio of ash to apparent density was 0.6 to be able to convert the density values for equation 1. The principal strain values at the specified rosette locations were used to compare to the output of the mechanical testing to FE strains for validation. Linear regression was used to compare the predicted FE strains and the experimental strains. The root mean square error and peak error were also calculated. The use of Eqn. 3 resulted in the highest correlation while the use of Eqn. (1) resulted in the lowest. Equation (3) was the only one that was not statistically significant in difference of the slope and intercept of the regression equation from unity and zero, respectively. The errors calculated for Eqn. (3) were also lower than those calculated for the other material application equations. The researchers concluded that Eqn. (3) relating density-elasticity best represented the femur properties in the FE model.

  Further investigation into improving the accuracy of the finite element model when considering a better estimation of bone density was completed by Schileo et al.

(2008). While the previously cited study by Schileo et al. focused on the density-elasticity relationship and the accuracy of applying those equations, this study focuses on the relation of density values measured by QCT, ash density, and apparent density and the influence of these relationships on the FE model over the range of densities found in a long bone such as a femur. Specimens were obtained from three human and three bovine specimens. The bovine specimens were only used to investigate the ρ_{qct}/ρ_{ash} relationship. The strain outputs obtained in the mechanical experiments mentioned in the previous Schileo et al. study were used in the validation process for these FE models and relationships. The CT scans obtained of the specimens were calibrated using the European Spine Phantom. There were a total of 60 cylindrical specimens from both the human and bovine cortical and trabecular bone. The ρ_{qct} was obtained by determining the average HU value of each specimen while limiting the volume considered to be able to reduce potential partial volume effects. Partial volume effects occur generally on the outer surface of the bone where voxels comprising of bone and the surrounding tissue will result in a reduced HU value. The reduced HU value could result in a false increase in stress or strain values on the outer surface when evaluating the FE model due to the partial volume effects. The ρ_{app} was calculated based on the wet weight/bulk volume of the specimen. The ash density was derived from the specimen's ash weight versus bulk volume. The relationships of QCT density, ash density, and apparent density derived from these 60 specimens were used to apply to the FE models. Eqn. (3) is the applied density-elasticity equation. A Poisson ratio of 0.3 was assumed. The linear regression for the ρ_{qct}/ρ_{ash} relationship for the cortical bone, trabecular bone, and the pooled values all had an R^2-value greater than 0.9 where the pooled trabecular and cortical specimens

40

linear regression resulted in the highest R^2-value of 0.997. The ρ_{ash}/ρ_{app} linear regression also had the best R^2 of 0.99 for the pooled specimen equation than the regressions considered cortical and trabecular separately. The error and correlation of the strains valued in this study compared to the previous Schileo et al. study resulted in a lower root mean square error, maximum strain error, and a greater R^2-value of the linear regression when comparing the FE model to the experimental data. The authors attributed the improved measures to a more accurate estimation of the apparent density resulting in a more accurate subject specific FE model.

A study conducted by Dragomir-Daescu et al. used Mimics (Materialise, Ann Arbor, Mi) to develop a subject specific finite element model of a femur (Dragomir-Daescu et al., 2011). This study investigated the convergence and robustness of their developed finite element models derived from QCT scans of the femur using experimental test data. Two sets of nine human adult femurs were obtained where each set consisted of three healthy, three osteopenic, and three osteoporotic specimens. The first set was used as the training set to derive parameters for the bone damage criterion. The second set was used as the validation set using the parameters determined by the first. Both sets would undergo mechanical testing. The bone damage criterion was based on the yield strain of the model. The yield strain was assigned a relationship with the ash density which was optimized to improve the agreement between the experimental and predicted fracture forces in the training set. The femora were scanned using QCT both before and after experimental testing. Applied loading simulated a sideways fall onto the hip where the shaft was fixed in place while the load was applied to the greater trochanter. Bones were loaded to fracture. Load cells at the femoral head and the

trochanter were used to measure vertical reaction forces. Another load cell was at the end of the fixed shaft measuring the triaxial moment and force components. In the finite element model, three uniform meshes were generated with maximum edge lengths of 5.0mm, 2.5mm, and 1.5mm. Another mesh method was also applied where maximum element edge length varied at different regions of the femur. The mean HU was calculated for each element. The material properties, which included relationships relating the Young's modulus and yield strain to the density, were applied to these elements based on 21 or 42 discrete bins across the distribution of the elements' HU values. To evaluate the displacement which corresponded to the ultimate load, the training set incrementally loaded the femur where after each step the elements whose von Mises strain exceeded the yield strain were adjusted such that their modulus was adjusted to 0.01MPa. There was no statistically significant difference in the estimation of stiffness and ultimate load for the two different sets of discrete bins to define the material properties. The linear regression model which used the training set derived stiffness and the femoral neck areal bone mineral density values. The stiffness predictor had an r^2-value of 0.87. The R^2-values for the predictor of the training set estimated ultimate load in the linear regression evaluating the model for the experimental ultimate load was 0.93. The predicted fracture patterns in the validation set had generally good agreement with the experimental results.

An additional aspect that must be considered when evaluating the application of the mechanical properties of the bone is the choice of the failure criterion that would be able to identify potential fractures of the bone. Multiple studies have evaluated which failure criterion would be able to best predict failure.

A study conducted by Schileo et al. evaluated femur fracture using the maximum principal strain as the failure criterion (Schileo, Taddei, Cristofolini, & Viceconti, 2008). Three femurs which had ranged from osteopenic to osteoporotic were scanned and then tested to experimentally simulate the reaction forces at the hip joint. The condyles were constrained while the load was applied at a constant displacement rate of 2mm/s to the head of the femur. The femurs would generally fail (or fracture) within 2-4 seconds. A high-speed camera was used to observe the location of the fracture which was then compared to the resulting fracture locations of the FE models. FE models were created for each of the femurs where different failure criteria could be evaluated. A linear FE model was used since the researchers were focused on identifying the criteria that would best characterize the conditions at the onset of failure. These failure criteria included (1) maximum principal strain with tensile and compressive limits used, (2) von Mises stress criterion, and (3) maximum principal stress criterion with tensile and compressive limits used. The results demonstrated similar failure patterns for the stress-based failure criteria (2 and 3) while the strain-based criterion differed. The region of failure was smaller for the strain-based criterion compared to the stress-based criteria. The distance to the experimentally determined locations of failure was approximately doubled for the stress-based criteria for the median and maximum value compared to the strain-based criterion. The stress-based criteria also demonstrated more clusters of elements further from the locations of failure. The researchers concluded that the strain-based failure criterion was better able to correctly identify the level of failure risk and the location of the fractures in all of the specimens.

Other studies have used the Drucker-Prager yield criterion which accounts for the contribution of hydrostatic stress in evaluating failure such as a study conducted by Bessho et al. (2007). The experimental testing involved uniaxial compressive loading of the specimens of 11 femoral specimens. FE models were developed where each element had defined density-dependent relationships for both the Young's modulus and yield stress. A nonlinear analysis was conducted where a bilinear elastoplastic relationship was used, and the assigned post-yield modulus was set as 5% of the elastic modulus. To evaluate failure in the model, the Drucker-Prager equivalent stress of an element was compared to the yield stress of that element. Outcomes including yield loads, fracture loads, and principal strains predicted in the FE models had significant correlations with the experimental data with the lowest R-value being 0.941. Other studies such as one conducted by Koivumäki et al. used a set of criteria to identify fracture locations (Koivumäki et al., 2012). This study also conducted a nonlinear FE analysis with the same approach of defining the post-yield modulus. The Drucker-Prager was used as yield criterion where the yield stress values were dependent upon the density of the element and separate yield-density relationships were defined for cortical and trabecular bone. Maximum principal stress criterion was used for failure in tension where the stress exceeded the ultimate tensile stress. Minimum principal strain was used for determining failure in compression where a value lower than -7300 microstrain was the failure threshold. The experimental testing simulated loading of a sideways fall onto a femur using 61 femora. The correlation between the experimental and predicted fracture load was high (R=0.931).

A limitation of using FE models to evaluate femur fracture is having failure criteria that can be attributed to partial volume effects. Partial volume effect occurs along the edges of the bone where the voxel of a CT scan may contain both bone and the surrounding soft tissue which lowers the HU of that voxel. Since fracture criteria can be dependent upon properties that are based on the density of the bone which is often defined by the HU values, this can result in failure occurring on the surface of the bone when there should not be. Some researchers have included additional criteria such as in a study by Keyak (2001) where a yield strain threshold was used but 15 contiguous, non-surface elements must have failed for it to be considered a fracture. Other studies such as one by Pistoia (2002) have specified a certain volume of the bone, which in this case was five percent of the bone, must have exceeded the specified thresholds to identify potential fractures.

2. Femur Injury Studies Using an *In-Silico* Model.

Hip fractures and femur injuries due to falls for the elderly is of a particular interest for many studies. These studies have demonstrated that it is possible to use an *in-silico* femur model with boundary conditions representative of a fall to estimate whether a fracture would occur and if so, the location of the fractures.

A study conducted by Trabelsi et al. demonstrated that an in-silico femur model could accurately predict femur fracture when compared to testing completed on human cadaveric femurs (Trabelsi, Yosibash, Wutte, Augat, & Eberle, 2011). The researchers conducted a double-blind validation study of their patient specific FE femur model. The researchers that created and evaluated the FE models differed from those conducting the

cadaveric femur experiments so that the knowledge of the results from either part of the study eliminating any potential influence on the outcomes. The 12 cadaveric femurs tested, which were obtained from 6 subjects where the left and right femur were used, were scanned using a QCT with a calibration phantom. Strain gauges and optical markers were used to determine strain and displacement values on the bone surface. Five uniaxial strain gauges were applied to the superior neck, inferior neck, and the medial shaft, lateral shaft, and the lesser trochanter. Optical markers were used to evaluate the local displacement of the bone for eight or nine locations on the femur. The distal end of the femur and the femoral head were both potted. The distal end was fixed while the femoral head was where the load was applied. Axial compression tests were conducted to be able to obtain the axial bone stiffness. This stiffness value was an average calculated from the linear force displacement curve of the loads between 200N and 1000N from three trials that were conducted for each femur. The FE model was developed based on the QCT scans. The geometry was then divided into cortical and trabecular regions where a calibrated bone mineral density value of 0.45g/cc was used as the threshold. The mesh was composed of tetrahedral elements where the total number of elements was generally 5000. The boundary conditions were representative of the experimental setup where the femoral head was load loaded to 1000N. Material properties were applied based such that the cortical and trabecular regions had different density-elasticity relationships. Strain, local displacement, and stiffness from the FE model and the experiment testing were compared by using a regression analysis. Both the displacement and strain categories demonstrated good agreement with R^2-values of 0.93 and 0.95, respectively, while the mean stiffness of the experimental and predicted measurements had a 62% correlation.

Other studies have used FE femur models to evaluate specific fall configurations. Grassi et al used an FE femur model to analyze a sideways fall loading configuration (Grassi et al., 2012). Three human cadaveric femora were evaluated both experimentally with the use of 16 triaxial strain rosettes and using an FE model. The FE models were developed using the same method as done by Schileo et al. (2008). The femora were fixed so that the distal two-thirds of the bone were potted. Each femur was tested in 12 different configurations which were a combination of different longitudinal rotations and different degrees of adduction. The loads were applied to the femoral head non-destructively and the strain rate was limited to 0.005/s. Each loading configuration was replicated 6 times. A regression analysis comparing the strains and displacements outcomes from the model to the experiments which resulted in a coefficient of determination greater than 0.9. While the regression analysis resulted in relatively good agreement, the root mean square error was 5-11% for the specimens in the study. Since the bone was not modeled as an anisotropic material, the predicted minimum principal strains were consistently overestimated. The researchers note that this overestimation could also be due to the partial volume effect when developing the FE model.

FE models have also been used to evaluate specific aspects of a fall such as fall direction. Bessho et al. used FE femur models to evaluate the difference in predicted fracture load and site with changing load and boundary condition (Bessho et al., 2009). Instead of cadaveric femurs, this study used femur CT scans from 42 patients that had experienced a hip fracture due to a fall. CT scans were obtained from each of these patients to develop a FE model which resulted in 42 FE femur models. A nonlinear FE analysis was conducted where the post-yield modulus was set as 5% of the elastic

modulus. The failure in tension was defined as the maximum principal stress exceeding the element ultimate stress which is 0.8 times the yield stress. The failure in compression was defined using the Drucker-Prager criterion when yielding and failing when the maximum principal strain was less than negative 0.01. Five different loading conditions were applied to the model including four falling configurations and one stance configuration. The fall loading configurations were adjusted so that the angle of loading onto the femoral head was adjusted so that it matched different potential landing configurations of a fall. The loading direction varied based on two different angles which were the angle with respect to the long axis of the femur in the coronal plane and the angle with respect to the femoral neck axis in the axial plane. Difference in fracture loads were evaluated across the different loading conditions. The results indicated that the strength of the femur was greater for a lateral fall than a posterolateral fall. The general location of fractures under the different loading conditions was also evaluated. For example, trochanteric fractures were most frequently predicted form of fracture except for the fall loading condition where the long axis of the femur is parallel to the ground and the load is applied at a 120° from the long axis of the femur, where femoral neck fractures were also predicted to have occurred. This fall loading condition best correlated to the fractures observed in the 42 patients. These results may allow physicians to provide better guidance to patients for prevention of fractures.

Other researchers, such as Bryan et al., have used subject specific FE femur models to consider larger populations to evaluate whether anatomical differences could be an important factor in predicting fracture (Bryan et al., 2009). These researchers developed a statistical model of a femur which was then used to generate 1000 virtual

femora. The statistical model was developed by using 21 subjects' CT scans. These scans were then used to develop a mesh that accounted for differences in geometry and bone mineral densities. This was completed by taking a base tetrahedral mesh where registration of this mesh onto each training subject's scans would allow for calculations of the deviations of the mesh of each training subject's scan at key locations from the base mesh to develop the statistical model. The loading conditions were applied to simulate an oblique fall backwards and to the side. Evaluation of the results showed that 28 of the femurs generated were at the highest risk of fracture. The volumetric percentage of cortical bone in the proximal femur was an important predictor as to the likelihood of a fracture occurring.

To the best of our knowledge, a study conducted by Li et al. is the only study of an infant femur evaluated using an *in-silico* model (Li et al., 2015). While this study did not compare the outcomes to a cadaveric study, it does take the assumptions and methods used to evaluate the risk of fracture of adult femora to evaluate infant femora such as those used by Ohman et al. (2011), Bayraktar et al. (2004), and Schileo et al. (2007). The main objectives of this study were to develop an *in-silico* adult femur model to femora from children 0-3 years old, accurately model the geometry and mechanical properties of these femora, and to perform a preliminary finite element analysis of the pediatric femora undergoing four-point bending. There were 15 sets of post-mortem QCT scans. A threshold level of 350 HU was used in the segmentation process as the threshold for the identification of ossified bone. The elasticity-density relationship (Eqn. 3) was used to apply the material properties. The finite element mesh consisted of 10-node tetrahedral elements. The boundary conditions were applied in accordance to a four-point bending

49

loading mechanism. Different loading conditions were considered where the orientation

was rotated in 10° increments around the longitudinal axis of the shaft with the same load

applied in each scenario. The maximum first and third principal strains were evaluated at

each node in region in the model for each orientation. This region spanned a portion of

the shaft surrounding the central point between the two forces applied. Loads were

incrementally increased by 10N until failure occurred. The predicted failure force for

each scenario was determined when the maximum first principal strain exceeded a yield

value of 0.73%. The yield value of 0.73% was the tensile yield strain of cortical bone

obtained from adult specimens as determined by Bayraktar et al. (2004). Further details

of the Bayraktar study is described in the "Mechanical Properties of Adult Bone" above.

The forces predicted to fracture the bone ranged from 120N to 1040N. The comparison of

the maximum first principal strain when the forces applied in the anterior-posterior (AP)

direction versus the medial-lateral (ML) direction illustrated that subjects younger than 6

months had a slightly higher strain in the AP direction while other ages were more

dependent on the difference in the diameters in each direction.

E. Using *In-Silico* Models to Evaluate Pediatric Femur Injuries Related to Child Abuse

In the field of pediatric injury biomechanics, few studies have evaluated the

biomechanics of the pediatric femur which is especially true for infants. Household falls

are a fairly common accidental injury mechanism as described in many clinical case

studies (Hinton, Lincoln, Crockett, Sponseller, & Smith, 1999; Togrul, Bayram, Gulsen,

Kalaci, & Özbarlas, 2005) especially for children younger than 6 years old. However,

femur fractures in non-ambulatory children have been found to be more likely due to

abuse. Research that aims to distinguish accidental and abusive femur fractures still needs more biomechanical evidence to better make this distinction. While there are still questions surrounding aspects of the finite element modeling process of the infant femur, including defining the failure criteria and whether the material property application used for adults is applicable to children, an *in-silico* femur model can be used to better understand the distribution of stress and strain values that occur due to accidental household falls. To the best of our knowledge, only one study conducted by Li et al. (2015) has evaluated infant femur injury but they only considered a bending loading condition. The *in-silico* femur model created for this study will be used to evaluate loads from previous testing of experimentally simulated household falls. The creation of this model will consider results from other studies such as one by Dragomir-Daescu et al. (2011) where they had used Mimics to apply the material properties and determined that the use of 21 or 42 bins did not result in statistically significant difference in outcomes. Another important aspect of the evaluation of the loads using this model is to determine the likelihood of fracture. Since the CT scan used as the basis for the *in-silico* femur model for this study had a bone enhancement algorithm applied, the maximum principal strain failure criteria used by Schileo et al. (2008) will be used since it is one of the theories that does not have a dependency on the density of the bone to define this criterion. The resulting distribution of stress and strain under these household fall conditions will help to further the understanding of the risk of injury of the femur due to common accidental household falls.

III. RESEARCH DESIGN AND METHODS

The purpose of this study is to investigate the likelihood of femur fracture of a healthy 12-month-old child in short-distance household falls using an *in-silico* model. The methods will follow the extraction of the model from the CT scan, the material application, development of the FE femur model and boundary conditions, validation of the geometry using a bone surrogate through comparison of the FE model predicted and experimental strains, FE analysis based upon ATD loading from experimental trials, and evaluating the outcomes of the FEA.
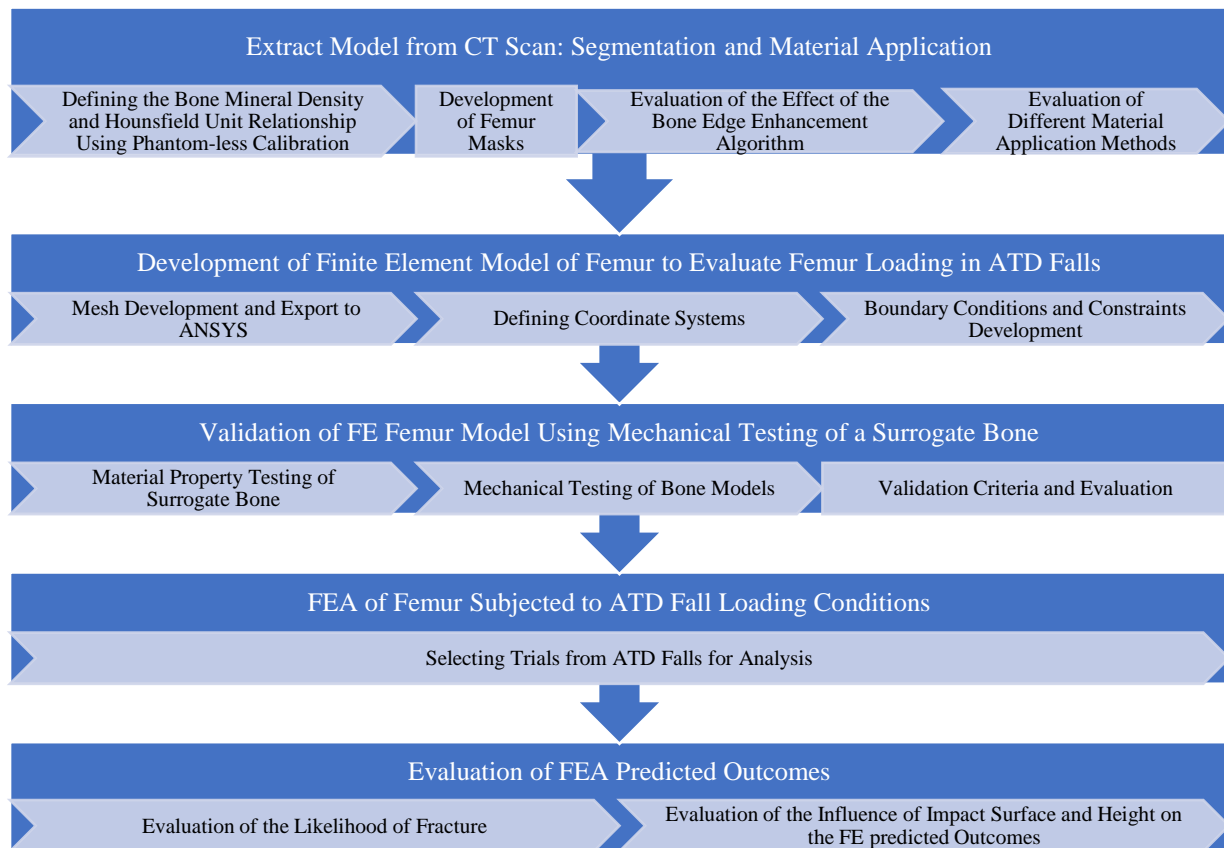
FIGURE 3. Flowchart of Research Design and Methods section.

A. Segmentation and Material Property Application

CT scans were obtained from the University of New Mexico (UNM) Radiology-

Pathology Center for Forensic Imaging. CT scans were performed using a Philips Brilliance Big

Bore with a scan resolution of 0.499 x 0.499 x 1.00 mm^3. A scan of an 11-month old child's

femur, which was the basis of the geometry of the diaphysis for the modified femur assembly of

the CRABI ATD used in simulating household falls by Thompson et al. (2018), had been

conducted using a bone enhancement algorithm. Further details of the modified femur assembly

can be found in section B (Biomechanical Testing Using Anthropomorphic Test Devices) of the

background. Mimics v15.0.1 (Materialise, Ann Arbor, MI) was used to segment the femur from

the lower extremity to create a 3D model. Several aspects of the original CT scan needed to be

addressed before further work could be conducted. The first issue was that the scan did not have

a calibration phantom which is necessary for accurately converting Hounsfield unit (HU) values

to the applied material properties. The second issue needed to address the post-processing bone

edge enhancement algorithm which affected the HU values of the CT scan.

1. Defining the Bone Mineral Density and Hounsfield Unit Relationship Using Phantom-less

Calibration

Since the CT scan to be used for development of the *in-silico* model did not have a

calibration phantom at the time of the scan, performing a phantom-less calibration was

necessary. Eight additional CT scans were obtained from UNM that used the same scanner and

similar scanning protocols; these scans included an Image Analysis Solid Calibration Phantom

(Figure 4). The selected scans were obtained from other children whom ranged in ages from 9 to

21 months old. The calibration phantom had three cylinders with different densities of calcium

hydroxyapatite (0, 75, and 150mg/cc) embedded in a resin that has a water-equivalent HU value. In Mimics, 16-mm diameter cylindrical objects were created for each insert of the phantom. Masks, or a named selection of the voxels of the scan, were then created for each cylinder. The mean HU value of each mask was obtained from the mask properties. This was repeated for each scan. The mean HU values of the cylinders were input into Excel along with the corresponding bone mineral density of the cylinder and the bone mineral density vs the HU value were plotted. Excel was then used to determine the linear regression for the relationship between the Hounsfield unit and the density of the calcium hydroxyapatite (CaHA). This equation was then used in the first step of applying the material properties to the femur model.
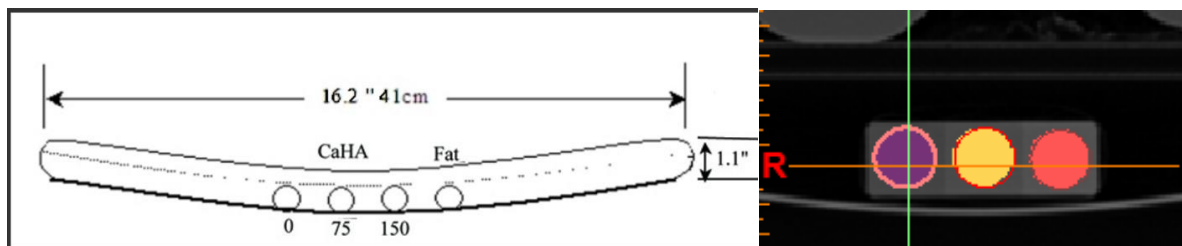
FIGURE 4.(Left) Image Analysis Solid Calibration Phantom figure.[1] Note: The fat equivalent insert was not included in the calibration phantom used in these scans. (Right) Example image of a calibration phantom in a scan where the colored circles represent cylinders of differing CaHA density. Purple, yellow, and red are the 0, 75, and 150mg CaHA/cc respectively.

2. Development of Femur Masks

The pre-defined thresholds in Mimics for pediatric cortical (586-1735 HU) and trabecular (156-585 HU) bone were used to create the masks. A whole bone threshold (156-1735 HU) was applied to be able to define the bone segments. For the enhanced scans, the upper threshold of the whole bone threshold value was adjusted to 2976 HU to ensure that the upper limit was not lower than the highest HU value in the femoral bone region. The region grow function in Mimics

---

[1] Retrieved from http://www.image-analysis.com/phantom

was used to segment the femur. This resulted in the mask of the femur which will be referred to as the whole bone mask. A new mask was created by applying the pediatric cortical threshold (586-1735 or 2976 HU). The boolean operation intersect was used to define the cortical regions of the femur from the intersection of the cortical threshold mask and the whole bone mask. Another mask was created with an applied threshold for the pediatric trabecular range (156-585 HU). The intersection operation was used once again to create the trabecular mask for the femur. An example of the creation of a cortical mask can be seen in Figure 5.
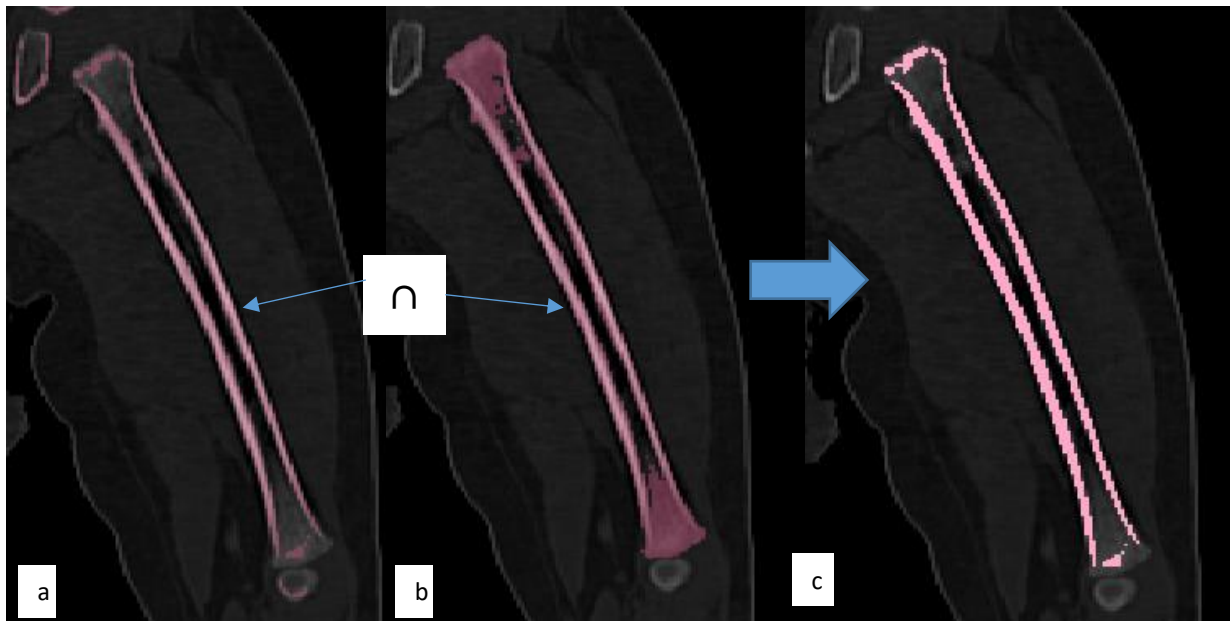
FIGURE 5. Representation of creation of the cortical mask where (a) the cortical threshold is applied and intersected with (b) the whole bone mask to create (c) the cortical mask of the femur.

3. Evaluation of the Effect of the Bone Edge Enhancement Algorithm

Since the CT used for development of the *in-silico* model was modified with an edge enhancement algorithm, further investigation of the effects of this algorithm on the prescribed material properties was necessary. Eight cases obtained from UNM that had both enhanced and unenhanced scans were used for this evaluation. These 8 sets were selected from the available UNM CT scans that had a calibration phantom, had both enhanced and unenhanced scans, and

were ±2 months in age to that of the child of the original scan. Masks in Mimics were created to view the distribution of Hounsfield unit values over each type of scan, enhanced and unenhanced. Mimics can overlay masks from one project of a scan to another project with the same scan that had a different post-processing algorithm used. This is possible since scans with different post-processing algorithms still have the same coordinate systems which is how the masks are defined.

a. Difference in Hounsfield Unit Distribution Between Scan Types. The creation of the whole bone, cortical, and trabecular masks, as described previously, was repeated for both enhanced and unenhanced scans. The masks created in the enhanced scans (hereafter referred to as enhanced masks) were exported and overlaid onto the unenhanced scans of the same subject. When these masks were then exported to a text file, the text file contained the coordinates and HU value of each voxel comprising the mask where a direct comparison of the distribution of the unenhanced and enhanced masks could then be made. For each scan evaluated, a total of 6 masks were created which included three masks (cortical, trabecular, and the whole bone) for each type of scan and the export of enhanced masks to the unenhanced scans. The masks were then exported to their own text files which resulted in 9 total text files for each subject. This process was completed for eight sets of scans. A paired t-test was conducted to determine if there was a difference between the mean HU of the enhanced mask of the cortical and trabecular bone in each type of scan for four subjects (case numbers 230, 329, 331, and 332) where the null hypothesis was that the mean difference is equal to zero ($\alpha = 0.05$).

b. Resulting Geometric Differences Between Scan Types. Another consideration between characterizing the difference between the enhanced and unenhanced scans was the difference in the resulting geometry between the two scans since there were differences in the

56

distribution of HU values. In Mimics, 3D objects of the femur for one case (331) from both the unenhanced scan and the enhanced scan were exported to Solidworks 2015. In Solidworks, planes were created to measure the area of the face at various sections of the femur. These measurements were then compared between the models originating from the enhanced scan and the unenhanced scan to look at the difference due to the enhancement algorithm.

4. Evaluation of Different Material Applications

The results of the previous section indicated that the geometry resulting from the enhanced scan was appropriate to use. The following section covers different material application methods considered.

a. Material Application Methods. Mimics can apply material properties to meshed files and can export them as ANSYS preprocessor files (.txt and .cdb for the material properties assignment and mesh files, respectively). Three different material properties can be applied using Mimics: density, elastic modulus, and Poisson ratio (Table I). The elastic modulus equation was simplified to one equation from two sources: (1) the set of equations used to define the elastic modulus from the equations developed by Morgan et al. (2003) for femoral neck specimens to define the material properties, and (2) the apparent to ash density relationship as used by Schileo et al. (2008).

TABLE I.

MATERIAL PROPERTY EQUATIONS APPLIED IN THE MIMICS MATERIAL PROPERTY EDITOR.

Property	Equation
Bone Mineral Density (mg CaHA/cc)	$0.7157 * HU - 12.591$
Elastic Modulus (MPa)	$0.4969 * \rho_{ash}^{1.49}$
Poisson Ratio	0.3

Note: ρ_{ash} = ash density and the output of the bone mineral density

Two methods were considered to apply the material properties to these bone mesh files. The first method (Method A) applies one set of materials to a mask where each material property is dividing into a specified number of equally spaced across the distribution of Hounsfield values of the part. The properties are then derived from the mean HU of each bin. The distribution of values would be set by the region of the mesh defined by the whole bone mask. The resulting distribution of properties as depicted on the femur can be seen in Figure 6. The notation for Method A will be A-Number where the number is indicative of the number of bins used (e.g. in Method A-5, the mask was divided into 5 equally spaced bins with different material properties based on the HU distribution). The second method (Method B) applies the median value of the cortical and trabecular mask from either the enhanced or unenhanced scan to their respective regions. Figure 8 displays the cortical and trabecular regions to which the material properties were applied for each mask. To evaluate the effect of different material property applications on stress-strain patterns, Method A-5, A-10, A-50, and Method B applications were compared. Based on lack of difference on the resulting outcomes between using 21 or 42 bins for Method A as observed by Dragomir-Daescu et al. (2011), which was discussed in the background section D subsection 1, an arbitrary bin of 50 was chosen to be representative of the true distribution of properties within the bone.

Due to the low resolution of the scans and the enhancement algorithm, which affects the Hounsfield unit values, the lower level bins may have negative density values. To account for this the lowest non-negative density for a material property was used for the material properties in bins with negative HU values for the material application Method A. For example, if the first non-negative density property is material property number four, which would correspond to the

bin of the fourth lowest bin of HU values, material properties one to three would have the same

properties (density and elastic modulus) as material property number four.
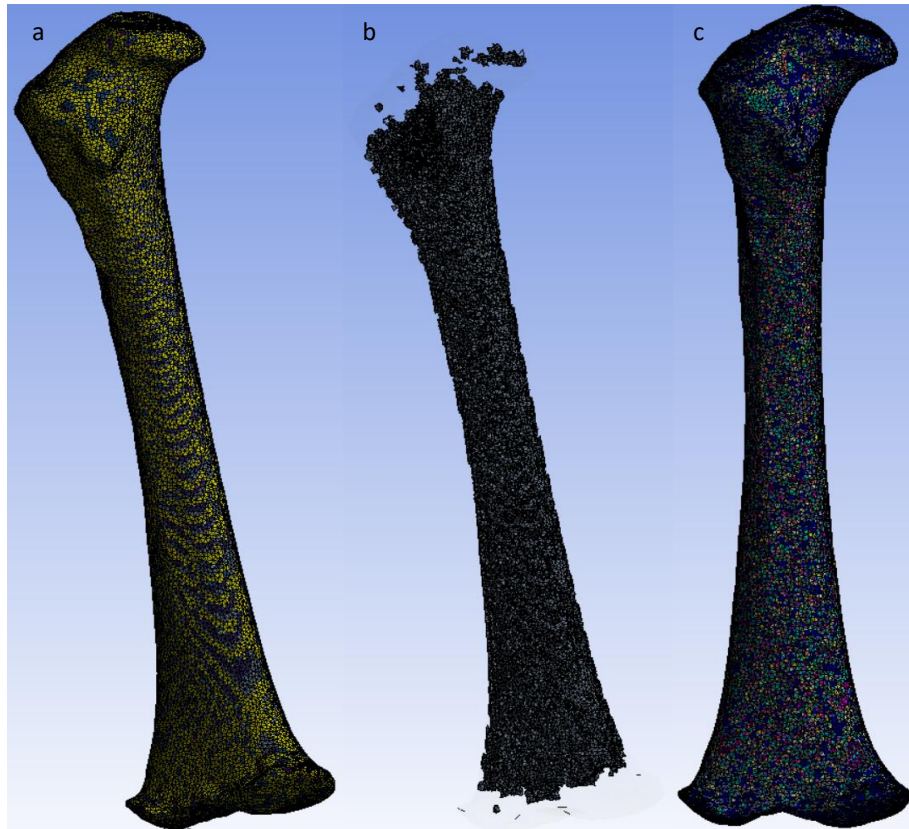
FIGURE 6. Example of the first material application method, Method A. The different colors represent the assigned bin material property for Method A-5 (a) and Method A-50 (c). (b) depicts the region of the 3rd bin of Method A-5 which has an assigned modulus of 9.735GPa.

As seen in Figure 7, the distribution of the material properties based on the HU values is

affected by the application method of these properties to the meshed model. By limiting the

application of the material model to the whole bone mask, which defines its boundaries, it

reduces the amount of negative HU values, which are due to the enhancement algorithm, in the

material application process. This difference can be seen in the transition of the distribution

between part (a) and part (b) of Figure 7. The remainder of the figure illustrates how the number

of bins approximates the distribution of these material properties where 50 bins is the reference

distribution (Method A-50). The 5 bins distribution (Method A-5) tends to skew the peaks of the

distribution differently than the original distribution in part (b).
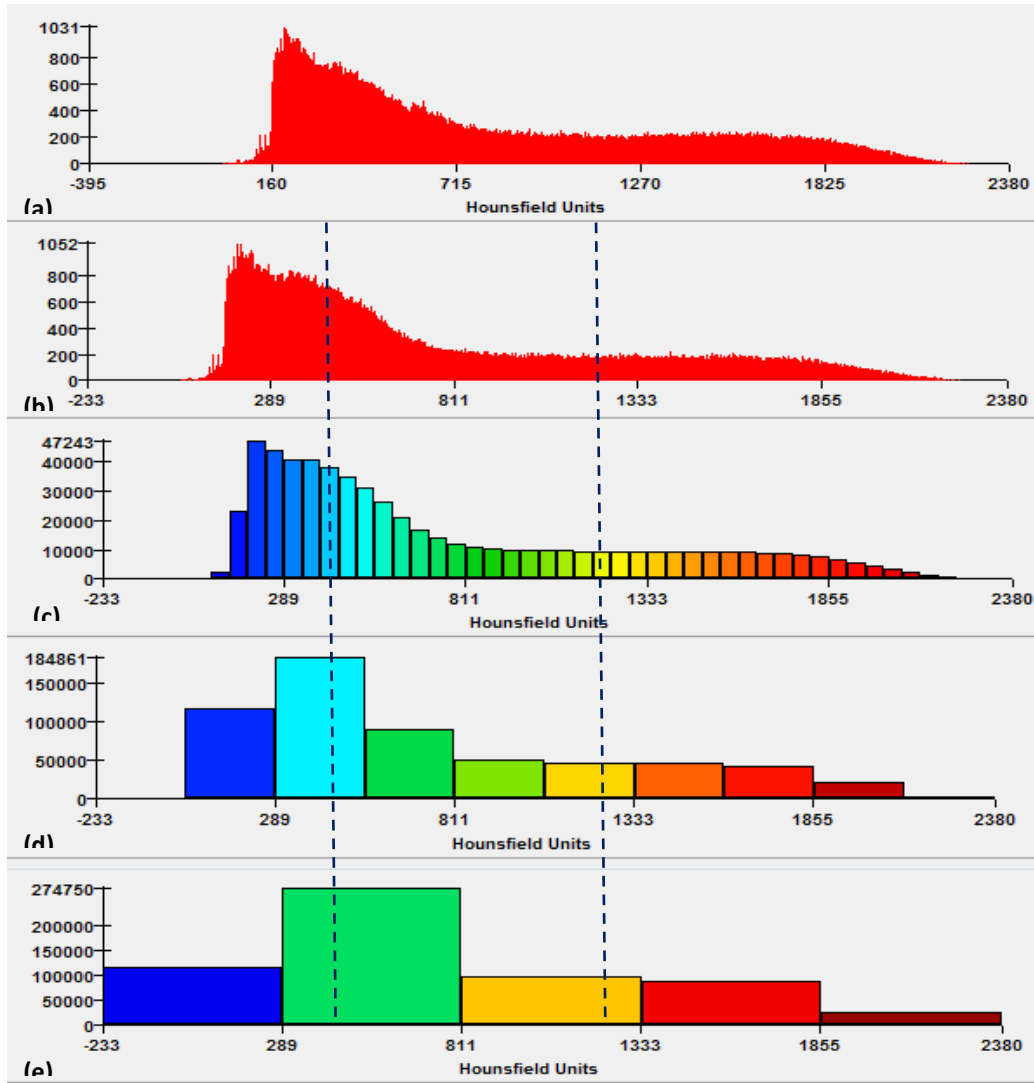
FIGURE 7. Histogram of the distribution of Hounsfield Units for the meshed volume in the material applications window in Mimics. (a) The original distribution before any material application. (b) The distribution when it has been applied to the mask of the femur. The distribution with 50 (c), ten (d), and five (e) bins applied corresponding to Method A-50, A-10, and A-5 respectively. The dotted lines in (b)-(e) represent the median Hounsfield unit values applied for the median mask where the left line is the trabecular median and the right line is the cortical median which are the values used for Method B.

The partial volume effect is where the edges of the bone have lower HU values that

correspond more closely to soft tissue than bone since the voxels share a region with non-bone

segments. Due to the partial volume effect and identified lower density regions on the CT scan

(as seen in Figure 30 and Figure 8), cortical regions along the edges of the shaft were incorrectly

identified as trabecular regions. Methods A and B were modified to account for this occurrence. The trabecular mask was edited to exclude the regions along the shaft that should be classified as cortical. This new mask (TRAB-new) was used to create a new cortical mask (CORT-new), which includes those now removed shaft points, from the whole bone mask. The new cortical and trabecular masks will be used in the same manner in Method B which involves applying the median HU value to their respective regions.
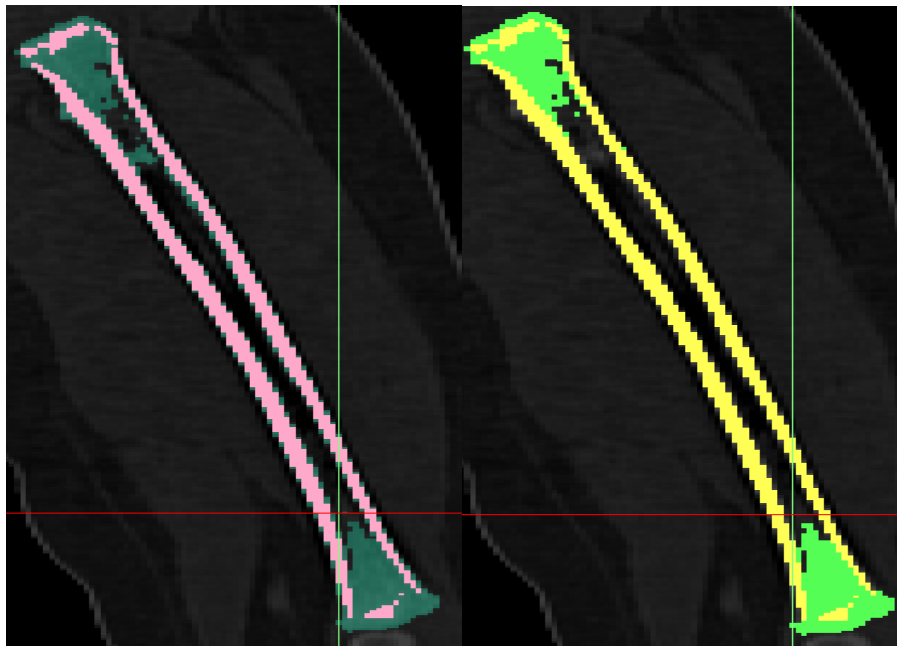
FIGURE 8. The femur with the original (left) and modified (right) cortical and trabecular masks are displayed. The trabecular masks are dark and light green. The cortical masks are pink and yellow. The light green is no longer along the shaft of the bone unlike the dark green which borders the pink along the shaft of the bone.

Method A-50 was also adjusted. A modified whole mask (WHOLE-mod) was created by subtracting TRAB-new from the original trabecular mask to identify the removed regions which will be referred to as the removed region mask. The removed regions were subtracted from the original whole mask to create WHOLE-mod. WHOLE-mod will be used as the mask for application of Method A-50. A summary of this process can be found in Table II. Another application of material properties was applied to the removed region mask to identify the removed regions in the material assignment document. This resulted in an output of two material

assignment documents from Mimics. ANSYS FE Modeler was used to identify the lowest

material number assignment associated with the cortical region of the femur which was material

bin number 27. Since some of the materials applied overlapped with the removed region's

designation when analyzing the output material assignment documents, those that were below

the identified minimum cortical level were replaced with the removed region material. This

modified application of Method A will be referred to as Method A2. Method B will be applied to

the new cortical and trabecular masks created (TRAB-New and CORT-New) and referred to as

Method B2. Figure 9 illustrates the distribution of the elastic moduli for both modified

applications discussed here which includes Method A2-50 and Method B.A summary of the

different material application methods can be found in Table III.

TABLE II.

IDENTIFICATION OF NEW MASKS CREATED

Mask Name	Created From	Process
TRAB-New	Trabecular	Remove the points that are along the femur shaft from the original trabecular mask (Figure 8)
Removed Regions	Trabecular and TRAB-New	The remaining regions when subtracting the TRAB-New mask from the original trabecular mask
CORT-New	Cortical and Removed Regions	The union of the cortical mask and the removed regions mask
WHOLE-modified	Whole bone mask and Removed Regions	Subtraction of the removed regions from the whole bone mask
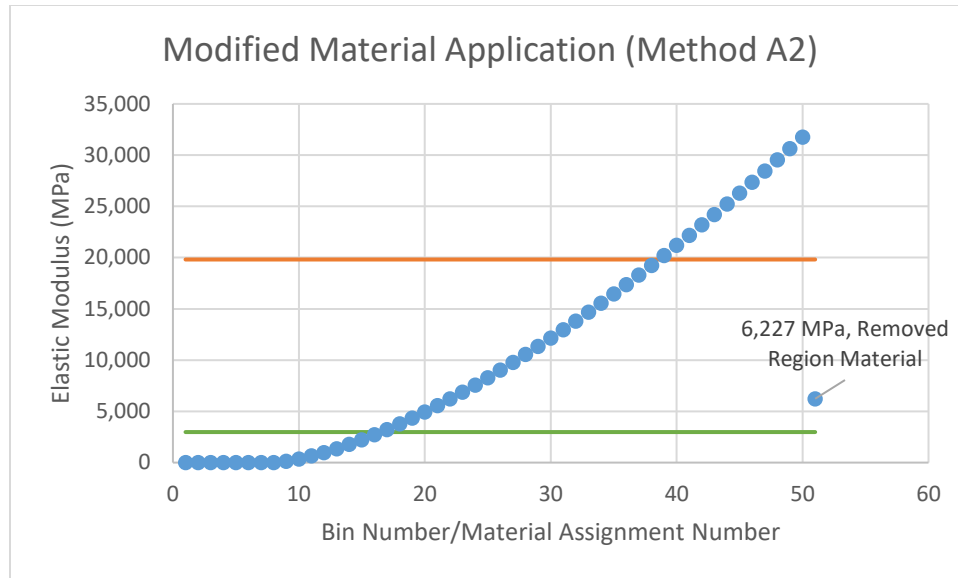
FIGURE 9. The elastic moduli of the modified application of materials, Method A2-50 and Method B2. The green and orange lines represent the converted median HU value for the cortical and trabecular as used in Method B2 regions, respectively.

TABLE III.

SUMMARY OF MATERIAL APPLICATION METHODS USED

Method Name	Applied to Masks*	Description
Method A-#	Whole bone mask (unmodified)	HU of mask is split into specified number (designated by #) of bins which are equally spaced. Mean HU of bin is applied to regions of bone whose density correspond to that bin.
Method A2-#	Whole-modified and Removed Region	Same as Method A-# but applied to the modified whole bone mask. One additional material property is added and applied to the Removed Region mask to be more representative of cortical bone.
Method B	Cortical and trabecular masks	Median HU of mask is used to apply the corresponding material property to either the cortical or trabecular mask. A total of two material properties are applied.
Method B2	modified masks (CORT-New and TRAB-new)	Same as Method B but applied to CORT-new and TRAB-new (modified masks)

*See TABLE II for descriptions of masks.

b. Finite Element Analysis to Evaluate Material Application Methods. A finite element analysis of a 3-point bending scenario was used to evaluate the different material applications.

Two different finite element analyses conducted in ANSYS which covered: (1) different material applications applied to case 331, which was used to look at the resulting volumetric differences between enhanced and unenhanced models, to evaluate the difference between material properties defined by enhanced and unenhanced scans and (2) different material applications applied to the 11-month-old femur model. Each material application only required a difference in the output file from Mimics that defines the material properties. This would allow for the same setup to be used where only the material assignment document would change. Nodal orientation was used to define the coordinate system so that the selected nodes used for the definition of the support and force were in the appropriate coordinate system. Nodal displacement was used in defining the supports to constrain the motion in the appropriate direction. Figure 10 illustrates the setup used in both scenarios. The forces were 500N and 200N for case 331 and the 11-month-old femur model, respectively. The reduction in forces was to apply forces more similar to those seen in the ATD trials where 500N was much higher than the shear forces observed. The following material application approaches were evaluated for both the enhanced and unenhanced scans of case 331: (1) Method B applied to the original cortical and trabecular masks; and (2) Method A-5, A-10, and A-50. The following material application approaches were evaluated for the 11 month old femur model: (1) the material application methods completed for case 331; (2) Method B applied to Cort-new and Trab-new, which takes the median HU of the new masks and applies it to their respective regions; and (3) Method A2-50, the modified 50 bin material application which resulted in a total of 51 bins.
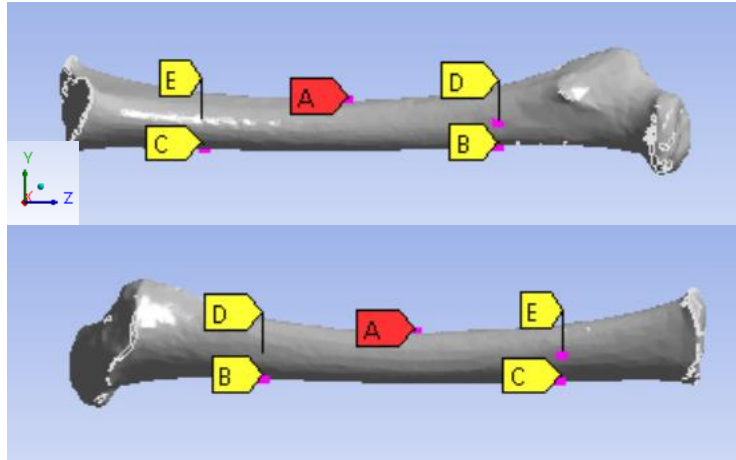
FIGURE 10. 3-point bending setup using case 331 where the top view is the medial view and the bottom is the lateral view. A - location of force application (500 N). B - constraint with no displacement in the y-direction. C – constraint with no displacement. D and E – constraints with no displacement in the x-direction. The same setup was applied to the 11-month-old model with an increased span from 71.5mm in case 331 to 83mm in 11-month-old.

B. Development of Finite Element Model of Femur to Evaluate Stress/Strain Associated with Femur Loading in ATD Falls

The output of the previous section determined that the geometry of the enhance scan is appropriate and material application Method A-10 was used to evaluate the loading of the femur in ATD falls. This section will focus on the components of the ANSYS setup to evaluate the femur loading conditions from ATD simulated household falls. First, the creation of a meshed model will be discussed. Next the other aspects of the setup in ANSYS will be discussed which includes application of the loads requiring defining the coordinate system used for the loads cells of the ATD femur assembly; determining the appropriate boundary conditions to use for analysis, where the strain gauge output of the ATD will be used to validate the boundary conditions used; and adjusting various settings of the ANSYS analysis to reduce the runtime to solve each analysis.

1. Mesh Development and Export

This section focuses on the creation of the meshed, 11-month-old femur model to be used to apply material properties and loading conditions due to household falls (as measured by the ATD). To create the tetrahedral mesh to which the material properties were applied, Materialise 3-matic v7.01 was used. The 3D model generated from the whole bone mask used to segment the femur in Mimics was exported into 3-matic. The following operations were completed in 3-matic. The *reduce* and *smooth* operations were used initially which reduces the number of elements and smooth the surface of the model, respectively. Tools provided by 3-matic, including an automatic re-meshing process and quality-preserving reduce function, were used in order to reduce the total number of elements as well as improving the mesh automatically with the built-in functions. A maximum geometrical error, which is a measure of how much the tetrahedron deviates from its mathematical representation, of 0.0625 was used. A maximum edge length of 1mm was used initially when developing the mesh and converting the surface mesh to a volume mesh. The maximum edge length was varied to be able to do a mesh refinement study. The surface mesh was then converted to a volume mesh which would be used in the evaluation of the household fall loading conditions.

Preliminary analysis of the mesh with a maximum edge length of 1mm resulted in large results files (10GB) of the finite element analyses. In order to reduce the file size, the maximum edge lengths of the volumetric elements were adjusted in 3-matic and evaluated to be able to both achieve convergence as well as reduce the output file size. 3-matic also has a function to be able to assign different maximum edge lengths to selected region. This was used to be able to have a smaller maximum edge length value in the cortical region of the bone due to its smaller features than the trabecular regions. A sample trial from the ATD falls (bed fall onto carpet; trial

66

9; left leg) was used in the preliminary FEA for mesh evaluation. The resulting maximum principal stress and strain values will be used to evaluate convergence. The output results file size will also be used in deciding optimum mesh parameters. The final mesh was composed of 420476 elements and can be seen in Figure 11.
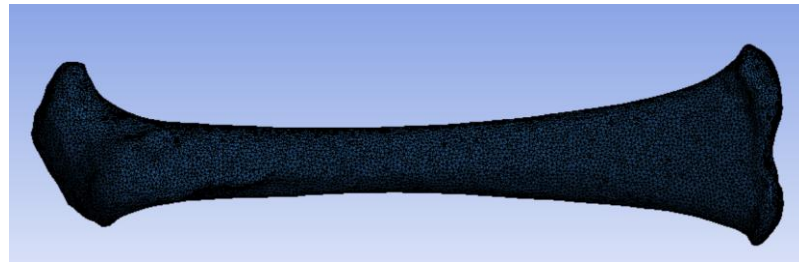
FIGURE 11. Final mesh of the FE model with designated maximum edge lengths of 1mm for the cortical region and 1.4mm for the trabecular region. The final model is composed of 420476 elements. (posterior view)

2. Defining Coordinate Systems

In order to apply loading conditions in ANSYS that were representative of those from the ATD experiments, a method to align the coordinate system of the load cells to the model was created by using objects created in the CT scan. The representative femur assembly of the ATD created in Solidworks was used to be able to create the objects in order to define this coordinate system. A cut was made on the ATD femur on the lateral side and parallel to the YZ-plane; this modified ATD's femur was then converted into a STL file and imported into Mimics. The STL registration feature in Mimics was used to align the STL of the ATD's femur with the femur model generated from the CT scan (Figure 12). Three planes were created in Mimics to define the proximal and distal faces of the STL femur and the YZ-plane which is defined by the face of the medial cut. These planes were then exported as STL files, imported
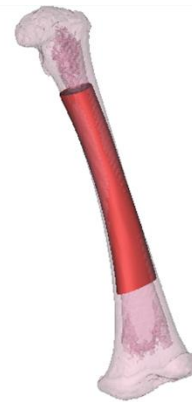
FIGURE 12. STL (red) used to align to the femur (pink) to be able to create planes in Mimics.

into ANSYS with the femur mesh model, and used as construction bodies to be able to create the appropriate coordinate systems. A representation of this process and the resulting planes can be found in Figure 13. In ANSYS, three coordinate systems were created. The first used the proximal and distal planes to define the Z-axis and the medial cut plane as the y-axis. The lesser trochanter feature on the femur was used to identify the posterior (positive) direction in the model. The origin of the first coordinate system was defined as the centroid of the bone as calculated by ANSYS. The other two coordinate systems were duplications of the first with a modified origin which was located at the center of both the distal and proximal planar surface bodies used to define the Z-axis and also to mark the location of both load cells.
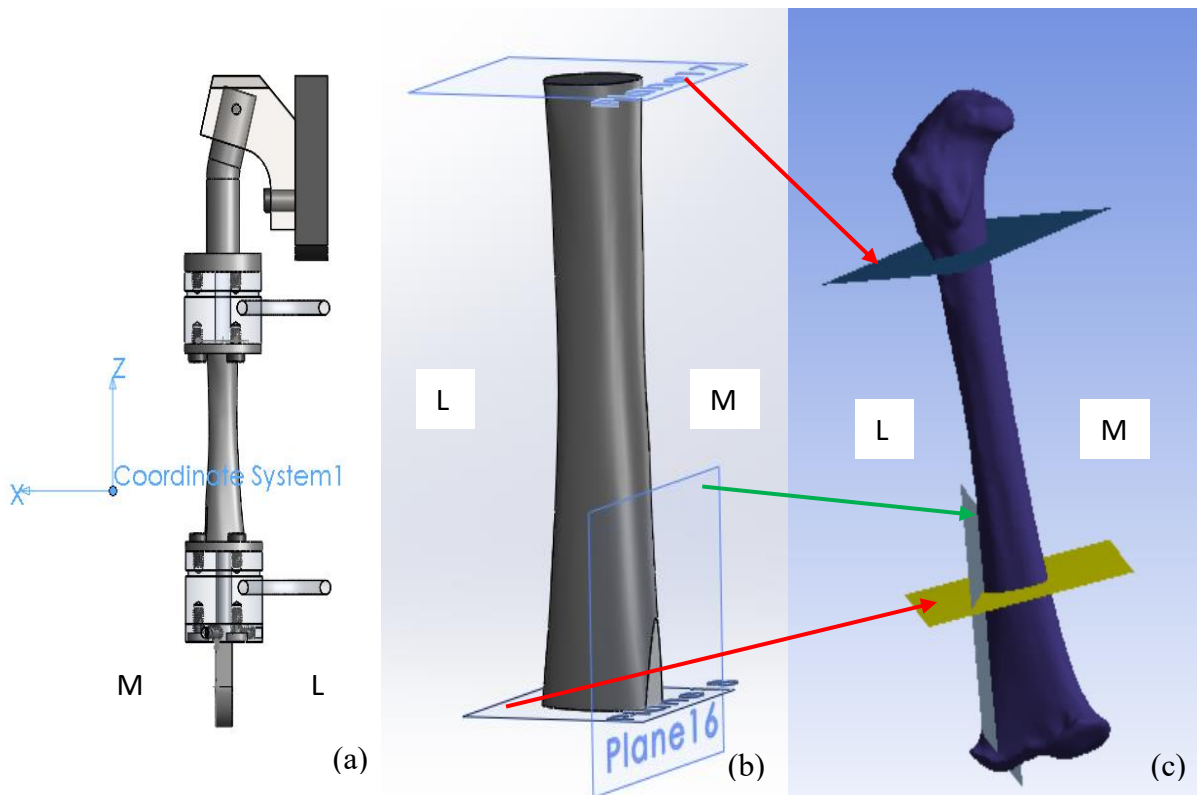
FIGURE 13. Visualization of planes used to define the coordinate system of the load cells. (a) Anterior view of the ATD femur assembly in Solidworks. The coordinate system of the load cells is shown. (b) Anterior view of the ATD femur model that was exported to Mimics to define the planes displayed. Plane 16 is the plane that defines the YZ-plane created by the cut on the lateral side of the femur. (c) The result of the planes created in Mimics are displayed in ANSYS FE Modeler (posterior view). The red arrows relate the planes used to define both the Z-axis and the location of the faces of the brackets used in the ATD assembly. The green arrow relates the YZ-plane on the medial side of the femur. Medial (M) and lateral (L) sides of the femur are indicated in the figure.

3. Boundary Conditions and Constraints Development

  a. Boundary Conditions and Constraints. Since the forces for this model were obtained

from the ATD fall experiments, the constraints of the representative femur will correspond to

ATD femur constraints. The location of the boundary conditions and constraints can be found in

Figure 14. The proximal constraint is a universal joint located at a node (Figure 14a) where the

translation is fixed in all directions and the rotation is fixed along the longitudinal axis of the

femur. Two different distal constraints were considered. The first of these distal constraints is a

fixed joint located at a node in the intercondylar region (Figure 14b). The second option is a

fixed displacement of the intercondylar region (Figure 14c). The intercondylar region was

selected and turned into a named selection or a selection of nodes with an assigned variable

name. The nodal displacement option was used in the setup component to fully constrain this

selection in all directions.
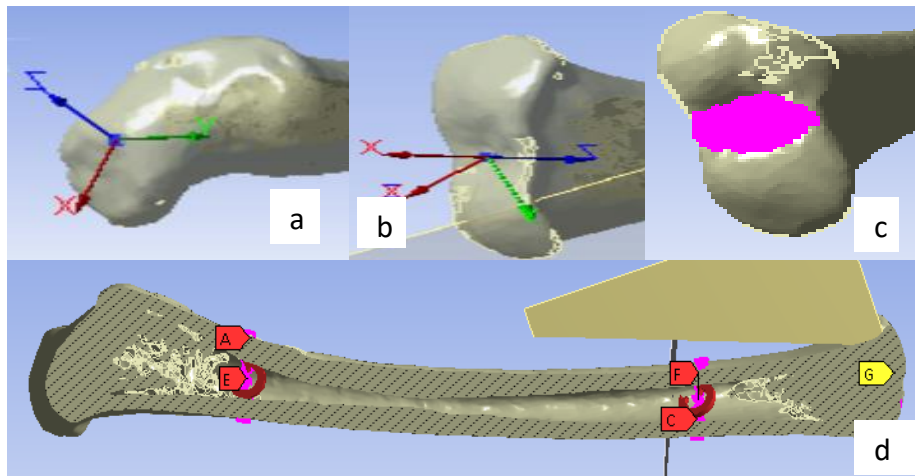
FIGURE 14. Setup in ANSYS showing the locations of (a) the proximally-located, universal joint; the distal constraints which are (b) a fixed joint and (c) fixed nodal displacement of the intercondylar region; and, (d) the location of the applied nodal forces and moments.

  b. ANSYS Analysis Settings and Application of ATD Femur Load Cell Forces and

Moments. The outputs of the load cells to use for the evaluation of the femur loading were

69

clipped to only include the initial impact loading. This will aid in reducing the runtime of the

model for each application of the loads. An example of how the interval of the loads were chosen

can be seen in Figure 15. To input these loads into ANSYS, the forces and moments from the

load cells of the ATD were defined by the proximal and distal locations of the 6-axis load cells.

These locations are 4mm away from the planes representing the load cell flanges created (Figure

13b) to define the coordinate system. To apply the loads, named selections were created where

elements were chosen that were between 4-4.25mm from the load plate, where this distance is

away from the central portion of the shaft. The load was applied to the nodes within the selected

region. The nodal force and moment options were used to apply the loads based on the named

selections created (Figure 14d). Operations in ANSYS were used to ensure that the loads were

applied in accordance with the coordinate system defined previously.
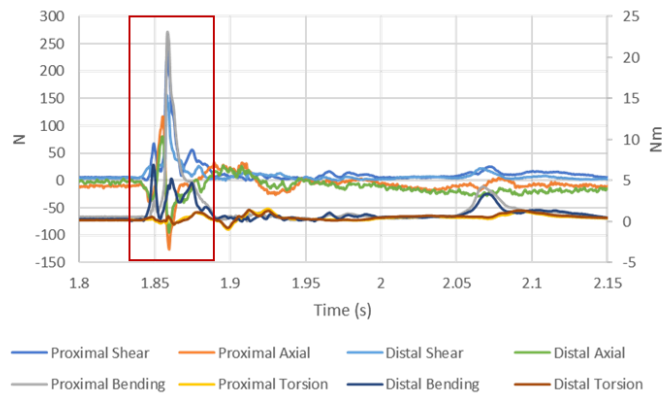
FIGURE 15. Sample of ATD femur forces and moments. The selected range of data used in the ANSYS analysis is shown by the red box. This represents the initial impact during the fall.

To evaluate loading conditions, ANSYS requires an input of the number of substeps

which defines the time step length. One of the bed fall loading

conditions from the ATD experiments (fall type: bed fall; impact

surface: carpet; trial 9, left leg) and the modified Method B material

application were used to evaluate the maximum time step (time step
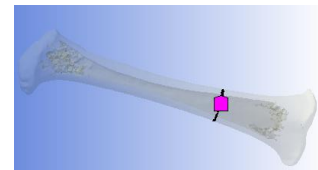
FIGURE 16. Location of ATD strain gauge's named selection

70

= interval of loading (time) ÷ number of substeps) to reduce error and achieve convergence. Two different number of substeps (25 vs 100) were considered for a 40ms time interval. The maximum principal strain and maximum principal stress resulted in a 1.7% difference between 25 and 100 substeps. A maximum timestep of 1.6ms (based on 25 substeps) was used in the evaluation of ATD loading conditions.

To simplify the process of inputting each trial into ANSYS, a MATLAB program was created for automation (Appendix II). Excel files for each fall were created of the outputs of the load cells from the ATD experiments. These excel files were analyzed through the MATLAB program to output the following: (1) the clipped data which represents the initial impact onto the floor; (2) the total duration of the clipped data; and, (3) the number of substeps needed to meet the requirement of the maximum time step which was determined previously. The clipped data is the output of the load cells which includes the triaxial forces and moments from both the proximal and distal load cell. The data was clipped visually by including at least the initial impact and the secondary impact for feet-first falls which corresponds to the impact of the pelvis. The video recording of an ATD trial was reviewed if the length of the impact was unclear from the graphed loading conditions.

c. Validation using ATD Strain Gauge Output. Evaluation of the FE femur model and associated boundary conditions was conducted by comparing the maximum principal strain measured by the strain gauge placed on the ATD femur during the experiments to the prediction of the FE model. The virtual strain gauge was positioned 7.14±0.03mm above the distal load cell plane (Figure 16) which is consistent with the experimental placement of the gage. Loading conditions from the bed fall onto linoleum (left leg – trial 9) were used for the validation process.

C. Validation of FE Femur Model Using Mechanical Testing of a Surrogate Bone

Validation of the model involved mechanical testing of a bone surrogate model. This surrogate bone model was tested under two loading conditions including bending, and axial loading until fracture. The output of the force-displacement curves and strain gauge time histories from the bone surrogate testing were compared to FE model predictions under corresponding loading conditions as a means to validate the model.

1. Material Property Testing of Surrogate Bone

The surrogate bone was 3D printed using glass fiber-filled nylon (polyamide 12) through selective laser sintering (SLS) using the Sinterstation 2500 Plus 3D Printer (Rapid Prototyping Center, University of Louisville). Since pediatric bone was unavailable, the goal was to use a material which will behave in a similar manner to pediatric bone for the surrogate bone. The target values for the material properties can be found in Table IV which consists of infant and pediatric bone material properties found in the literature. Different combinations of glass fiber and nylon were tested, which included 35% and 45% glass fiber by weight. Material property testing was conducted for each batch of different percentages of glass fibers by weight to evaluate the tensile, compressive, and flexural properties. The testing was done in accordance with ASTM D638 (tensile testing), D695 (compressive testing), and D790 (flexural testing) (ASTM D638-02a, 2003; ASTM D695-02a, 2002; ASTM D790-03, 2003). The tensile property testing was conducted first to determine if the properties are within the specified ranges. In order to maximize the tensile strength, the glass fiber content was increased from 35% to 45%. The flexural and compressive properties of the 45% glass fiber mixture, which was used to produce the surrogate bone models, were evaluated.

72

TABLE IV.

TARGET MATERIAL PROPERTIES

Property	Target Value/Range
Tensile Strength (MPa)	50-130[2,5]
Tensile Strain (%)	2-6[2,3,5]
Bending Strength (MPa)	160[1]
Flexural Modulus (GPa)	80-100[1]
Compressive Strength (MPa)	130[6]
Compressive Yield Strain (%)	1.1[4]
Elastic Modulus (GPa)	8-11[2]

[1](Currey & Butler, 1975); [2](Hirsch & Evans, 1965); [3](Lindahl & Lindgren, 1967); [4](Ohman et al., 2011); [5](Vinz, 1969); [6](Roberts, 1971)

2. Mechanical Testing of Bone Models

A total of 32 femora (Table V.) printed from the chosen nylon-fiberglass blend were used for mechanical testing. The surrogate bones were used to evaluate two loading conditions: three-point bending and compression (Figure 17). All were tested to failure for their assigned loading condition at the maximum loading rate capable of the uniaxial testing machine (eXpert 2610, AD-MET) which is 100in/min (42.3mm/s). Table V also lists the number of specimens tested with a strain rosette (Model Number: C2A-13-031WW-350, Vishay Micro-Measurements). The time history of the minimum principal strain from the strain gauges were used for comparison to the FE prediction. The output of the strain gauge was recorded using LabView v6.1 (National Instruments, Austin TX, USA) sampled at 10kHz.
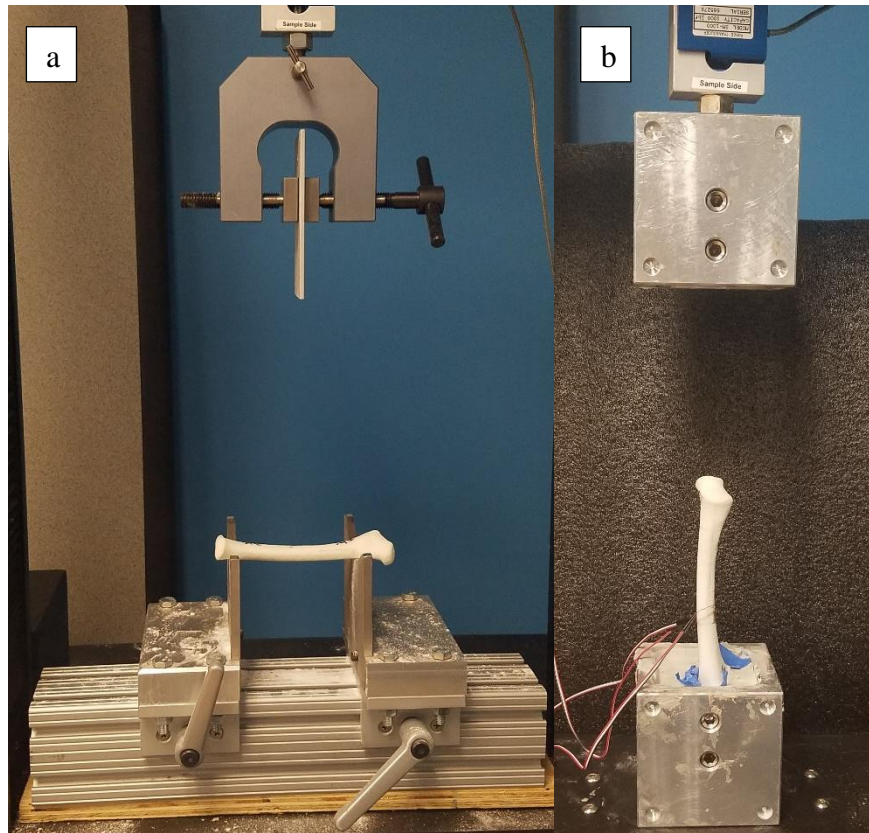
FIGURE 17. Setup for mechanical testing of the surrogate bone specimens for the (a) three-point bending loading condition and (b) compression loading condition.

TABLE V.

DESCRIPTION AND QUANTITY OF BONE MODELS PRODUCED WITH THEIR DESIGNATED TESTING CATEGORY.

Category Name	Bone Model Description	Qt.	Qt. for Bending Testing	Qt. for Compression Testing
Solid	Solid Bones (Bones without medullary canal)	11 (2)	8 (1)	3 (1)
Hollow	Bones with cavity (medullary cavity)	17 (12)	12 (7)	5 (5)
Reduced Metaphyses	Bones with 20% infill level at the metaphyses and a medullary cavity	4 (1)	0	4 (1)

Note: The Quantity in parenthesis is the number of specimens tested with a strain gauge.

a. Three-point Bending Testing. To include the entirety of the diaphyseal region as modeled by the ATD femur, the proximal boundary of the modeled region was one end of the span which was 87mm. To align the surrogate bones in the setup, two blocks with cavities with molds of the surrogate bone were used (Figure 18): a block that fits the distal portion of the

74

femur up to the proximal boundary of the ATD femur model and a block that fits the diaphyseal

region as model by the ATD femur. Once the proximal boundary mark has been made using the

block in Figure 18(a), the one in (b) will be used to mark: (1) the location of the distal boundary

of the diaphyseal region, (2) the location of the edge of the strain gauge for the bending and

compression testing, and (3) the load application location for the bending testing. The distance

between the distal boundary, strain gauge line, and the load application line was 10mm. The

strain gauge was then applied, if applicable.
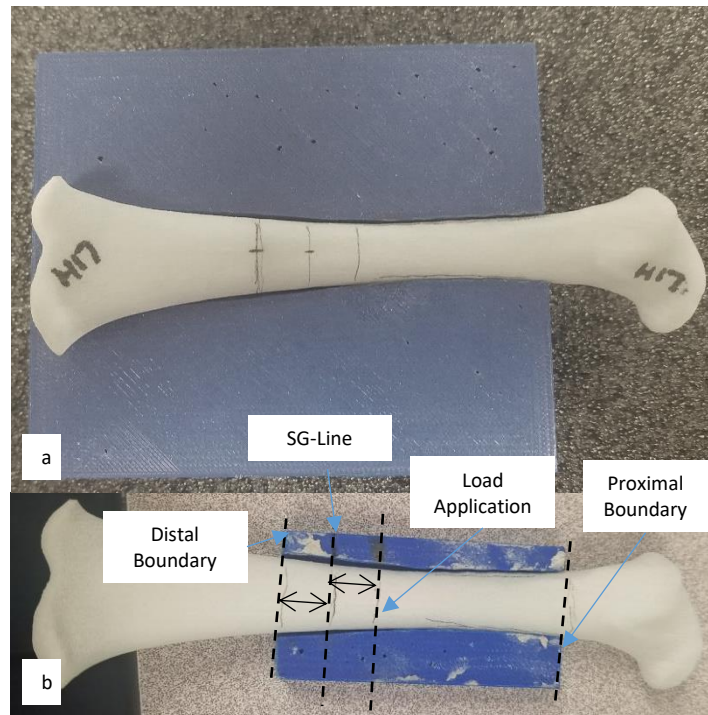
FIGURE 18. The surrogate bone in both alignment blocks where (a) depicts the block used to mark the proximal boundary and (b) is used to denote the remaining alignment marks. In (b), the dashed lines represent the four alignment markings on the bone which included the proximal boundary line, the location of the load application for the three-point bending, the location of the edge for the strain gauge (SG – Line), and the distal boundary mark which also denotes the location of the edge for the strain gauges used in compression testing. The mid-point marks used to align the center of the strain gauge can be seen in the markings on the surrogate bone in (a). The distance marked by the black arrows in (b) are 10mm.

The setup for the three-point bending testing can be seen in Figure 19. The center line is

the load application line from Figure 18 which was used to align the bar used to apply the force

with the bone surrogate. The alignment block was used to ensure that the bone was properly

aligned with the edge of the support structure. To conduct the testing, the bone was loaded in the

anterior-posterior direction at 100in/min where the initial position of the crosshead was at least

six inches above the bone to ensure that it was being loaded at the appropriate rate. The AD-

MET was set to record the data at 500Hz. A digital video recorder was used to record each trial.

The force-displacement curves were exported from the program.
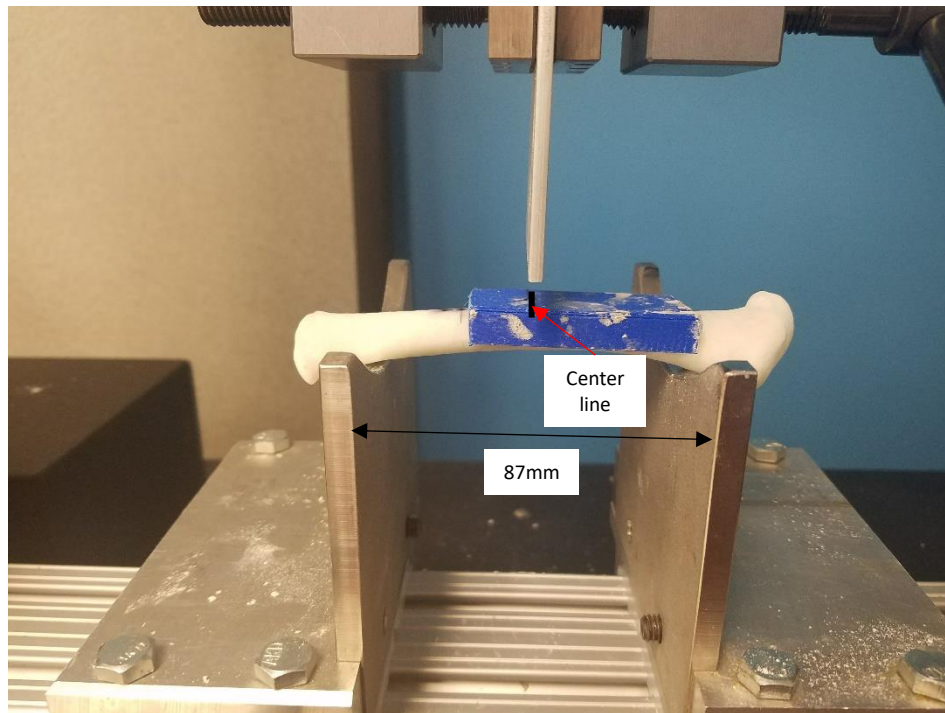
FIGURE 19. Three-point bending test setup depicting the span length (87 mm) and the center line marking used to ensure that the setup was properly aligned with the load cell.

b. Compression Testing. Two blocks were filled with a mixture of 3M Bondo All-

Purpose Putty and 3M Bondo Fiberglass Resin Repair where one of the surrogate bones was

used to create molds of the proximal and distal end of the femur (Figure 20). Blue painters tape

was used on the ends of the bone where it would encounter the Bondo mixture while it was

setting. The proximal mold was created by using the alignment block from Figure 18(a) which

was designed so that the longitudinal axis of the femur was aligned with the center of the block.

Once the proximal mold had set, the distal mold was created by placing both blocks into their

respective positions in the test frame where the proximal block was attached to the load cell. The

distal portion of the bone was set in the Bondo mixture as seen in Figure 20 (b) and (c).
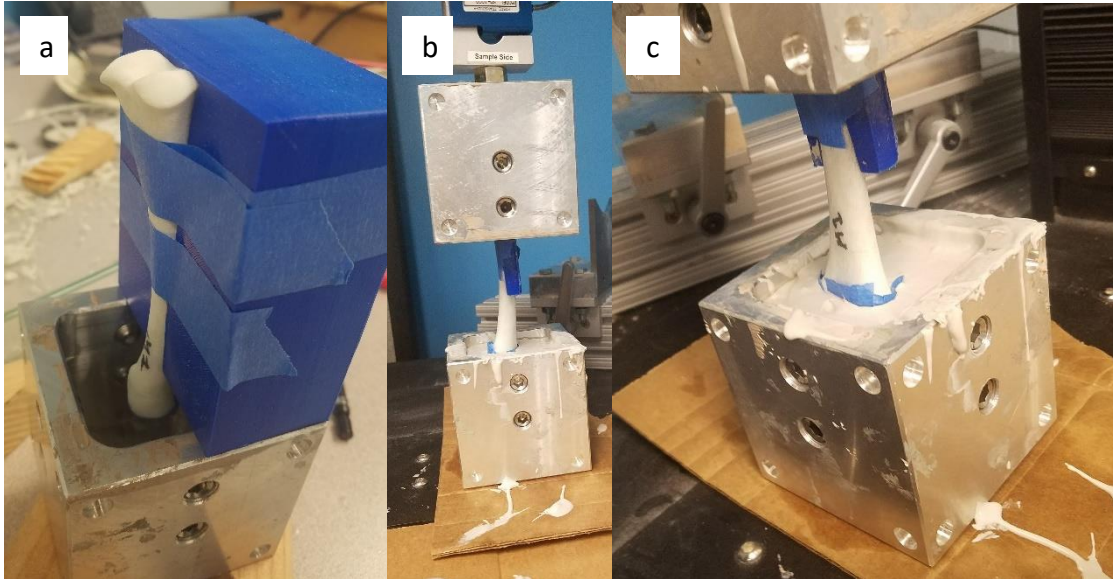
FIGURE 20. Blocks and alignment of bone to create the molds for the compression testing. The mold is composed of a mixture of 3M Bondo All-Purpose Putty and 3M Bondo All-Purpose Fiberglass Resin. (a) depicts the alignment block from Figure 18(a) used to hold the bone to create a mold of the proximal end of the bone. (b) and (c) depict two views of the block with the proximal mold attached to the load frame aligned with the other block in order to set the mold for the distal end.

For each specimen, a strain gauge was attached, if used, so that the upper edge was along

the strain gauge line as marked in Figure 18. The surrogate bone was set in the distal block while

the proximal block was initially placed at least 6 in above the proximal end of the femur (Figure

17b). The bone was loaded at 100in/min until fracture where the AD-MET was set to record at

500Hz. Higher threshold for failure was set to ensure that the testing did not stop if the bone was

not fully aligned with the proximal mold and experienced an adjustment which would reach

forces up to 100lbf (445 N).

3. Validation Criteria and Evaluation

The finite element analysis for both loading conditions had boundary conditions that were

representative of the mechanical testing of the surrogate bones. Processing the outcomes of the

mechanical testing to use to evaluate the validation criteria as well as describing the validation process are outlined.

a. FE model setup. A bilinear isotropic material model was applied to the finite element model which incorporated the surrogate material properties. The defined material properties included: (1) density of $1675kg/m^3$, (2) elastic modulus of 1302MPA, (3) Poisson's ratio of 0.4, (3) yield strength of 30MPa, (4) tangent modulus of 633MPa, (5) tensile ultimate strength of 55MPa, and (6) compressive ultimate strength of 60MPa.The analysis incorporated the boundary conditions associated with each test setup as seen in Figure 21.
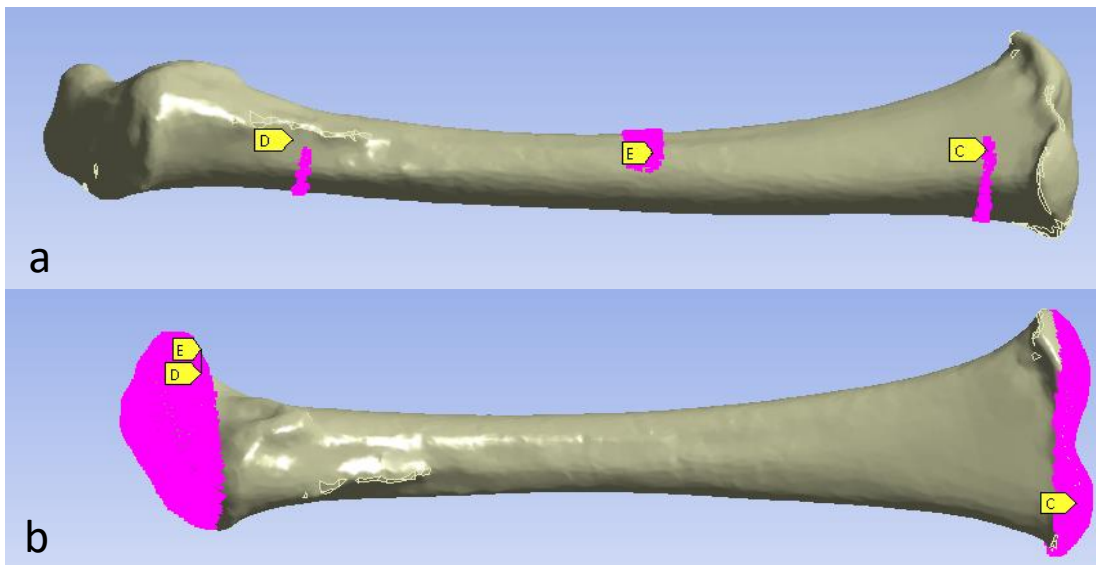
FIGURE 21. FEA setup for (a) three-point bending and (b) compression. In (a), the supports (C and D) and the load application (E) at a rate of 100in/min are displayed. In (b), the distal support (C), which was defined as the region 3cm below the distal load cell, was fixed in all directions while the proximal support (D), which was defined as the region 8.6cm below the distal load cell, had a fixed translation. The load was applied to (E), which is the same selection of nodes as (D) in (b) at a rate of 100in/min.

The bending setup (Figure 21a) consisted of three sets of nodal selections which are located at the proximal boundary of the modeled region in the ATD femur assembly, 87mm inferior to the proximal boundary, and at the load application which was 20mm superior to the distal boundary of the modeled region included in the ATD femur assembly. The proximal boundary nodal selection was fixed in x- and y-directions which corresponded to the medial-

lateral and anterior-posterior directions. The distal boundary nodal selection was fixed in all directions. The load was applied to the central nodal selection located with a thickness of 3.31mm where a nodal displacement at a rate of 100in/min was applied for 0.12 seconds.

The compression setup (Figure 21b) consisted of two nodal selections at the proximal and distal end of the femur which mimics the region which sat within the molds. The proximal nodal selection was set to include all nodes 86mm above the distal boundary line and the translation was fixed. A nodal displacement at a rate of 100 in/min was applied to the proximal nodal selection for 0.12 seconds. The distal nodal selection was set to include nodes 30mm inferior to the location of the distal boundary line and was fully fixed.

b. Data Processing. The experimental outcomes considered are the loads to fracture in each condition and the peak minimum principal strain, when strain rosettes were used, where the mean for each loading condition and specimen type was reported. For each experimental trial, the data was adjusted to compensate for the toe region of the force-deformation curve. An example of how this was accomplished can be seen in Figure 22. This was necessary due to the cross-head beginning 6 inches above the specimen making it necessary to account for potential slack upon initial loading. The initial linear region was used to determine the slope to extrapolate the x-intercept, or displacement shift of the curve. Since control of the crosshead was defined by a displacement rate, the displacement shift corresponds to a time shift as well. The displacement vector of the trial was adjusted with now-defined displacement shift of the trial. The toe region was excluded when comparing the finite element predicted values. The strain gauge-time curve was aligned to the force curve by aligning the drop-offs for each.

The peak load, stiffness of the linear region, area under the curve (AUC) of the force-displacement curve from the end of the toe region to the peak load were calculated and recorded

for all specimens. The flexural modulus (Equation 4) for bending test specimens, which was dependent upon the moment of inertia, I (Equation 5), was also determined. The AUC was approximated by using the trapezoidal rule. The modulus was calculated based off the cross-section of the fractured region which was consistent across all specimens.

$$Modulus = \frac{FL^3}{48IE} \tag{4}$$

$$I = \frac{\pi}{64}(D^4 - d^4) \tag{5}$$

F is the applied force. L is the span which is 87mm. I is the moment of inertia, D is the outer diameter of 11.7mm, and d is the inner diameter of 6mm. The inner diameter would be zero for solid specimens. E is the elastic modulus which was derived from material property testing.
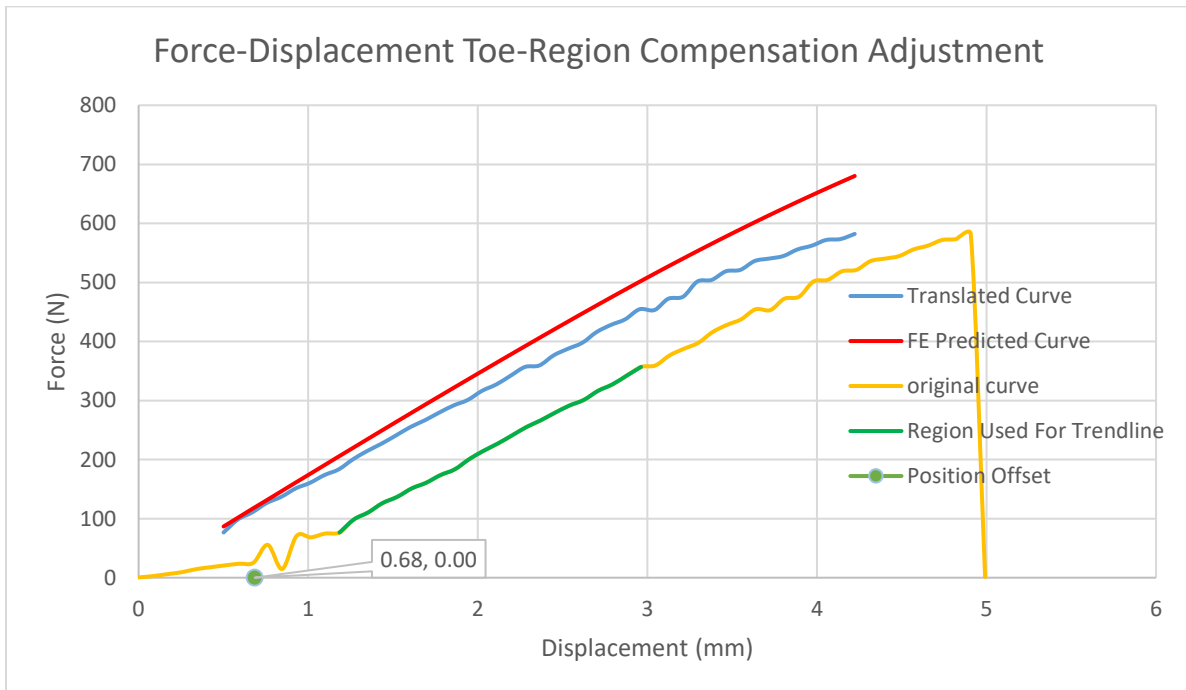
FIGURE 22. Force-Displacement curve representing the adjustments made for the toe-region. The linear region used to determine the offset of 0.68mm can be seen (green). This position offset was applied to obtain the translated curve (blue) where the toe-region has been excluded. The corresponding FE predicted force-displacement curve can be seen in red.

c. Validation Criteria and Assessment. Only the hollow specimens were used in evaluation of the validation criteria since these specimens most closely resemble bone with the inclusion of the medullary cavity. The following section describes the process for evaluating the validation criteria which compares the force-displacement data and the strain-time histories to the FE predicted values in order to validate the geometry of the FE model. An Anderson-Darling test was used to test the normality of the experimental outcomes, which includes loads and strain data. If the data followed a normal distribution, a one-way ANOVA (α =0.05), which compares the means between the trials where the null hypothesis is that they are equal, was used to determine if the trials can be grouped together for evaluation of the validation criteria. If the data was non-normal, a mood's median test (α =0.05) was used instead where the null hypothesis is the medians of each trial are equal. If the trials cannot be grouped, the criteria for validation (listed in Table VI) were evaluated for each trial individually and the mean of the trials was used. A summary of this process can be found in Figure 23.

Grouping trials where each trial is a factor level

null hypothesis: all means or medians are equal

• Data is normal: One-Way ANOVA
• Data is non-normal: Mood's Median Test

Inputs: Force or Strain data from either bending or compression testing.

Normality Test: Anderson-Darling

Evaluated for each trial individually

Evaluation of each validation criterion

• All trials grouped if previous p-value > 0.05
• Else, each trial evaluated individually

FIGURE 23. Flowchart of process to evaluate whether to group trials in order to evaluate the validation criteria.

81

The following FE predicted versus experimental data were assessed using validation criteria: (1) force-deformation curves of the bending and compression testing and (2) strain-time histories for the bending and compression testing. For each data point of each curve, experimental data was compared to the corresponding FE predicted value. Mean and standard deviation of the absolute percentage error (Equation 6) were determined.

$$\text{Absolute Percent Error} = 100\% \sum_{k=i}^{N} \left| \frac{FE(i) - Exp(i)}{Exp(i)} \right| \tag{6}$$

N is the number of data points. FE is the FE predicted value and Exp is the experimental value at the specified point (by time or position). The linear regression, where the experimental outcome is the dependent variable and the FE predicted variable is the independent variable, was determined using Minitab. The intercept was evaluated as a percent of the peak value of the experimental outcome for that data set.

TABLE VI.

TABLE OF ACCEPTANCE RANGE FOR THE VALIDATION CRITERIA

Criterion	Absolute Percentage Error		Linear Regression		
	Mean	Std. Dev.	Slope	Intercept	R^2
Acceptance Range	≤20%	≤20%	[0.8, 1.2]	≤20%	≥0.8

D. Finite Element Analysis of Femur Subjected to Fall Loading Conditions

1. FEA of Fall Loading Conditions

Once the mesh refinement and model validation process were completed, loads from the ATD fall experiments were evaluated. The material property equation applied from Table III used to define the modulus was modified to include a correction factor, as determined by Schileo et al. (2008), for converting the bone mineral density to ash density (ρ_{ash}). The apparent density was used to define the density property in Mimics where the conversion from the bone mineral density value, derived from the phantom-less calibration, and equations used to define the properties in Mimics can be found in Table VII.

TABLE VII.

SUMMARY OF MATERIAL PROPERTY EQUATIONS USED IN EVALUATION OF FALL LOADING CONDITIONS

Property	Equation
Bone Mineral Density (mg CaHA/cc)	$0.7157 * HU - 12.591$
Apparent density (ρ_{app})	$\dfrac{0.878 * BMD + 0.07895}{600}$
Elastic Modulus (MPa)	$6850 * \rho_{app}^{1.49}$
Poisson Ratio	0.3

Finite element analyses were conducted for various fall conditions where the factors of interest are fall type (bed falls and feet first falls), impact surface (carpet and linoleum), fall height (69cm and 119cm for feet-first falls), and fall dynamics. Fall dynamics are descriptive categories for how the ATD fell during the experiment such as the upper leg impacting the ground before the lower leg during a bed fall. The fall dynamic categories were previously identified by Thompson et al. (2018) by reviewing the videos of each fall. A random selection of three trials for each unique combination of factors was used.

A preliminary analysis of the resulting loading conditions from the ATD experiments determined if fall dynamics should be considered when selecting the trials to run for FEA. A

mixed effects model (alpha = 0.05) was completed where the random factor is the fall dynamic, the fixed factors are the fall height and impact surface, and the response being the maximum loads (compression, bending, shear, and torsion for both the proximal and distal load cells) seen in the fall for the feet first fall scenario. An ANOVA (alpha = 0.05) was completed where both impact surface and fall dynamics are fixed factors for the bed fall scenario. If the fall dynamics influenced any of the loads (alpha = 0.05), it would be included as a factor in the analysis of the FE predicted outcomes.

Loading from the three randomly selected trials for the interaction of the factors selected (Table VIII) was then used as inputs to the finite element analysis. The trials were selected by using the random sampling (sampling without replacement). The factors included were impact surface and fall dynamics for bed falls and impact surface and hall height for feet-first falls. A total of 24 trials from the ATD experiments were used. The FE predicted outcomes considered were the peak maximum first principal stress and strain and peak von Mises stress over the interval of applied loading of the diaphysis, which is the region included in the ATD femur assembly.

TABLE VIII.

TYPE AND NUMBER OF FALLS EVALUATED IN FEA.

Fall Type	Factor 1	Factor 1 Levels	Factor 2	Factor 2 Levels	Total Number of Trials
Bed Fall	Impact Surface	Carpet	Fall Dynamic	Upper Leg Hits First	12
		Linoleum		Lower leg hits first	
Feet-First Fall	Impact Surface	Carpet	Fall Height	69cm	12
		Linoleum		119cm	

2. Evaluation of FE Predicted Outcomes

      a. Statistical Analysis. All alpha levels will be set at 0.05 unless otherwise specified. The

statistical analysis was completed using Minitab v18.1 (Minitab Inc., State College, PA). An

ANOVA was performed to evaluate the FE predicted maximum principal strain, where the left

leg outcome of the trial will be the dependent variables for each grouping of the fall types (feet-

first and bed). The ANOVA was used to evaluate whether each factor of each fall type (e.g. fall

height, impact surface, fall dynamic) affected the maximum principal strain. The residuals of the

ANOVA were evaluated for normality, a mean of zero, and constant variance of residuals. If the

ANOVA showed that a difference existed between the levels of a factor, a post-hoc test such as

the Tukey's test was used to determine which factor levels result in a greater likelihood of

fracture.

      Since both fall types have different levels of sub-factors such as no overlap of the fall

heights evaluated for each fall type, a secondary ANOVA to compare the FE predicted outcomes

for the fall types was not completed. The descriptive statistics, such as the mean and standard

deviation, for the fall types was reported instead to compare the fall types.

      b. Evaluation of the Likelihood of Fracture (Failure). Classifying a FE simulation as a

failure (or likely that a fracture may have occurred) was dependent upon the maximum principal

strain theory (Schileo, Taddei, et al., 2008). The maximum principal strain theory states where

failure (fracture) occurs when the maximum principal strain is greater than or equal to that of the

yield strain (tensile or compressive). This failure theory considers the onset of fracture rather

than the actual fracture. Since the yield strain tends to vary based on anatomic location and even

between the different locations on the femur, such as the diaphysis, greater trochanter, and

femoral neck, a conservative estimate of failure where the lowest yield strain found for the femur

was used. A yield strain limit of 0.73% (which is the tensile yield strain of adult femoral cortical bone as determined by Bayraktar et al. (2004)) was used in evaluation as to whether a potential fracture occurred.

Each trial was assigned one of four failure classification (A through D; Table IX). The differentiation between category A and B was used to identify trials where a potential fracture was most likely due to partial volume effects. The number of potential fractures as identified by the strain threshold was reported. An ordinal logistic regression was also considered based on the failure categories identified below.

TABLE IX.

FAILURE CATEGORY ASSIGNMENT AND DESCRIPTION OF EACH.

Failure Classification	Classification Description	Criteria Description
A	Potential Fracture	Meets the criteria of B and does not have a ribbon pattern. Elements that are not on the surface may have also exceeded the threshold.
B	Potential fracture associated with partial volume effects	Elements exceed the threshold and 5 or more elements are contiguous. Typically appears in a ribbon pattern.
C	Scattered failure	Elements exceed the threshold, but less than 5 elements are contiguous.
D	No failure	No elements exceed the threshold

In addition to strain, two stress-based criteria were also used to evaluate potential fracture (Table X). The ultimate tensile strength of pediatric bone as measured by Vinz (1969) was compared to the FE predicted maximum principal stress outcome. The ultimate flexural strength as measured by Currey and Butler (1975) was compared to the FE predicted maximum principal stress outcome. Potential fracture was defined as exceeding one stress-based criteria in

conjunction with exceeding the Element Criteria (Table X). In summary, potential fracture was

determined using either yield strain or stress-based criteria, along with element-based criteria.

TABLE X.

DESCRIPTION OF FRACTURE THRESHOLDS WITH CORRESPONDING FE PREDICTED OUTCOME FOR
COMPARISON.

FE Model Predicted Outcome	Threshold Description	Threshold Value	Additional Element Criteria
Maximum Principal Strain	Yield Strain	0.73% (Bayraktar et al., 2004)	A minimum of 5 contiguous elements must have exceeded the threshold.
Maximum Principal Stress	Ultimate Flexural Strength	157.8MPa (Currey & Butler, 1975)	
	Ultimate Tensile Strength	100MPa (Vinz, 1969)	

IV. RESULTS

A. Development of Femur Model and Material Property Applications

The following section includes the development of the FE femur model and the evaluation of the material property applications which includes developing the phantom-less calibration equation which was used to define relationship between the bone mineral density and the HU. Results of the investigation of the effect of the bone edge enhancement algorithm has on the resulting geometry, distribution of HU, and different material application methods are discussed. The results of evaluating different material property methods are also covered.

1. Phantom-less Calibration

The mean HU value of the mask of the calibration phantom insert was obtained from the mask properties. This was repeated for nine additional scans with a calibration phantom. Excel was then used to determine the linear regression for the relationship between the Hounsfield unit and the density of the calcium hydroxyapatite (CaHA) (Figure 24). It is important to note that the scans with the enhanced algorithm resulted in the same HU values for the calibration phantom as the scans without it.
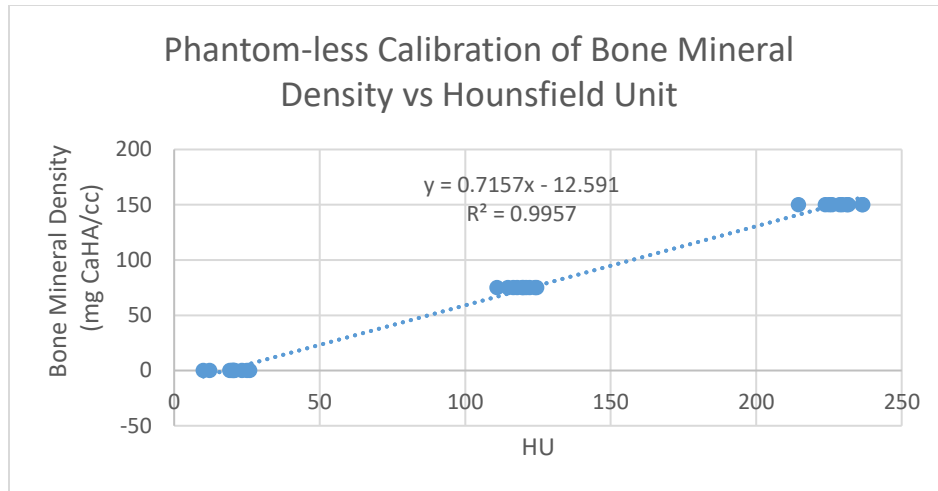
FIGURE 24. Scatterplot for the phantom-less calibration of bone mineral density vs the measured HU value. The resulting linear regression of this relationship is displayed.

2. Effect of the Bone Edge Enhancement Algorithm

Examples of the resulting distributions of the cortical and trabecular masks for both scan types, enhanced and unenhanced, for case 331 can be found in Figure 27 and Figure 25, respectively. The masks were exported as text files to be able to compare the distribution of Hounsfield Unit values of each mask in Minitab.

As seen in Figure 25, the trabecular mask in both the unenhanced and enhanced scans tend to have similar distributions of Hounsfield unit values but with mostly lower frequency of values in the enhanced scan. A paired t-test comparing the difference in HU between the enhanced trabecular mask (trabecular mask originating from the enhanced scan, Figure 26) in each scan type (enhanced and unenhanced) resulted in only one case out of four having a p-value > 0.05, indicating no statistically significant difference. Cases 230, 329, and 332 had a statistically significant difference where the mean difference in the HU between the mask in different scan types was 8.068HU, -1.388HU, and 5.387HU, respectively. Although a difference

was determined, 8HU is only 5% of the lowest HU threshold (156HU) used to create the masks

which does not translate to a large difference in the applied material properties.
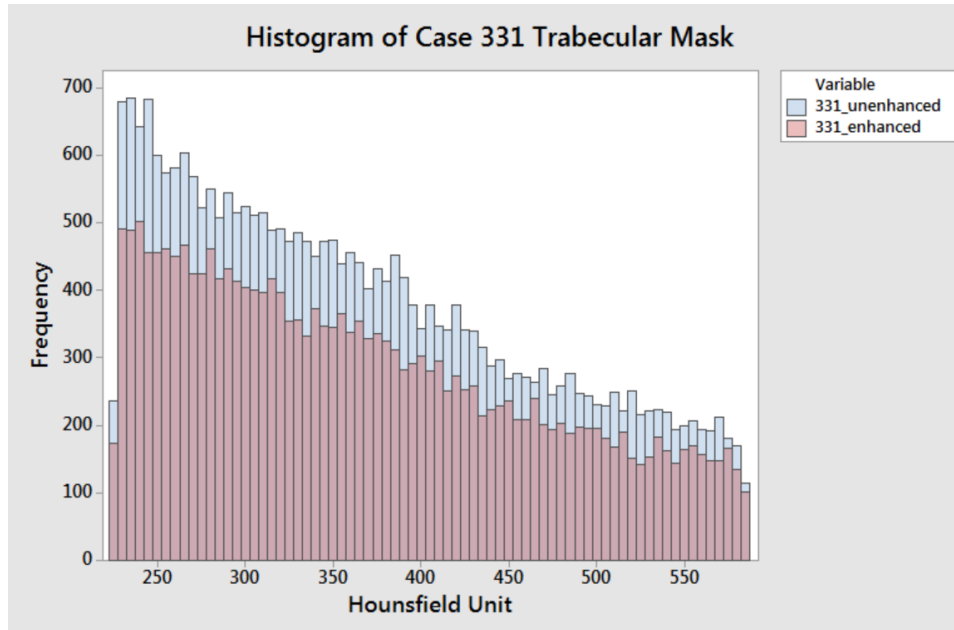
FIGURE 25. Histogram of case 331's trabecular mask for both the unenhanced scan (blue) and the enhanced scan (red). The trabecular mask from the enhanced scan tends to follow a similar distribution of values but have a lower frequency which can be seen above.
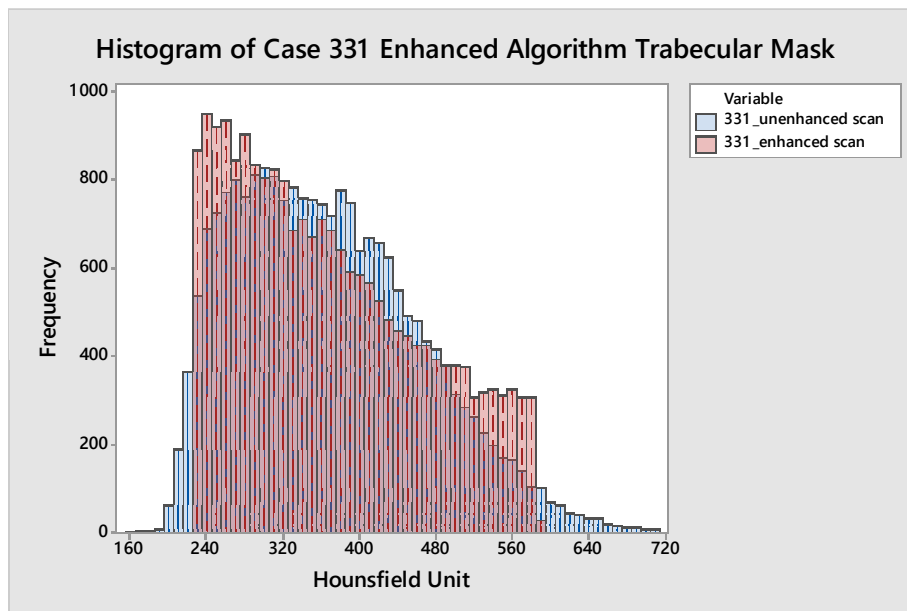
FIGURE 26. Histogram of the HU values of the trabecular mask created in the enhanced scan and applied to both scan types, enhanced and unenhanced.

The distribution of the scans that used the enhancement algorithm for the cortical mask tended to result in a maximum HU of over 2000 HU (Figure 27) compared to a peak HU of 1600-1800 HU for unenhanced scans. The cortical masks created in the unenhanced scans files which were then exported to the enhanced scan illustrated that the bone enhancement algorithm would emphasize the edges of the cortical region by reducing the intensity of the surrounding regions to the extent that negative Hounsfield unit values were observed (Figure 28). In Figure 28, the yellow and purple seen in the upper image on the cross sections of the bone represent the decrease and increase in the HU of the bone due to the enhancement algorithm, respectively. The plot in Figure 28 represents the HU when following a line across the diaphysis of the bone in the transverse plane. In the enhanced plot, the HU values are negative along the edges of the bone which allows the edges of the bone to be better defined. The peaks of both plots differ by 200HU indicating that the enhancement algorithm also increases the HU value of the cortical bone in order to create a greater contrast with the surrounding soft tissue. In summary, the bone edge enhancement algorithm does influence the resulting trabecular region, but it is minimal. The enhancement has a much greater effect on the cortical region by increasing the contrast to better define the edges of the bone.
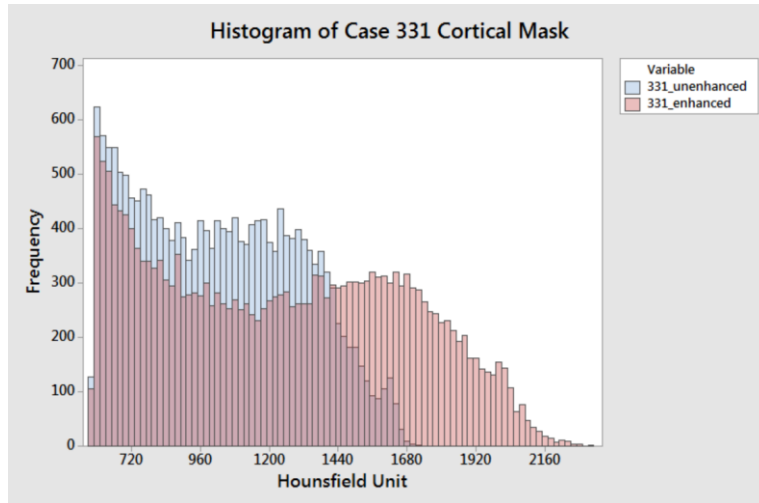
FIGURE 27. Histogram of case 331's cortical mask for both the unenhanced scan (blue) and enhanced scan (red).
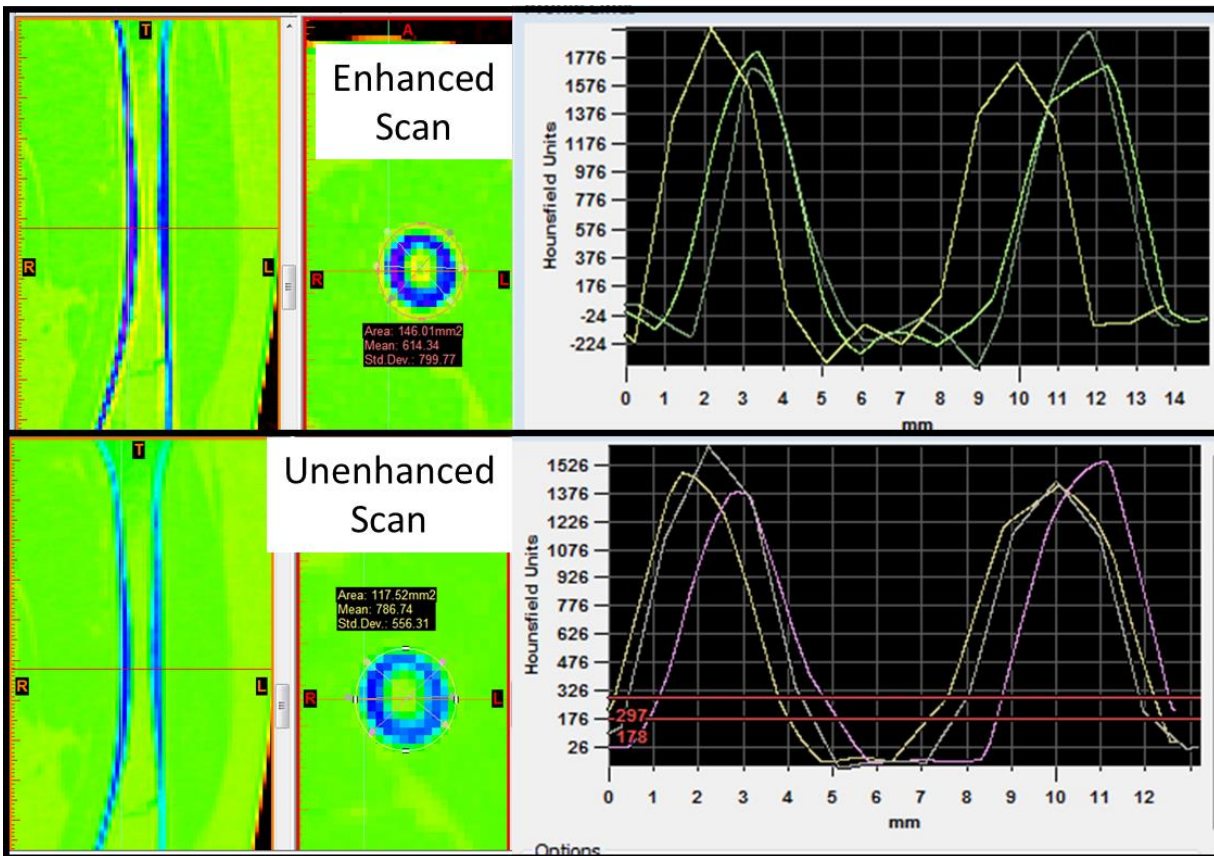
FIGURE 28. Comparison of the diaphysis of the femur of the same femur in both an enhanced and unenhanced scan. From left to right, the images represent: (1) a cross-section of the longitudinal view of the axis, (2) a cross section of the transverse plane of the mid-diaphysis, and (3) line of the HU value across the diameter of (2). The figure illustrates how the enhanced scan decreases the HU values at the boundaries of the bone while increasing the HU value towards the central band of the bone.

In Solidworks, planes were created to measure the area at various cross-sections of the

femur (Figure 29) for case 331 where two 3D models, originating from the unenhanced scan and

92

enhanced scan, were compared. These measurements had shown that there were mostly differences along the boundaries of the 3-D model where the enhanced 3D model had smaller areal measurements at the specified cross-sections. The largest deviations in the boundaries tended to occur along the interface between the cortical and trabecular bone where changes in the HU, as discussed previously, due to the enhancement algorithm typically occurs. When determining the material properties of bone, the edges may be excluded due to the partial volume effects which can result in lower HU values due to the inclusion of both soft tissue and bone. Due to the low resolution of these scans, the unenhanced scans had partial volume effects along the edges of the bone. When comparing the boundaries of the enhanced and unenhanced geometries, many of the partial volume effects can be found along the edges where the differences in the geometries predominantly occur. Figure 30 illustrates the partial volume effect in an unenhanced scan where the right side of the image indicates parts of the trabecular mask, which is the pink region, that exists along the shaft, or the cortical region. The left side of this figure indicates that these regions have low HU and would most likely be excluded in a manual segmentation process. Since the bone edge enhancement algorithm reduces these regions with partial volume effects, the resulting geometry created in the enhanced scans would be appropriate to use for the *in-silico* model. Further investigation into the difference in the resulting material properties of the two scans was conducted to account for differences in the distributions of the bone in the enhanced and unenhanced model.
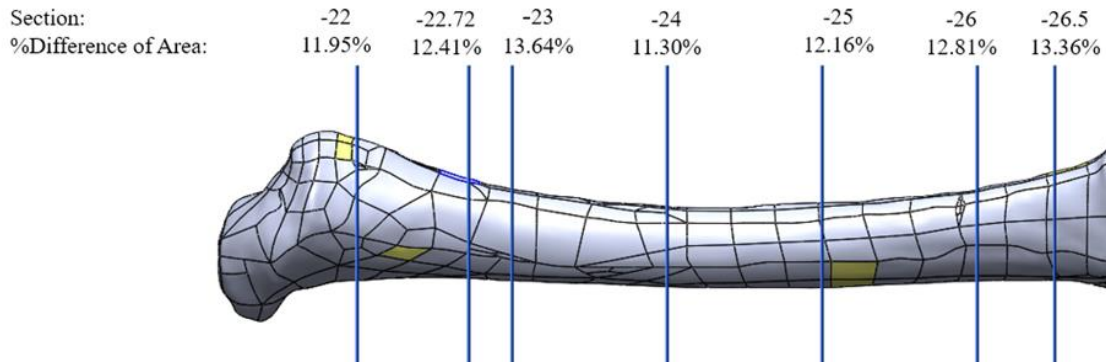
FIGURE 29. Representative figure of the planes used to measure the area and perimeter values of the cross-section. Blue lines represent each plane where a measurement was taken. The percent difference (absolute) in area results are between the enhanced and unenhanced with reference to the unenhanced area resulting 3D models of Case 331 where enhanced was smaller.
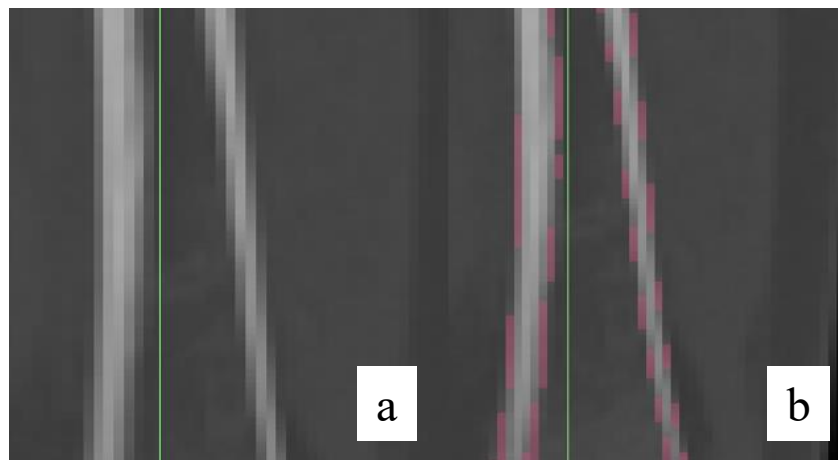
FIGURE 30. Above is a portion of the shaft of the femur from Case 332's unenhanced CT scan. Both (a) and (b) depict the same region of bone from the same scan where (b) has the trabecular mask (pink) displayed. The trabecular mask region along the shaft is applied to areas where a partial volume effect is expected to have occurred.

3. Evaluation of Different Material Applications

The following section covers the evaluation of the different material property application methods. The first section covers how the enhancement algorithm affects the application of material properties. The second section discusses potential modifications of the material property application to account for partial volume effects as well as selection of the method to use in evaluating the ATD fall experiments using finite element analysis.

a. Evaluation of the Enhancement Algorithm. To compare different material application methods derived from the enhanced scan to one derived in the unenhanced scan, a three-point bending analysis using case 331 was conducted. Figure 31 illustrates the percent difference in the maximum principal stress and strain for the different material applications applied to the enhanced scans with respect to the maximum values for Method A-50 derived with the unenhanced scan. Method A-50 (of the enhanced scan) had the best agreement of stress and strain values where Method 10 had the next best agreement which was consistent with how 10 bins results in a similar distribution of material properties compared to using 50 bins (Figure 7). For the evaluation of the loading of the femur in the experimentally simulated ATD falls, the use of material properties defined by the enhanced scan would likely result in an overestimation of the stresses and underestimation of the strains.
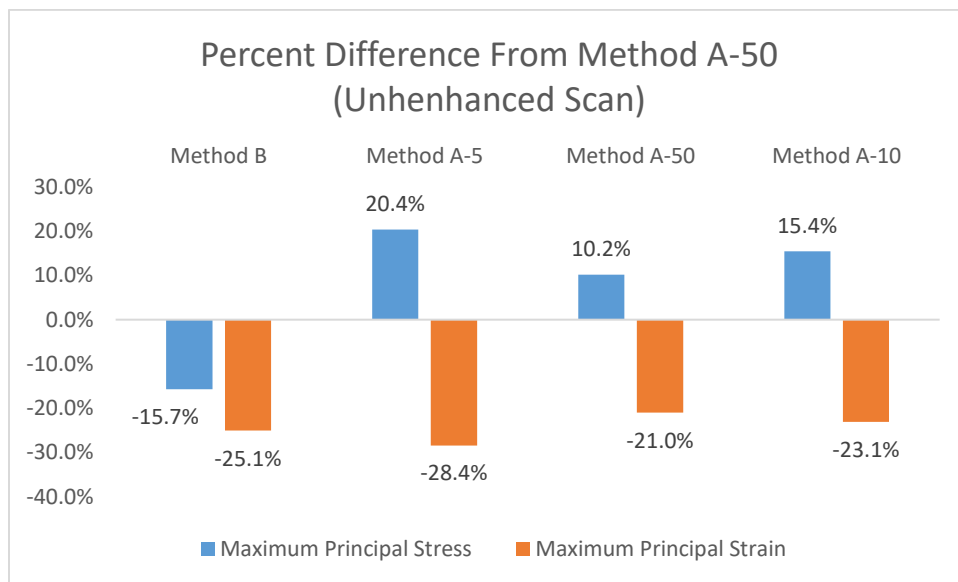
FIGURE 31. Chart of the percent difference of the maximum principal stress and strain for the other material application methods (Method B, Method A-5, Method A-10, and Method A-50) used on the enhanced scan from the application of Method A-50 to the unenhanced scan for case 331. These values were obtained from a 3-point bending analysis.

b. Evaluation of Properties when Applied to ATD Femur Model. Modified Method A (Method A2) and Method B2 to apply three-point bending loading conditions to the ATD Femur

model investigating how the modified material applications, which accounts for partial volume effects, changes the peak outcomes and distribution of stress and strain. The peak maximum principal stress and strain for the different material applications considered can be seen in Figure 32 where the region considered for the maximum values was between the applied support locations. The goal of the modified masks was to reduce the ribbon effect (or the striations as seen in Figure 33a) of higher stress and strain values due to the partial volume effect (Figure 30). The difference can be seen in Figure 33 where both the original (Method B) and modified (Method B2) material application methods where the median HU of the defined cortical and trabecular regions are used to define the material properties in those regions. The striations seen in Figure 33(b) are due to the lower HU values along the cortical region of the bone which had been miscategorized as trabecular instead of cortical. When adjusting the masks to account for the false categorization, the distribution of the strain no longer had the striations which are associated with the partial volume effect. The modification in the material application between Method B and B2 reduced the peak stress to a value more similar to method A-50. Method A2-50 resulted in a reduced peak stress and strain compared to Method A-50 and a similar peak strain as compared to Method A-5.
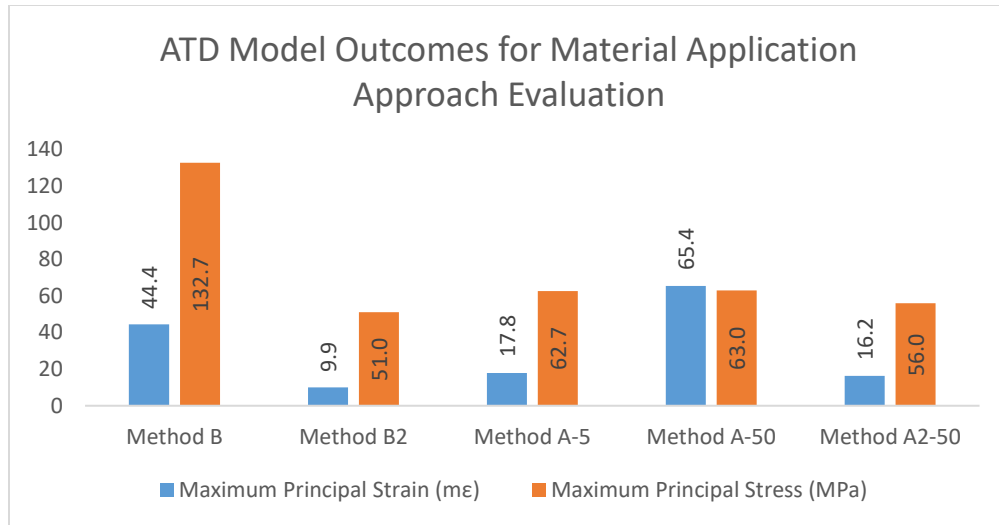
FIGURE 32. The maximum of the maximum principal stress and strain for all material application methods considered for the ATD model. The region considered for the maximum is limited to the area between the supports.
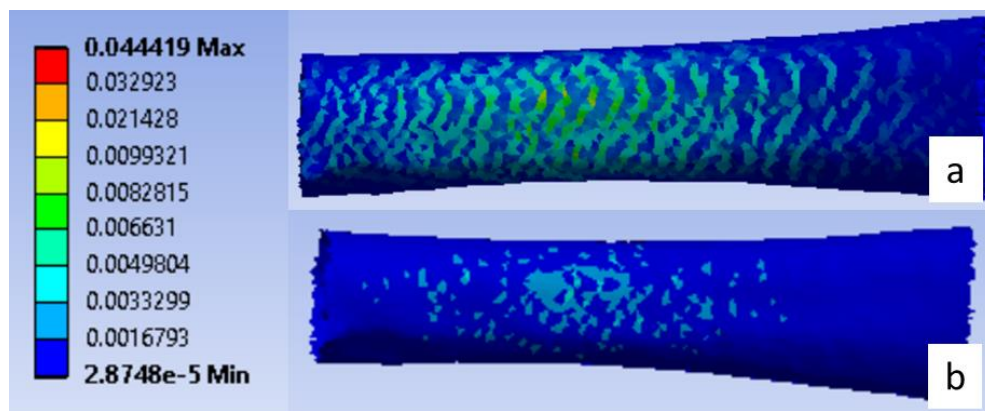
FIGURE 33. The difference in the distribution of the maximum principal strain for the (a) Method B (the original 2-bin material application) and Method B2 (the modified 2-bin material application). The region displayed is ±3cm from the point of load application. The scale for both is displayed on the left.

The difference in maximum principal strain varied between the original material applications (Method B, Method A-5, and Method A-50) and the modified material applications which account for partial volume effects. The minimum material property for Method A-5 had an elastic modulus of 10MPa which would account for the much higher strain compared to Method A-50 as seen in Figure 32. The reduction in the maximum principal strain for the modified material application methods is in part due to the outer surface bone being reassigned as cortical as opposed to trabecular.

97

Although the modified material applications changed the distribution of the stress and strain as desired, the difference in material property application may not be more representative of the actual behavior of pediatric bone. The original material application methods were used in the evaluation through finite element analysis of potential femur fracture in household falls as simulated in the ATD experiments. Additional criteria for identifying potential fractures such as identifying patterns in the stress and strain distribution that could be attributed to partial volume effects as seen in FIGURE 33a were included in the final evaluation. Method A-10 was the material property used in this evaluation since it resulted in the smallest number of bins used to define the material properties and produced stress and strain outcomes equivalent to Method A-50.

B. FE Model Boundary Conditions and Constraints Development

The two distal constraints considered were a fixed intercondylar region constraint and a fixed joint located in the intercondylar region. This section covers the results of the comparison the experimentally measured strains through the ATD strain rosette output in order to determine which distal constraint to use.

1. Constraint Evaluation Using ATD Strain Gauge Output

The maximum principal strain over time is displayed for both distal constraint setups, fixed joint and fixed intercondylar region constraints, used to evaluate the FE model and the experimental output of the strain gauge from the channel that was aligned with the longitudinal axis of the femur in Figure 34. The loads originated from the output of the load cells from the ATD experiments of a bed fall onto linoleum. The fixed intercondylar region constraint more

closely followed the behavior of the ATD strain gauge output as well as having a maximum at similar time points. The fixed intercondylar region constraint was used in further evaluation of the loads from the ATD experiments.
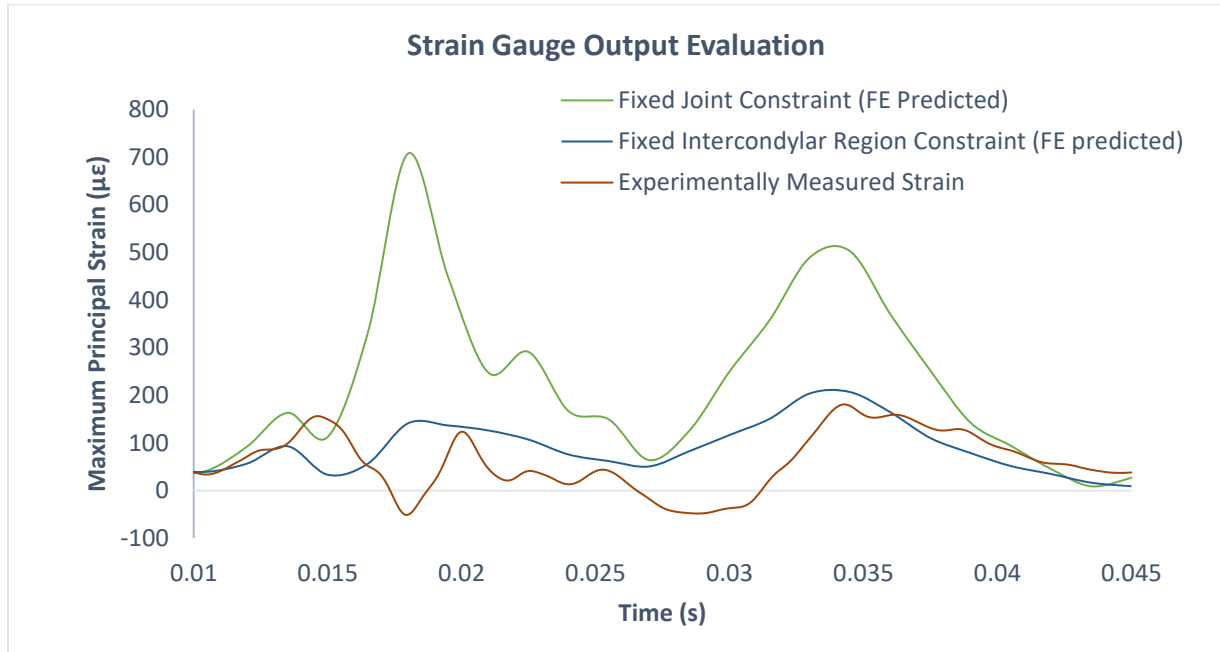
FIGURE 34. Time histories of the peak maximum principal strain for the FE prediction where two analyses with different distal constraints considered (fixed joint and fixed intercondylar region) and the experimental strains as measured by the ATD strain gauge.

C. Validation of FE Model Using Surrogate Bone Testing

The following section covers selection of the proportion of glass fiber and nylon to use in the bone surrogate and the material property testing of different blends. The results of the mechanical testing of the surrogate bone with the chosen blend used in validating the geometry of the FE femur model. The assessment of the validation criteria for the force-displacement and strain time histories when comparing the experimental data to the FE model predicted data is also included.

1. Surrogate Bone Material Property Testing

An initial 35% glass fiber (GF) by weight blend was printed to evaluate the material properties and tested as a potential material for the surrogate bones. Only the tensile properties were tested. Since the ultimate tensile strain was higher than desired, the next batch was increased to 45% glass fiber (GF) by weight. This value was chosen since literature suggests that a blend of approximately 40-50% of glass fiber would yield the maximum tensile strength properties to achieve the target range specified (BASF Corporation, 2003). Tension, compression and bending material properties were evaluated for the 45%GF blend.

a. 35% Glass Fiber/65% Nylon Blend Evaluation. Figure 35 depicts the stress-strain curve for the tensile property testing of five specimens. All tensile test specimens, except for specimen 5 had failed outside of the gauge length region, as defined by the region bounded by the extensometer used in testing, (Figure 36) which could indicate that the test setup was not fully aligned. The mean tensile properties can be found in . The mean values were 52.5MPa, 8.06%, and 1.08GPa for the ultimate tensile strength, ultimate tensile strain, and tensile elastic modulus, respectively.

FIGURE 35. Stress-strain curve for the tensile testing of the 35%GF blend for five specimens A sample 0.2% offset curve for specimen 1 (dotted line) and the yield stress (triangle) are displayed.

FIGURE 36. 35%GF blend tensile test specimens. All specimens except for specimen 5 had failed outside of the gauge length. The dark lines represent the placement of the extensometer during testing.

TABLE XI.

TENSILE TEST PROPERTIES FOR THE 35%GF MIXTURE.

Specimen Id	Ultimate Tensile Strength (MPa)	Ultimate Tensile Strain	Elastic Modulus (MPa)
1	55.2	8.68%	1150
2	52.4	7.94%	998
3	53.9	7.94%	1110
4	49.7	7.59%	1020
5	51.6	8.17%	1120
Mean	**52.5**	**8.06%**	**1080**
S.D.	**2.1**	**0.40%**	**67**

b. 45% Glass Fiber/55% Nylon Blend Evaluation. Figure 37 depicts the stress-strain curve for the tensile property testing. All tensile test specimens, except for specimen 4 which had not failed, had failed outside of the gauge length region (Figure 38)) which could indicate that the test setup was not fully aligned. Specimen 4 had not yet failed by the time the 5kN load cell used had reached its safety limit. Specimen 4 had the thickest cross-section and most other specimens were also close to the safety limit at their failure loads. The specimens for the 45%GF blend used a thicker width than the 35%GF blend which resulted in the increased failure load and resulting in a specimen that had not failed. The mean tensile properties from the tensile testing can be found in Table XII. The mean values were 55MPa, 7.06%, and 1.30GPa for the ultimate tensile strength, ultimate tensile strain, and tensile elastic modulus, respectively.

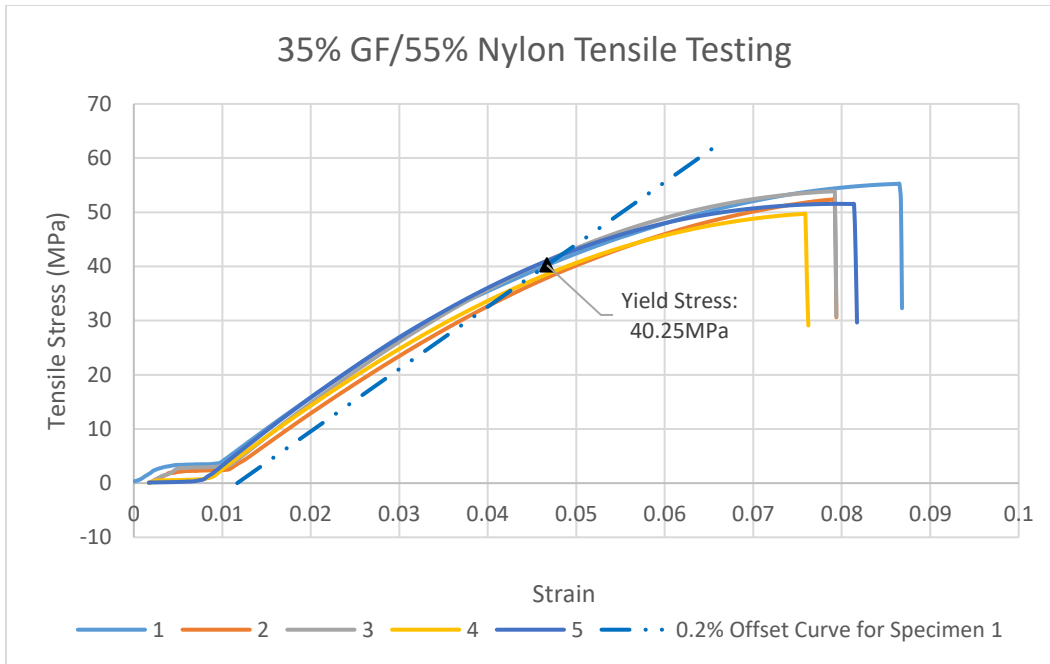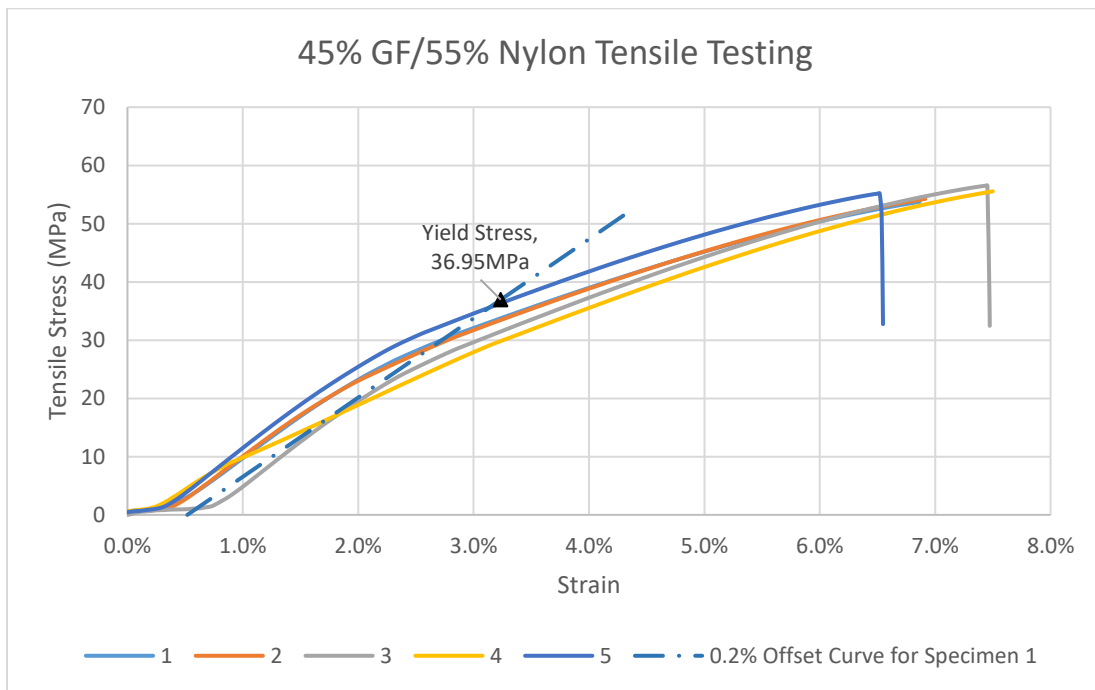FIGURE 37. The stress-strain curves for the tensile property testing of the 45%GF blend for five specimens. specimens A sample 0.2% offset curve for specimen 1 (dotted line) and the yield stress (triangle) are displayed. Note: Specimen 4 did not fail.
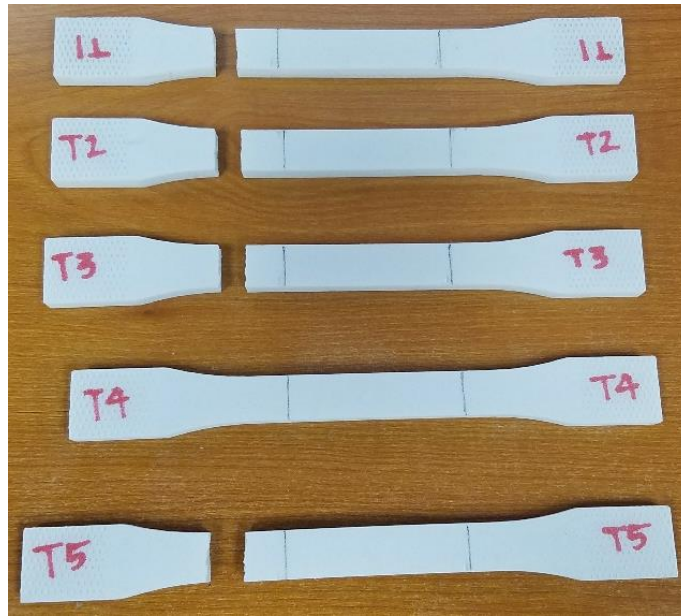
FIGURE 38. Tensile test specimens for the 45%GF blend. The lines represent the gauge length where the extensometer was placed. As seen above, the fourth specimen (T4) did not break.

TABLE XII.

TENSILE TESTING PROPERTIES FOR THE 45%GF BLEND.

Specimen ID	Ultimate Tensile Strength (MPa)	Ultimate Strain (%)	Elastic Modulus (MPa)
1	53.7	6.87%	1360
2	54.2	6.91%	1400
3	56.5	7.47%	1420
4*	55.5	7.50%	912
5	55.2	6.55%	1420
Mean	**55.0**	**7.06%**	**1302**
S.D.	**1.1**	**0.41%**	**219.6**

*Specimen did not fail

Figure 39 depicts the stress-strain curve for the flexural property testing. The resulting

fractured specimens can be seen in Figure 40. The fracture occurred at the same location, which

was at the point of load application, for each specimen. The mean flexural properties from the

testing can be found in Table XIII. The mean ultimate flexural strength, ultimate flexural strain,

and flexural elastic modulus were 79.7MPa, 3.10%, and 4.51GPa, respectively.
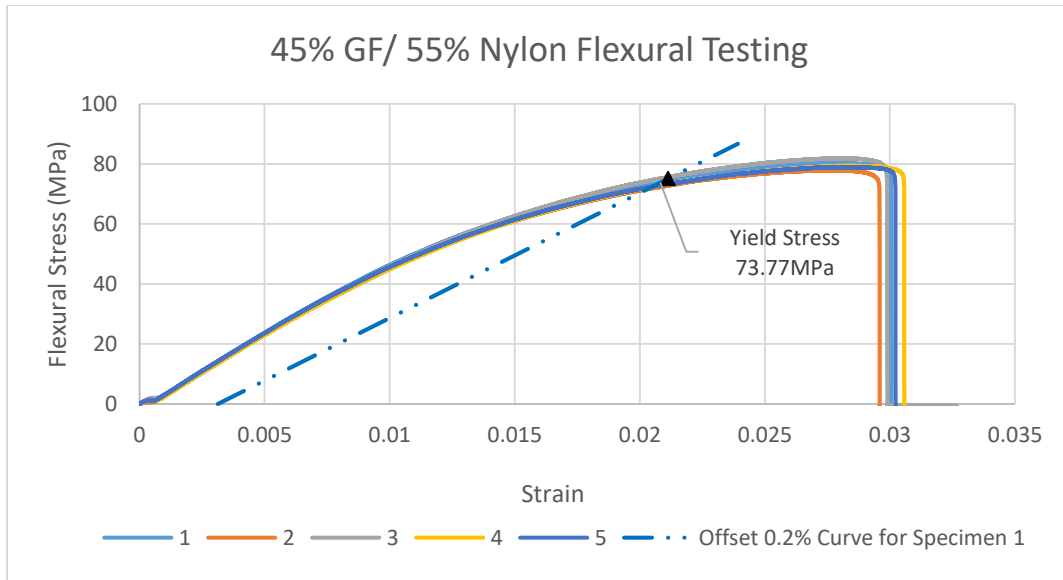
FIGURE 39. The stress-strain curves for the flexural property testing of the 45%GF blend for five specimens. A sample 0.2% offset curve for specimen 1 (dotted line) and the yield stress (triangle) are displayed.
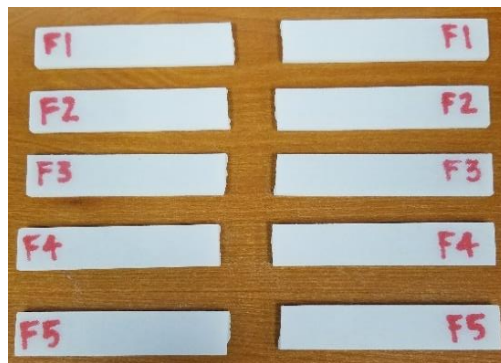
FIGURE 40. Flexural test specimens for the 45%GF blend.

TABLE XIII.

FLEXURAL TESTING PROPERTIES OF THE 45%GF BLEND

Specimen ID	Ultimate Flexural Strength (MPa)	Ultimate Flexural Strain (%)	Flexural Modulus (MPa)
1	80.2	3.09%	4170
2	77.9	2.99%	4640
3	81.9	3.27%	4750
4	79.4	3.09%	4540
5	79.0	3.06%	4450
Mean	**79.7**	**3.10%**	**4510**
S.D.	**1.5**	**0.10%**	**221**

The compression property testing of the 45%GF blend resulted in only three specimens which were evaluated deviating from the five specimens as specified by ASTM D695 (ASTM D695-02a, 2002). Specimens where excess shearing was observed were excluded from inclusion in evaluation of the compressive properties. The specimens had buckled as a result of the compressive loading (Figure 41). The stress-strain curves were derived (Figure 42) and the ultimate strength, compressive modulus, and ultimate strain were calculated (Table XIV) for each specimen.
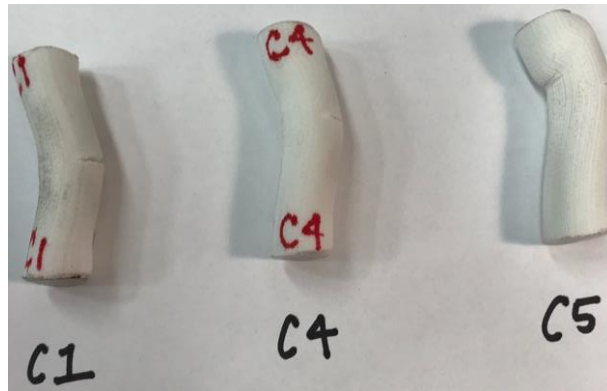
FIGURE 41. Compression test specimens for the 45%GF blend. Note: C1, C4, and C5 correspond to specimen 1, 2, and 3 respectively in Figure 42 and Table XIV.
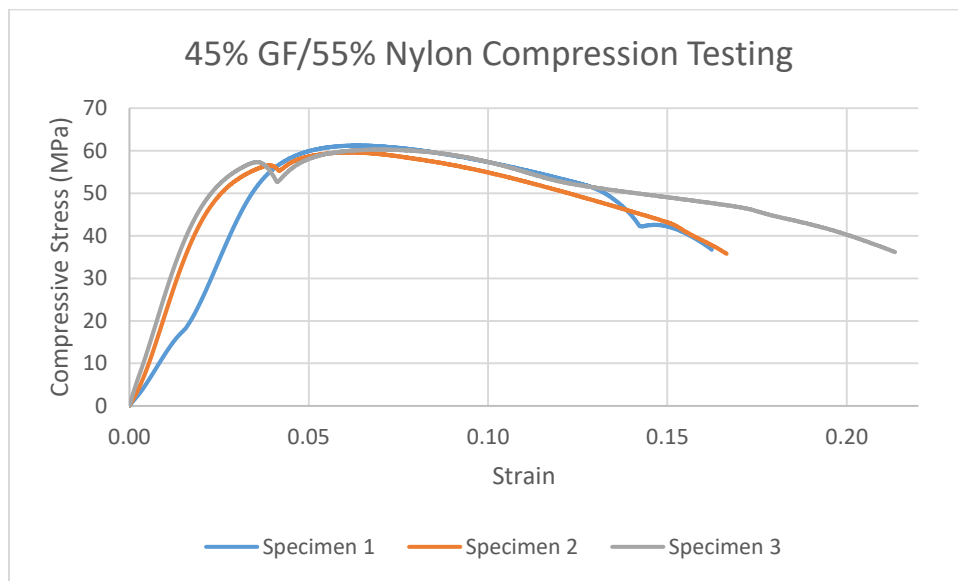
FIGURE 42. Stress-strain curves for compression testing 45%GF blend for three specimens.

TABLE XIV.

COMPRESSION TESTING PROPERTIES OF THE 45% GF BLEND

Specimen ID	Ultimate Compressive Strength (MPa)	Compressive Modulus (MPa)	Ultimate Compressive Strain
1	61.2	1845	6.33%
2	59.6	2480	6.18%
3	60.3	2605	7.23%
Mean	60.38	2310	6.58%
S.D	0.82	407	0.57%

c. Selection of GF/Nylon Blend to Use in Surrogate Bone Models. Table XV shows the target values desired for the surrogate bone and the resulting properties evaluated for the 35% and 45% GF/nylon blends. The 45% GF blend resulted in a greater tensile strength as well as a lower ultimate tensile strain, compared to the 35% GF, both of which are preferable. However, both the flexural modulus and ultimate strength were well below target values. A combination of different materials and different manufacturing processes would be required in order to meet all target property values. Since the purpose of this section was to define the material properties in order to 3D print a surrogate bone model to use to validate the geometry of the FE femur model, the 45%GF was found to be acceptable to use as the basis of the surrogate bone.

TABLE XV.

SUMMARY OF THE OBTAINED MATERIAL PROPERTIES FOR THE GF BLENDS CONSIDERED AND TARGET VALUES OR RANGES OF PROPERTIES.

Property	Target Value/Range	35% GF	45% GF
Ultimate Tensile Strength (MPa)	50-130[2,5]	52.5	55.0
Ultimate Tensile Strain (%)	2-6[2,3,5]	8.06	7.06
Ultimate Bending Strength (MPa)	160[1]	*	79.7
Flexural Modulus (GPa)	80-100[1]	*	4.74
Ultimate Compressive Strength (MPa)	130[6]	*	60.4
Elastic Modulus (GPa)	8-11[2]	1.08	1.30

[*]Not evaluated.

[1](Currey & Butler, 1975); [2](Hirsch & Evans, 1965); [3](Lindahl & Lindgren, 1967); [4](Ohman et al., 2011); [5](Vinz, 1969); [6](Roberts, 1971)

2. Mechanical Testing of Surrogate Bone

The 45%GF/nylon blend was used to create bone surrogates using the SLS process to create three different types of femur surrogates: (1) solid specimens which do not have a medullary cavity, (2) hollow specimens which have a medullary cavity, and (3) reduced metaphysis specimens which have a medullary cavity and reduced infill at the metaphyses. The results of the hollow specimens are discussed below. The results of the other specimens (solid and reduced metaphyses) tested in three-point bending, where only hollow and solid specimens were evaluated, and the compression testing, where all specimen types were evaluated, are discussed in Appendix V.

a. Three-point Bending Test Results. The resulting fracture pattern (Figure 43) was consistent in both its location and type across all specimens tested using the three-point bending setup. The fracture was transverse and occurred at the distal end of the force application region for all specimens tested. A total of 8 hollow specimens and were tested for the three-point bending loading condition.

FIGURE 43. Sample fracture pattern of a hollow (labeled H7) as a result of three-point bending loads. Posterior view (left) and transverse plane view (right).

The force-displacement curve for the hollow specimens tested can be found in three-point bending Figure 44 where accommodations for the toe region were made. The FE model

predicted force-displacement curve was also included for comparison. The fracture load and stiffness for each hollow specimen can be found in Table XVI. The mean fracture load was 552.1N ± 28.8N. The mean stiffness was 145.3N/mm ± 9.0N/mm. The mean AUC was 1208 Nmm ± 107 Nmm. The mean flexural modulus was 2339 MPa ± 87 MPa.
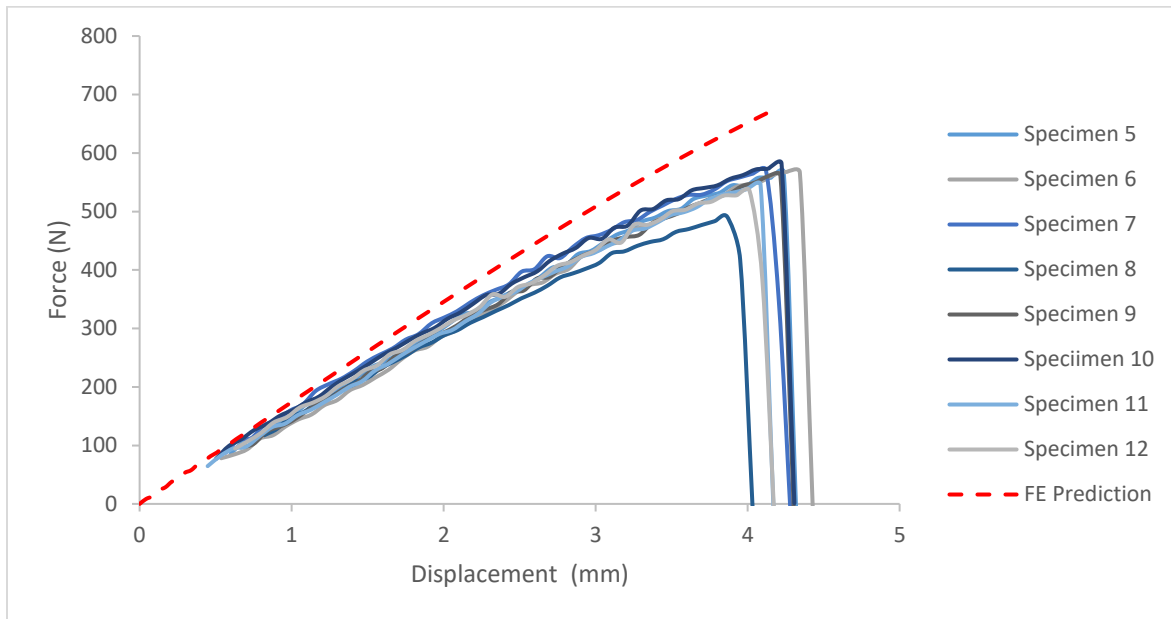
FIGURE 44. Force-displacement curves for the hollow specimens tested under the three-point bending loading conditions and the FE prediction (red). The curves displayed have been adjusted for the toe-region.

TABLE XVI.

OUTCOMES FOR HOLLOW SPECIMENS IN THREE-POINT BENDING

Hollow Specimen ID	Fracture Load (N)	Stiffness (N/mm)	Area Under the Curve (Nmm)	Modulus (MPa)
5	567.8	143.5	1279	2349
6	562.7	145.5	1256	2280
7	570.7	154.7	1266	2454
8	490.6	125.7	985	2207
9	561.5	145.0	1236	2300
10	582.2	153.0	1326	2462
11	546.0	144.3	1179	2303
12	535.3	150.6	1137	2358
Mea	552.1	145.3	1208	2339
Standard Deviation	28.8	9.0	107	86.6

The resulting minimum principal strain curve from the strain gauge for both hollow and solid specimens can be found in Figure 45. The mean peak strain of the hollow specimens was -0.619%. The peak strain of the solid specimen was greater at -0.952%.
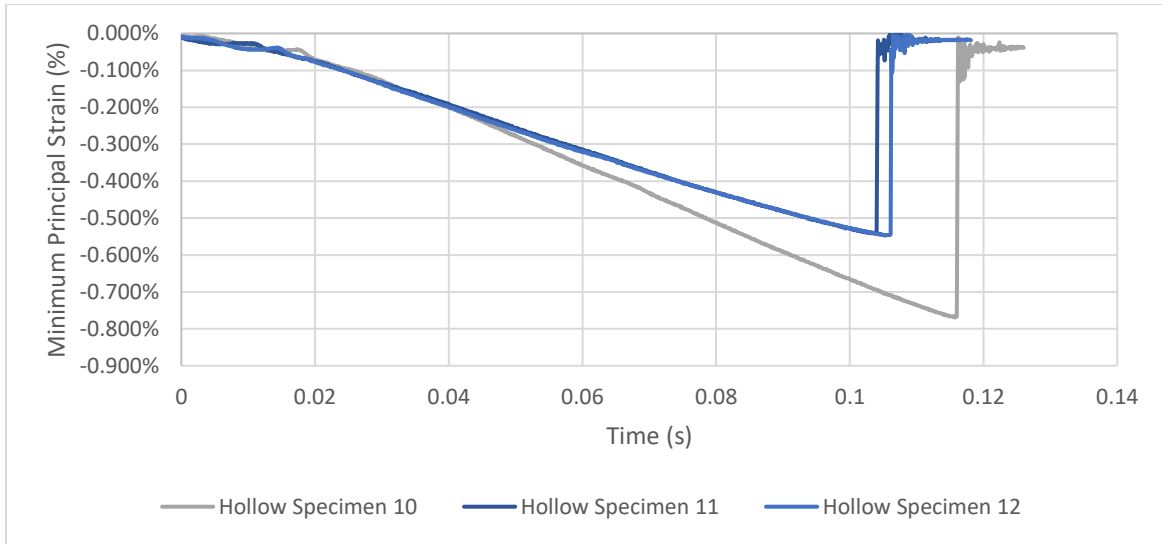
FIGURE 45. Minimum principal strain time history for three-point bending loading condition.

b. Compression Test Results. The compression tests resulted in a range of fracture patterns. The occurrence of these patterns in each specimen type can be seen in Figure 46 and a representative view of each fracture type can be found in Figure 47. Grouping of fracture types was done with the location of positive or distal wedges produced and the degree to which the plane of the fracture deviated from being parallel to the transverse plane. A total of 3 reduced metaphyses specimens, 5 hollow specimens, and 3 solid specimens were tested for the compression loading condition. Information regarding the results of the solid and reduced metaphyses specimens tested can be found in Appendix V.
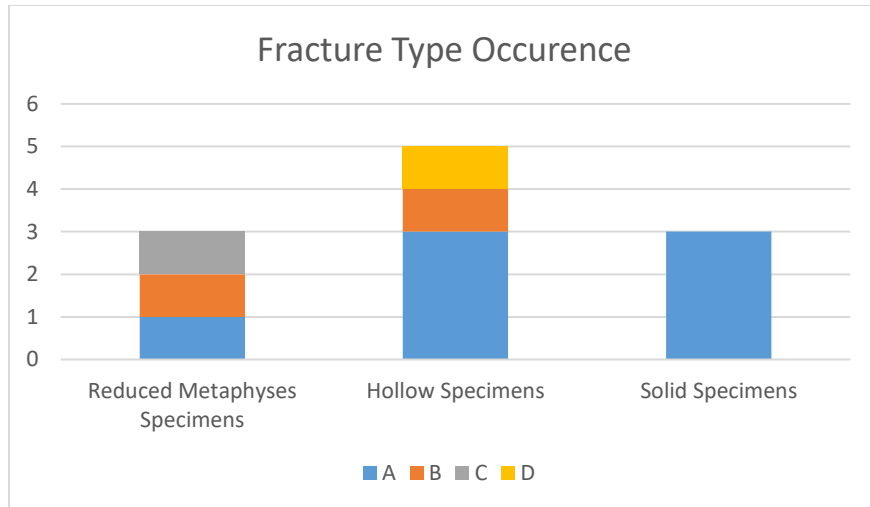
FIGURE 46. Occurrence of each fracture type as a result of the compression loading condition. A representative image of each fracture type can be found in FIGURE 47.
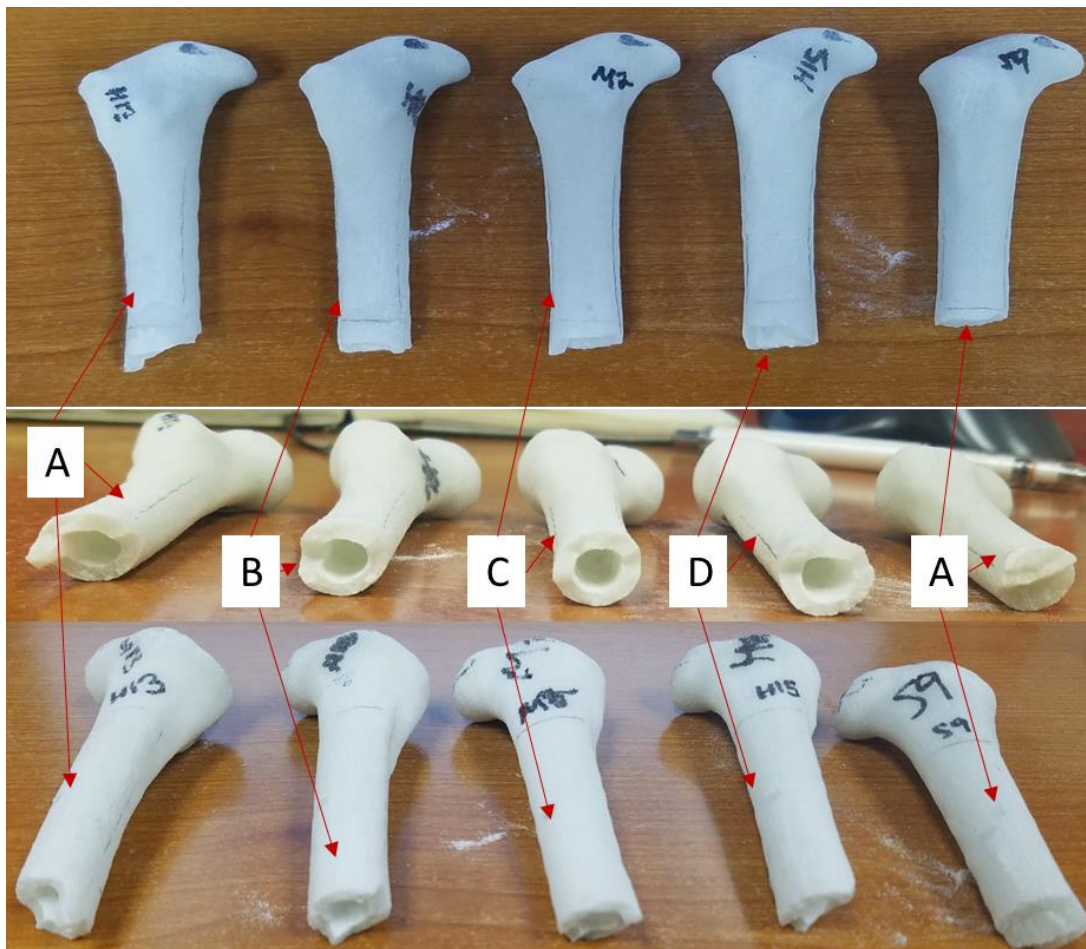
FIGURE 47. Representative image of each fracture type where in the order of A to D (labeled with red arrows) from left to right and the final specimen is a representation of a solid bone. The top, middle, and bottom image represent the posterior, transverse, and anterior views, respectively.

The force-displacement curve for the hollow specimens tested in compressive loading can be found in Figure 48 where accommodations for the toe region were made. A representative curve where no toe region accommodations were made and the FE predicted force-displacement curve are also displayed. The fracture load and stiffness for each hollow specimen can be found in Table XVII. The mean fracture load was 2816 N ± 109 N. The mean stiffness was 951.3N/mm ± 17.1N/mm. The mean AUC was 6390 Nmm ± 555Nmm. The post-yield region of the FE prediction appeared to result in greater deviations from the experimental curves.
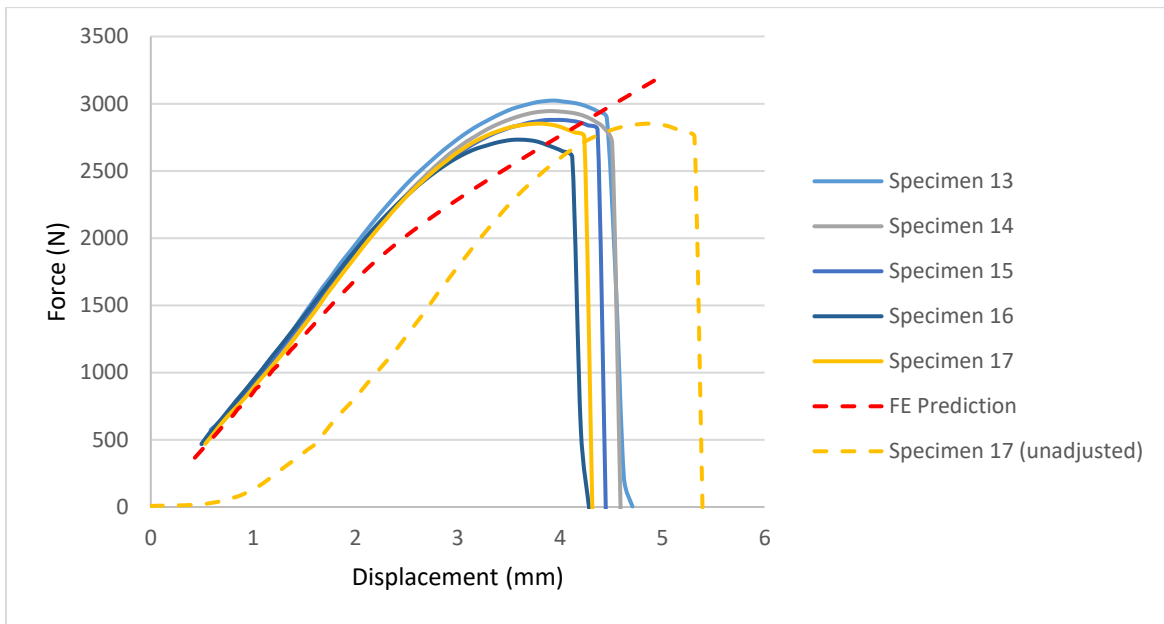
FIGURE 48. Force-displacement curve of the hollow specimens tested under the compressive loading condition. The curves displayed have been adjusted to accommodate for the toe-region. A sample of the original curve for Specimen 17 is displayed for comparison to the adjusted curves. The FE predicted curve is displayed in red.

TABLE XVII.

OUTCOMES FOR HOLLOW SPECIMENS IN COMPRESSION

Hollow Specimen ID	Fracture Load (N)	Stiffness (N/mm)	Area Under the Curve (Nmm)
13	3023	981.7	6907.5
14	2945	941.9	6630.4
15	2879	945.1	6680.1
16	2732	946.1	5497.3
17	2851	941.7	6233.7
Mean	2886	951.3	6389.8
S.D.	109	17.1	554.8

111

The strain gauge time histories of the resulting minimum principal strain can be found in Figure 49. It is important to note that the strain gauge used was only capable of recording a range of ±3% strain. Hollow specimen 17 had reached this maximum limit of the strain gauge. The mean peak minimum principal strain was -1.42% ± 1.23% for the hollow specimens. Due to the different fracture patterns (Figure 47) observed in testing of the hollow specimens, differing time histories of the minimum principal strain were expected.
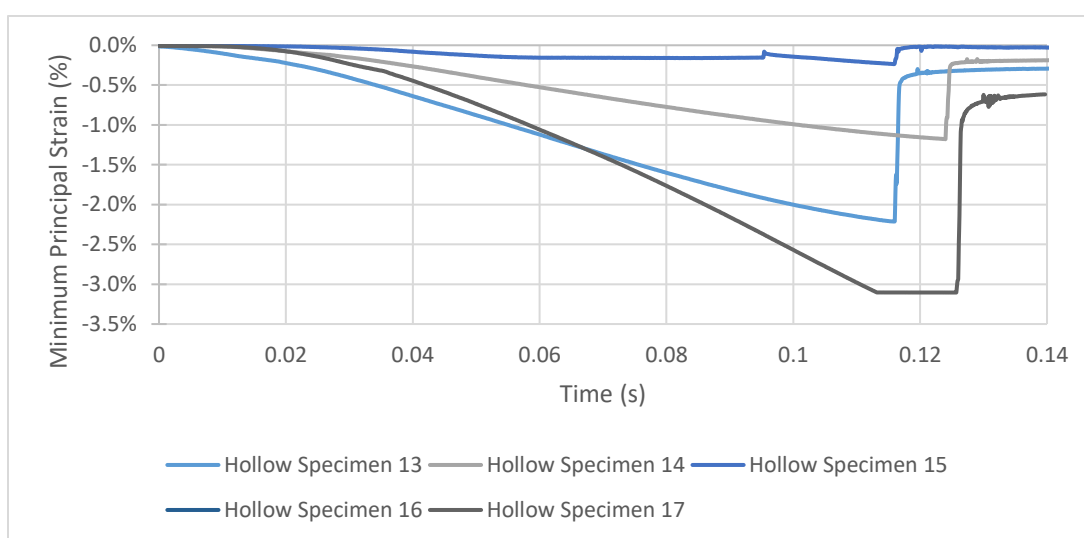
FIGURE 49. Minimum principal strain time histories for all specimens tested with a strain gauge under the compression loading conditions. Note: The curves have not been adjusted to accommodate the toe-region.

3. Comparison to FE Prediction and Validation Evaluation

A comparison of the experimental outcomes (fracture load, stiffness, and area under the curve) to the FE predicted values for both the three-point bending and compression loading conditions. The outcomes of the hollow specimens were used in the evaluation of the validation criteria since it most closely resembled the FE model with the exception that the experimental bone surrogates included powder, which was not sintered, in the medullary cavity. The assessment of the validation criteria of the comparison between the experimental data and the FE

112

prediction are also presented. The experimental curves (force-displacement and strain time histories) were compared to the FE predicted curve where evaluations included calculation of the absolute percent error (mean and standard deviation) between the two curves and deriving the linear regression where the FE predicted load was the predictor for the experimental loads. In order to determine whether the data of all the trials could be grouped to calculate these values, an ANOVA or Mood's median test, which depended upon the results of the Anderson-Darling test (where the null hypothesis is that the distribution is normal), was used.

a. Three-point Bending Outcomes Comparison. The FE model predicted outcomes (fracture load, stiffness, and AUC) were higher consistently than the mean of the hollow specimens (Figure 50).
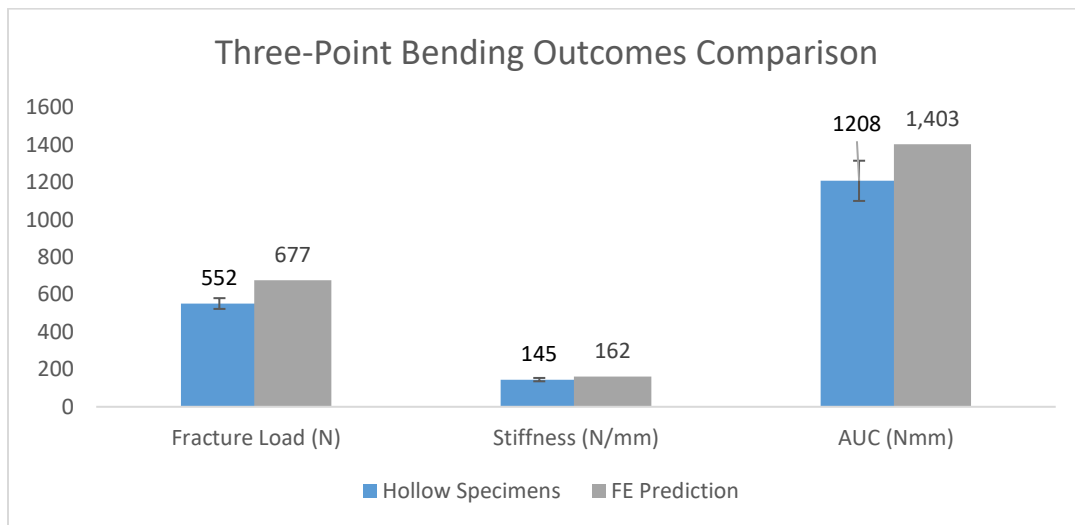
FIGURE 50. Comparison of the outcomes (fracture load, stiffness, and area under the curve or AUC) for the validation three-point bending testing of the surrogate bones to the FE predicted values. Experimental values are mean ± standard deviation.

To compare the experimental force data from the hollow specimens loaded in three-point bending to the FE model prediction, each trial was first evaluated using the Anderson-Darling test where the minimum p-value was 0.06 indicating the data followed a normal distribution. Thus, a one-way ANOVA was conducted which determined that the difference in mean force of

113

the trials was not statistically significant (p-value = 0.916; $r^2 = 0$). All trials were then grouped

to derive the values needed for evaluation of the validation criteria. The scatterplot of the

experimental versus the FE predicted load and the associated linear regression can be seen in

Figure 51. The slope of the linear regression (0.84) indicated that the FE model predicted a

higher force than what was observed experimentally. The figure of the regression demonstrates a

good relationship between the linear regression and scatterplot. The mean absolute percent error

when comparing the FE model predicted and experimental forces at each displacement point as

recorded by the AD-MET was 16.6% ± 4.95%.
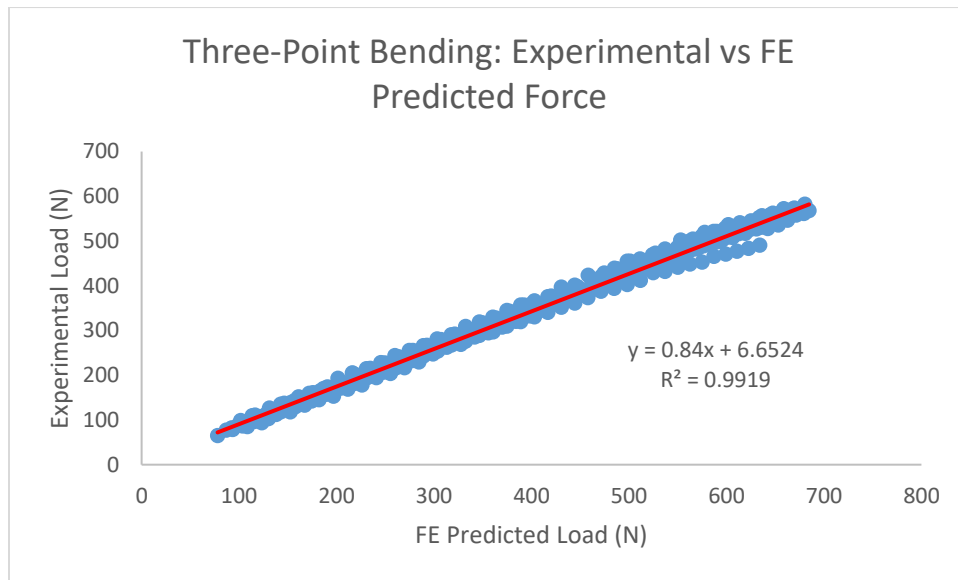
FIGURE 51. Experimental vs FE model predicted loads (N) for the three-point bending loading condition. The linear regression line (red) and its equation are displayed.

To compare the experimental strain data from the hollow specimens loaded in three-point

bending to the FE model prediction, each trial was first evaluated using the Anderson-Darling

where the minimum p-value was 0.101 indicating that all trials followed a normal distribution.

A one-way ANOVA determined that the mean of at least one trial resulted was significantly

different, thus the trials could not be grouped together (p-value of 0.013, $r^2 = 0.07$) to assess the

validation criteria. The regression was evaluated by considering specimen ID as a categorical

factor and the corresponding FE strain to the experimental strain (dependent variable) as the

continuous predictor. The model resulted in an r^2 of 0.9972. The scatterplot of the experimental

and FE prediction of strain with the associated linear regression can be seen in Figure 52 and the

values of each regression can be found in Table XXI. The FE model prediction had the best

agreement with specimen 10 where the slope of the linear regression was closest to unity. The

absolute percent error values were also the lowest for specimen 10 when comparing the

minimum principal strain of the experiment and FE prediction at each corresponding time point.

The shape of the curvature of the data in the scatterplot (Figure 52) in comparison with the

determined linear regression equation appears to be more quadratic than linear, especially

compared to the shape of the scatterplot of the force data (Figure 51). The use of the linear

regression to compare the FE model prediction to the experimental minimum principal strain.

TABLE XVIII.

LINEAR REGRESSION AND ABSOLUTE PERCENT ERROR VALUES FOR THE PREDICTION OF THE MINIMUM
PRINCIPAL STRAIN FOR THE BENDING LOADING CONDITION

Specimen ID	Linear Regression		Absolute Percent Error	
	Intercept	Slope	Mean	Standard Deviation
10	0.012%	1.026	3.20%	2.18%
11	0.012%	0.770	38.33%	4.34%
12	-0.014%	0.752	26.52%	3.84%
Mean	0.003%	0.849	22.69%	3.45%
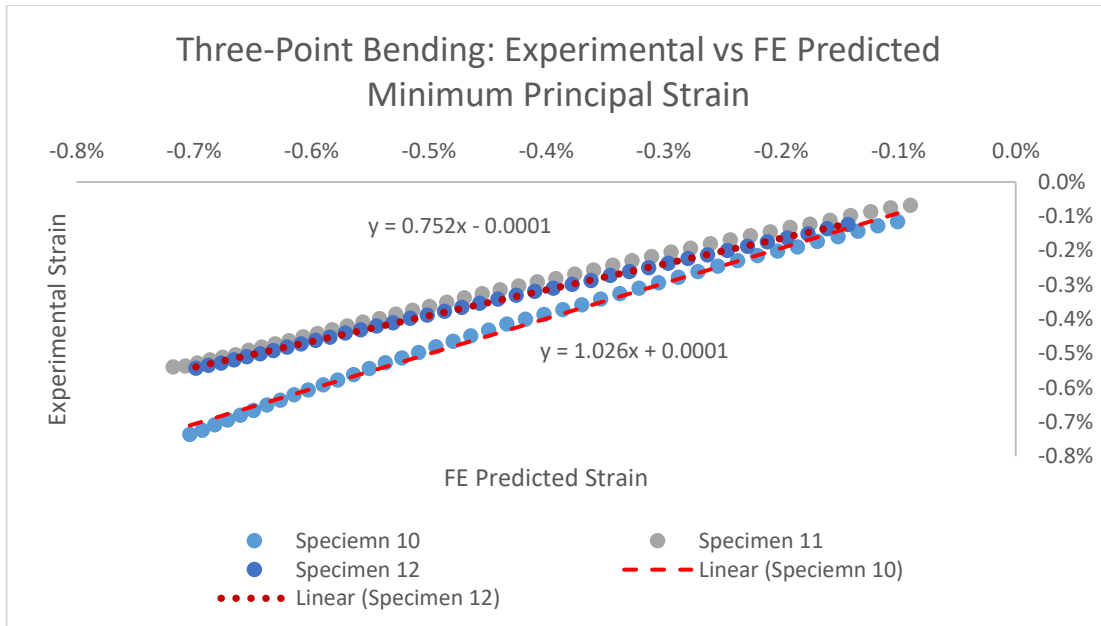
FIGURE 52. Experimental vs FE predicted minimum principal strain at the strain gauge for the three-point bending loading condition. A sample linear regression line for Specimen 10 (dashed, red) and Specimen 12 (dotted, red) and their respective equations are displayed.

b. Compression Outcomes Comparison. The FE prediction was consistently lower when compared to the bone surrogate outcomes types tested for the means of the fracture load, stiffness, and area under the curve outcomes (Figure 53).
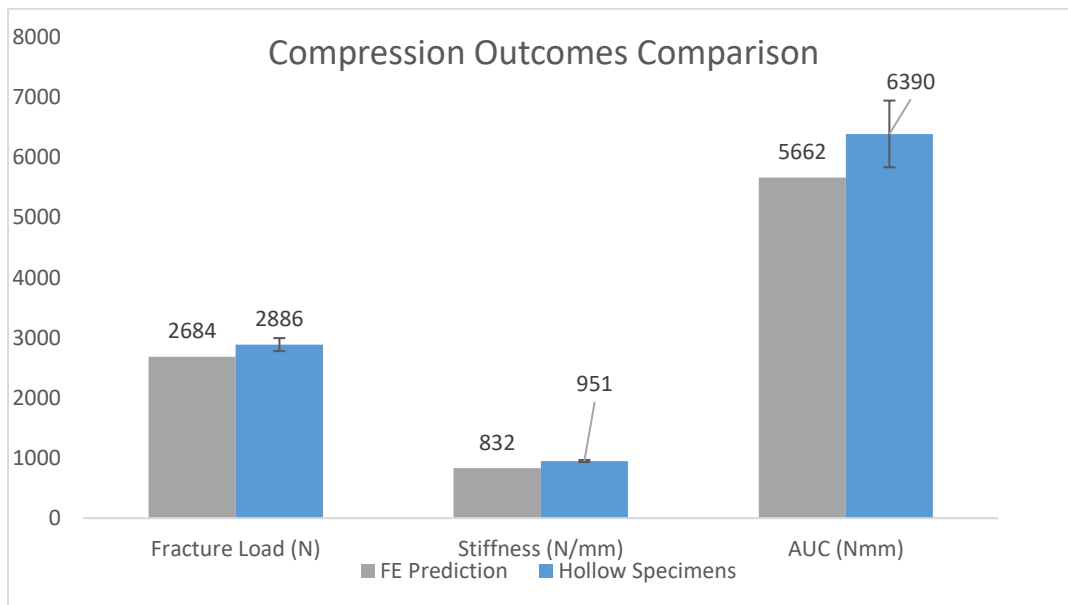
FIGURE 53. Comparison of the outcomes for the validation compression testing of the hollow surrogate bones to the FE predicted values. Experimental values are mean ± standard deviation.

To compare the experimental force data from the hollow specimens loaded compression to the FE model prediction, each trial was first evaluated using the Anderson-Darling test which indicated that the distribution of the force data from hollow specimen 13 is non-normal (p-value <0.005). The mood's median test was then evaluated to compare the medians of each trial where the median of all trials was not found to be significantly different (p-value = 0.965). All trials were then able to be grouped to derive the values needed for evaluation of the validation criteria The scatterplot of the experimental and FE model prediction of the load can be seen in Figure 54. The linear regression where the FE model predicted loads were compared to the experimental load at each displacement point is also displayed. Compared to the visual fit of the linear regression of the force data from the compression testing compared to that of the bending, the FE prediction of the force of the compression loading varied and the shape of the curvature of the scatterplot is less linear. As seen in the force-displacement curve compression for those tested in compression (Figure 48), the FE model prediction tends to deviate more from the experimental outcomes in the post-yield region which may be indicative of limitations in how the material properties were applied or the FE model's inability to represent the post-yield region (or the region where loads are greater than 2000N) in compression. The mean absolute percent error between the FE model prediction and the experimental data was 10.5% ± 3.1% which was less than that of the absolute percent error calculated for the bending loading condition.
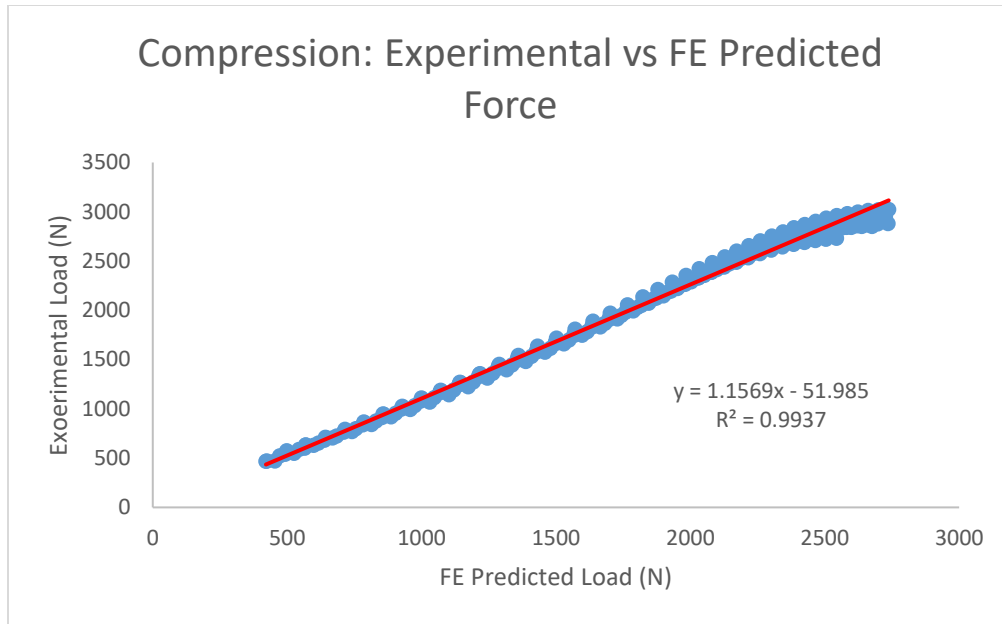
FIGURE 54. Experimental vs FE predicted loads (N) for the compression loading condition. The linear regression line (red) and its equation are displayed.

To compare the experimental strain data from the hollow specimens loaded in three-point bending to the FE model prediction, each trial was first evaluated using the Anderson-Darling test which indicated that the distribution of the strain data from hollow specimen 13 was non-normal (p-value = 0.039). The mood's median test to compare the median minimum principal strain of all experimental trials resulted in at least one trial being significantly different (p-value = 0). A linear regression for the experimental strain versus the predicted strain were calculated for each trial. The curves used for the linear regression can be seen in Figure 55. The relationships determined, and the absolute percent error values calculated for each trial can be found in Table XIX. The reduced agreement between the FE predicted and experimental data especially in comparison to that of the bending data. The derived values for the strain data in the compression loading condition demonstrated a wide range of values where those with B and D fracture types (Figure 47) resulted in the poorest agreement of the FE predicted and experimental data. The range of reported values may be attributed to the distribution of glass fibers within each specimen differing whereas the FE model assumed a homogenous application of materials.

118

Similar to the comparison of the force-displacement curve, the comparison of the strains also resulted in a poor agreement for greater strains, which are those exceeding -2%, further supporting potential limitations in defining the material properties for the post-yield region of the specimens tested in compression.
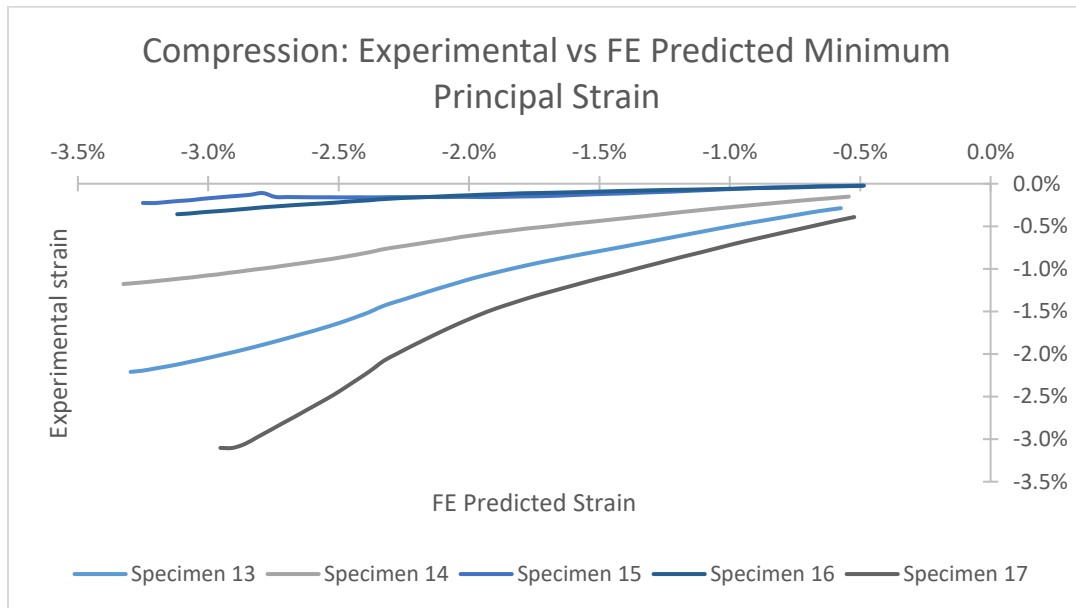
FIGURE 55. Experimental vs FE predicted minimum principal strain for the compression loading condition.

TABLE XIX.

LINEAR REGRESSION RESULTS FOR THE FE MODEL PREDICTION VS EXPERIMENTAL IN COMPRESSION FOR HOLLOW SPECIMENS

Hollow Specimen ID	Intercept	Slope	R² (%)	Absolute Percent Error		Fracture Type
				Mean	Standard Deviation	
13	3.00E-03	0.747	98.7	70%	21%	A
14	1.31E-03	0.395	99.2	214%	33%	A
15	-1.71E-04	0.057	81.0	1483%	326%	D
16	7.65E-04	0.122	92.6	1279%	324%	B
17	5.00E-03	1.158	96.2	21%	14%	A

c. Validation Criteria Assessment.

Table XX contains the values used to assess the validation of the model. The comparison of the strain values for the compression loading condition are means of the trials due to the

119

inability to group the data. The comparison of the FE model prediction and the experimental falls

within the validation criteria with the exception of the absolute percent error calculations for the

comparison of the strain in compression. When excluding the strain data, the absolute percent

error values are within the specified criteria. As discussed previously, deviations in the

prediction of the strains in compression were expected due to the differing fracture types as a

result of the compressive loading and the homogenous application of material properties. The

range of the comparison of the strains due to bending suggest similar limitations in estimation of

the strain although a greater sample size would be needed for both in order to improve the

assessment. The assessment of the comparison of the FE model and the experimental outcomes

suggest that the model may be more adept at predicting the response of the bone due to bending

rather than compression.

TABLE XX.

TABLE OF VALUES FOR THE VALIDATION ASSESSMENT FOR EACH CATEGORY EVALUATED. THE VALUES IN
BOLD INDICATE A FAILURE OF THE VALIDATION VALUE.

	Loading Condition	Three-Point Bending		Compression			
	Data to Compare	Force	Strain	Force	Strain*	Mean	Acceptance Range
Absolute Percent Error	Mean (%)	16.56	22.69	10.47	613	**126.68 (16.6)†**	≤20%
	Standard Deviation (%)	4.95	3.45	3.14	143	**27.89 (3.84)†**	≤20%
Linear Regression	Slope	0.84	0.85	1.16	0.50	0.83	[0.8, 1.2]
	Intercept as % of Peak	1.14	2.13	1.72	13.94	3.68	≤20%
	R^2	99.2%	99.72%	99.4%	93.54%	97.8%	≥80%

† The parenthetical statements contain the mean values of that criteria without the strain comparisons for the compression loading condition.

D. Finite Element Analysis of Femur Subjected to Fall Loading Conditions

The following section covers the factors used to randomly select the ATD trials to evaluate using finite element analysis. The section also includes the outcomes (maximum principal stress and strain and von Mises stress) of the FEA and the evaluation of the stress and strain-based failure criteria.

1. Data Analysis for Evaluating Factors to Include for Selecting Fall Trials

Below is a table of the resulting p-values for whether to include fall dynamics as a factor when randomly selecting trials (Table XXI). The p-value from the general linear model represents whether fall dynamics significantly affects the loading type as the random or fixed term in the feet-first or bed falls, respectively ($\alpha = 0.05$). For the load type, the abbreviations represent: 1) which leg (left), 2) which load cell (proximal, distal, or an average), and 3) the output load.

TABLE XXI.

P-VALUES FOR WHETHER FALL DYNAMICS HAD SIGNIFICANTLY AFFECTED THE LOAD TYPES RESULTING FROM THE ASSOCIATED FALL TYPES. (A < 0.05). FOR THE LOAD TYPE, THE ABBREVIATIONS REPRESENT: 1) WHICH LEG (LEFT), 2) WHICH LOAD CELL (PROXIMAL, DISTAL, OR AN AVERAGE), AND 3) THE OUTPUT LOAD.

Fall Type	Load Type	p-value
Bed Falls	L Avg Fz	0.043
Feet-First Falls	L Avg Fz	0.244
	L Prox Shear	0.335
	L Prox Bending	0.305
	L Dist Shear	none
	L Dist Bending	0.258
	L Prox Torsion	none
	L Dist Torsion	0.243

Only one bed fall load type is included since it showed a statistically significant contribution of the fall dynamics to the measured ATD load. All feet-first measured loads were found to have fall dynamics not significantly affect the outcome. A value of "none" in the table represents that the fall dynamics random factor term did not contribute to the total variance of the mixed effects model as estimated and therefore no p-value was generated. An example of each fall dynamics, where the lower or upper leg impacts first, in bed falls can be found in Figure 56.
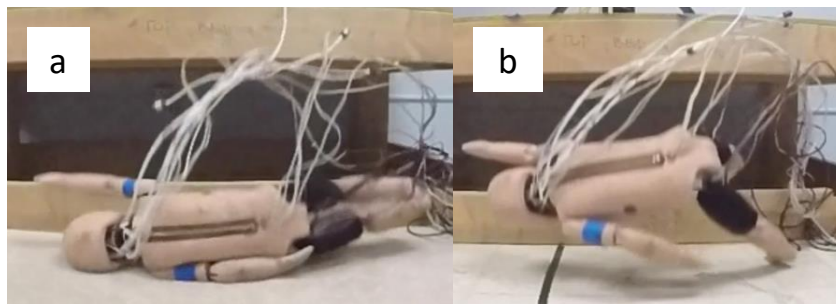
FIGURE 56. Representative images of the fall dynamics in bed falls where either the upper (a) or lower (b) leg impacts the ground first.

2. Evaluation of FE Model Predicted Outcomes

The following section summarizes the outcomes of the FEA when loading from ATD trials of two different fall types were applied to the model. A comparison of the peak maximum principal stress and strain and maximum von Mises stress between the two fall types is outlined. A summary of the evaluation of the yield strain threshold and stress-based failure criteria is also presented.

a. Evaluation of Bed Falls. Figure 57 is a representation of the application of loading from one fall onto linoleum to the FE model. The time histories of the loading derived from the ATD load cells and the corresponding time history of the FE model predicted outcomes are displayed along with key frames of the fall displayed on the left.
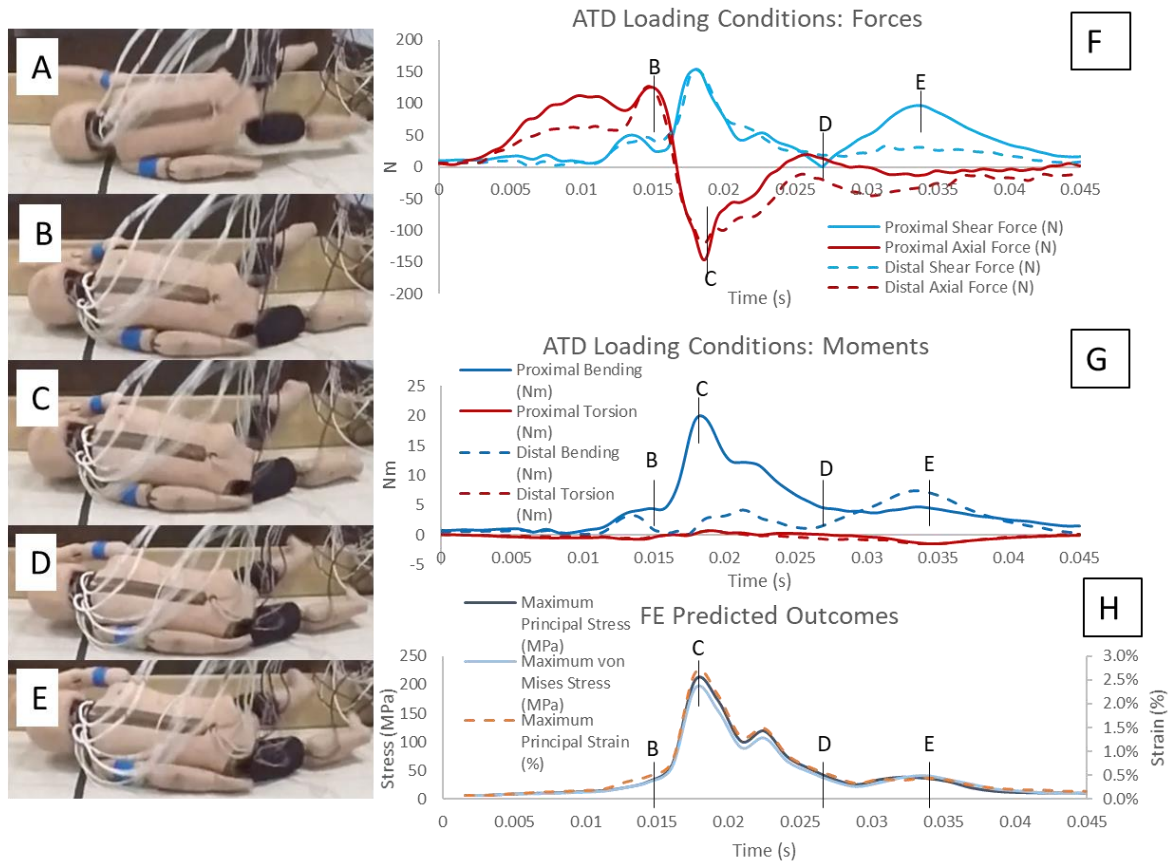
FIGURE 57. Loading conditions and FE predicted outcomes of a bed fall onto linoleum. Forces (F) and moments (G) of the ATD loading conditions and the FE model predicted outcomes (H). The corresponding fall dynamics for time points B-D are displayed. A corresponds to time zero. B corresponds to when the lower leg first begins to impact. C corresponds to when the pelvis impacts the ground and the peak axial force, bending moment, and FE predicted outcomes. D corresponds to when the leg rebounds off the ground and the forces are approximately zero at this point. E corresponds to the second peak shear force and bending moment where the upper leg hits the ground again.

The range of the peak maximum principal stress and peak von Mises stress can be found in Figure 58. The mean peak maximum principal stress and peak von Mises stress for the falls onto carpet were 108 MPa and 104 MPa, respectively. The mean peak maximum principal stress and peak von Mises stress for the falls onto linoleum were 141 MPa and 134 MPa, respectively.

FIGURE 58. FE predicted means for the peak maximum principal stress and mean von Mises stress for bed falls grouped by impact surfaces, carpet and linoleum. Error bars represent the range of values (n=6).

A further breakdown of the peak stresses with respect to the fall dynamics can be seen in Figure 59. There were two different fall dynamics for bed falls: (A) when the lower leg impacts the ground first and (B) when the upper leg impacts first. Dynamic A (lower leg impacts first typically resulted in higher peak stresses. The mean peak stress for fall dynamic A onto linoleum were 179 MPa and 162 MPa for the peak maximum principal stress and von Mises stress, respectively. The mean peak stress for fall dynamic B onto linoleum were 103 MPa and 106 MPa for the peak maximum principal stress and von Mises stress, respectively. The mean peak stress for fall dynamic A onto carpet were 164 MPa and 148 MPa for the peak maximum principal stress and von Mises stress, respectively. The mean peak stress for fall dynamic B onto carpet were 52 MPa and 59 MPa for the peak maximum principal stress and von Mises stress, respectively.
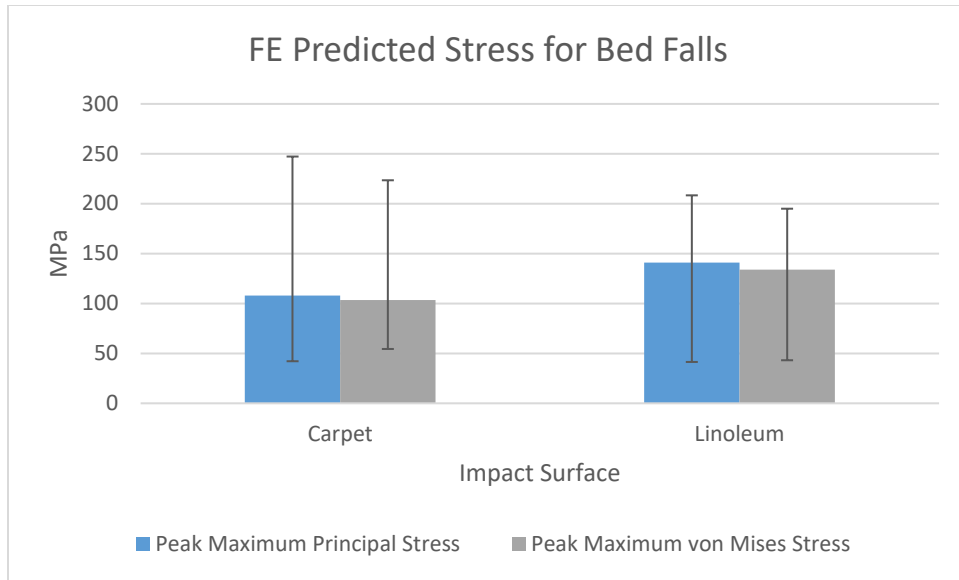
124

FIGURE 59. FE predicted means for the peak maximum principal stress and peak maximum von Mises stress for bed falls grouped by impact surface and fall dynamic. Fall dynamic categories correspond to when the lower (A) or upper (B) leg impacts first. Error bars represent the range of values (n=3).

The fall dynamic was the only factor where there was a significant difference in mean peak strains between its defined levels (p=0.021) when conducting the ANOVA of the peak strain for the bed falls. The lower leg impacting first (fall dynamic A) resulted in a higher mean peak strain of 2.25% compared to the upper leg impacting first (fall dynamic B) 1.15%. Impact surface, the other factor considered in the ANOVA, did not have a significant difference between the means of the peak strain of falls onto linoleum or carpet. The range of peak strains for the interaction of the fall dynamics and impact surfaces can be found in Figure 60.
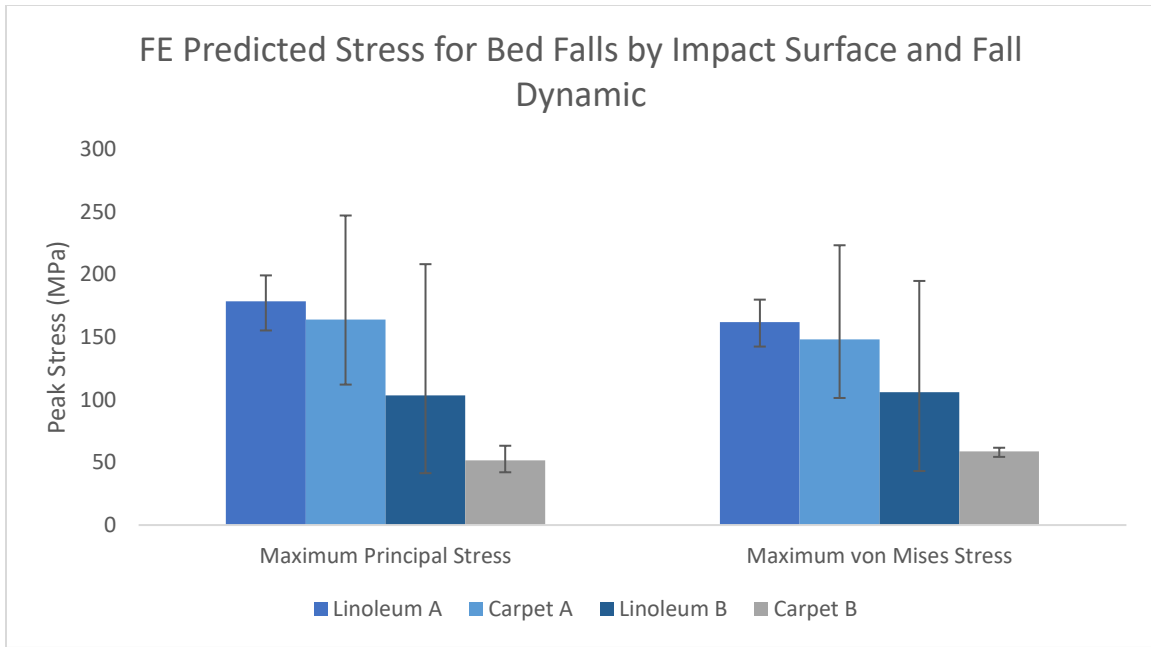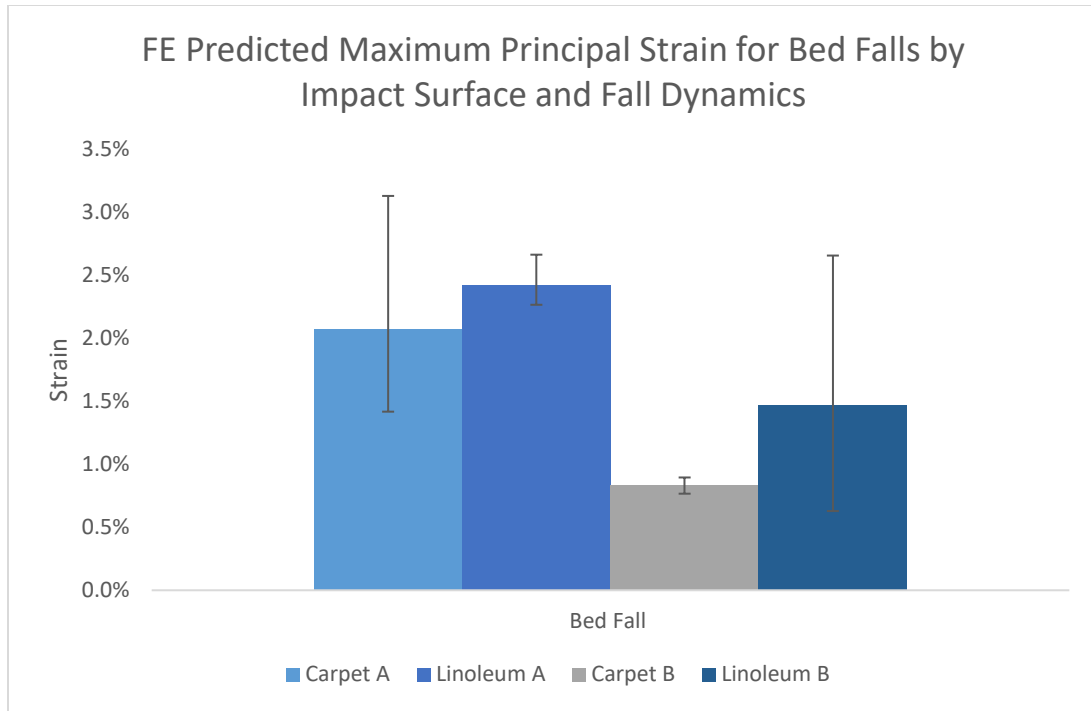
FIGURE 60. FE predicted means for the peak maximum principal strain for bed falls grouped by impact surface and fall dynamic. Fall dynamic categories correspond to when the lower (A) or upper (B) leg impacts first. Error bars represent the range of values (n=3).

b. Evaluation of Feet-first Falls. Figure 61 is a representation of the application of loading to the FE model from a 119cm fall onto linoleum. The time histories of the loading derived from the ATD load cells and the corresponding time history of the FE model predicted outcomes are displayed along with key frames of the fall displayed at the top of the figure.
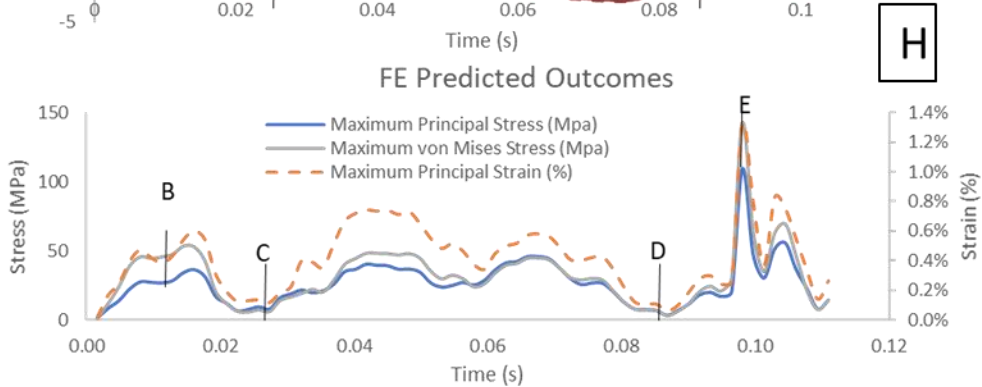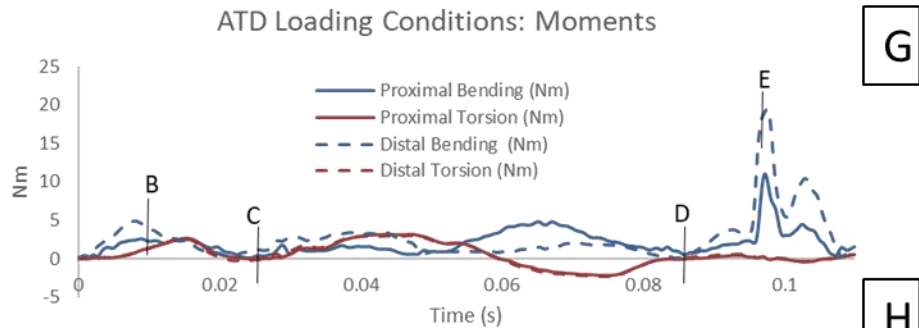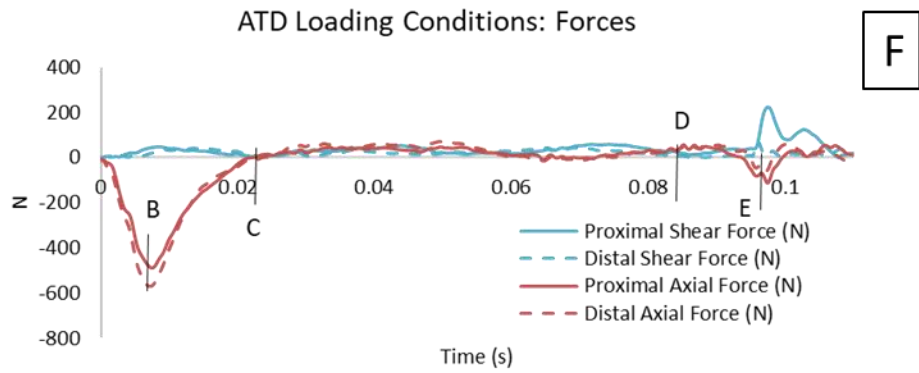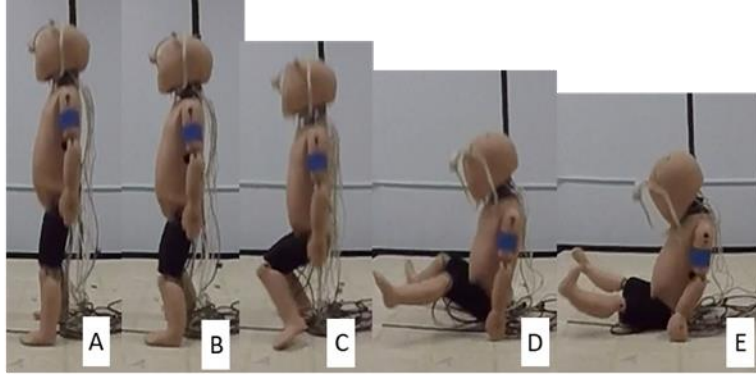
FIGURE 61. Fall dynamic sequence and corresponding time history of both the loading condition and FE outcomes for a 119cm fall onto linoleum. Forces (F) and moments (G) of the ATD loading conditions and the FE model predicted outcomes (H). A corresponds to when the feet initially impact which is the beginning of the time displayed on the chart. B corresponds to the peak compressive force. C corresponds to when the feet begin to rebound off the ground and swing forward. D corresponds to when the pelvis begins to impact the ground. E corresponds to the peak moment, secondary peak axial force, and peak FE predicted outcomes when the pelvis fully impacts.

127

The peak maximum principal stress and peak maximum von Mises stress can be found in Figure 62. Falls from 69cm onto carpet had a mean maximum principal stress and von Mises stress of 42 MPa and 52 MPa, respectively. Falls from 69cm onto linoleum had a mean maximum principal stress and von Mises stress of 55 MPa and 70 MPa, respectively. Falls from 119cm onto carpet had a mean maximum principal stress and von Mises stress of 179 MPa and 163 MPa, respectively. Falls from 119cm onto linoleum had a mean maximum principal stress and von Mises stress of 112 MPa and 148 MPa, respectively.
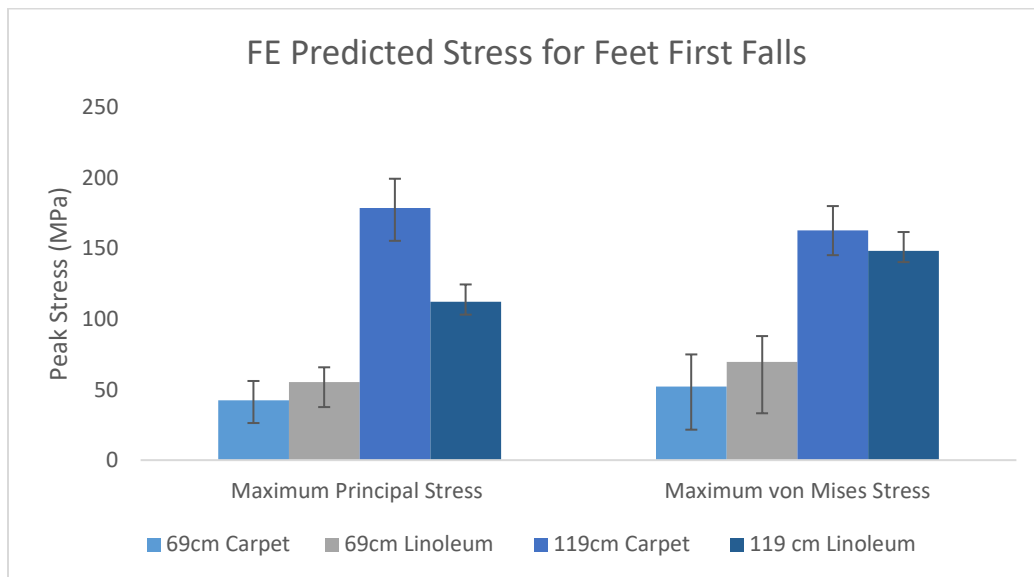
FIGURE 62. FE predicted means for the peak maximum principal stress and peak maximum von Mises stress for bed fall trials grouped by impact surface and fall height. Error bars represent the range of values (n=3).

The different fall heights (69cm and 199cm) resulted in significantly different peak strain (p-value < 0.05) in the ANOVA for the peak strain of feet-first falls when considering fall heights and impact surfaces as factors. The Tukey pairwise comparison indicated that the mean peak maximum principal strain for the 119cm fall height (1.98%) was significantly greater (α = 0.05) than the 69cm fall height (0.66%). The results of this ANOVA where the greater fall height resulted in greater outcomes led to a failure to reject hypothesis 2 which stated that the greater height would correspond to an increase in outcomes. The increase in outcomes are assumed to be

associated with an increase in fracture likelihood. The mean peak maximum principal strain for impacts onto linoleum were 1.31% and onto carpet were 1.33% which were not found to be significantly different. A breakdown of the interaction of the fall height and impact surface for the peak strain in feet-first falls can be found in Figure 63.
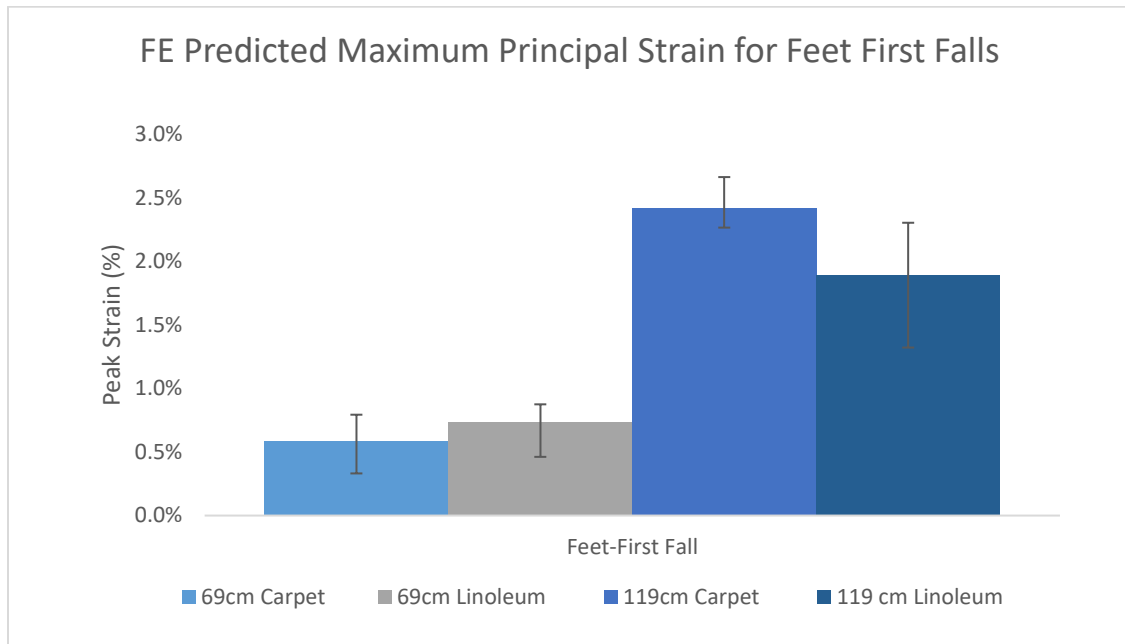
FIGURE 63. FE predicted means for the peak maximum principal strain for feet-first falls grouped by impact surface and fall height. Error bars represent the range of values (n=3).

c. Comparison of Feet-first and Fed Falls. A comparison of the peak maximum principal strain between the bed falls and the feet-first falls can be seen in Figure 64 below. The mean maximum principal strain for the falls onto carpet were 1.46% and 1.33% for the bed falls and feet-first falls, respectively. The mean maximum principal strain for the falls onto linoleum were 1.95% and 1.31% for the bed falls and feet-first falls, respectively. Although the mean peak strain for bed falls was higher for falls onto linoleum, the trial with the highest peak strain occurred for a fall onto carpet where the lower leg impacted first (fall dynamic A). For both feet-first falls and bed falls, impact surface was not a significant factor in the corresponding ANOVAs where the outcome is the peak strain resulting in a rejection of hypothesis one which

stated that the linoleum surface would result in greater outcomes than carpet. Of the loads input into the finite element analysis from the ATD load cells, it is possible that the impact surface does not significantly affect the loading in a way that translates to a difference in the peak outcomes of the diaphysis of the femur.
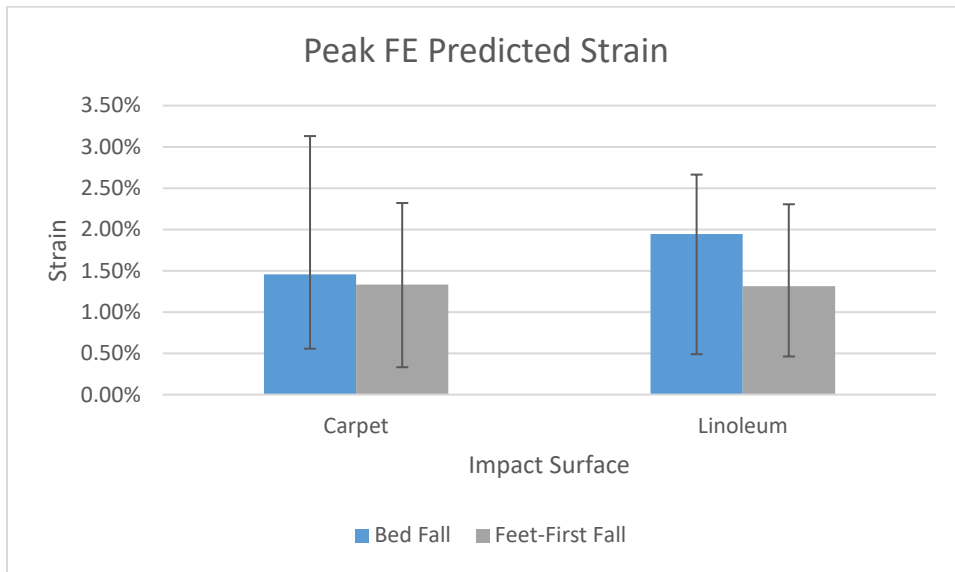
FIGURE 64. FE predicted means for the peak maximum principal strain grouped by fall type and impact surface. Error bars represent the range of values (n=6).

d. Fracture Threshold Evaluation. Figure 65 shows the occurrence of each failure classification for the different impact surfaces of each fall type. Refer to Table IX for the description of the failure classification. Since the data resulted in a quasi-complete separation of data, which means that all categories were not included in all factors of interest, a logistic regression was not conducted. A total of four trials (of 24) resulted in no elements above the tensile yield strain threshold. Classification A occurred more often in bed fall trials (6 trials; 50%) versus feet-first fall trials (none). Classification B occurred more in feet-first trials (6 trials; 50%) versus bed fall trials (1 trial; 8.3%).
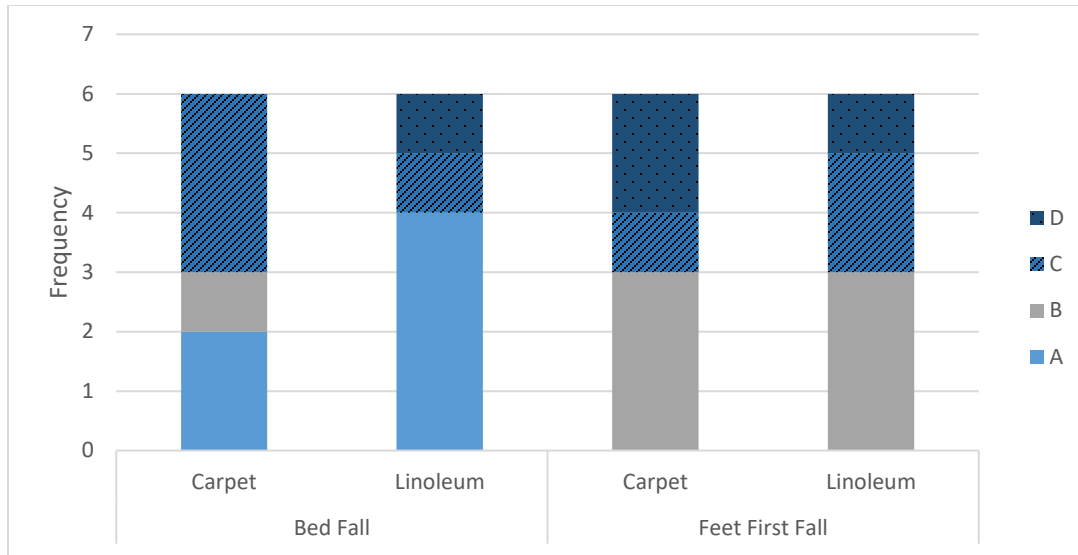
FIGURE 65. Frequency of trials for each failure classification based on the yield strain threshold for each fall type and impact surface. Classification A refers to a potential fracture. Classification B refers to a fracture that is attributed to PVE. Classification C refers to a few elements exceeding the threshold with less than 5 contiguous elements. Classification D refers to no elements having exceeded the threshold.

A representative view of classifications A-C can be seen in Figure 66. The left side of the figure represents the maximum principal strain distribution for three different falls. The right side of the figure depicts the diaphysis with the yield strain threshold (0.73%) applied. Examples of failure classification A (top set of images), B, (center set of images), and C (bottom set of images) are displayed.
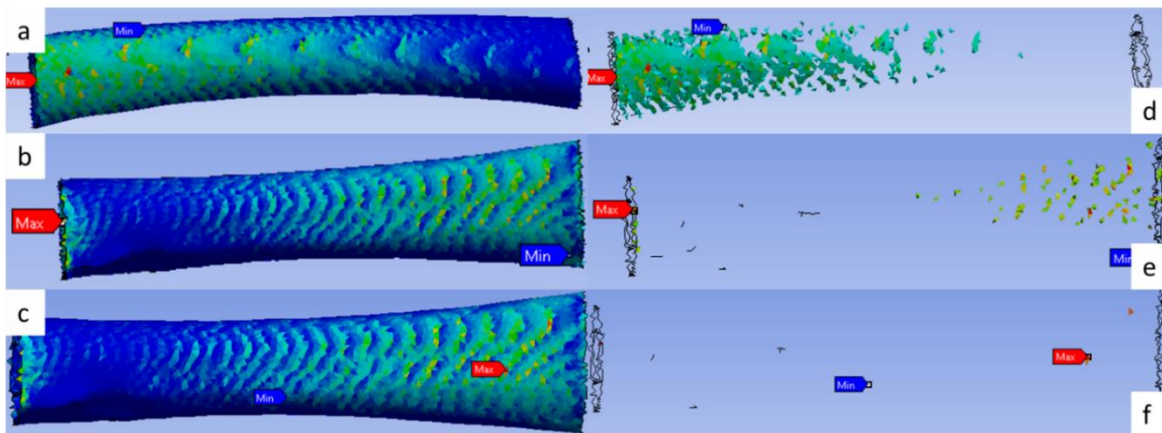
FIGURE 66. Maximum principal strain distributions for classification A (a, d), B (b, e) and C (c, f) where the left side (a-c) is with no thresholding applied and the right side (d-f) is a threshold where the minimum value displayed is 0.73% strain. (a) and (d) show the medial view of the peak strain for a bed fall onto linoleum. (b) and (d) depicts the posterior view for a 119cm feet-first fall onto linoleum. (c) and (f) depicts the posterior view of the peak strain for a 69cm feet-firt fall onto carpet. Classification A refers to a potential fracture. Classification B refers to a fracture that is attributed to partial volume effects. Classification C refers to a few elements exceeding the threshold with less than 5 contiguous elements.

All 119cm feet-first falls exceeded fracture classification B. For the 69cm falls, falls exceeded fracture classification C (linoleum, n=2; carpet, n=1) and D (linoleum, n=1; carpet, n=2). All bed falls onto linoleum exceeded fracture classification A for when the lower leg impacted first (fall dynamic A) and A, C, and D for when the upper leg impacted first (fall dynamic B). The bed falls onto carpet exceeded fracture classification C for all trials when the upper leg impacted first (n=3) and a classification of A (n=2) and B (n=1) for when the lower leg impacted first. The higher frequency of classifications as A or B for the higher levels of fall height (feet-first falls) and fall dynamics (bed falls) was consistent with those deemed significant by the ANOVA (119cm falls versus 69cm feet-first falls and the lower leg impacting first in bed falls).

The trials classified as A (potential fracture) and B (potential fracture associated with partial volume effects) were evaluated to determine what percent volume of the region between the load cells, or the diaphysis, exceeded the yield strain threshold (0.73%). Feet-first falls typically had greater volume exceeding the threshold compared to bed falls even though feet-first falls were only classified as a B classification (Figure 67). This can be attributed to the fact that feet-first falls had elements that were exceeded across the entirety of the diaphysis while bed falls with an A classification were concentrated in one location.
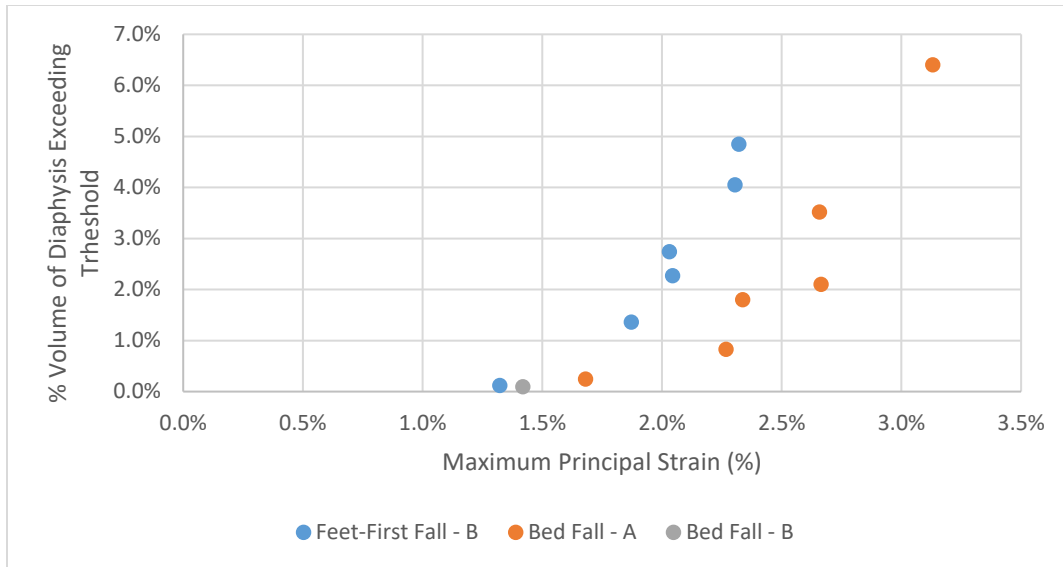
FIGURE 67. Percent volume of the diaphyseal region (or the region between the location of the two load cells) which exceeded the yield strain threshold of 0.73%. Feet-first falls and bed falls classified as a potential fracture due partial volume effects (B classification) are displayed in blue and grey, respectively. Bed falls classified as a potential fracture (A classification) is displayed in orange.

For the ultimate tensile strength fracture threshold, all trials that exceeded the strain fracture threshold (A classification) also exceeded the tensile strength fracture threshold (A classification). Only two bed fall trials exceeded the ultimate flexural strength fracture threshold (A classification) which included one fall onto linoleum where the upper leg impacted first (dynamic B) and one fall onto carpet where the lower leg impacted first (dynamic A). A summary of the number of trials that exceeded the failure criteria can be found in Table XXII.

TABLE XXII.

DESCRIPTION OF STRAIN AND STRESS-BASED FAILURE CRITERIA WITH THE CORRESPONDING FREQUENCY OF BED FALLS (N=12) AND FEET-FIRST FALLS (N=12) EXCEEDING EACH THRESHOLD AND ALSO MET THE CRITERIA FOR FAILURE CLASSIFICATION A.

FE Model Predicted Outcome	Threshold Description	Threshold Value	Additional Criteria	Feet First Falls Exceeding Threshold	Bed Falls Exceeding Threshold
Maximum Principal Strain	Yield Strain	0.73%	A minimum of 5 contiguous elements must have exceeded the threshold.	0	6
Maximum Principal Stress	Ultimate Flexural Strength	157.8MPa		0	2
	Ultimate Tensile Strength	100MPa		0	2

V. DISCUSSION

A finite element model representing an 11-month-old femur was developed. The stress and strain distributions across the diaphysis of the femur were evaluated based on the application of loading conditions derived from previously conducted ATD experiments simulating bed and feet-first falls. Comparisons of the FE predicted outcomes to stress and strain-based thresholds were made to identify potential fractures. Identification of potential fractures may be limited by aspects of the FE model, the ATD experiments from which the loading conditions were derived, and lack of extensive research of pediatric mechanical properties. In spite of these limitations, the FE femur model may be useful to be able to evaluate correlations of different factors such as impact surfaces and fall heights with the likelihood of potential fractures.

The validation of the FE femur model's geometry was accomplished by comparing FE predicted outcomes to experimental results of three-point bending and compression testing of glass fiber reinforced nylon bone surrogates. The material model of the FE representing the bone surrogate material was a homogenous bilinear isotropic material. Assessment of the validation criteria values indicated that the FE model prediction of the force-displacement data and strain time history comparison had an overall better agreement for specimens tested under the bending loading condition. The specimens tested in compression resulted in a variety of resulting cross-sections of the fracture with different degrees of obliqueness in both the anterior-posterior and medial-lateral directions. The fracture types of the compression tested specimens also corresponded to a wide range of recorded minimum principal strain obtained using a strain rosette. Thus, the FE model predicted strain time history of the compression loading condition compared to the experimental resulted in a poor overall agreement and can likely be attributed to

135

the application of material properties. Using the current FE femur model to identify potential

fractures due to household falls may be limited in the model's ability to respect the response

(through stress and strain outcomes) of the bone in bending and compression. The results of the

validation testing suggest that the model may be more effective at evaluating bending loads

compared to loading in compression.

Though there are many studies evaluating femur fracture using finite element analysis,

we cannot directly compare our results due to differences such as region of femur evaluated for

fracture, the population evaluated, and the material models used. Comparison of the outcomes of

the FEA of bed and feet first falls to other studies that use finite element analysis to investigate

femur fracture is limited because those studies generally focus on the proximal region of the

femur where the femoral head is typically loaded, and where fractures outside of the femoral

diaphysis would be expected. Studies investigating femur fracture focuses on elderly subjects

who may be susceptible to hip or femur fractures when falling due to bone fragility conditions

such as osteoporosis or osteopenia such as one study by Grassi et al. (2012) investigating three

different sideways loading configurations of the impact of onto the ground where the loading

applied was static rather than dynamic. Other studies may have applied non-linear material

models, such as a bilinear elastoplastic model, using a set of yield and ultimate stress criterion to

identify fractures such as one by Koivumäki et al. (2012) investigating identification of fracture

locations in sideway falls onto a femur compared to this study which used a linear material

model.

In the only other known pediatric finite element fracture evaluation conducted by Li et al.

(2015), the FE model developed for both the Li study and the current study were similar in

density-elasticity relationships used to define the material applications and the yield strain

thresholds used. There are many differences between the development of the models including the CT scan used to develop the approximately one-year old femur, which is approximately the same age as the subject's femur evaluated in the current study, from the Li study compared to the current study including having a smaller scan thickness (0.625mm versus 1mm in the current study), a higher threshold used to segment the femur (350HU versus 156HU in the current study), a static versus a dynamic load application in the current study, and different programs used to apply the material properties. The result of these differences could result in different geometries since a higher threshold HU threshold was used in their study and different resulting distribution of material properties due to the higher resolution of their scans and different programs which likely defines the material properties differently. Despite these differences, a similar estimation fracture due to bending was estimated in both studies. Li predicted a 600N fracture load for the one-year old FE femur model which when considering the length of the support span, translates to an estimated 23Nm bending moment. The bed falls where a potential fracture was identified using the tensile yield strain threshold, which was the threshold used in the Li study, had lower but similar bending loads ranging from 14-23Nm.

A. Likelihood of Pediatric Femur Fracture due to Bed and Feet-First Falls

The only trials identified as a potential fracture using any of the specified thresholds (tensile yield strain, ultimate tensile strength, and ultimate flexural strength) were bed falls. Six trials (25% of all; 50% of bed falls) exceeded the tensile yield strain threshold and the ultimate tensile strength threshold while only two of the six trials (8% of all; 16% of bed falls) exceeded the ultimate flexural strength. The dynamics of bed falls differed from feet-first in that the peak bending moment and compressive load usually occurred upon initial impact in bed falls. Feet-

first falls had two primary impacts where the first is where the peak compressive load upon impact of the feet was observed and the peak bending moment was observed during the second impact of the pelvis impacting. The peak maximum principal strain typically occurred at the corresponding peak bending or torsional load, where higher torsional loads were only found in feet-first falls, for all trials. The bending moments observed in bed falls were generally greater than those in feet-first where trials that had exceeded the yield strain threshold exceeded 14Nm bending moment compared to only one feet-first fall evaluated exceeding 14Nm. Feet-first falls resulted in greater compressive loads where the peak ranged from 63N to165N for bed falls and 148N to 530N for feet first falls.

1. Identification of Potential Femur Fractures in Bed Falls.

Half of the twelve bed fall trials evaluated were categorized as having a potential fracture when compared to the yield strain threshold. The location of peak strains in trials where potential fractures were identified was proximally on the medial side of the femoral diaphysis. Trials that exceeded the tensile yield strain threshold also exceeded the ultimate tensile strength threshold and only two of those also exceeded the ultimate flexural strength threshold. Clinical studies generally observe few fractures due to bed falls, or other furniture, especially from a height of only two feet (61cm). Studies such as one by Pomerantz et al. (2012) evaluated injuries resulting in hospitalization in children up to 5 years old found femur injuries in 21.7% of falls from furniture which includes beds, couches, and tables. Other studies observed a lower frequency (3%) of fractures due to falls from furniture including a study by Helfer et al. (1977) who also evaluated children up to 5 years old for falls less than 90cm. The difference between the two studies may be a result of how the data was collected where Helfer used voluntary surveys of parents' observations while Pomerantz only consulted hospitalization records which may skew

towards a greater number of fractures observed. Other studies may have no observed femur

fractures where Lyons and Oates (1993) observed only two fractures in children younger than six

years old for falls from furniture occurring in a hospital from cribs or beds. Another study by

Nimityonskul and Anderson (1987) also observed no femur fractures in hospital furniture falls

for children younger than 16 years old where only two notable injuries that were not minor

lacerations or bruising which included a skull and tibial fracture where the latter was in a subject

with osteogenesis imperfecta. Of the bed fall trials evaluated through finite element analysis, fall

dynamics resulted in a significant difference in peak strains observed in the femoral diaphysis for

when the lower leg impacts first compared to the upper leg. There was no significant difference

of the peak strains between the different impact surfaces (carpet and linoleum).

a. Ultimate Tensile Strength Threshold. All trials exceeding the tensile yield strain

criteria also exceeded the tensile strength threshold of 100MPa. Two pediatric bone studies have

considered the ultimate tensile strength of the femur which ranged from 86MPa to 115MPa for

children ranging from six months old to 1.5 years old (Hirsch & Evans, 1965; Vinz, 1969). The

higher end of the range in the study by Hirsch was tested at a higher displacement rate of

10mm/min versus 0.5 to 1mm/min as tested by Vinz et al. These displacement rates are lower

than what is observed in the common household falls evaluated compared to estimated impact

velocities of a minimum of 2.1m/s in the ATD falls. Some studies suggest that the ultimate

tensile strength may increase with increasing strain rates (Currey, 1975) although some studies

such as one by Pithioux et al. (2004) found lower ultimate stress and strain values of bovine

cortical bone under dynamic loading compared to quasi-static.

b. Ultimate Flexural Strength Threshold. The failure loads observed in studies evaluating

the flexural properties of bone are typically much greater than that observed in the ATD loading

conditions evaluated in the finite element analysis (C. Albert, Jameson, Smith, & Harris, 2014;

G. Bertocci, Thompson, & Pierce, 2017; Currey & Butler, 1975; Miltner & Kallieris, 1989). The

fracture loads observed in the literature ranged from 3-5kN at 1mm/s and 1.2-4.8kN at 50mm/s.

For comparison, the ATD forces were less than 500N at estimated impact velocities of 2.1m/s for

bed falls to 3.8m/s for 119cm feet-first falls. In the study by Miltner et al., the tests were

conducted where the impact velocity was 15km/hr (or 4m/s) and resulted in no fractures where

the observed forces were up to 750N in a one-year-old child. The FE predicted outcomes of bed

falls exceeded the ultimate stress observed in the study by Albert et. al (2014) of 83MPa while

only two bed falls had exceeded the ultimate strength observed in the study by Currey and Butler

(1975) of 157MPa. The youngest subjects from which the specimens were evaluated in each of

these studies were three and two years old, respectively. Since many of the pediatric bone

biomechanics studies in the literature were evaluated at quasi-static loading conditions, the

ultimate flexural strength of pediatric bone would be expected to be higher based on work by

Miltner (1989), Bertocci (2017), and Cheong (2017) where an increase in the strain rate resulted

in an increased failure load. The true ultimate flexural strength would likely be for higher the

strain rates observed in the simulated falls resulting in fewer trials having exceeded the flexural

strength.

2. Identification of Potential Femur Fractures in Feet-First Falls

No feet-first fall trials were categorized as having a potential fracture when compared to

any threshold (tensile yield strain, ultimate tensile strength, and ultimate flexural strength)

outlined in the methodology. The peak strain for feet first falls was typically associated with the

peak torsional or bending moment, which occurred during the secondary impact of the pelvis, of

the ATD loading profile. Of the feet-first trials analyzed, the fall height significantly affected the

peak strain while the different impact surfaces did not. Even though the peak strain of many trials exceeded the yield strain threshold value, many appeared to be due to partial volume effects or isolated elements (B and C classifications, respectively).

The trends in the maximum principal strain for feet-falls where higher falls resulted in a higher strain is consistent with some of the literature evaluating fall height and injury (Hinton et al., 1999). While falls from a height may result in femur fractures, these fractures when they do occur tend to happen at higher heights which are typically higher than those evaluated in the ATD experiments. In a study by Wang et al. (2001), only 24% of femur fractures in children younger than 15 years old were due to falls less than 15 feet and the lowest recorded fall was 4 feet. This comparison is limited since clinical case studies evaluating femur fractures are often lacking in specific injury mechanisms (e.g., fall height, impact surface, and fall dynamics) or have accidental few femur fractures.

a. Fall Dynamics and Peak FE Model Predicted Outcomes. Two predominant fall dynamics were apparent in the loading of the ATD femur due to feet-first falls which are those where the ankles did (Figure 68) and did not overextend (Figure 61). This overextension was predominantly observed in falls from higher heights. When the ankles had not overextended, the peak strain predominantly occurred at the peak bending moment which corresponded to the secondary impact of the pelvis. In these falls, the peak compressive load was higher than those where the ankles did overextend. When the ankles had overextended, the peak strain corresponded to the peak torsional load (8-11Nm in the trials evaluated) which occurred due to the femur rotating along the longitudinal access after the initial impact and reaching the rotational limit of the hip for the ATD femur assembly. Using the pattern of which peak loads corresponded to which dynamic when comparing the loading conditions of the feet-first falls

evaluated through FEA and the unevaluated ATD trials, the conditions appear to be similar and suggests that very few if any may be categorized as a potential fracture. The unevaluated feet-first falls exceeding the peaks of those evaluated included one with a peak bending moment of 48 Nm and others with peak torsional loads up to 10-25Nm, although the dynamics of these falls may be the result of limitations in the biofidelity of the ATD response such as limits in the range of motion of the ATD femur assembly.
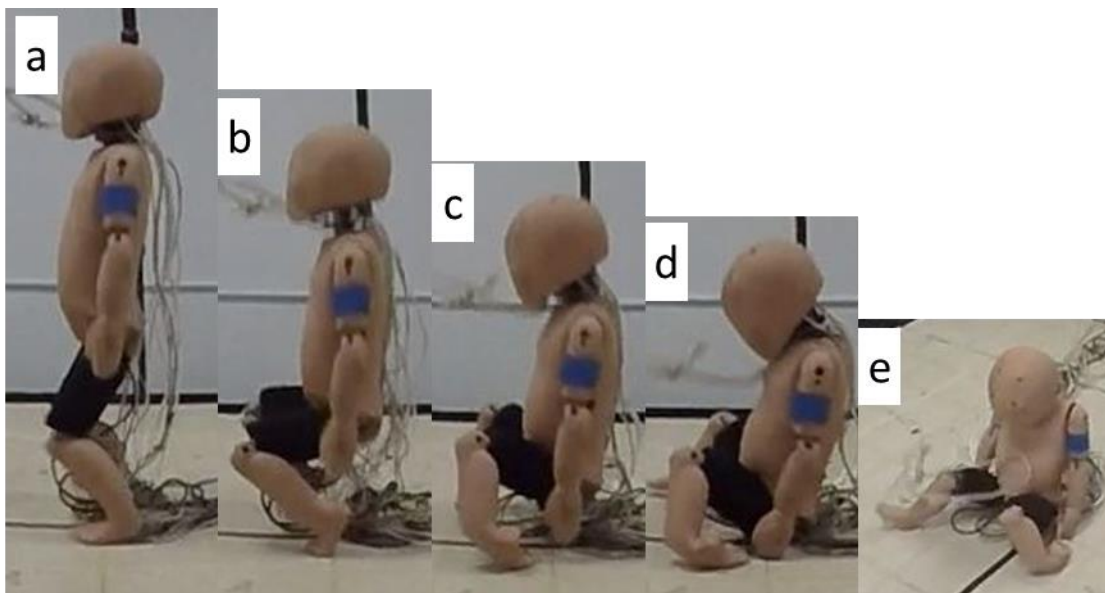

FIGURE 68. Progression of a 119cm feet-first fall onto linoleum following the initial impact where the side view (a-d) of the ankles overextending and the feet folding underneath followed by the leg rotating can be viewed. Anterior view of (d) can be seen in (e).

b. Compressive Thresholds Evaluation. A compressive strength and yield strain threshold were not included in the fracture criteria evaluated since it was assumed that the femur would fail first in tension. The lack of feet-first fall trials that resulted in a potential fracture could be in part due to not considering compression-specific failure thresholds. An ultimate compressive strength and a compressive yield strain threshold were evaluated for 119cm feet-first falls onto linoleum (n=3), which was the fall scenario in feet-first falls associated with the

highest compressive loads, to evaluate if any potential fractures could be identified due to this failure mechanism.

If any fractures were to be identified from exceeding compressive thresholds in feet-first falls, it would be expected for it to occur upon initial impact where compression is the predominant loading condition. The compressive yield strain was used to evaluate a few of the feet-first trials where failure may be due to compressive loading which differs from the initial yield strain threshold evaluation that used the tensile yield strain. All 119cm falls onto linoleum where the trial with the highest compressive load of 572N of all ATD experimental trials was included, were evaluated to examine whether the compressive yield strain was exceeded when comparing to the FE predicted minimum principal strain. The compressive yield strain used as the threshold was 1.1% (Ohman et al., 2011). The resulting minimum principal strain mirrored the maximum principal strain values where the peak strain was observed at the secondary impact of the pelvis. None of the trials evaluated exceeded the compressive yield strain threshold. Figure 69 contains the time history of the maximum and minimum principal strain and a view of the diaphysis of the femur where the elements exceeding the tensile or compressive yield strain are also displayed for a 119cm fall onto linoleum.
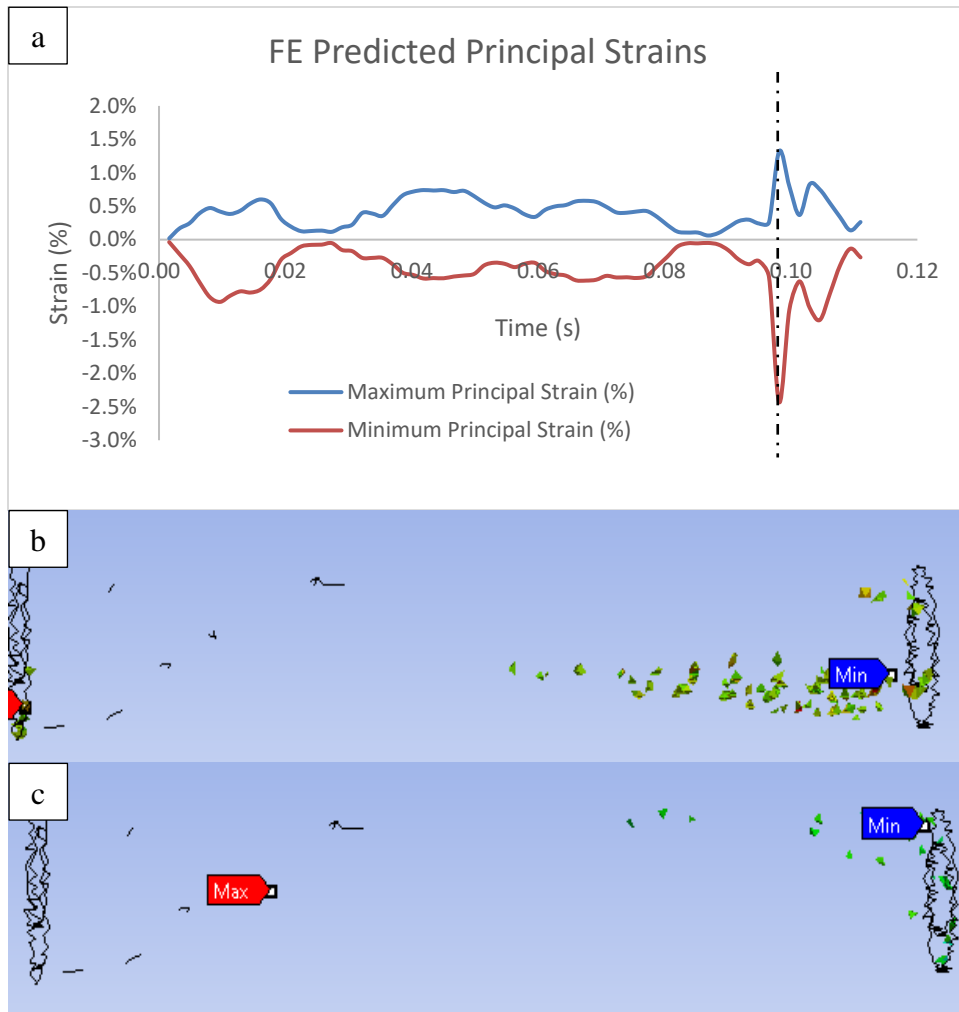
FIGURE 69. Time histories of the FE predicted maximum and minimum principal strains (a) with the corresponding volume showing the elements exceed the applied tensile yield strain threshold of 0.73% (b) and the compressive yield strain threshold of 1.1% (c). The trial displayed is a 119cm feet-first fall onto linoleum. The diaphyseal region displayed is the lateral view of the femur with the proximal end of the femur on the left. The time history of the loading conditions can be found in FIGURE 61.

Further comparison of the compressive loads to previously established thresholds for adult femurs also indicated that no potential fractures would be identified. Fracture thresholds developed for adult femurs in motor vehicle accidents range from 7.8kN to 10kN for the peak axial force in impact durations greater than 20ms (FMVSS 208 and UNECE R94) (NHTSA, 2008). Both thresholds are much greater than the compressive loads observed in the ATD trials where the peak recorded load was 572N in the feet-first falls, although the adult automotive thresholds are for strain rates much greater than those observed in a household fall.

144

Many studies evaluating the compressive properties of bone in the literature have focused on microstructural properties (Imbert et al., 2015; Ohman et al., 2011; Yamada & Evans, 1973). The ultimate stresses tended to range from 38MPa for fetal specimens as evaluated by Yamada et al. (1973), to 68MPa (Imbert et al., 2015) for pediatric specimens (subjects aged 8 years and older), and to 200MPa (Ohman et al., 2011) for adult specimens. All of which were conducted at quasi-static loading conditions. The minimum principal stress of the initial impact of the ATD, which is where the peak compressive load was observed for feet first falls, was compared to the 68MPa value for 119cm falls onto linoleum (n=3). The minimum principal stress ranged from 25-57MPa which does not exceed the ultimate compressive strength value indicating that a failure most likely would not result from the initial impact of the feet-first fall.

3. Influence of Impact Surface on Fracture Identification

Impact surface (carpet and linoleum) did not result in a significant difference in the peak strains in either feet first falls or bed falls. Impact surface did result in a significant difference of the different load inputs to the model which may indicate what loads are important in evaluating fracture in these injury scenarios (A. Thompson et al., 2018). For feet-first falls, the different impact surfaces resulted in a significant difference of the inputs to the FEA only for the peak compressive loads. The peak strain was typically associated with the peak bending moment or torsional loads for feet-first falls. Therefore, the lack of influence of the impact surface in feet-first falls is consistent with the trials evaluated. For bed falls, the different impact surfaces resulted in a significant difference of the inputs to the FEA for peak compressive and shear forces and bending moments. The peak strains in bed falls tended to occur at the peak bending moment. The smaller sample of the bed falls evaluated could have been why the impact surface did not influence the peak strain.

4. Influence of Fall Height on Fracture Identification

No potential fractures were identified for the feet-first trials evaluated. The fall heights considered (69cm and 119cm) did result in a significant difference in mean peak strains where a higher fall height corresponded to greater peak strains. This trend is consistent with literature where higher fall heights are associated with increased fracture occurrence as discussed previously. Based on the maximum principal strain theory used, an increased fall height being associated with an increased peak strain would partially support the hypothesis that the increased fall height would result in an increased likelihood of failure.

B. Limitations in Identifying Pediatric Femur Fractures

The ability to determine pediatric femur fracture through finite element analysis is limited by the lack of defined pediatric bone properties. In addition to this limitation, limitations in the biofidelity of the CRABI ATD used to generate the input loading conditions for the analysis also influence the ability to identify potential femur fractures due to common household falls.

1. Limitations in Loading Conditions Derived from ATD Experiments

Improving ATDs to be more biofidelic in order to better predict injury has been the focus of many studies. Improvements were made by Thompson et al. (2018) to the ATD's femur assembly such as modifying the soft tissue surrounding the femur to be more biofidelic and modeling of the femur geometry-based on a child's femoral diaphysis. While these may improve the biofidelic response, other aspects of the lower extremity assembly such as the range of motion and stiffness of the joints could also result in dynamics that are not wholly representative of an infant. Due to the limited information in the literature regarding these properties, it is

difficult to fully account as to how this could affect the resulting loading conditions used as inputs to the finite element analysis.

The limitations in the ATD's femur biofidelity are apparent in the feet-first fall dynamics where the peak stress and strain for many of the 119cm falls occurred at the peak torsional loads (8-11Nm). The peak torsional load can be attributed to the CRABI ATD's inability to rotate at the hip joint along the longitudinal axis of the femur compared to a greater degree of internal and external rotation observed in one study which measured the internal rotation in flexion to be 45° for two-year-old children (Sankar, Laird, & Baldwin, 2012). In many of the falls evaluated, the feet would buckle causing the femur to rotate while the pelvis was still falling (Figure 68). The femur assembly would likely hit the rotational limit in between the initial and secondary impact resulting in the observed high torsional loads. The response of the foot and ankle assembly by the overextension of the ankle and the foot folding underneath the ankle upon impact corresponds to a dynamic that is unlikely to be representative of an infant falling. In falls where the foot did not buckle in this manner, higher compressive loads were typically seen in the initial impact resulting in a peak compressive load up to 530N as seen in Figure 61 versus the peak compressive load of 280N as seen in Figure 68 which were both from the same fall height. The difference in compressive loads is likely associated with how the feet impacted the ground initially.

An additional factor impacting the ATD response of the experiments is the stiffness of the leg assembly such as the soft tissue material and the joints (ankle, knee, and hip). Even if the fall dynamics are representative of an infant, improving the biofidelity, such as the soft tissue response, across the ATD could affect how much loading the femur experiences. For example, THOR (Test device for Human Occupant Restraint) is an ATD representative of an adult with

improved biofidelity when compared to the Hybrid III. The THOR's femur included a compliant

component allowing the femur to be less stiff when dynamically loaded. The improvement of the

response of the THOR ATD's knee-femur complex was compared to both the Hybrid III and

cadavers (Rupp, Reed, Madura, & Schneider, 1977). The THOR ATD's knee-femur complex

response was more comparable to the cadavers' than the Hybrid III and less stiff than the Hybrid

III when loading in compression similar to what would be observed in a motor-vehicle accident

for a seated passenger. While little to no data exists to quantify the stiffness of the lower

extremity for infants, a comparison of the response of the modified ATD to that of an infant

similar to the evaluation of the THOR's and Hybrid III's response would be beneficial in better

identifying potential fractures. Due to the composition of the ATD femur assembly, where the

diaphysis is aluminum, the response is likely much stiffer than a human child's and may benefit

from future work improving the response to be more biofidelic. An improved biofidelic response

of the ATD extends beyond modifications only to the lower extremity, especially for the upper

extremities which the femur assembly impacted in many bed falls (Figure 70). The response of

the upper extremity is likely stiffer than a human and similar modifications as those made to the

femur assembly by Thompson et al. (2018) may be beneficial in improving the accuracy of

recorded femur loads.

FIGURE 70. View of the initial impact of an ATD simulating a bed fall onto linoleum where the ATD had landed on its arm.

The limitations of the loading conditions from the ATD experiments including of the

lower extremity assembly such as the range of motion, materials of the femur assembly being

stiffer than that of infant bone, and stiffness of the lower extremity assembly's response to

dynamic loading would likely result in higher loading conditions than what would be actually

observed in an infant. This could lead to a greater number of identified potential fractures than

what might occur.

2. FE Model Limitations

The development of the FE femur model and the results of the validation testing

illustrated many additional limitations of this study. The segmentation and material application

methods used resulted in partial volume effect errors that may overestimate the number of trials

categorized as resulting in a potential fracture. Other limitations in the CT scan from which the

model was derived including the bone edge enhancement algorithm which affects the HU

distribution of the cortical region may also affect the interpretations of the FE model predicted

outcomes.

a. Development of FE Model from CT Scan. One of the main limitations of this project

is how errors due to the partial volume effect of the CT scans can lead to an overestimation of

potential fractures in the model which is especially true when evaluating the yield strain criteria

where the peak values typically occur on the outer surface. Studies that develop subject specific

finite element models tend to use micro-CT scans with resolutions of 0.4x0.4x0.4 mm^3

(Dragomir-Daescu et al., 2011) and 0.185x0.185x0.5 mm^3 (Bessho et al., 2007). In this study a

diagnostic CT scan (0.5x0.5x1.00 mm^3) was used which is a lower resolution and errors in

approximating the geometry as well as defining the material properties could be introduced. The

lower density values assigned to the regions affected by the partial volume effect could result in false peak strain values which could result in some trials being identified as having a potential fracture when there should be none. In order to reduce the number of trials being categorized as a potential fracture due to partial volume effects, those which exhibited the ribbon pattern on the surface (Figure 33) and assigned lower material properties were categorized as a B classification to potentially reduce these misclassifications.

In addition to partial volume effects, the bone edge enhancement algorithm influences the HU distribution of cortical bone when compared to an unenhanced CT scan. The comparison of the effect of the bone edge enhancement algorithm on the application of material properties conducted here indicates that there may be an underestimation of the peak maximum principal strain due to bending in the FEA of the ATD trials. Properly accounting for the bone edge enhancement algorithm may lead to more trials being categorized as a potential fracture by using the yield strain threshold although more investigation into the difference between the material properties derived from the enhanced and unenhanced CT scans would need to be conducted for more subjects and loading conditions.

b. Surrogate Bone Validation Testing. The minimum principal strain time history and force-displacement curve comparisons between the FE model predictions and the experimental test data had much better agreement in bending than in compression. Deviations in the FE model and the experimental data were expected due to the lack of an appropriate depth to span ratio which was approximately 1:7.5 compared to 1:16 as recommended in ASTM D790 (ASTM D790-03, 2003). A lower span than the recommendation is associated experimentally with increased contribution of shear forces. A study by Kourtis et al. (2014) provided correction factors for the modulus to account for the increased response due to shear rather than pure

bending loads using Euler-bernoulli beam theory. Using the cross section at the point of fracture with an outer diameter of 11.71mm and an inner diameter of 9.65mm, an approximate elastic to shear modulus ratio between 0.3-0.4, and a sharp radius of the supports, a correction factor of 0.86-0.91 would be expected from the charts generated by Kourtis et al. In other words, a ratio of the modulus of the experimental data (2339 MPa) to the FE predicted data (2705 MPa) of 0.86 to 0.91. The resulting ratio was 0.86 which falls within expectations.

A major difference in the results of the experimental data for the bending and compression testing is that the fracture types as a result of the compressive loading conditions varied greatly across the trials Figure 46. The different fracture types also translated to a wide range of variability in the time history of the minimum principal strain values between the different trials which led to poor agreement with the FE model. The material application of the FE model assumed a homogenous, isotropic application of the materials, when in actuality this can vary greatly depending on the orientation and dispersion of the glass fibers throughout the bone surrogate. The 3D printing direction of the bones was parallel to the longitudinal axis of the bone. Application of the compressive loading was aligned with the longitudinal axis, which is parallel to the printing direction, while the bending test was loaded perpendicular to the printing direction. The difference in the applied loading conditions as well as the direction of the glass fibers have been found to have an effect on strain. An evaluation by Forderhase et al. (1995) of using glass-fiber reinforced nylon for SLS observed anisotropy with respect to the printing direction. The load application of the three-point bending testing was perpendicular to the printing direction while the load application of the compression testing was parallel. Other studies such as one by Notta-Cuvier (2013) have evaluated the orientation of short fibers in composite materials and the effect on strength where the tensile moduli decreased with off-axis

151

(with respect to the fibers) loading. Although a mold was created to conform to the surface of the proximal end of the femur (where the load was applied) so that the load would be applied over the entirety of the proximal surface of the femur, deviations in the loading direction upon contact with the testing machine platen could have been introduced if the femur was not perfectly aligned. Table XIX compares the strain data to validation criteria for the different classifications of the fracture pattern. Those with a fracture type of A typically had lower absolute percentage error values and the slopes of their regression were much closer to unity than the other failure classification groupings. This could be due to different specimens having more similar distribution and orientations of the glass fibers throughout the surrogate bone. The different distribution of glass fibers between bending specimens, where two had similar linear regressions (Table XVIII), could be possible although the cross-sections of those tested in bending appeared to be fairly similar. A greater sample size of those tested with strain rosettes for each loading condition could provide more insight into defining the material properties when using a glass fiber reinforced nylon blend as the basis of the bone surrogates. The outcomes of the validation indicated better FE model prediction of the experimental outcomes for the three-point bending loading condition when compared to compression which may indicate that the response of the FE model due to the ATD loading conditions may better estimate the response when bending is the predominant loading condition. The FE predicted outcomes of the compression testing tended to have the greatest deviations in the prediction for the defined non-linear region of the material model applied. The use of a more homogeneous material to evaluate the compression loading condition to reduce any potential errors in the material application to the FE femur model may result in a better agreement. The results of the bone surrogates evaluated may indicate that the FE prediction may overestimate the response as measured by the minimum principal strain of the

152

model in compression when evaluating the ATD trials although no potential fractures of the ATD trials were associated with the peak compressive load.

3. Fracture Criteria Limitations

There is a lack of data on the mechanical properties of pediatric bone, especially in regard to evaluating femur fracture through finite element analysis. Limitations in the material property application includes only using a linear material model to define the material properties in order to be able to use the yield strain threshold which estimates the onset of fracture rather than a fracture itself which would require the use of an ultimate stress or strain threshold instead. In addition, the viscoelasticity of the bone was not modeled in the material property application which would also affect the estimation of fracture. Lack of pediatric bone mechanical properties, especially for the post-yield region, are not well defined thus a linear material model had been used for this study. The stress-based thresholds used were defined based on properties of pediatric bone as determined in the literature but limitations in how stress-based fracture criteria are typically evaluated for FE femur models may adjust the number of fractures identified using these thresholds.

a. Yield Strain Threshold. Studies that have used the yield strain criteria to predict failure have typically underestimated the actual fracture force such as one by Schileo (2014) where the standard error of the estimate between the experimental and FE predicted fracture force was 814N where the fracture forces ranged from 1.1kN to 12kN. The main benefit of using the yield strain threshold is that it has been found to correlate well with fracture predictions and allows for the application of a linear model where the post-yield properties of the bone do not need to be defined. This is especially beneficial for this study where, due to the lack of defined post-yield

properties of pediatric bone, a simpler material property application can be used for an initial evaluation of potential femur fracture due to the household falls evaluated. The yield strain threshold evaluates the onset of fracture rather than the actual fracture itself since it is not considering any post-yield behavior of the bone nor is it the ultimate strain of the bone. While trials were categorized as potential fractures due to this criterion, it may be more appropriate to state that they are more likely to result in a fracture than the other trials and the results present a correlation with a potential fracture occurring rather than injury predictions.

b. Stress-Based Thresholds. The stress-based criteria used were the ultimate tensile and flexural strength of pediatric bone and defined by biomechanical studies of pediatric bone found in the literature. Previous studies that have used stress values for predicting fracture typically use stress-density relationships instead of one general threshold (Bessho et al., 2007). Since the stress-density relationships have not been extended to an application of pediatric bone, general comparisons of the peak stresses to ultimate stresses of pediatric bone previously defined in the literature were made instead. For the trials exceeding the maximum flexural strength, the peak stresses typically occurred midway between the outer and inner surfaces of the bone where the bone density was higher. If a density-stress relationship was used to define the threshold, these trials may not have exceeded the ultimate flexural strength threshold which would result in none of the trials identified as potential fractures when using stress-based criteria. A study by Schileo (2014) found that the stress-based criterion for predicting fracture overestimated the number and were further away from the location of fractures compared to strain-based criteria. While comparisons to ultimate strength values in the literature can be made, lack of defined properties for infant bone with respect to the post-yield properties of bone and having a linear material model used for the material application may not be as reliable or informative of a comparison

than using strain-based criteria, in conjunction with a linear material model, for fracture evaluation once the limitations relating to using the yield strain criteria have been addressed. In addition, the use of a linear material model in this study indicates that the model had not appropriately considered the post-yield region to be able to make a proper comparison to the ultimate strength thresholds used and would likely lead to an overestimation of trials that may result in failure due to this threshold.

     c. Other Fracture Threshold Evaluation Methods. While the fracture thresholds used are more common for linear material model applications, other methods may prove to be more effective at identifying potential femur fracture especially in infant bone. These fracture thresholds may incorporate additional criteria in addition to the tensile yield strain threshold such as percent volume of the femur that has exceeded the specified thresholds. Other thresholds such as energy to failure thresholds may also prove to be more effective at identifying potential fractures. Due to the lack of pediatric bone properties that have been defined and validated using finite element analysis, it is difficult to know what would best identify potential fractures in pediatric bone.

     Other thresholds to consider may be those such as one used by Pistoia (2002) where a certain percent volume of the elements exceeding a threshold could be used to identify potential fracture. A threshold of 2% in the Pistoia study corresponded to an overestimation of the fracture load. In the current study, two-thirds (4/6) of the feet-first falls classified as a B fracture classification (potential fracture attributed to partial volume effects) exceeded a 2% volume of the diaphysis although the volume of the diaphysis was only 29% of the total volume of the modeled femur, which excluded the epiphyses (Figure 67). The elements exceeding the yield strain threshold in feet-first falls were distributed across the entirety of the femur compared to a

155

more concentrated set of elements as observed in bed falls classified as a potential fracture. Only half of the bed falls (3/6) classified as a potential fracture (A classification) exceeded this 2% volume when considering the yield strain threshold although this reduces to one trial when considering the total volume of the modeled femur. The one trial was a bed fall onto carpet where the lower leg impacted the ground first, which is the fall dynamic attributed to higher peak strains and was associated with one of the greater peak bending moments of the bed falls evaluated.

The aim of using the ultimate strength thresholds were to have criteria that were defined by some of the pediatric bone properties that had been evaluated in the literature. Another property not considered was energy to failure which has also been evaluated by some studies for immature animal bone where they ranged from 2.9J to 8J for a bending loading condition (G. Bertocci et al., 2017; Cheong, Karunaratne, Amis, & Bull, 2017). These values are much greater than observed in those classified as a potential fracture in bed falls which was 1E-4J for the trial associated with the greatest peak strain. The low energy values observed may indicate that a fracture would likely not occur due to a threshold defined by energy to failure although these are not energy measurements from a human infant femur.

d. Effect of Strain Rate. By not considering a viscoelastic material model, the analysis did not consider the effect of strain rate on the material properties. Many studies have demonstrated that the ultimate stress and strain and other mechanical properties would be altered due to the increased strain rate. As previously discussed, the ultimate flexural strength has been found to typically increase with increasing strain rate (Cheong et al., 2017; Miltner & Kallieris, 1989). Other studies such as one by Hansen et al. (2008) observed that while ultimate compressive properties tend to increase with increasing strain rate, ultimate tensile properties

156

tends to decrease. Zioupos et al. (2008) found that the tensile yield strain was mostly invariant over the range of strain rates evaluated although specimens from only two subjects were evaluated. Although the modulus-density relationship used may need to be adjusted, the yield strain threshold may still be appropriate to use for the dynamic loading conditions. Few studies have defined the relationship between mechanical properties and strain rate. A study conducted by Carter and Hayes (1976) determined a relationship between ultimate compressive strength and strain rate although this relationship was defined using only trabecular bone. While there are few defined relationships between strain rate and mechanical properties, especially for infant bone, they have demonstrated that further investigation into the validity of the material properties applied and the thresholds used would be necessary in order to better identify potential infant femur fractures through finite element analysis especially for loads that extend beyond just one type (e.g. bending, compression, tension).

VI. CONCLUSIONS

- A FE femur model of an 11-month old child was developed based on CT images. The FE femur model was used to assess stress and strain due to loading associated with simulated bed and feet-first falls. The FE model was used to predict the likelihood of femur fracture.

- None of the feet-first falls exceeded any of the specified stress or strain-based thresholds.

- Fifty percent (50%) of bed falls were identified as having a potential fracture when using a tensile yield strain and ultimate tensile strength threshold. Identified potential fractures was reduced to 2/12 trials when using the ultimate flexural strength threshold.

- Bending and torsion appeared to be the predominant loading conditions that resulted in higher strains which may correlate with potential fractures.

- Increased fall height in feet-first falls corresponded to an increase in the maximum principal strain.

- The impact surface did not result in a significant difference in the maximum principal strain between carpet and linoleum for either fall type, bed or feet-first falls.

- The different fall dynamics for bed falls resulted in a significant difference in the maximum principal strain; when the lower leg impacted first resulted in higher strains than when the upper leg impacted the ground first.

- Half the bed falls were identified as having a potential fracture when using a tensile yield strain threshold and an ultimate tensile strength threshold which was reduced to two (out of 12) of the bed falls evaluated when using the ultimate flexural strength threshold.

- Future improvements to the model may be necessary to improve accuracy in fracture prediction due to limitations in the material property application and the thresholds used due to a lack of pediatric bone data in the literature.

A. Clinical Relevance

The results of this study indicate that bed falls where the lower leg impacted the ground first corresponds to an increased likelihood of femur fracture. Reported bed fall injury mechanisms resulting in diaphyseal femur fractures may be more likely to be due to accidental mechanisms can be biomechanically compatible based upon model predictions. These findings may aid clinicians in correctly identifying when encountered femur fractures are due to the reported accidental mechanisms evaluated in this study or should be suspected of abuse. Evaluated feet-first falls had no likelihood of potential femur fracture, although biomechanical measures associated with fracture increased with greater fall heights. Fractures reported as being due to feet-first falls from up to 74cm (child's feet to ground for the 119cm falls) are unlikely and thus, should raise concern for non-accidental injury mechanisms based on model predictions. In addition, different fall dynamics identified in feet-first falls were attributed to varying model-predicted biomechanical outcomes and indicated the importance of obtaining detailed injury histories to both aid in identifying whether or not fall dynamics are realistic and to better identify which accidental injury mechanisms are more likely to result in fractures.

VII. Recommendations

To better evaluate the likelihood of pediatric femur fracture, limitations of the current model should be addressed. These limitations include aspects of the FE model such as material applications methods, lack of pediatric bone mechanical properties and the application to a finite element model, and the biofidelity of the ATD. Addressing these limitations would provide a better foundation to predict pediatric femur fracture due to bed falls and feet-first falls.

Aspects of developing the FE model may be improved to better identify potential fractures such as further investigation into the effect of the bone edge enhancement algorithm on the HU distribution and application of the material properties especially for evaluating the femur loading in ATD falls. An alternative method may incorporate the application of material properties defined by an unenhanced CT scan with the use of the geometry from the enhanced scan if both scan types for the same subject are available.

Further improvement of the model can also be made through conducting more extensive validation testing. When using glass-fiber reinforced nylon bone surrogates, improving the application of the material properties with the use of a non-homogenous application would be beneficial in potentially improving the comparison of the experimental and FE model predicted strains. A greater sample size of those tested with a strain rosette would also improve the comparison of the experiment and FE model prediction. Future work could also incorporate better modeling of the glass fiber material in the FE model such as switching to a linear material model in addition to evaluating model-predicted fracture potential in the validation testing.

Research related to the mechanical properties of pediatric bone is still limited. Studies are needed to define the biomechanical response of pediatric bone to loading and to identify fracture

strength under various loading conditions. Further studies validating the application of adult

mechanical properties, such as the density-elasticity relationship used in this study and the yield

strain threshold used to evaluate fracture potential, to pediatric FE femur models is still

necessary. In addition, more research into how properties change with respect to dynamic

loading rates where most properties are defined at quasi-static loading conditions and definition

of the post-yield properties of pediatric bone would greatly improve model fracture predictions.

To be able to predict the occurrence of femur fractures, further evaluation of the stress and

strain-based thresholds is still necessary to evaluate pediatric bone fractures which may include

applying stress-density relationship to the stress thresholds used or the use of yield and ultimate

thresholds in conjunction with the application of a non-linear material model.

Greater understanding of the mechanical properties of pediatric bone would also benefit

improving the biofidelity of ATDs. Aspects of the lower extremity that would improve the FE

femur model includes improving the ankle and foot response and the knee-femur complex

response upon impact especially for feet-first falls where the initial impact is greatly affected by

this response. Improving hip joint range of motion by allowing for greater internal and external

rotation would also be beneficial since the limitations in this movement appeared to be

associated with potentially artificial increase of torsional loads observed in feet-first falls.

The FE femur model could also be used to evaluate loading in different directions and

planes to identify when potential fractures may occur due to more simple loading conditions.

This could be used to isolate which loading conditions (bending, torsion, shear or compression)

are within the range of a potential fracture without having to conduct the finite element analysis

for future ATD simulations of accidental injury mechanisms. Expansion of the analysis of fall

loading conditions to other femora from other healthy one-year old children who may have

differing distributions of bone density and geometry would allow for broader assessment on fracture potential due to household falls. This broader evaluation would benefit clinicians and other professionals who encounter children with femur fractures and are required to determine whether the fracture is compatible with the stated cause.

References

Agnew, A. M., Schafman, M., Moorhouse, K., White, S. E., & Kang, Y. (2015). The effect of age on the structural properties of human ribs. *Journal of the Mechanical Behavior of Biomedical Materials*, *41*, 302–314.

Albert, C. I., Jameson, J., & Harris, G. (2012). Design and validation of bending test method for characterization of miniature pediatric cortical bone specimens. *Proceedings of the Institution of Mechanical Engineers, Part H: Journal of Engineering in Medicine*, *227*(2), 105–113.

Albert, C., Jameson, J., Smith, P., & Harris, G. (2014). Reduced diaphyseal strength associated with high intracortical vascular porosity within long bones of children with osteogenesis imperfecta. *Bone*, *66*, 121–130.

ASTM D638-02a. (2003). Standard test method for tensile properties of plastics. *ASTM International*. West Conshohocken, PA.

ASTM D695-02a. (2002). Standard Test Method for Compressive Properties of Rigid Plastics 1. *ASTM International*. West Conshohocken, PA.

ASTM D790-03. (2003). *Standard Test Method for Flexural Properties of Unreinforced and Reinforced Plastics and Electrical Insulation Materials*. *ASTM International*. West Conshohocken, PA.

BASF Corporation. (2003). *AN ADVANCED HIGH MODULUS (HMG) SHORT GLASS – FIBER REINFORCED NYLON 6 : PART II - MECHANICAL.*

Bayraktar, H. H., Morgan, E. F., Niebur, G. L., Morris, G. E., Wong, E. K., & Keaveny, T. M. (2004). Comparison of the elastic and yield properties of human femoral trabecular and cortical bone tissue. *Journal of Biomechanics*, *37*(1), 27–35.

Bertocci, G. E., Pierce, M. C., Deemer, E., Aguel, F., Janosky, J. E., & Vogeley, E. (2003). Using Test Dummy Experiments to Investigate Pediatric Injury Risk in Simulated Short-Distance Falls. *Archives of Pediatrics & Adolescent Medicine*, *157*(5), 480.

Bertocci, G., Thompson, A., & Pierce, M. C. (2017). Femur fracture biomechanics and morphology associated with torsional and bending loading conditions in an in vitro immature porcine model. *Journal of Forensic and Legal Medicine*, *52*, 5–11.

Bessho, M., Ohnishi, I., Matsumoto, T., Ohashi, S., Matsuyama, J., Tobita, K., … Nakamura, K. (2009). Prediction of proximal femur strength using a CT-based nonlinear finite element method: Differences in predicted fracture load and site with changing load and boundary conditions. *Bone*, *45*(2), 226–231.

Bessho, M., Ohnishi, I., Matsuyama, J., Matsumoto, T., Imai, K., & Nakamura, K. (2007). Prediction of strength and strain of the proximal femur by a CT-based finite element method. *Journal of Biomechanics*, *40*(8), 1745–1753.

Boot, A. M., de Ridder, M. A. J., van der Sluis, I. M., van Slobbe, I., Krenning, E. P., & de Muinck Keizer-Schrama, S. M. P. F. (2010). Peak bone mineral density, lean body mass and fractures. *Bone*, *46*(2), 336–341.

Bryan, R., Nair, P. B., & Taylor, M. (2009). Use of a statistical model of the whole femur in a large scale, multi-model study of femoral neck fracture risk. *Journal of Biomechanics*, *42*(13), 2171–2176.

Budoff, M. J., Malpeso, J. M., Zeb, I., Gao, Y. L., Li, D., Choi, T.-Y., … Mao, S. S. (2013). Measurement of phantomless thoracic bone mineral density on coronary artery calcium CT scans acquired with various CT scanner models. *Radiology*, *267*(3), 830–6.

Caouette, C., Rauch, F., Villemure, I., Arnoux, P.-J., Gdalevitch, M., Veilleux, L.-N., … Aubin, C.-E. (2014). Biomechanical analysis of fracture risk associated with tibia deformity in children with osteogenesis imperfecta: a finite element analysis. *Journal of Musculoskeletal & Neuronal Interactions*, *14*(2), 205–12.

Carter, D., & Hayes, W. (1976). Bone compressive strength: the influence of density and strain rate. *Science*, *194*(4270), 1174–1176.

Carter, D., & Hayes, W. (1977). The compressive behavior of bone as a two-phase porous structure. *The Journal of Bone & Joint Surgery*, *59*(7), 954–962.

Chan, G. M., Hess, M., Hollis, J., & Book, L. S. (1984). Bone mineral status in childhood accidental fractures. *American Journal of Diseases of Children (1960)*, *138*(6), 569–70.

Cheong, V. S., Karunaratne, A., Amis, A. A., & Bull, A. M. J. (2017). Strain rate dependency of fractures of immature bone. *Journal of the Mechanical Behavior of Biomedical Materials*, *66*(October 2016), 68–76.

US Department of Health & Human Services, Administration for Children and Families, Administration on Children, Youth and Families, Children's Bureau. (2016). *Child Maltreatment 2014*.

Clark, E. M., Ness, A. R., Bishop, N. J., & Tobias, J. H. (2006). Association Between Bone Mass and Fractures in Children: A Prospective Cohort Study. *J Bone Miner Res*, *21*(9), 1489–1495.

Clarke, N. M. P., Shelton, F. R. M., Taylor, C. C., Khan, T., & Needhirajan, S. (2012). The incidence of fractures in children under the age of 24 months - In relation to non-accidental injury. *Injury*, *43*(6), 762–765.

Coffey, C., Haley, K., Hayes, J., & Groner, J. I. (2005). The risk of child abuse in infants and toddlers with lower extremity injuries. *Journal of Pediatric Surgery*, *40*(1), 120–123.

Cook, S. D., Harding, A. F., Morgan, E. L., Doucet, H. J., Bennett, J. T., O'Brien, M., & Thomas, K. A. (1987). Association of bone mineral density and pediatric fractures. *Journal of Pediatric Orthopedics*, *7*(4), 424–7.

Cristofolini, L., Conti, G., Juszczyk, M., Cremonini, S., Sint Jan, S. Van, & Viceconti, M. (2010). Structural behaviour and strain distribution of the long bones of the human lower limbs. *Journal of Biomechanics*, *43*(5), 826–835.

Currey, J. D. (1975). The effects of strain rate, reconstruction and mineral content on some mechanical properties of bovine bone. *Journal of Biomechanics*, *8*(1), 83–86.

Currey, J. D., & Butler, G. (1975). The Mechanical Properties of Bone Tissue in Children. *Journal of Bone and Joint Surgery*, *57–A*, 810–814.

Dalton, H. J., Slovia, T., HELFER, R. E., Comstock, J., Scheurer, S., & Riolo, S. (1990). Undiagnosed Abuse in Children Younger Than 3 Years With Femoral Fracture. *Archives of Pediatrics & Adolescent Medicine*, *144*(8), 875.

Dong, X. N., Acuna, R. L., Luo, Q., & Wang, X. (2012). Orientation dependence of progressive post-yield behavior of human cortical bone in compression. *Journal of Biomechanics*, *45*(16), 2829–2834.

Dragomir-Daescu, D., Op Den Buijs, J., McEligot, S., Dai, Y., Entwistle, R. C., Salas, C., … Amin, S. (2011). Robust QCT/FEA models of proximal femur stiffness and fracture load during a sideways fall on the hip. *Annals of Biomedical Engineering*, *39*(2), 742–755.

Forderhase, P., Mc Alea, K., & Booth, R. (1995). The development of an SLS composite material. *Solid Freeform Fabrication Proceedings*, (1), S. 287-297.

Grassi, L., Schileo, E., Taddei, F., Zani, L., Juszczyk, M. M., Cristofolini, L., & Viceconti, M. (2012). Accuracy of finite element predictions in sideways load configurations for the proximal human femur. *Journal of Biomechanics*, *45*(2), 394–399.

Hansen, U., Zioupos, P., Simpson, R., Currey, J. D., & Hynd, D. (2008). The Effect of Strain Rate on the Mechanical Properties of Human Cortical Bone. *Journal of Biomechanical Engineering*, *130*(1), 11011.

Helfer, R. E., Slovis, T. L., & Black, M. (1977). Injuries resulting when small children fall out of bed. *Pediatrics*, *60*(4), 533–535.

Hinton, R. Y., Lincoln, A., Crockett, M. M., Sponseller, P., & Smith, G. (1999). Fractures of the femoral shaft in children. Incidence, mechanisms, and sociodemographic risk factors. *The Journal of Bone and Joint Surgery. American Volume*, *81*(4), 500–509.

Hirsch, C., & Evans, F. (1965). Studies on some physical properties of infant compact bone. *Acta Orthopaedica Scandinavica*, *503*(August), 300–313.

Ibrahim, N. G., & Margulies, S. S. (2010). Biomechanics of the toddler head during low-height falls: an anthropomorphic dummy analysis. *Journal of Neurosurgery. Pediatrics*, *6*(July), 57–68.

Imbert, L., Aurégan, J.-C., Pernelle, K., & Hoc, T. (2015). Microstructure and compressive

mechanical properties of cortical bone in children with osteogenesis imperfecta treated with bisphosphonates compared with healthy children. *Journal of the Mechanical Behavior of Biomedical Materials*, *46*, 261–270.

Keller, T. S. (1994). Predicting the compressive mechanical behavior of bone. *Journal of Biomechanics*, *27*(9), 1159–1168.

Keyak, J. H., Skinner, H. B., & Fleming, J. A. (2001). Effect of force direction on femoral fracture load for two types of loading conditions. *Journal of Orthopaedic Research*, *19*(4), 539–544.

Koivumäki, J. E. M., Thevenot, J., Pulkkinen, P., Kuhn, V., Link, T. M., Eckstein, F., & Jämsä, T. (2012). Ct-based finite element models can be used to estimate experimentally measured failure loads in the proximal femur. *Bone*, *50*(4), 824–829.

Koo, M. W. M., Yang, K. H., Begeman, P., Hammami, M., & Koo, W. W. K. (2001). Prediction of Bone Strength in Growing Animals Using Noninvasive Bone Mass Measurements. *Calcified Tissue International*, *68*(4), 230–234.

Kourtis, L. C., Carter, D. R., & Beaupre, G. S. (2014). Improving the Estimate of the Effective Elastic Modulus Derived from Three-Point Bending Tests of Long Bones. *Annals of Biomedical Engineering*, *42*(8), 1773–1780.

Leventhal, J. M., Thomas, S. A., Rosenfield, N. S., & Markowitz, R. I. (1993). Fractures in young children. Distinguishing child abuse from unintentional injuries. *American Journal of Diseases of Children (1960)*, *147*(1), 87–92.

Li, X., Viceconti, M., Cohen, M. C., Reilly, G. C., Carré, M. J., & Offiah, A. C. (2015). Developing CT based computational models of pediatric femurs. *Journal of Biomechanics*, *48*(10), 2034–2040.

Lindahl, O., & Lindgren, A. G. H. (1967). Cortical Bone in Man 1. Variation of the Amount and Density with Age and Sex. *Acta Orthopaedica Scandinavica*, *38*(1–4), 133–140.

Lyons, T. J., & Oates, R. K. (1993). Falling out of Bed: A Relatively Benign Occurence. *Pediatrics*, *92*(1), 125–127.

Miltner, E., & Kallieris, D. (1989). Quasi-static and dynamic bending stress of the pediatric femur for producing a femoral fracture. *Zeitschrift Fur Rechtsmedizin Journal of Legal Medicine*, *102*(8), 535–544.

Morgan, E. F., Bayraktar, H. H., & Keaveny, T. M. (2003). Trabecular bone modulus-density relationships depend on anatomic site. *Journal of Biomechanics*, *36*(7), 897–904.

Morgan, E. F., & Keaveny, T. M. (2001). Dependence of yield strain of human trabecular bone on anatomic site. *Journal of Biomechanics*, *34*(5), 569–577.

NHTSA. (2008). Final Rule, FMVSS 208, Occupant Crash Protection. *Federal Motor Vehicle*

Safety Standards (FMVSS), (Title 49 Code of Federal Regulations (CFR) Part 571 Section 208).

Nimityongskul, P., & Anderson, L. D. (1987). The likelihood of injuries when children fall out of bed. *Journal of Pediatric Orthopedics*, *7*(2), 184–6.

Notta-Cuvier, D., Lauro, F., Bennani, B., & Balieu, R. (2013). An efficient modelling of inelastic composites with misaligned short fibres. *International Journal of Solids and Structures*, *50*(19), 2857–2871.

O'Neill, J. A., Meacham, W. F., Griffin, J. P., & Sawyers, J. L. (1973). Patterns of injury in the battered child syndrome. *The Journal of Trauma*, *13*(4), 332–9.

Ohman, C., Baleani, M., Pani, C., Taddei, F., Alberghini, M., Viceconti, M., & Manfrini, M. (2011). Compressive behaviour of child and adult cortical bone. *Bone*, *49*(4), 769–776.

Pandya, N. K., Baldwin, K., Wolfgruber, H., Christian, C. W., Drummond, D. S., & Hosalkar, H. S. (2009). Child abuse and orthopaedic injury patterns: analysis at a level I pediatric trauma center. *J Pediatr Orthop*, *29*(6), 618–625.

Pierce, M. C., Valdevit, A., Anderson, L., Inoue, N., & Hauser, D. (2000). Biomechanical Evaluation of Dual-Energy X-Ray Absorptiometry for Predicting Fracture Loads of the Infant Femur for Injury Investigation: An In Vitro Porcine Model. *Journal of Orthopaedic Trauma*, *14*(8), 571.

Pistoia, W., van Rietbergen, B., Lochmüller, E.-M., Lill, C. A., Eckstein, F., & Rüegsegger, P. (2002). Estimation of distal radius failure load with micro-finite element analysis models based on three-dimensional peripheral quantitative computed tomography images. *Bone*, *30*(6), 842–848.

Pithioux, M., Subit, D., & Chabrand, P. (2004). Comparison of compact bone failure under two different loading rates: Experimental and modelling approaches. *Medical Engineering and Physics*, *26*(8), 647–653.

Pomerantz, W. J., Gittelman, M. A., Hornung, R., & Husseinzadeh, H. (2012). Falls in children birth to 5 years. *Journal of Trauma and Acute Care Surgery*, *73*(4 Suppl 3), S254–S257.

Rauch, F., & Schoenau, E. (2002). Skeletal development in premature infants: a review of bone physiology beyond nutritional aspects. *Archives of Disease in Childhood. Fetal and Neonatal Edition*, *86*(2), F82–F85.

Roberts, V. L. (1971). Strength of biological materials. *Journal of Biomechanics*, *4*(2), 159.

Rupp, J. D., Reed, M. P., Madura, N. H., & Schneider, L. W. (1977). COMPARISON OF KNEE / FEMUR FORCE-DEFLECTION RESPONSE OF THE THOR , HYBRID III , AND HUMAN CADAVER TO DYNAMIC FRONTAL-IMPACT KNEE LOADING, 1–9.

Sankar, W. N., Laird, C. T., & Baldwin, K. D. (2012). Hip range of motion in children: What is

the norm? *Journal of Pediatric Orthopaedics*, *32*(4), 399–405.

Schileo, E., Balistreri, L., Grassi, L., Cristofolini, L., & Taddei, F. (2014). To what extent can linear finite element models of human femora predict failure under stance and fall loading configurations? *Journal of Biomechanics*, *47*(14), 3531–3538.

Schileo, E., Dall'Ara, E., Taddei, F., Malandrino, A., Schotkamp, T., Baleani, M., & Viceconti, M. (2008). An accurate estimation of bone density improves the accuracy of subject-specific finite element models. *Journal of Biomechanics*, *41*(11), 2483–2491.

Schileo, E., Taddei, F., Cristofolini, L., & Viceconti, M. (2008). Subject-specific finite element models implementing a maximum principal strain criterion are able to estimate failure risk and fracture location on human femurs tested in vitro. *Journal of Biomechanics*, *41*(2), 356–367.

Schileo, E., Taddei, F., Malandrino, A., Cristofolini, L., & Viceconti, M. (2007). Subject-specific finite element models can accurately predict strain levels in long bones. *Journal of Biomechanics*, *40*(13), 2982–2989.

Servaes, S., Brown, S. D., Choudhary, A. K., Christian, C. W., Done, S. L., Hayes, L. L., … Slovis, T. L. (2016). The etiology and significance of fractures in infants and young children: a critical multidisciplinary review. *Pediatric Radiology*, *46*(5), 591–600.

Skellern, C. Y., Wood, D. O., Murphy, A., & Crawford, M. (2000). Non-accidental fractures in infants: Risk of further abuse. *Journal of Paediatrics and Child Health*, *36*(6), 590–592.

Stewart, G., Meert, K., & Rosenberg, N. (1993). Trauma in infants less than three months of age. *Pediatric Emergency Care*, *9*(4), 199–201.

Taitz, J., Moran, K., & Meara, M. O. (2004). Long bone fractures in children under 3 years of age : Is abuse being missed in Emergency Department presentations ? *Journal of Paediatrics and Child Health*, *16*(August 2003), 170–174.

Theobald, P. S., Qureshi, A., & Jones, M. D. (2012). Biomechanical investigation into the torsional failure of immature long bone. *Journal of Clinical Orthopaedics and Trauma*, *3*(1), 24–27.

Thompson, A., Bertocci, G., Kaczor, K., Smalley, C., & Pierce, M. C. (2015). Biomechanical Investigation of the Classic Metaphyseal Lesion Using an Immature Porcine Model. *American Journal of Roentgenology*, *204*(5), W503–W509.

Thompson, A., Bertocci, G., & Smalley, C. (2018). Femur loading in feet-first fall experiments using an anthropomorphic test device. *Journal of Forensic and Legal Medicine*.

Thompson, A. K., Bertocci, G., & Pierce, M. C. (2009). Assessment of Head Injury Risk Associated With Feet-First Free Falls in 12-Month-Old Children Using an Anthropomorphic Test Device. *The Journal of Trauma: Injury, Infection, and Critical Care*, *66*(4), 1019–1029.

Togrul, E., Bayram, H., Gulsen, M., Kalaci, A., & Özbarlas, S. (2005). Fractures of the femoral neck in children: Long-term follow-up in 62 hip fractures. *Injury*, *36*(1), 123–130. https://doi.org/10.1016/j.injury.2004.04.010

Trabelsi, N., Yosibash, Z., Wutte, C., Augat, P., & Eberle, S. (2011). Patient-specific finite element analysis of the human femur-A double-blinded biomechanical validation. *Journal of Biomechanics*, *44*(9), 1666–1672.

Vinz, H. (1969). [Mechanical principles of typical fractures in children]. *Zentralblatt Fur Chirurgie*, *94*(45), 1509–14.

Wang, M. Y., Kim, K. A., Griffith, P. M., Summers, S., McComb, J. G., Levy, M. L., & Mahour, G. H. (2001). Injuries from falls in the pediatric population: An analysis of 729 cases. *Journal of Pediatric Surgery*, *36*(10), 1528–1534.

Yamada, H., & Evans, F. G. (Francis G. (1973). *Strength of biological materials.* Robert E. Krieger Pub. Co.

Zioupos, P., Cook, R. B., & Hutchinson, J. R. (2008). Some basic relationships between density values in cancellous and cortical bone. *Journal of Biomechanics*, *41*(9), 1961–1968.

APPENDIX I. ADDITIONAL DEVELOPMENT OF FEMUR MODEL AND MATERIAL

APPLICATION RESULTS

The raw data to derive the linear regression of the phantom-less calibration equation can be found in Table XXIII.

TABLE XXIII.

HU VALUES FOR EACH CALIBRATION PHANTOM ROD.

	Case Number	Concentration of CaHA (mg/cc)		
		0	75	150
HU Values	331	25.9	122.1	231.1
	332	12.2	114.7	223.7
	333	23.3	124.0	236.4
	334	10.0	110.9	214.6
	335	25.0	124.5	236.6
	336	20.2	117.8	225.0
	452	19.1	116.5	226.0
	466	20.7	120.9	229.6
	463	20.5	120.0	228.7
	448	19.8	119.7	231.7

A representative distribution to compare the difference in HU of the trabecular mask derived in the enhanced scan with the values found for the same regions in the bone for the unenhanced scan can be found in Figure 71.
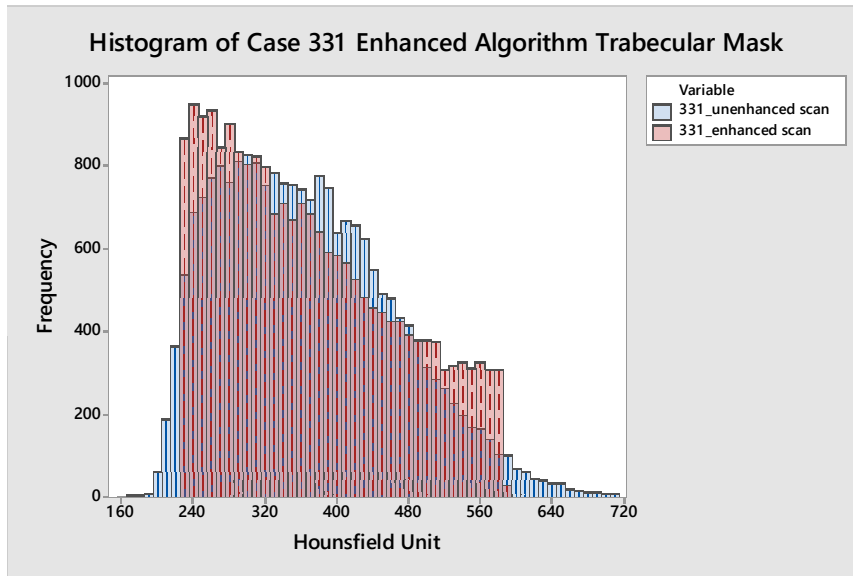
FIGURE 71. Distribution of HU of the trabecular mask derived in the scan with a bone edge enhancement algorithm compared to the same region in the unenhanced scan.

The areal measurements used to compare the enhanced and unenhanced geometries can

be found in Table XXIV.

TABLE XXIV.

AREAL MEASUREMENTS OF CROSS-SECTIONS AT SPECIFIED DISTANCES FROM THE FRONT PLANE FOR THE GEOMETRY DERIVED FROM THE ENHANCED AND UNENHANCED SCANS

Distance from front plane (in)	Area of Section (mm^2)		
	Unenhanced Geometry	Enhanced Geometry	Absolute Percent Difference
-22	173.7	152.9	12.0%
-22.72	132.6	116.1	12.4%
-23	129.0	111.4	13.6%
-24	117.8	104.5	11.3%
-25	110.4	97.0	12.2%
-26	134.0	116.9	12.8%
-26.5	166.9	144.6	13.4%
		Average	12.5%

Table XXV displays the peak stress and strain for the material property application method where a comparison to properties derived in the unenhanced scan were compared to the those derived in the enhanced scan in a three-point bending loading condition.

TABLE XXV.

MAXIMUM PRINCIPAL STRESS AND STRAIN VALUES FOR THREE-POINT BENDING LOADING CONDITION WHERE MATERIAL PROPERTIES DERIVED IN THE ENHANCED AND UNENHANCED SCAN ARE DISPLAYED.

Material Application Method	Derived from Scan Type	Maximum Principal Stress (MPa)	Maximum Principal Strain (%)
Method A-50	Unenhanced	268.0	3.00
Method A-50	Enhanced	295.3	2.37
Method A-10	Enhanced	309.4	2.31
Method A-5	Enhanced	322.7	2.15
Method B	Enhanced	226.0	2.25

APPENDIX II. ATD TRIALS EVALUATED THROUGH FINITE ELEMENT ANALYSIS

The following appendix contains the Minitab output for the statistics used in evaluating whether fall dynamics should be considered as a subfactor for feet-first and/or bed falls. The MATLAB code used to trim each trial in addition to the time histories of the clipped trials are displayed.

A. MATLAB Code Used to Clip ATD Trials

```
%directory notes

baseFolder = input('Enter the directory name,
e.g. G:\bedfall_linoleum\:  ','s');

listing = dir(strcat(baseFolder, '*.xlsx'));


fileNames = {listing.name};

numFiles = length(fileNames);
```

```
sumFileName = strcat(baseFolder, 'summary');
%remove basename

sumIndex = 1;

sumFileColumnNames = {'Trial Name', 'Leg
Side', 'Time Interval (s)', 'Maximum Step Size',
'Original Start Time', 'Original End Time',
'ignore'};

xlswrite(sumFileName, sumFileColumnNames,
strcat('A', num2str(sumIndex), ':G',
num2str(sumIndex)))

sumIndex = 2;
```

```matlab
%loop through each file
for j = 1:1:numFiles

    myFile = fileNames(j)

    tempbase = char(myFile);

    baseName = 
strcat(tempbase(1:length(tempbase)-5));

    myFile = strcat(baseFolder, myFile);

    %myFile = strcat(baseFolder, baseName, 
num2str(j)) %hide

    myTime = xlsread(myFile{1}, 'data', 
'A3:A50002');

    lTable = xlsread(myFile{1}, 'data', 
'S3:AD50002');

    rTable = xlsread(myFile{1}, 'data', 
'AE3:AP50002');


    i = 0;

    myTable = lTable;

    %prompts texts

    pr1 = 'Do you want to adjust the time values? 
(y/n)  ';

    pr2 = 'Do you want to adjust the start time? 
(y/n)  ';

    pr3 = 'What is the new start time(s)?  ';

    pr4 = 'Do you want to adjust the end time? 
(y/n)  ';

    pr5 = 'What is the new end time(s)?  ';

        nameEnd = 'Left';

        %clipping data

    while i<2

    [offset_values, foundStarts] = 
findStarts(myTime, myTable);

        estStart = mean(foundStarts) - 0.2;

        [maxf, iforce] = 
max(horzcat(myTable(:,1:3),myTable(:,7:9)));

        [maxf2, maxi] = max(maxf);

        forceIndex = iforce(maxi);


        [maxm, imoment] = 
max(horzcat(myTable(:,4:6),myTable(:,10:12))
);

        [maxm2, maxi] = max(maxm);

        momentIndex = imoment(maxi);


        timeInd = [forceIndex momentIndex];

        maxTime = myTime(max(timeInd));

        minTime = myTime(min(timeInd));

        if(i==1)

            if(myStart > 0.1)

                myStart = myStart - 0.1;

            end

        elseif(minTime < 1)

            myStart = 0;

        else

            myStart = minTime - 1;

        end


        if(myStart < estStart)

            myStart = estStart;

        end
```

174

```matlab
    if(i==1)

        myEnd = myEnd + 0.5;

    elseif(maxTime > 3.49)

        myEnd = 4.99;

    else

        myEnd = maxTime + 1.5;

    end


    figure

    subplot(2,2,[1 2])

    yyaxis left

    plot(myTime, myTable(:,1:3));

    yyaxis right

    plot(myTime, myTable(:,4:6));

    legend('FxP', 'FyP', 'FzP', 'MxP', 'MyP',
'MzP', 'Location', 'eastoutside')

    legend('boxoff')

    xlim([myStart myEnd]);

    axp = gca;


    subplot(2,2,[3 4])

    yyaxis left

    plot(myTime, myTable(:,7:9));

    yyaxis right

    plot(myTime, myTable(:,10:12));

    legend('FxD', 'FyD', 'FzD', 'MxD', 'MyD',
'MzD', 'Location', 'eastoutside')
```

```matlab
    xlim([myStart myEnd]);

    axp.XLim = [myStart myEnd];

    pr1A = 'y';

    while strcmp(pr1A, 'y')

        pr3A = input(pr3);

        if(not(isempty(pr3A)))

            myStart = pr3A;

            xlim([myStart myEnd]);

            axp.XLim = [myStart myEnd];

        end

        pr5A = input(pr5);

        if(not(isempty(pr5A)))

            myEnd = pr5A;

            xlim([myStart myEnd]);

            axp.XLim = [myStart myEnd];

        end

        pr1A = input(pr1, 's');

    end


    %writing clipped data

    iStart = find(myTime==myStart);

    iEnd = find(myTime==myEnd);

    adjTime = myTime(iStart:iEnd);

    adjTable = myTable(iStart:iEnd,:);

    adjTable = adjustData(adjTable,
offset_values);

    timeInt = myEnd - myStart;

    maxStep = timeInt/0.0016; %max timestep
could change!!!!!
```

```matlab
    adjTime = adjTime - myStart;

    outputName = strcat(baseFolder,
baseName, nameEnd);

    adjOut = horzcat(adjTime, adjTable(:,1:3),
adjTime, adjTable(:,4:6), adjTime,
adjTable(:,7:9), adjTime, adjTable(:,10:12));

    outVars = {baseName, nameEnd, timeInt,
maxStep, myStart, myEnd};

    outVars(7:18) = num2cell(foundStarts(:));

    outVars(19:30) =
num2cell(offset_values(:));

    xlswrite(sumFileName, outVars, strcat('A',
num2str(sumIndex), ':AD',
num2str(sumIndex)))

    sumIndex = sumIndex + 1;

    extraInfo = {'order of data is prox force
prox moment dist force dist moment with
groups of 4'};

    xlswrite(outputName, extraInfo);

    xlswrite(outputName, adjOut, 'Clipped
Data')

    %add in adding to sheet of order of output
data

    %reset to right side

    myTable = rTable;

    i = i+1;

    nameEnd = 'Right';


    %a pause to look at graphs

    %input('press enter to resume')

    close all

  end
```

```matlab
end

function [ adj_value, foundStarts ] =
findStarts(myTime, myInput)

  d = size(myInput);

  %output_vector = zeros(d(1),d(2));

  adj_value = zeros(1, d(2));

  foundStarts = zeros(1,d(2));

  for i = 1:1:d(2)

    %current load settings: load vector and
whether a force or moment

    currentLoad = myInput(:,i);

    if(or(i<4,and(i>6,i<10)))

      isForce = true;

    else

      isForce = false;

    end

     %find starts

    timeIndex = findStart(myTime,
currentLoad, isForce);

    foundStarts(1,i)= myTime(timeIndex);

        close all

  end
end

function [ loadStartTime  ] = findStart(
myTime, input_vector, isForce )

  d = length(myTime);

  inDeriv = zeros(d-2, 1);

  %inD2 = zeros(d-3);

  %create derivative vector

  for i = 2:1:d-1
```

```
    inDeriv(i-1) = (input_vector(i)-
input_vector(i-1))/(myTime(i)-myTime(i-1));

  end

      j=1;

  if(isForce)

    curLimit = 2000;

    meanLim = 3;

  else

    curLimit = 70;

    meanLim = 0.2;

  end

  loadStartTime = 1;

  while j<d-100

    curDer = inDeriv(j:j+20);

    curAvg = mean(curDer);

    meanVal = mean(input_vector(j:j+20));

    if(and(or(curAvg<-
curLimit,curAvg>curLimit),or(meanVal<-
meanLim,meanVal>meanLim)))

      if(j<101)

        loadStartTime = j;

      else

        loadStartTime = j-100;

      end

      break

    end

    j = j+1;

    end

figure

plot(myTime, input_vector)

hold on

%yyaxis right

%plot(myTime(1:d-2),inDeriv)

lineT = myTime(loadStartTime);

line([lineT lineT], [min(input_vector)
max(input_vector)], 'Color', 'green')

end
```

<u>B. Time Histories of Femur Loading of Selected Trials from the ATD Falls</u>

The time histories of the loading conditions from the ATD trials. Each chart contains the forces and moments from the proximal and distal load cells. These loads are annotated where the first letter is whether it is a force (F) or moment (M). The second letter denotes the axis (x, y, or z). The third and final letter denotes whether the load is from the proximal (P) or distal (D) load cell.

1.Time Histories of Femur Loading of ATD Bed Falls
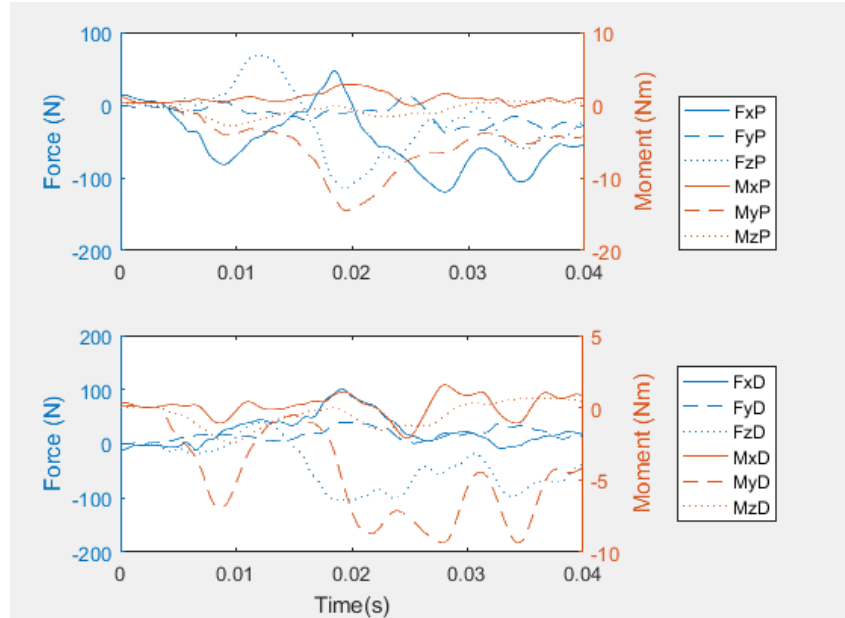
FIGURE 72. Time history of the loading conditions (forces and moments) for a bed fall onto carpet where the lower leg hit first (ATD experiment: trial 12). The loading conditions from both proximal (top chart) and distal (bottom chart) load cells are displayed. These loads are annotated where the first letter is whether it is a force (F) or moment (M). The second letter denotes the axis (x, y, or z). The third and final letter denotes whether the load is from the proximal (P) or distal (D) load cell.
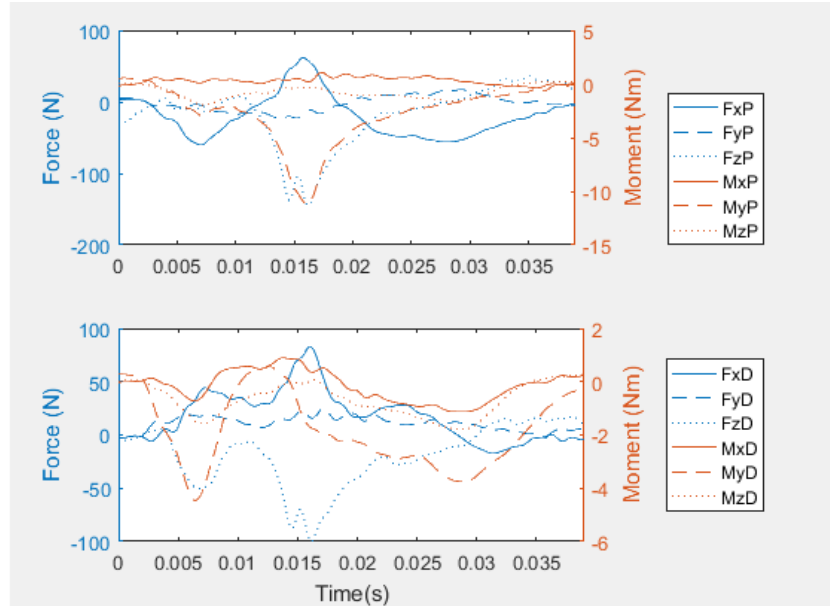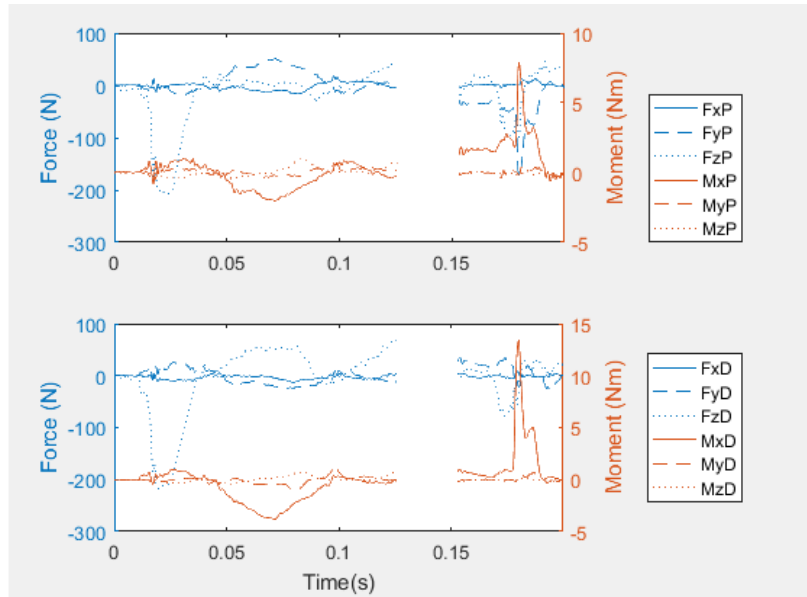

FIGURE 73. Time history of the loading conditions (forces and moments) for a bed fall onto carpet where the lower leg hit first (ATD experiment: trial 8). The loading conditions from both proximal (top chart) and distal (bottom chart) load cells are displayed. These loads are annotated where the first letter is whether it is a force (F) or moment (M). The second letter denotes the axis (x, y, or z). The third and final letter denotes whether the load is from the proximal (P) or distal (D) load cell.
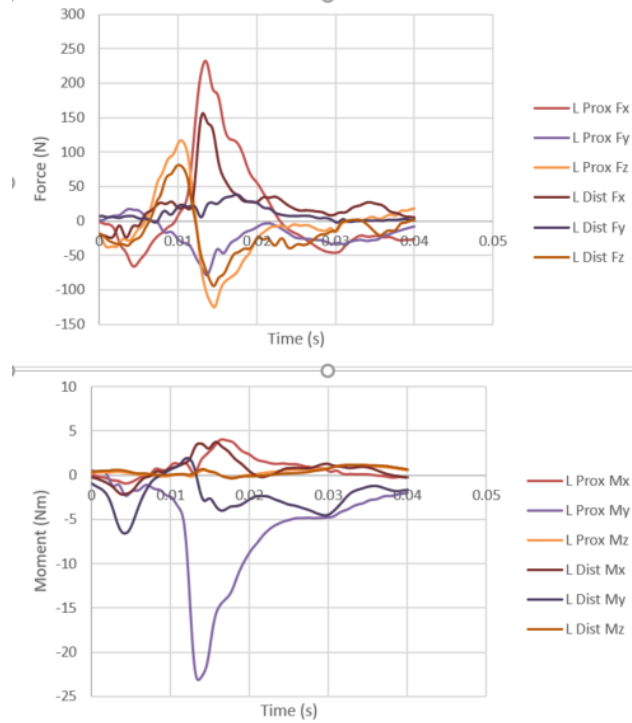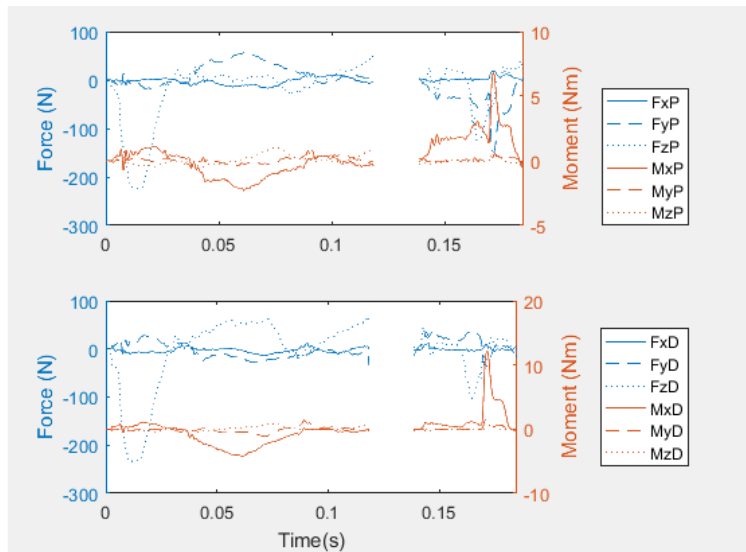
FIGURE 74. Time history of the loading conditions (forces (top) and moments (bottom)) for a bed fall onto carpet where the lower leg hit first (ATD experiment: trial 9). The loading conditions from both proximal (Prox) and distal (Dist) load cells are displayed. These loads are annotated where the first letter is whether it is a force (F) or moment (M). The second letter denotes the axis (x, y, or z).
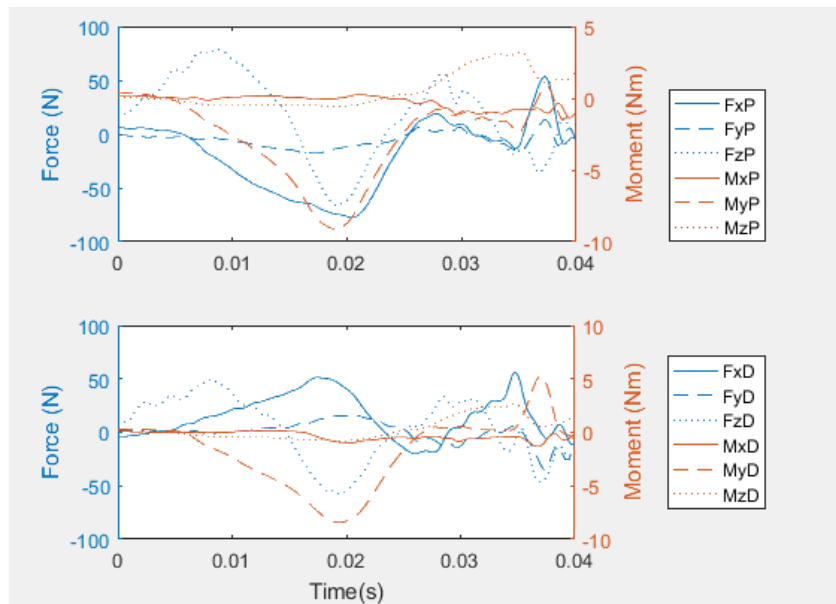
FIGURE 75. Time history of the loading conditions (forces and moments) for a bed fall onto carpet where the upper leg hit first (ATD experiment: trial 4). The loading conditions from both proximal (top chart) and distal (bottom chart) load cells are displayed. These loads are annotated where the first letter is whether it is a force (F) or moment (M). The second letter denotes the axis (x, y, or z). The third and final letter denotes whether the load is from the proximal (P) or distal (D) load cell.
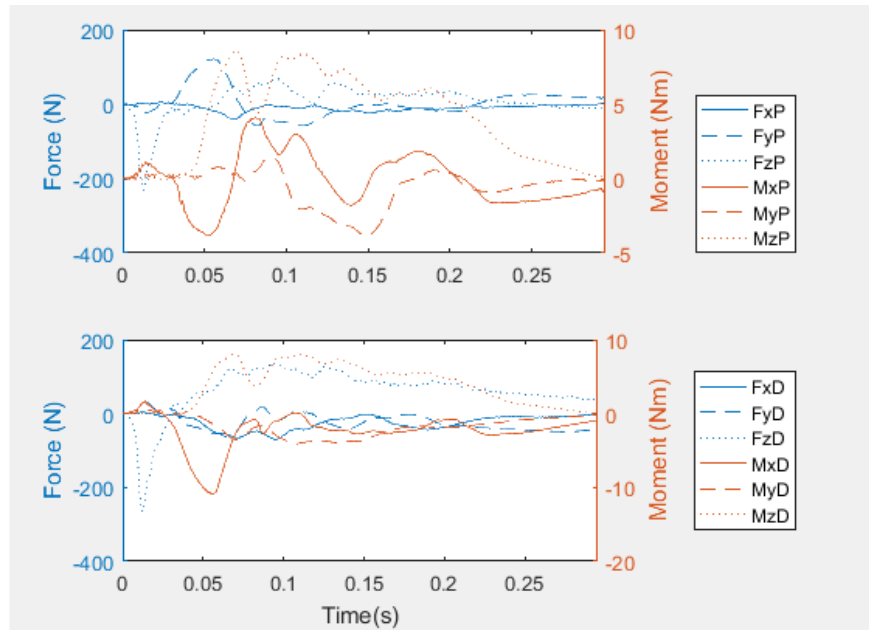
179
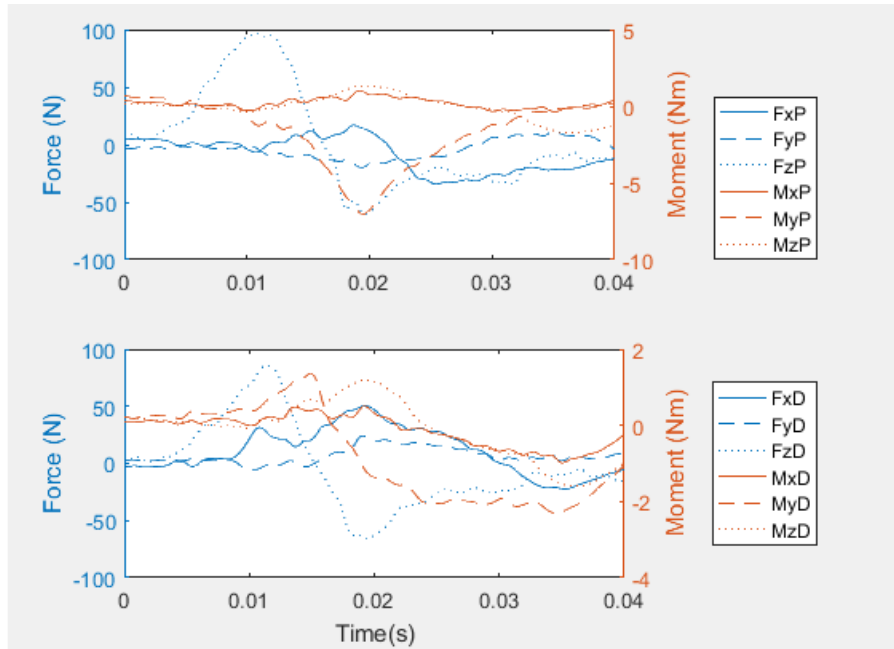
FIGURE 76. Time history of the loading conditions (forces and moments) for a bed fall onto carpet where the upper leg hit first (ATD experiment: trial 7). The loading conditions from both proximal (top chart) and distal (bottom chart) load cells are displayed. These loads are annotated where the first letter is whether it is a force (F) or moment (M). The second letter denotes the axis (x, y, or z). The third and final letter denotes whether the load is from the proximal (P) or distal (D) load cell.
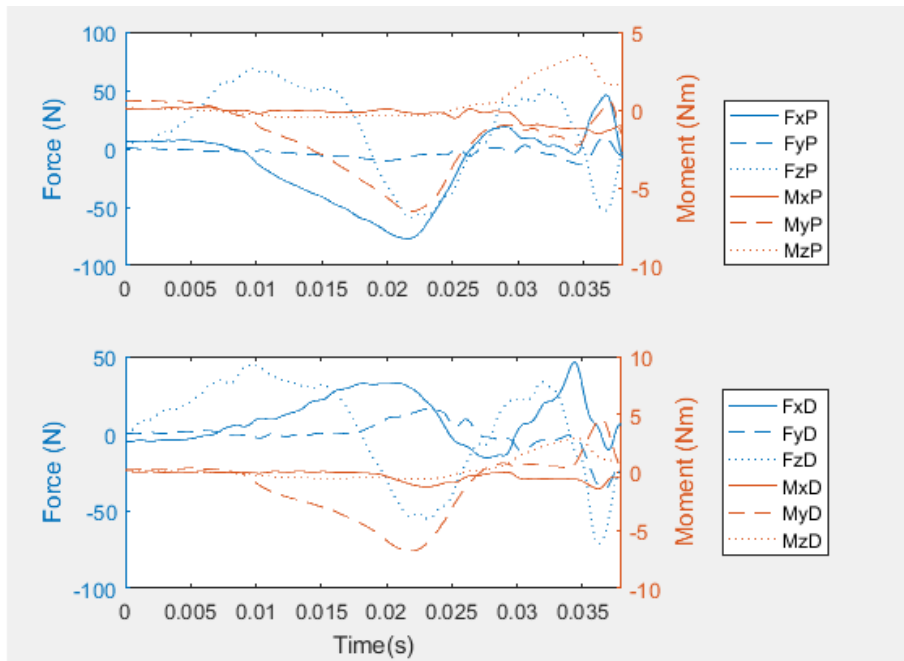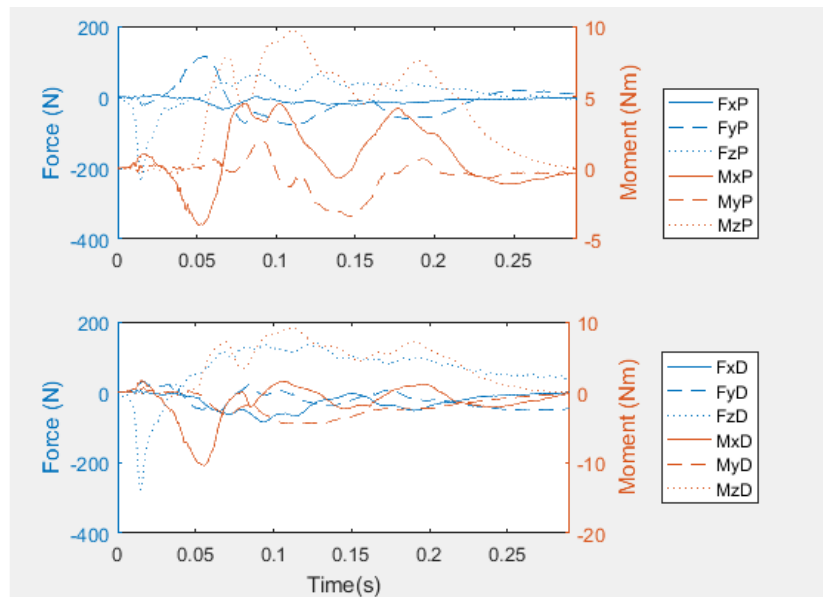

FIGURE 77. Time history of the loading conditions (forces and moments) for a bed fall onto carpet where the upper leg hit first (ATD experiment: trial 3). The loading conditions from both proximal (top chart) and distal (bottom chart) load cells are displayed. These loads are annotated where the first letter is whether it is a force (F) or moment (M). The second letter denotes the axis (x, y, or z). The third and final letter denotes whether the load is from the proximal (P) or distal (D) load cell.
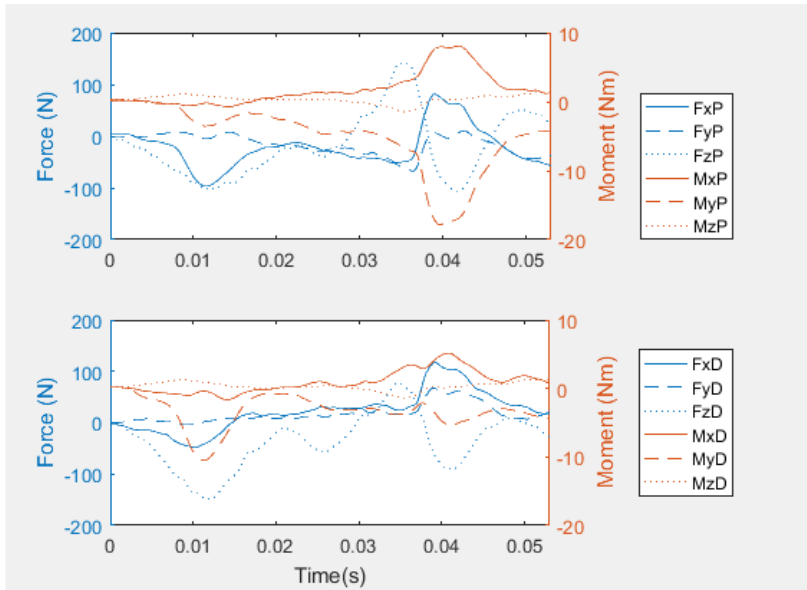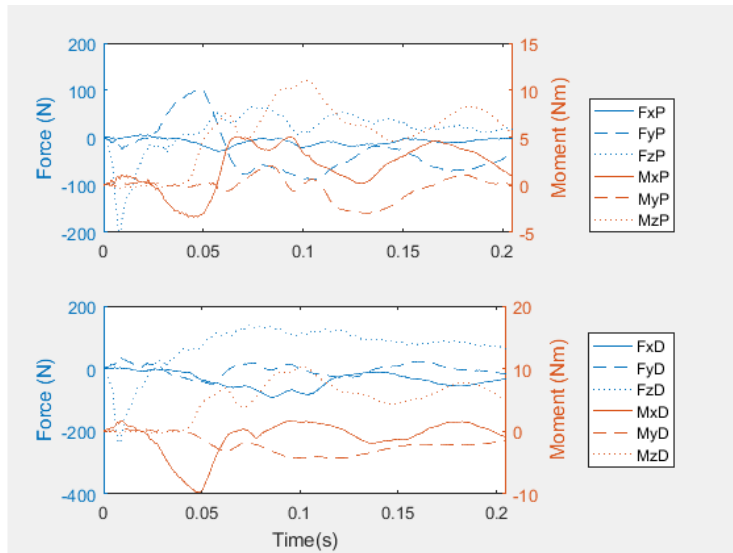
FIGURE 78. Time history of the loading conditions (forces and moments) for a bed fall onto linoleum where the lower leg hit first (ATD experiment: trial 10). The loading conditions from both proximal (top chart) and distal (bottom chart) load cells are displayed. These loads are annotated where the first letter is whether it is a force (F) or moment (M). The second letter denotes the axis (x, y, or z). The third and final letter denotes whether the load is from the proximal (P) or distal (D) load cell.
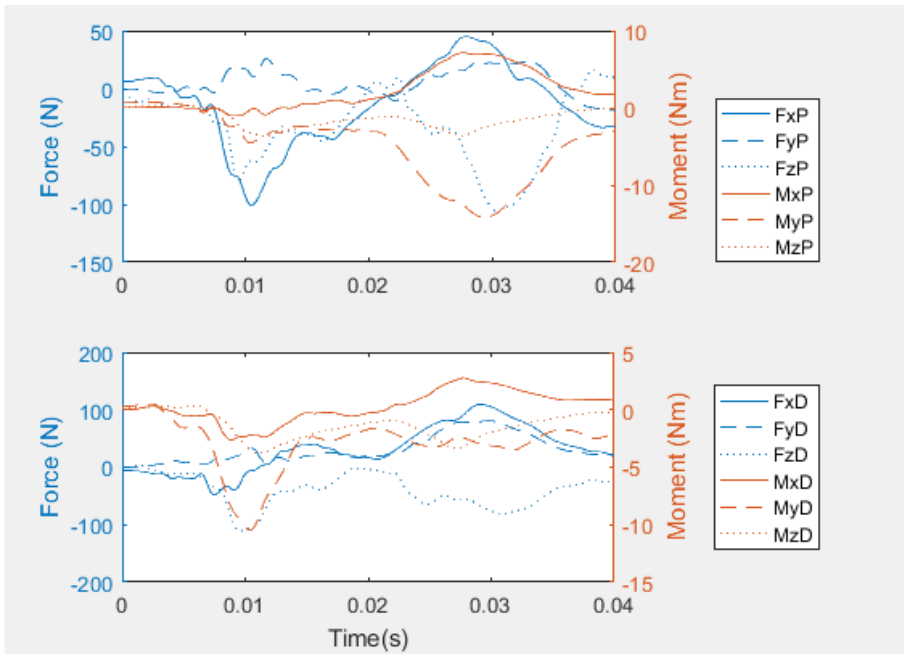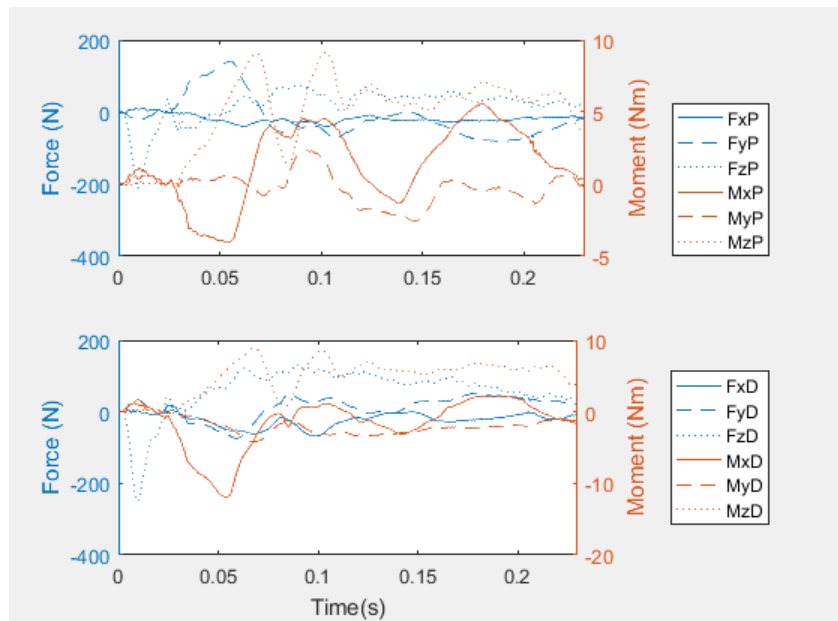

FIGURE 79. Time history of the loading conditions (forces and moments) for a bed fall onto linoleum where the lower leg hit first (ATD experiment: trial 6). The loading conditions from both proximal (top chart) and distal (bottom chart) load cells are displayed. These loads are annotated where the first letter is whether it is a force (F) or moment (M). The second letter denotes the axis (x, y, or z). The third and final letter denotes whether the load is from the proximal (P) or distal (D) load cell.

181
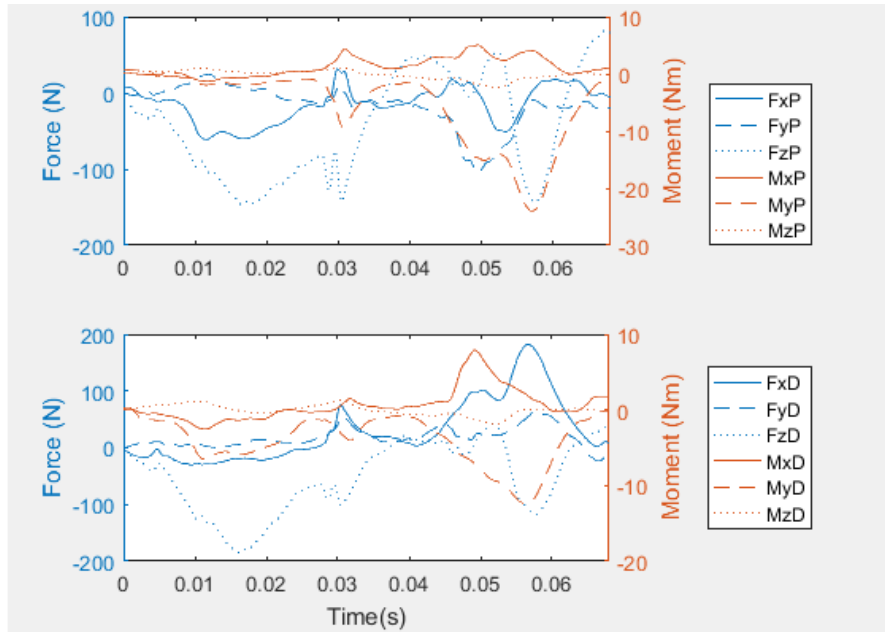
FIGURE 80. Time history of the loading conditions (forces and moments) for a bed fall onto linoleum where the lower leg hit first (ATD experiment: trial 2). The loading conditions from both proximal (top chart) and distal (bottom chart) load cells are displayed. These loads are annotated where the first letter is whether it is a force (F) or moment (M). The second letter denotes the axis (x, y, or z). The third and final letter denotes whether the load is from the proximal (P) or distal (D) load cell.
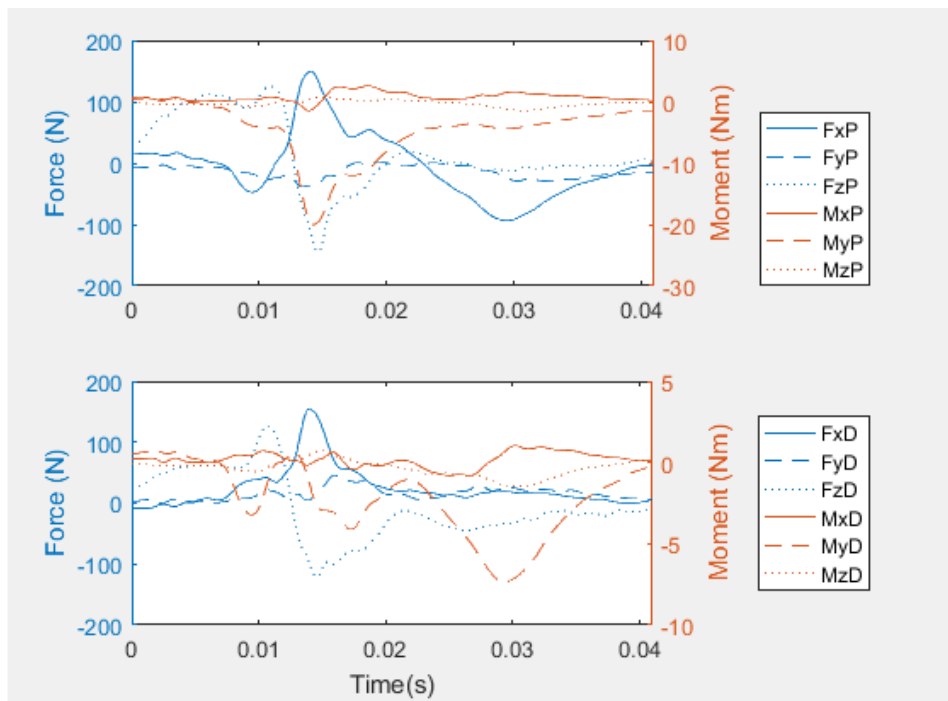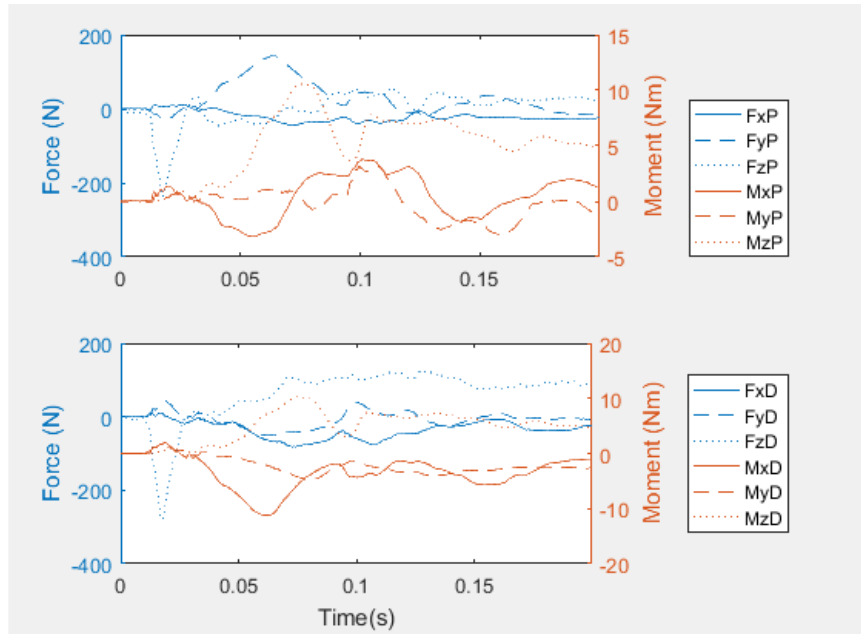

FIGURE 81. Time history of the loading conditions (forces and moments) for a bed fall onto linoleum where the upper leg hit first (ATD experiment: trial 9). The loading conditions from both proximal (top chart) and distal (bottom chart) load cells are displayed. These loads are annotated where the first letter is whether it is a force (F) or moment (M). The second letter denotes the axis (x, y, or z). The third and final letter denotes whether the load is from the proximal (P) or distal (D) load cell.
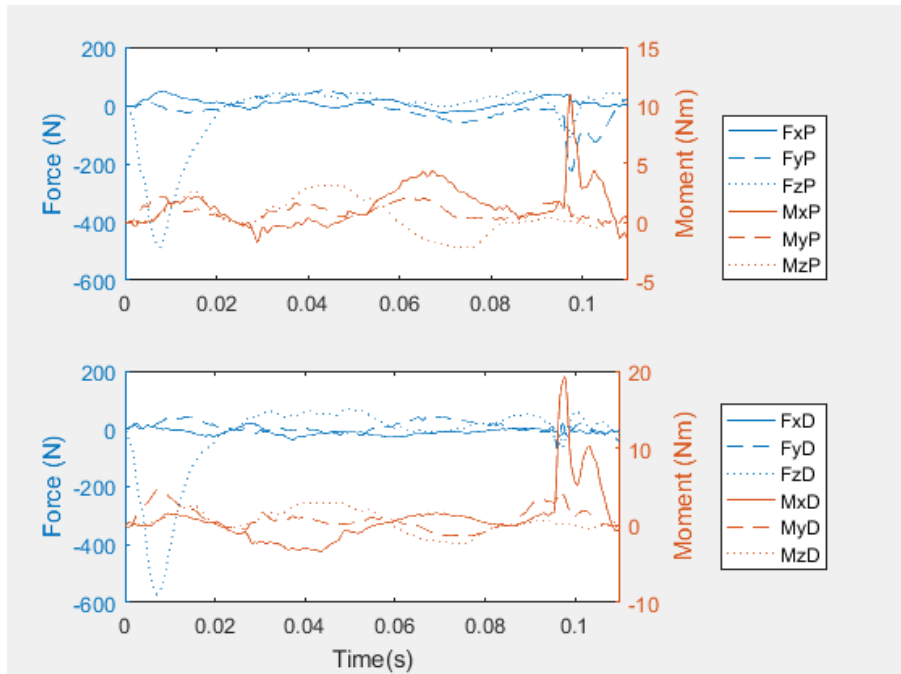
182
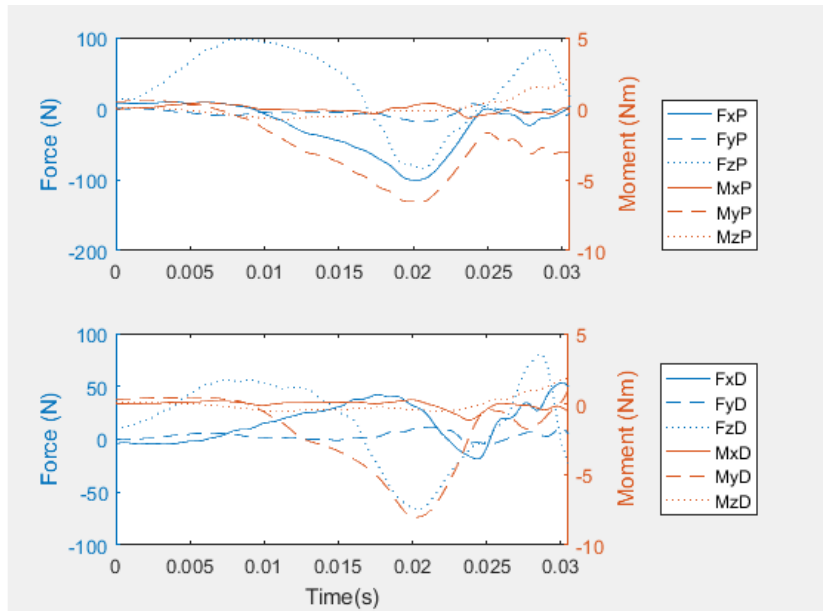
FIGURE 82. Time history of the loading conditions (forces and moments) for a bed fall onto linoleum where the upper leg hit first (ATD experiment: trial 11). The loading conditions from both proximal (top chart) and distal (bottom chart) load cells are displayed. These loads are annotated where the first letter is whether it is a force (F) or moment (M). The second letter denotes the axis (x, y, or z). The third and final letter denotes whether the load is from the proximal (P) or distal (D) load cell.
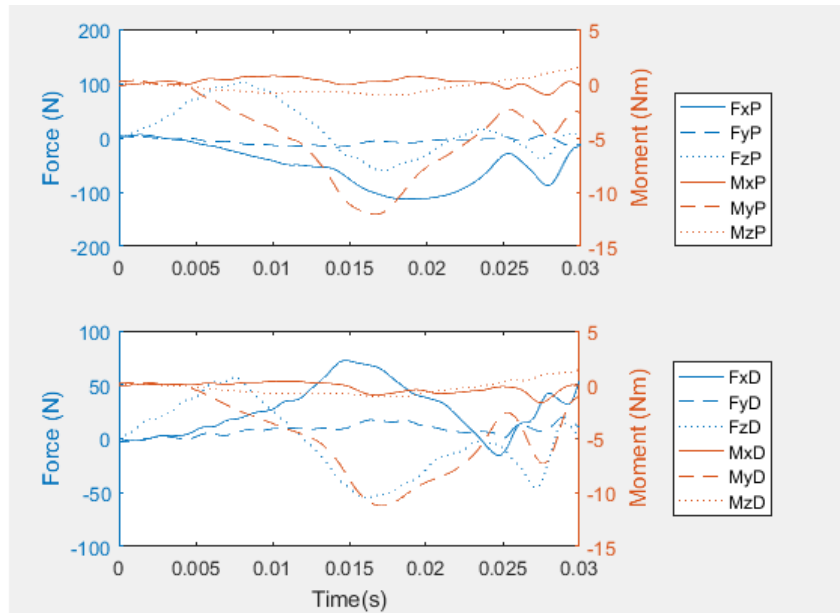
FIGURE 83. Time history of the loading conditions (forces and moments) for a bed fall onto linoleum where the upper leg hit first (ATD experiment: trial 12). The loading conditions from both proximal (top chart) and distal (bottom chart) load cells are displayed. These loads are annotated where the first letter is whether it is a force (F) or moment (M). The second letter denotes the axis (x, y, or z). The third and final letter denotes whether the load is from the proximal (P) or distal (D) load cell.

2. Time Histories of Femur Loading of ATD Feet-First Falls
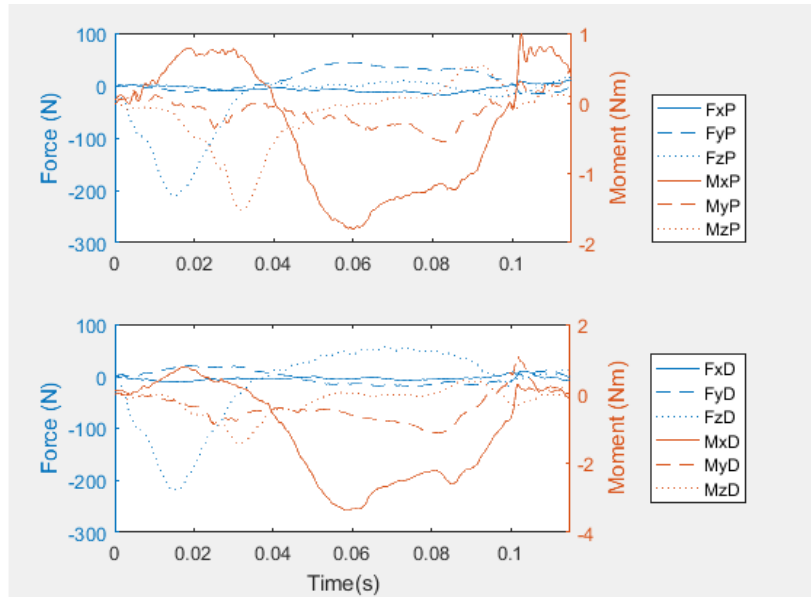
FIGURE 84. Time history of the loading conditions (forces and moments) of the left leg for a 69cm feet-first fall onto carpet (ATD experiment: trial 2). The loading conditions from both proximal (top chart) and distal (bottom chart) load cells are displayed. These loads are annotated where the first letter is whether it is a force (F) or moment (M). The second letter denotes the axis (x, y, or z). The third and final letter denotes whether the load is from the proximal (P) or distal (D) load cell.
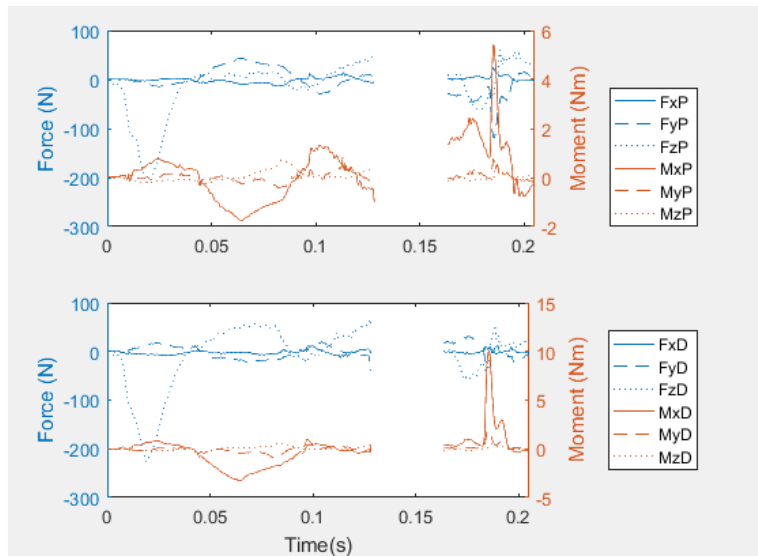
FIGURE 85. Time history of the loading conditions (forces and moments) of the left leg for a 69cm feet-first fall onto carpet (ATD experiment: trial 3). The loading conditions from both proximal (top chart) and distal (bottom chart) load cells are displayed. These loads are annotated where the first letter is whether it is a force (F) or moment (M). The second letter denotes the axis (x, y, or z). The third and final letter denotes whether the load is from the proximal (P) or distal (D) load cell.

184
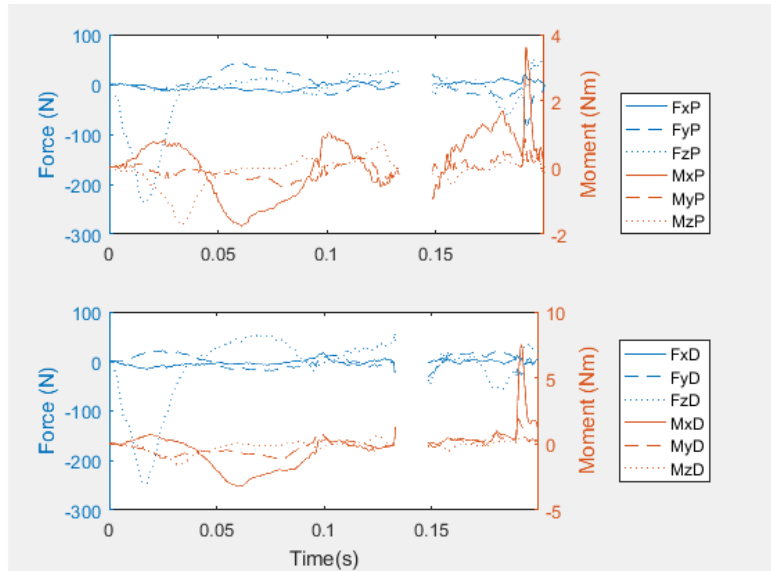
FIGURE 86. Time history of the loading conditions (forces and moments) of the left leg for a 69cm feet-first fall onto carpet (ATD experiment: trial 5). The loading conditions from both proximal (top chart) and distal (bottom chart) load cells are displayed. These loads are annotated where the first letter is whether it is a force (F) or moment (M). The second letter denotes the axis (x, y, or z). The third and final letter denotes whether the load is from the proximal (P) or distal (D) load cell.
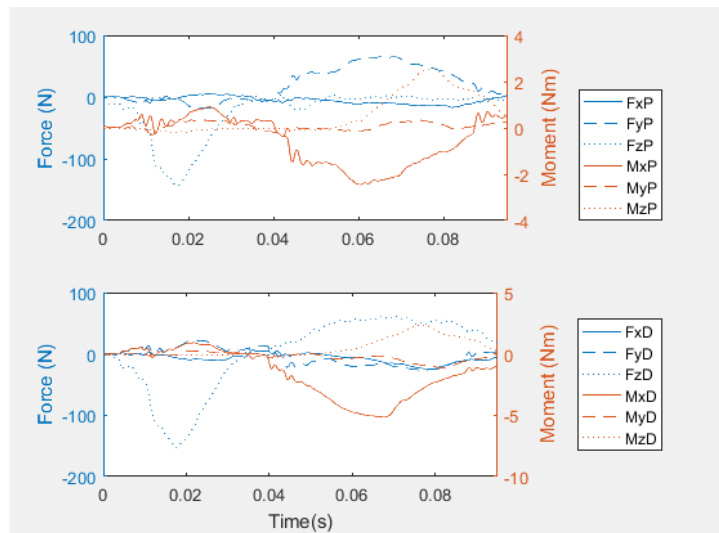
FIGURE 87. Time history of the loading conditions (forces and moments) of the left leg for a 69cm feet-first fall onto linoleum (ATD experiment: trial 3). The loading conditions from both proximal (top chart) and distal (bottom chart) load cells are displayed. These loads are annotated where the first letter is whether it is a force (F) or moment (M). The second letter denotes the axis (x, y, or z). The third and final letter denotes whether the load is from the proximal (P) or distal (D) load cell.

185

FIGURE 88. Time history of the loading conditions (forces and moments) of the left leg for a 69cm feet-first fall onto linoleum (ATD experiment: trial 8). The loading conditions from both proximal (top chart) and distal (bottom chart) load cells are displayed. These loads are annotated where the first letter is whether it is a force (F) or moment (M). The second letter denotes the axis (x, y, or z). The third and final letter denotes whether the load is from the proximal (P) or distal (D) load cell.

FIGURE 89. Time history of the loading conditions (forces and moments) of the left leg for a 69cm feet-first fall onto linoleum (ATD experiment: trial 9). The loading conditions from both proximal (top chart) and distal (bottom chart) load cells are displayed. These loads are annotated where the first letter is whether it is a force (F) or moment (M). The second letter denotes the axis (x, y, or z). The third and final letter denotes whether the load is from the proximal (P) or distal (D) load cell.

186

FIGURE 90. Time history of the loading conditions (forces and moments) of the left leg for a 119cm feet-first fall onto carpet (ATD experiment: trial 3). The loading conditions from both proximal (top chart) and distal (bottom chart) load cells are displayed. These loads are annotated where the first letter is whether it is a force (F) or moment (M). The second letter denotes the axis (x, y, or z). The third and final letter denotes whether the load is from the proximal (P) or distal (D) load cell.

FIGURE 91. Time history of the loading conditions (forces and moments) of the left leg for a 119cm feet-first fall onto carpet (ATD experiment: trial 7). The loading conditions from both proximal (top chart) and distal (bottom chart) load cells are displayed. These loads are annotated where the first letter is whether it is a force (F) or moment (M). The second letter denotes the axis (x, y, or z). The third and final letter denotes whether the load is from the proximal (P) or distal (D) load cell.

187

FIGURE 92. Time history of the loading conditions (forces and moments) of the left leg for a 119cm feet-first fall onto carpet (ATD experiment: trial 9). The loading conditions from both proximal (top chart) and distal (bottom chart) load cells are displayed. These loads are annotated where the first letter is whether it is a force (F) or moment (M). The second letter denotes the axis (x, y, or z). The third and final letter denotes whether the load is from the proximal (P) or distal (D) load cell.

FIGURE 93. Time history of the loading conditions (forces and moments) of the left leg for a 119cm feet-first fall onto linoleum (ATD experiment: trial 3). The loading conditions from both proximal (top chart) and distal (bottom chart) load cells are displayed. These loads are annotated where the first letter is whether it is a force (F) or moment (M). The second letter denotes the axis (x, y, or z). The third and final letter denotes whether the load is from the proximal (P) or distal (D) load cell.

188

FIGURE 94. Time history of the loading conditions (forces and moments) of the left leg for a 119cm feet-first fall onto linoleum (ATD experiment: trial 4). The loading conditions from both proximal (top chart) and distal (bottom chart) load cells are displayed. These loads are annotated where the first letter is whether it is a force (F) or moment (M). The second letter denotes the axis (x, y, or z). The third and final letter denotes whether the load is from the proximal (P) or distal (D) load cell.

Figure 95. Time history of the loading conditions (forces and moments) of the left leg for a 119cm feet-first fall onto linoleum (ATD experiment: trial 9). The loading conditions from both proximal (top chart) and distal (bottom chart) load cells are displayed. These loads are annotated where the first letter is whether it is a force (F) or moment (M). The second letter denotes the axis (x, y, or z). The third and final letter denotes whether the load is from the proximal (P) or distal (D) load cell.

189

APPENDIX III. FE PREDICTED OUTCOMES OF FEMUR LOADING DUE TO ATD

FALLS

The following appendix covers the peak outcomes of each trial evaluated in addition to any statistical analysis conducted for each fall type.

A. Bed Fall Outcomes

TABLE XXVI.

PEAK OUTCOMES FOR EACH BED FALL TRIAL AND WHICH STRESS-BASED THRESHOLDS WERE EXCEEDED

Trial ID	Impact Surface	Fall Dynamic	FD and Impact ID	Max Principal Stress (MPa)	Max Principal Strain	Max von Mises Stress (Mpa)	Fracture ID	Exceeds Tensile Strength Threshold?	Exceeds Flexural Strength Threshold?
3	Carpet	Upper	Carpet B	42.2	0.77%	54.5	C	N	N
4	Carpet	Upper	Carpet B	49.8	0.84%	61.8	C	N	N
7	Carpet	Upper	Carpet B	63.4	0.90%	60.1	C	N	N
8	Carpet	Lower	Carpet A	112.2	1.42%	101.5	B	N	N
9	Carpet	Lower	Carpet A	247.3	3.13%	223.5	A	Y	Y
12	Carpet	Lower	Carpet A	132.8	1.68%	119.9	A	Y	N
2	Linoleum	Lower	Linoleum A	199.4	2.66%	180.1	A	Y	N
6	Linoleum	Lower	Linoleum A	155.4	2.27%	142.6	A	Y	N
9	Linoleum	Upper	Linoleum B	208.4	2.66%	195.0	A	Y	Y
10	Linoleum	Lower	Linoleum A	181.2	2.34%	163.4	A	Y	N
11	Linoleum	Upper	Linoleum B	41.4	0.63%	43.2	D	N	N
12	Linoleum	Upper	Linoleum B	60.6	1.12%	79.9	C	N	N

TABLE XXVII.

BED FALLS EXCEEDING AN A OR B FRACTURE CLASSIFICATION WITH THE ASSOCIATED PERCENT OF THE TOTAL DIAPHYSEAL VOLUME OF ELEMENTS THAT HAD EXCEEDED THE YIELD STRAIN THRESHOLD

Fall condition	ATD Trial ID	% of total diaphyseal volume	Fracture Classification
Carpet	8	0.095%	B
Carpet	9	6.400%	A
Carpet	12	0.244%	A
Linoleum	2	2.10%	A
Linoleum	6	0.83%	A
Linoleum	9	3.52%	A
Linoleum	10	1.80%	A

B. Outcomes for Feet-First Falls

TABLE XXVIII.

PEAK OUTCOMES FOR EACH FEET-FIRST FALL TRIAL AND WHETHER THE STRESS-BASED THRESHOLDS WERE EXCEEDED

Trial ID	Impact Surface	Fall Height (in.)	Max Principal Stress (MPa)	Max Principal Strain	Maximum Von Mises (MPa)	Fracture ID	Exceeds Tensile Strength Threshold?	Exceeds Flexural Strength Threshold?
2	Carpet	27	26.3	0.33%	21.6	D	N	N
3	Carpet	27	56.1	0.79%	74.9	C	N	N
5	Carpet	27	44.5	0.64%	60.3	D	N	N
3	Carpet	47	94.9	1.87%	132.7	B	N	N
7	Carpet	47	100.7	2.03%	153.4	B	N	N
9	Carpet	47	114.2	2.32%	175.0	B	N	N
3	Linoleum	27	37.6	0.46%	33.2	D	N	N
8	Linoleum	27	62.7	0.88%	87.8	C	N	N
9	Linoleum	27	65.8	0.88%	87.9	C	N	N
3	Linoleum	47	103.1	2.04%	140.4	B	N	N
4	Linoleum	47	124.5	2.31%	161.7	B	N	N
9	Linoleum	47	109.2	1.32%	142.6	B	N	N

Table XXIX.

FEET-FIRST FALLS EXCEEDING AN A OR B FRACTURE CLASSIFICATION WITH THE ASSOCIATED PERCENT OF THE TOTAL DIAPHYSEAL VOLUME OF ELEMENTS THAT HAD EXCEEDED THE YIELD STRAIN THRESHOLD

Fall condition	ATD Trial ID	% of total diaphyseal volume	Fracture Classification
119cm onto carpet	3	1.36%	B
119cm onto carpet	7	2.74%	B
119cm onto carpet	9	4.85%	B
119cm onto linoleum	3	2.27%	B
119cm onto linoleum	4	4.05%	B
119cm onto linoleum	9	0.12%	B

APPENDIX IV. STRESS AND STRAIN DISTRIBUTIONS FOR EACH TRIAL

The following appendix contains the stress and strain distribution for each ATD trial evaluated. If the yield strain threshold was exceeded, the elements which exceeded the threshold are also displayed.
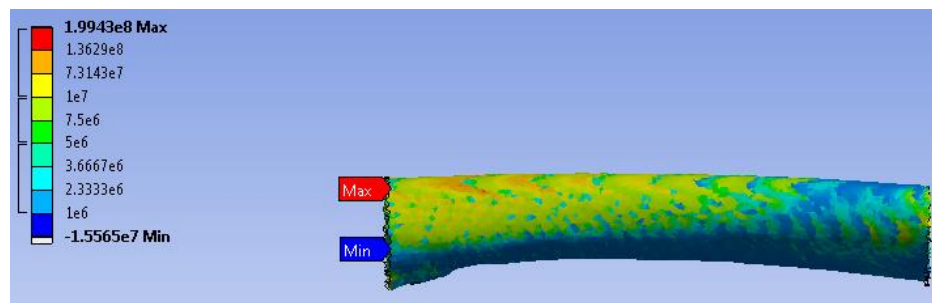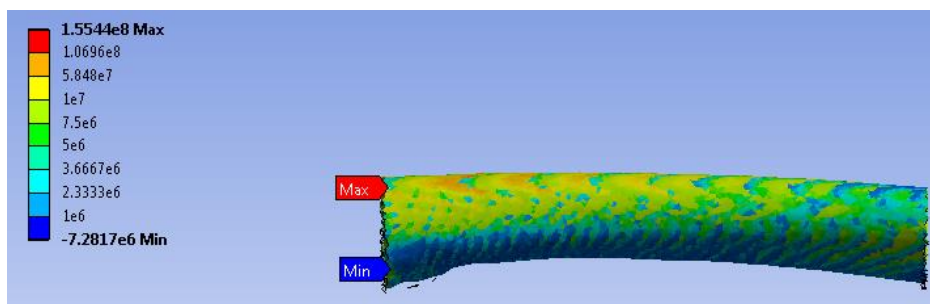
A. Stress and Strain Distribution of Bed Fall Trials

1. Falls onto Carpet
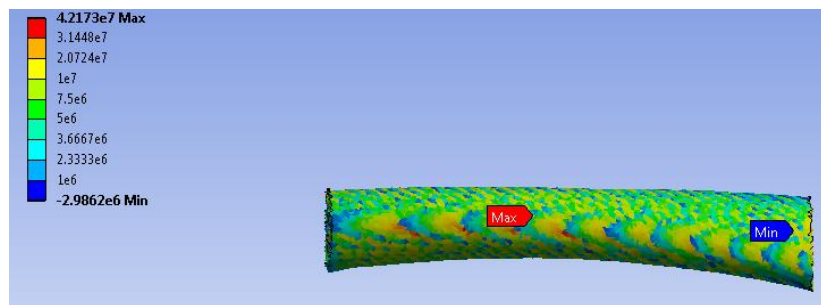
FIGURE 96. Distribution of the peak maximum principal stress (Pa) across the diaphysis of the femur for a bed fall onto carpet (ATD experiment: trial 3). Medial view.
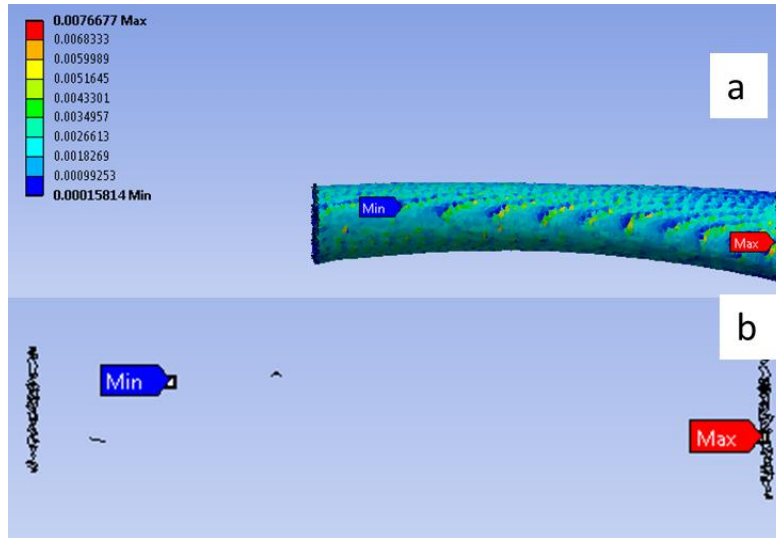
FIGURE 97. Distribution of the peak maximum principal strain across the diaphysis of the femur for a bed fall onto carpet (ATD experiment: trial 3). Medial view. (a) shows the distribution without a threshold and (b) displays the elements with strains greater than 0.73% (the yield strain threshold).
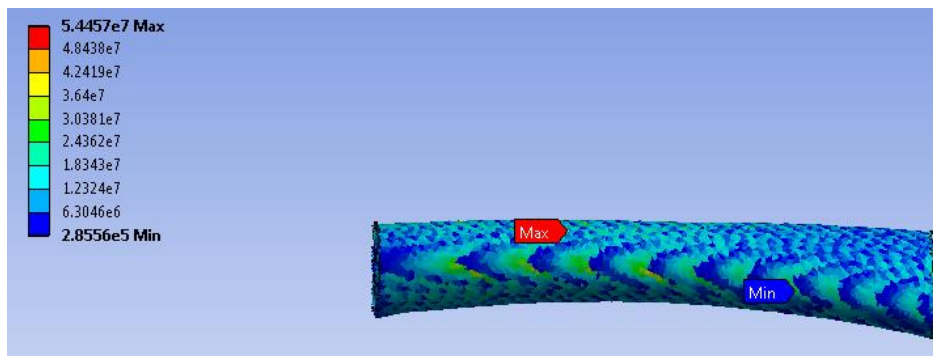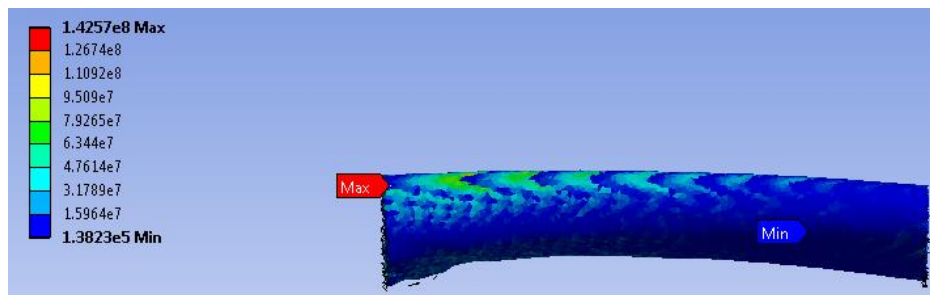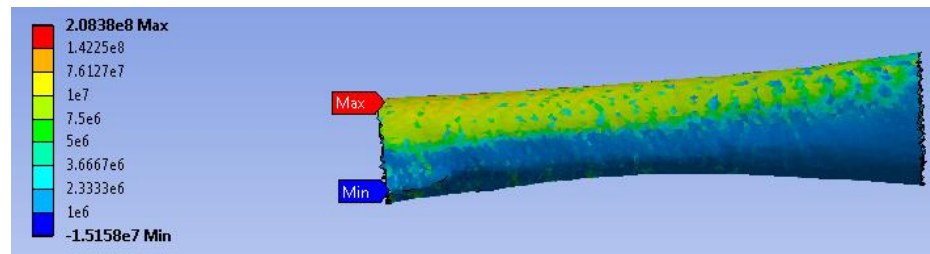

FIGURE 98. Distribution of the maximum von Mises stress (Pa) across the diaphysis of the femur for a bed fall onto carpet (ATD experiment: trial 3). Medial view.
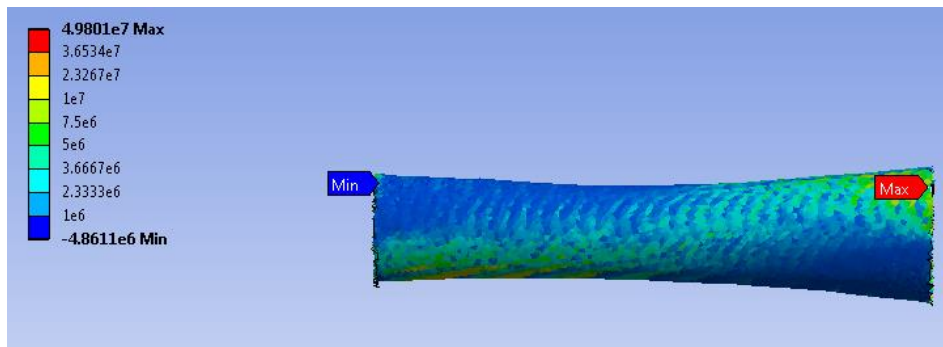
FIGURE 99. Distribution of the peak maximum principal stress (Pa) across the diaphysis of the femur for a bed fall onto carpet (ATD experiment trial 4). Anterior view.
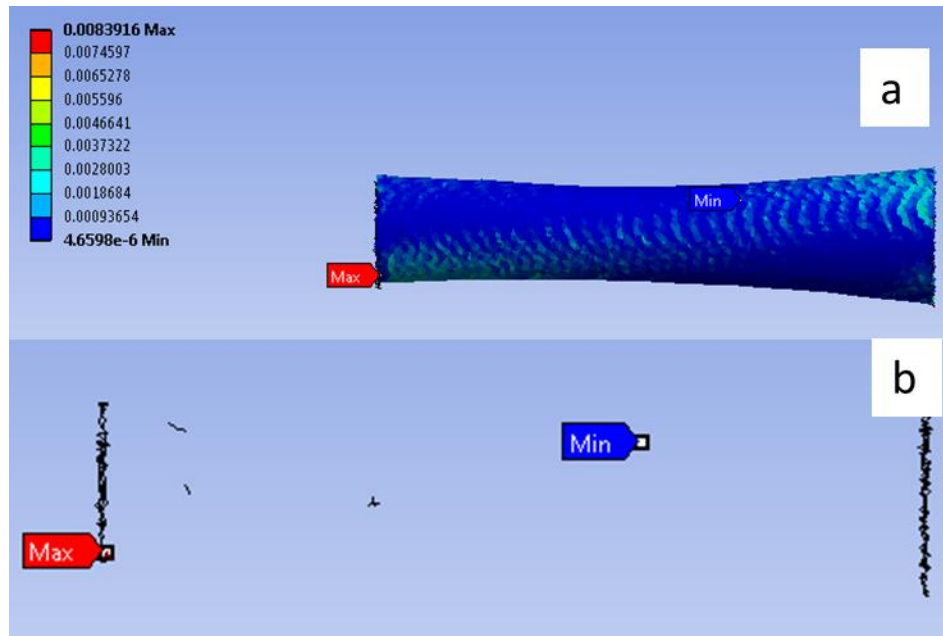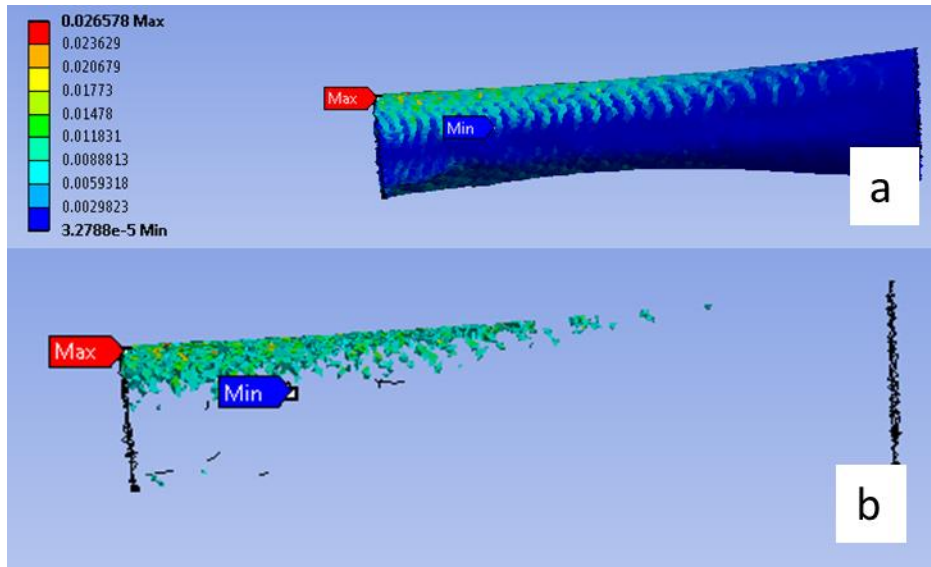
FIGURE 100. Distribution of the peak maximum principal strain across the diaphysis of the femur for a bed fall onto carpet (ATD experiment trial 4). Anterior view. (a) shows the distribution without a threshold and (b) displays the elements with strains greater than 0.73% (yield strain threshold).
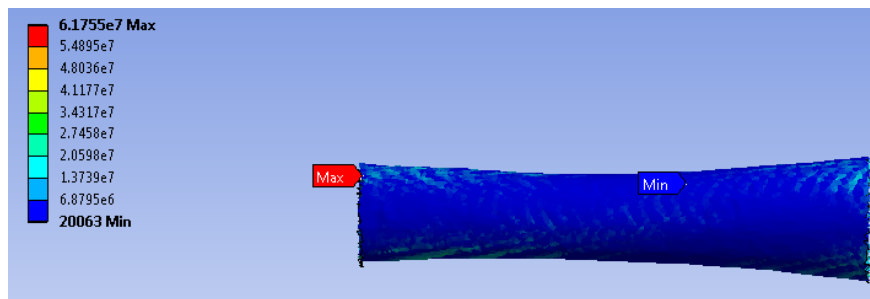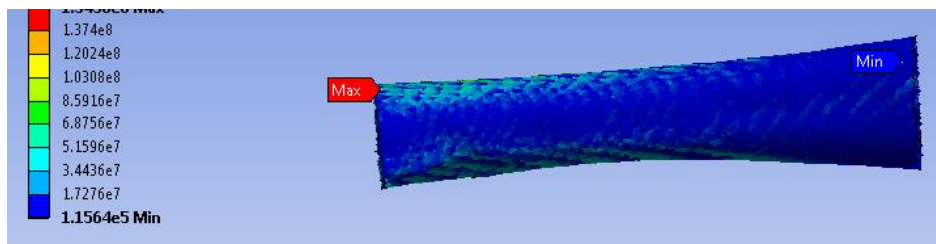

FIGURE 101. Distribution of the maximum von Mises stress (Pa) across the diaphysis of the femur for a bed fall onto carpet (ATD experiment trial 4). Anterior view.
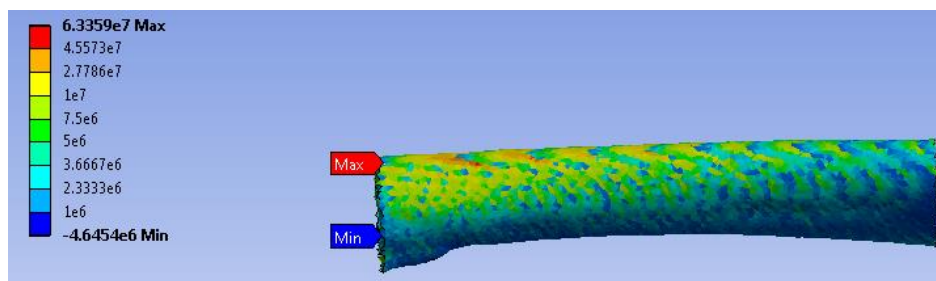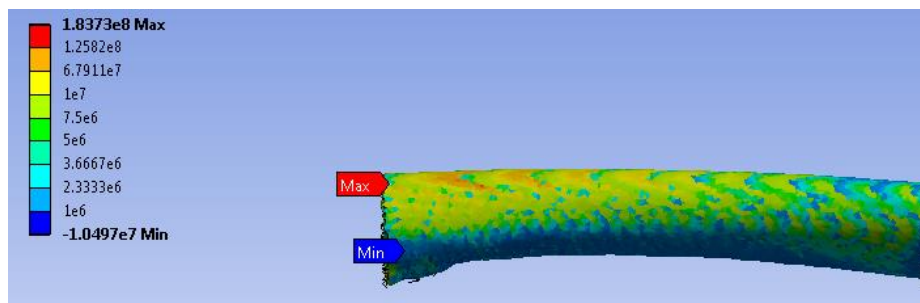

FIGURE 102. Distribution of the peak maximum principal stress (Pa) across the diaphysis of the femur for a bed fall onto carpet (ATD experiment: trial 7). Posterior-Medial view.
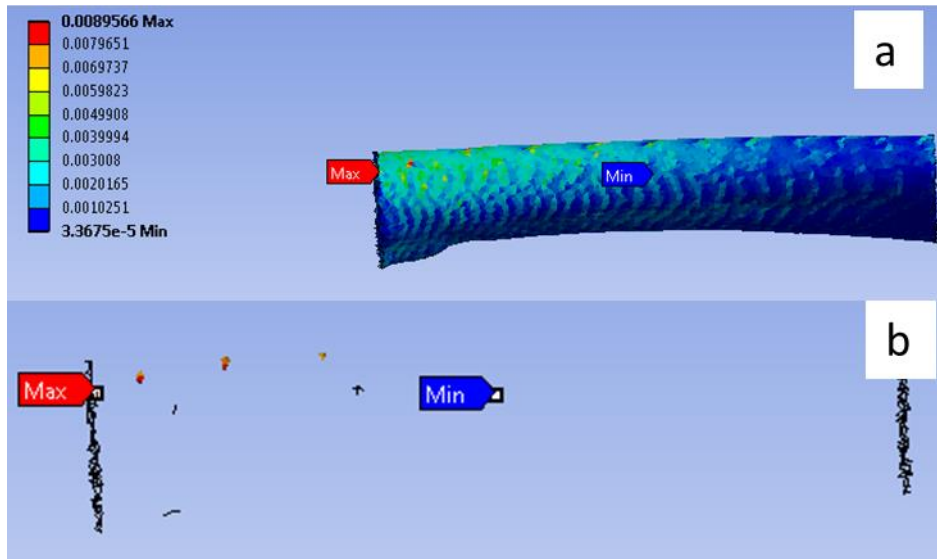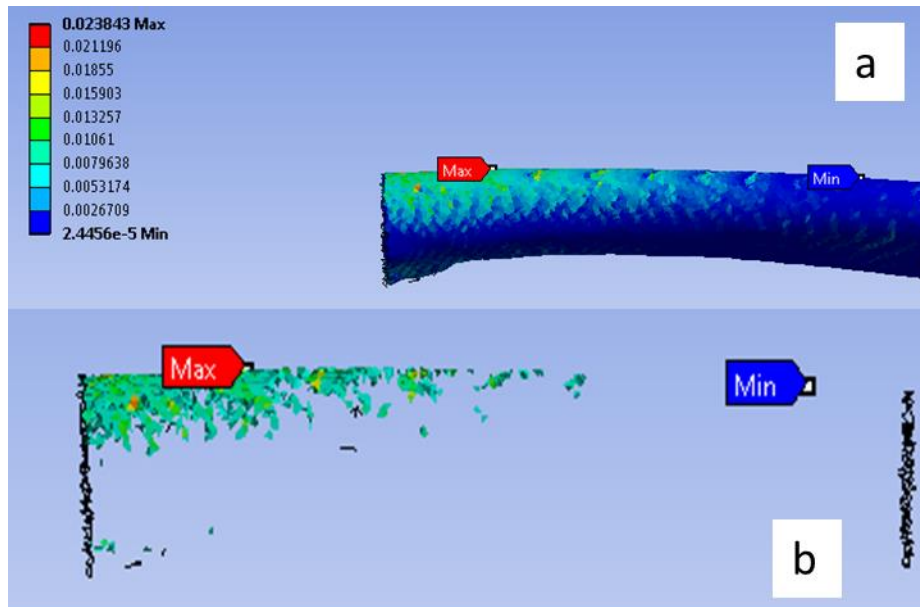
FIGURE 103. Distribution of the peak maximum principal strain across the diaphysis of the femur for a bed fall onto carpet (ATD experiment: trial 7). Posterior-Medial view. (a) shows the distribution without a threshold and (b) displays the elements with strains greater than 0.73% (yield strain threshold).
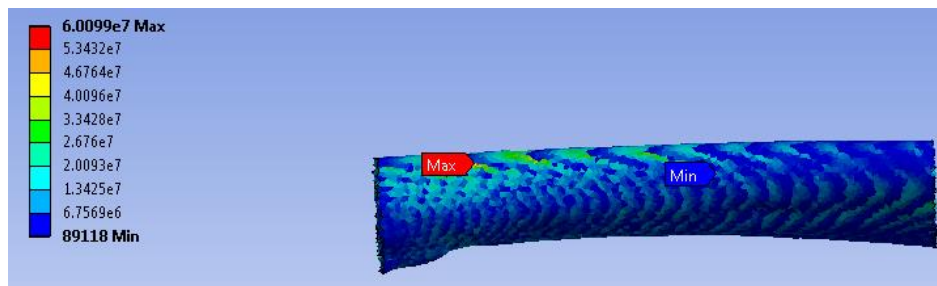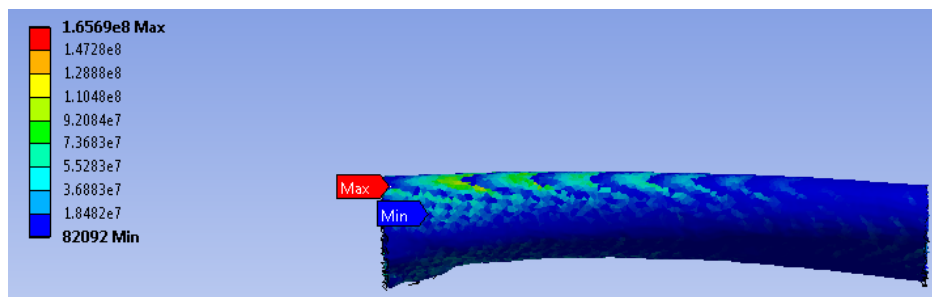

FIGURE 104. Distribution of the maximum von Mises stress (Pa) across the diaphysis of the femur for a bed fall onto carpet (ATD experiment: trial 7). Posterior-Medial view.
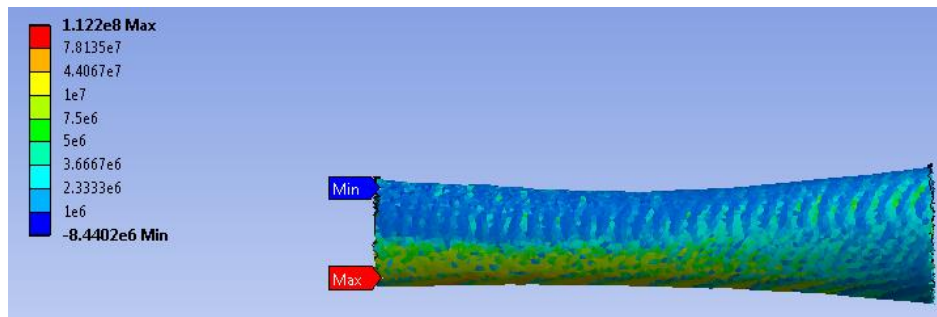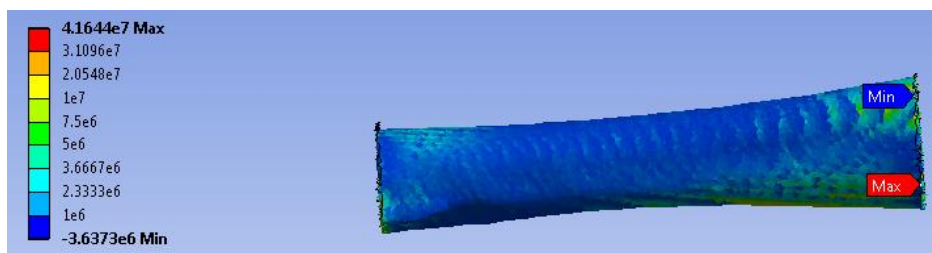

FIGURE 105. Distribution of the peak maximum principal stress (Pa) across the diaphysis of the femur for a bed fall onto carpet (ATD experiment: trial 8). Anterior view.

196
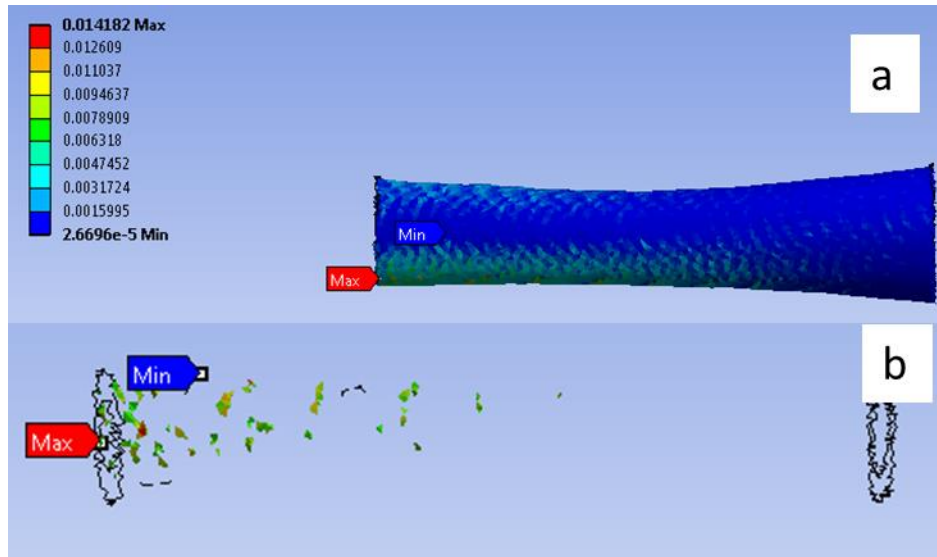
FIGURE 106. Distribution of the peak maximum principal strain across the diaphysis of the femur for a bed fall onto carpet (ATD experiment: trial 8). (a) shows the anterior view of the distribution without a threshold and (b) displays the medial view of the elements with strains greater than 0.73% (yield strain threshold).
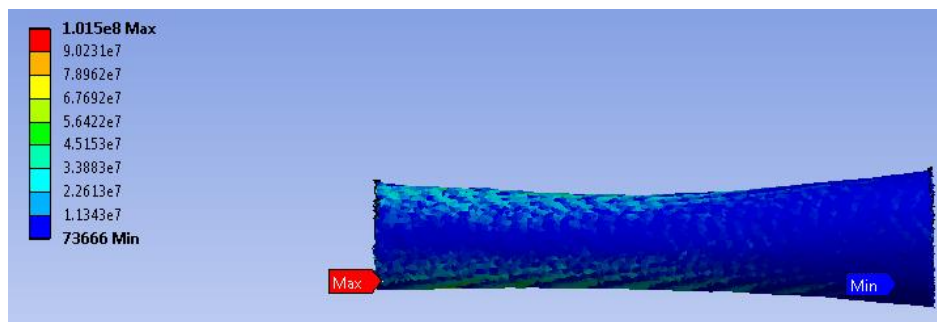
FIGURE 107. Distribution of the maximum von Mises stress (Pa) across the diaphysis of the femur for a bed fall onto carpet (ATD experiment: trial 8). Anterior view.
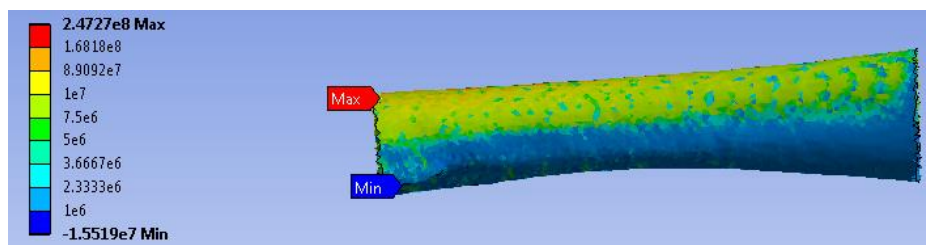
FIGURE 108. Distribution of the peak maximum principal stress (Pa) across the diaphysis of the femur for a bed fall onto carpet (ATD experiment trial 9). Posterior view.
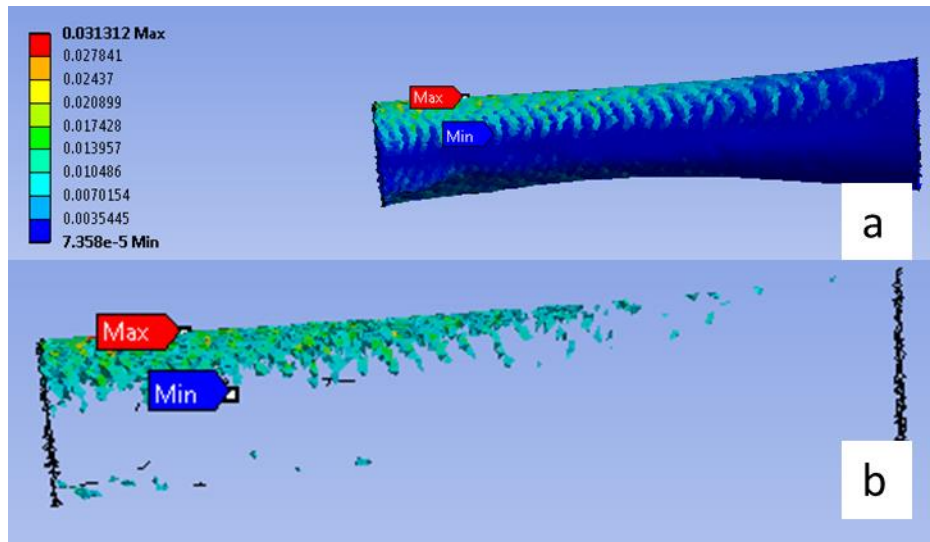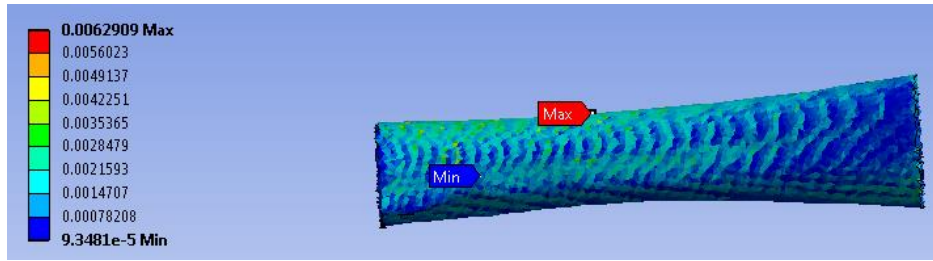
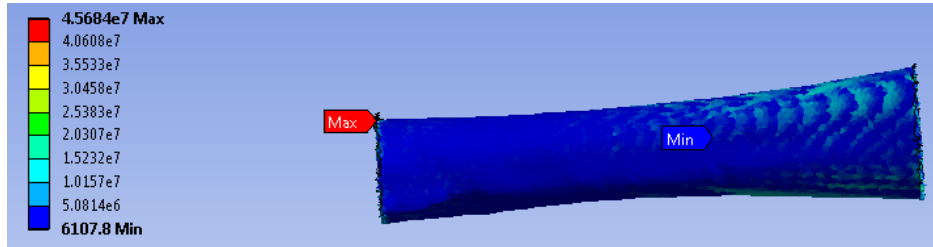FIGURE 109. Distribution of the peak maximum principal strain across the diaphysis of the femur for a bed fall onto carpet (ATD experiment trial 9). Posterior view. (a) shows the distribution without a threshold and (b) displays the elements with strains greater than 0.73% (yield strain threshold).
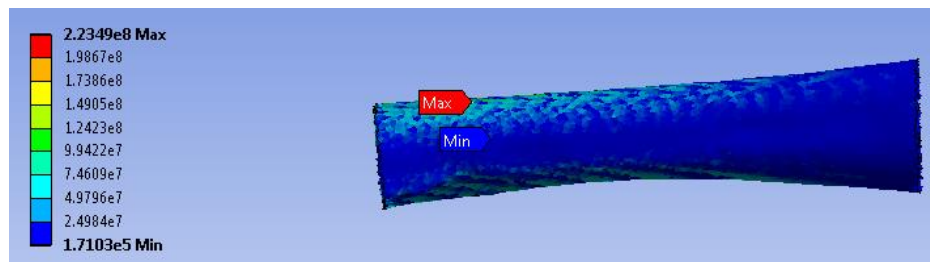
FIGURE 110. Distribution of the maximum von Mises stress (Pa) across the diaphysis of the femur for a bed fall onto carpet (ATD experiment trial 9). Posterior view.
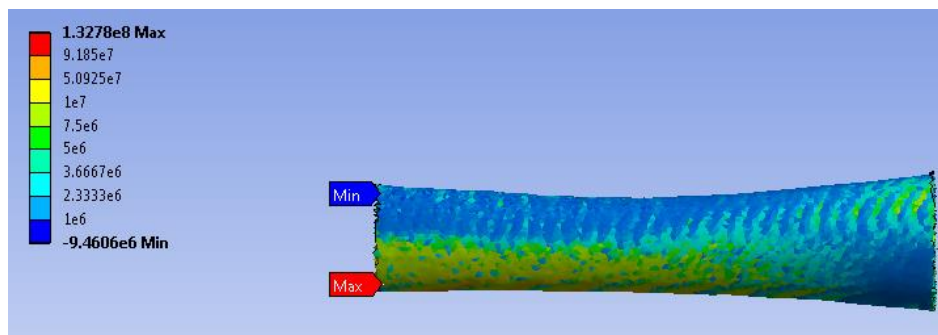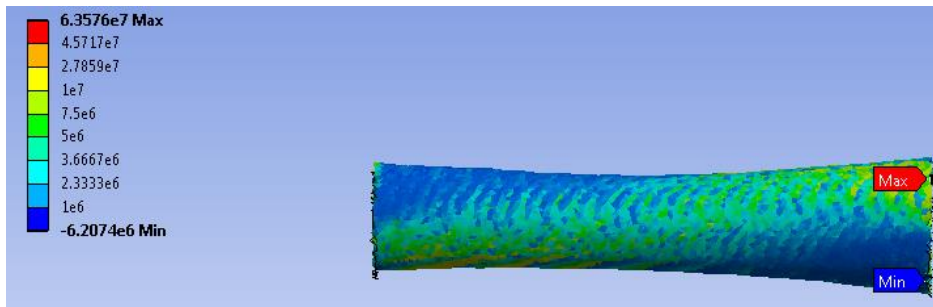

FIGURE 111. Distribution of the peak maximum principal stress (Pa) across the diaphysis of the femur for a bed fall onto carpet (ATD experiment trial 12). Anterior view.
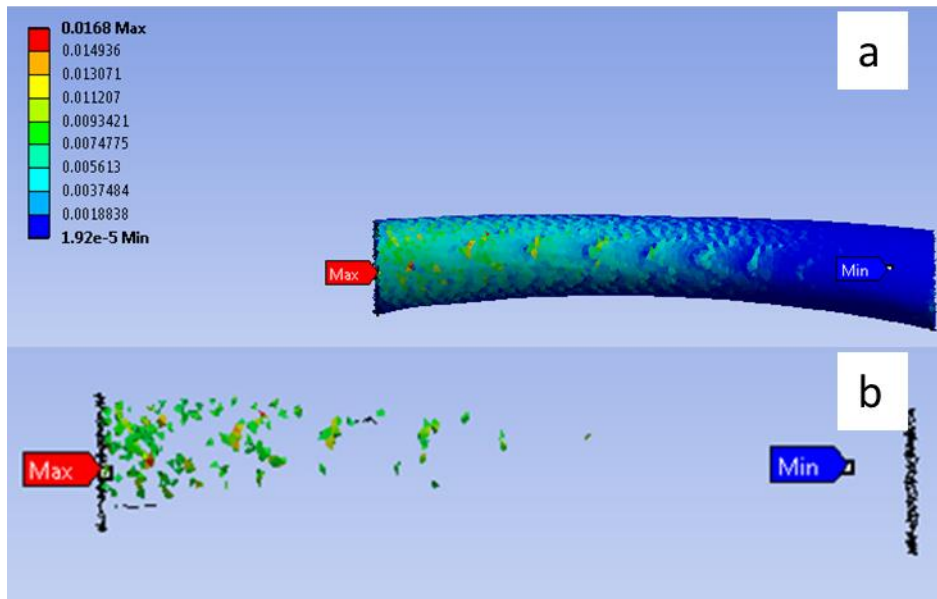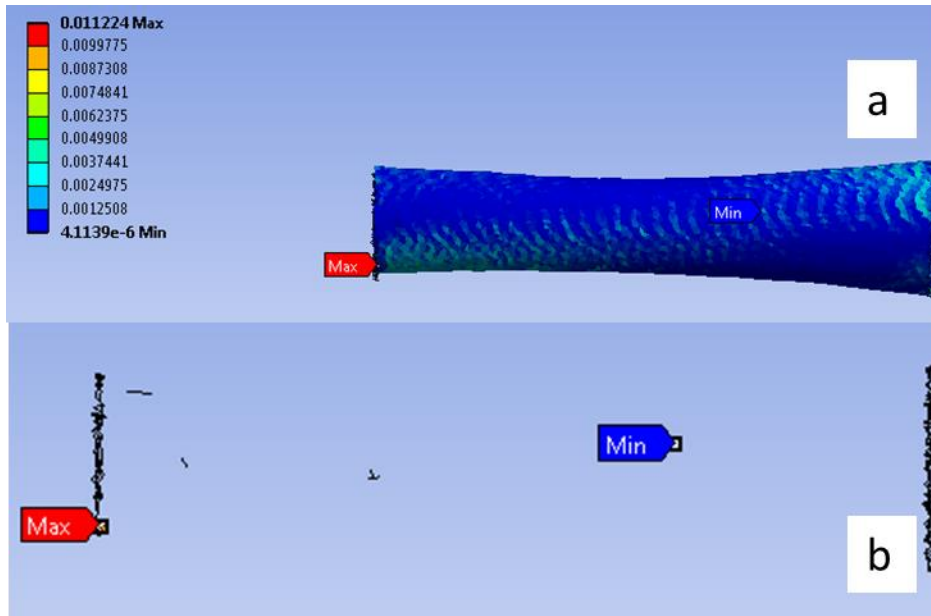
FIGURE 112. Distribution of the peak maximum principal strain across the diaphysis of the femur for a bed fall onto carpet (ATD experiment trial 12). Medial view. (a) shows the distribution without a threshold and (b) displays the elements with strains greater than 0.73% (yield strain threshold).
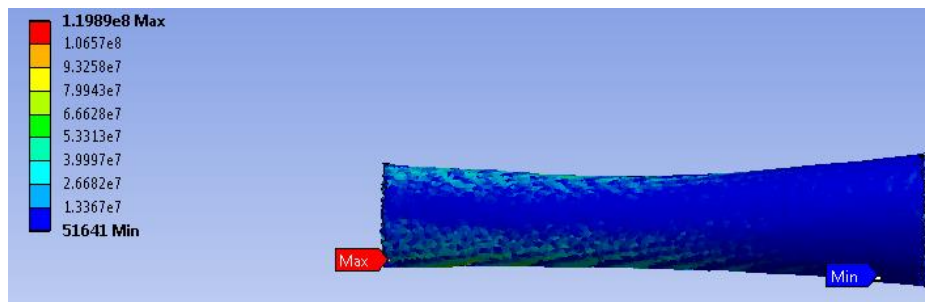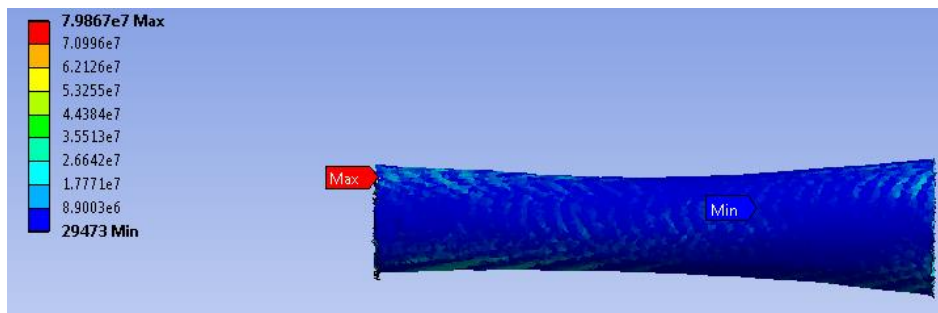

FIGURE 113. Distribution of the maximum von Mises stress (Pa) across the diaphysis of the femur for a bed fall onto carpet (ATD experiment trial 12). Anterior view.
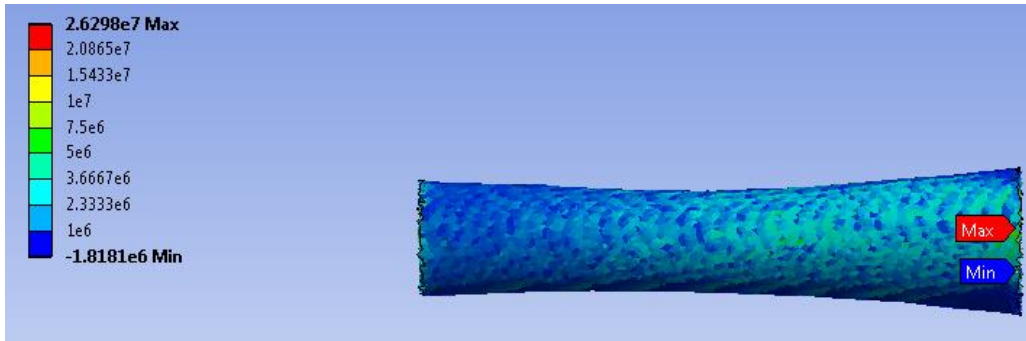
2. Falls onto Linoleum

FIGURE 114. Distribution of the peak maximum principal stress (Pa) across the diaphysis of the femur for a bed fall onto linoleum (ATD experiment trial 2). Posterior-medial view.
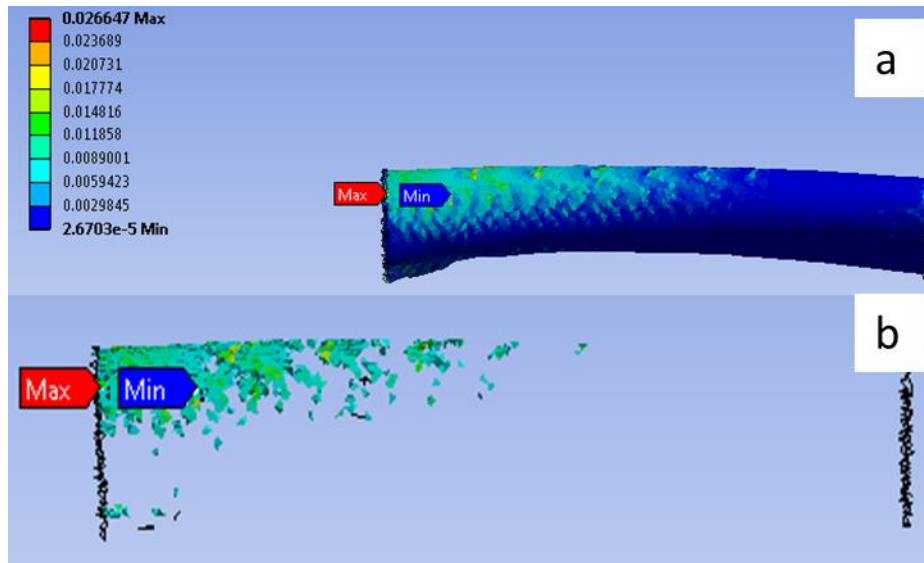
FIGURE 115. Distribution of the peak maximum principal strain across the diaphysis of the femur for a bed fall onto linoleum (ATD experiment trial 2). Posterior-medial view. (a) shows the distribution without a threshold and (b) displays the elements with strains greater than 0.73% (yield strain threshold).
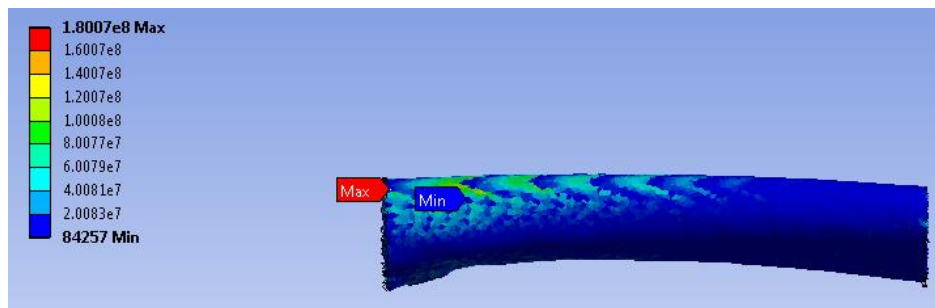
FIGURE 116. Distribution of the maximum von Mises stress (Pa) across the diaphysis of the femur for a bed fall onto linoleum (ATD experiment trial 2). Posterior-medial view.

FIGURE 117. Distribution of the peak maximum principal stress (Pa) across the diaphysis of the femur for a bed fall onto linoleum (ATD experiment trial 6). Posterior-medial view.

200
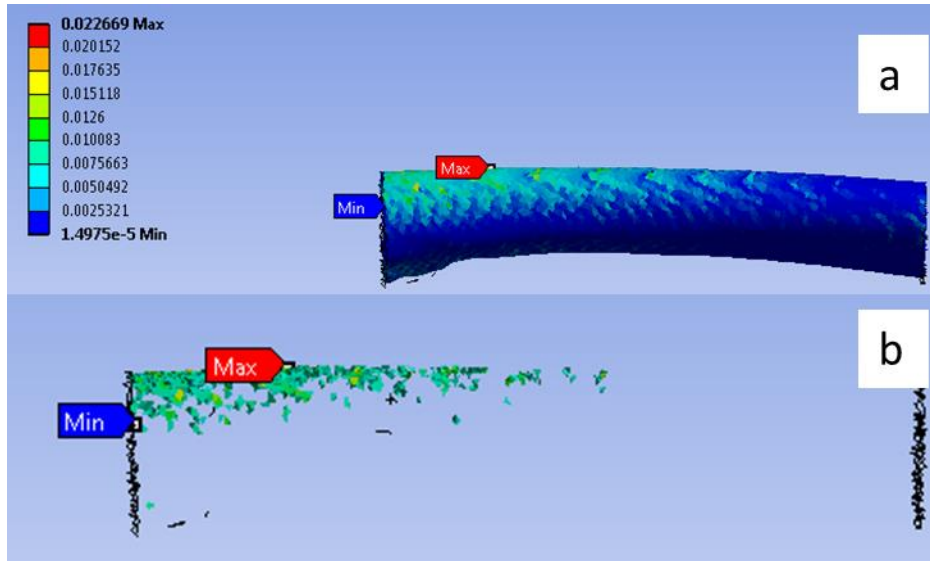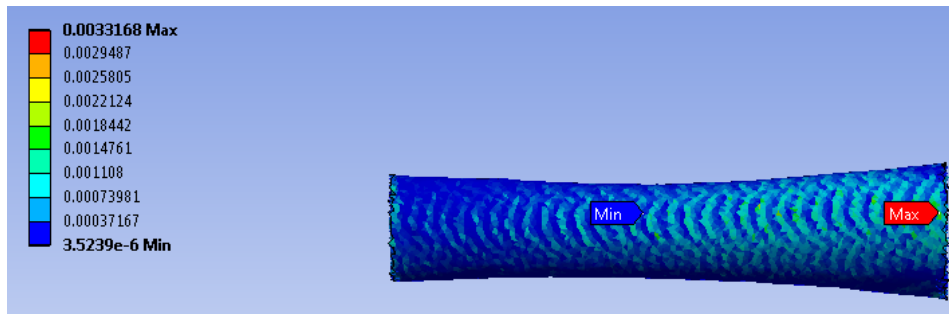
FIGURE 118. Distribution of the peak maximum principal strain across the diaphysis of the femur for a bed fall onto linoleum (ATD experiment trial 6). Posterior-medial view. (a) shows the distribution without a threshold and (b) displays the elements with strains greater than 0.73% (yield strain threshold).
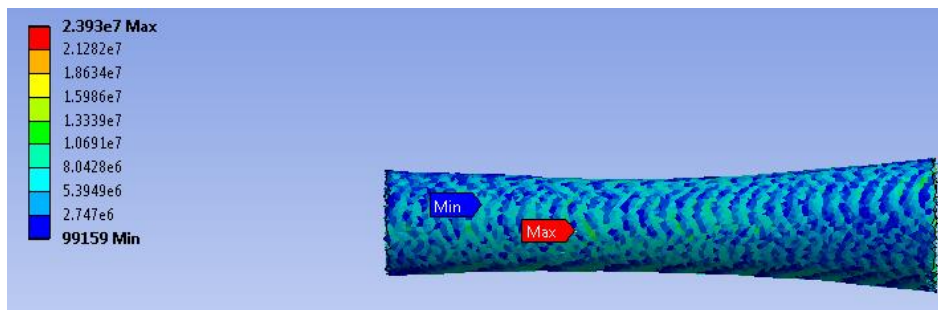

FIGURE 119. Distribution of the maximum von Mises stress (Pa) across the diaphysis of the femur for a bed fall onto linoleum (ATD experiment trial 6). Posterior-medial view.
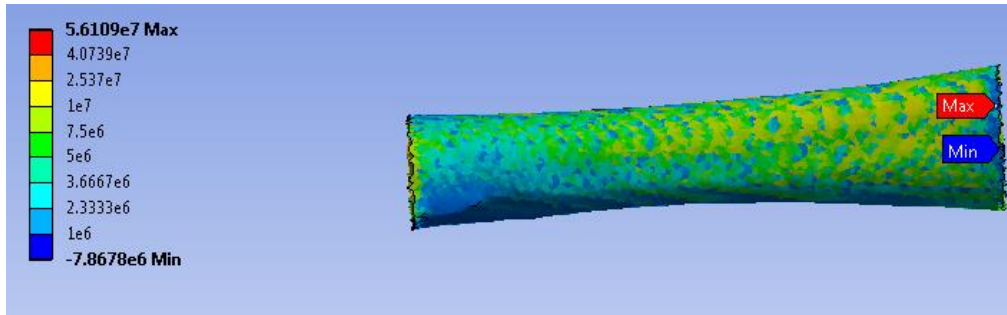

FIGURE 120. Distribution of the peak maximum principal stress (Pa) across the diaphysis of the femur for a bed fall onto linoleum (ATD experiment trial 9). Posterior view.
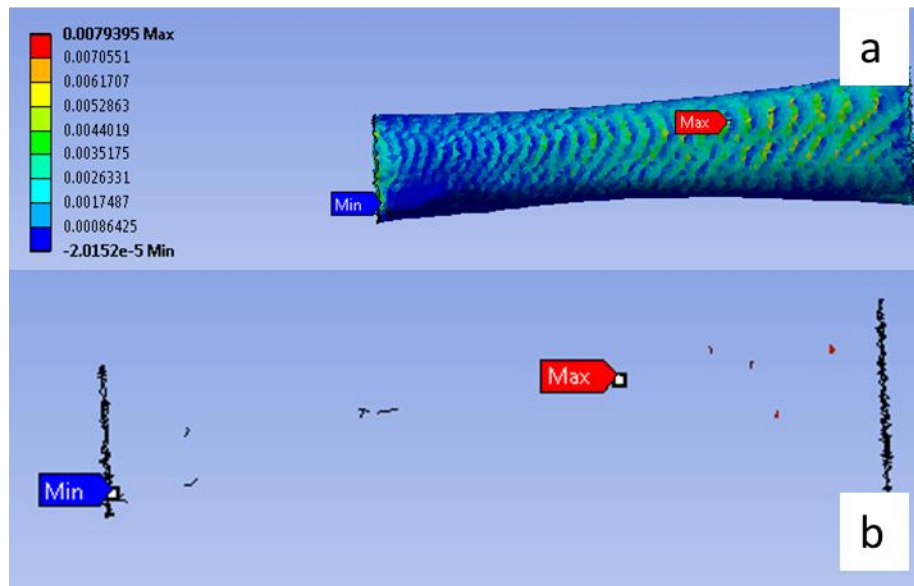
FIGURE 121. Distribution of the peak maximum principal strain across the diaphysis of the femur for a bed fall onto linoleum (ATD experiment trial 9). Posterior view. (a) shows the distribution without a threshold and (b) displays the elements with strains greater than 0.73% (yield strain threshold).
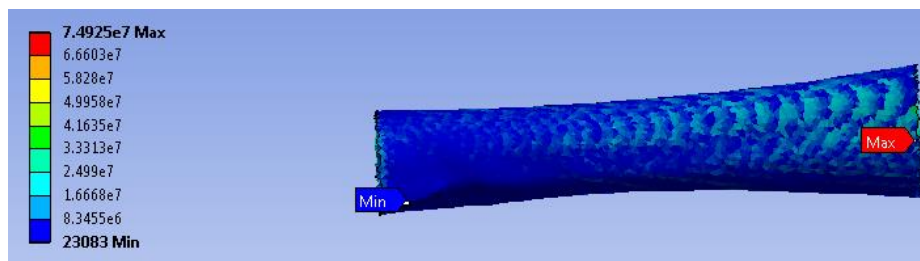

FIGURE 122. Distribution of the maximum von Mises stress (Pa) across the diaphysis of the femur for a bed fall onto linoleum (ATD experiment trial 9). Posterior view.
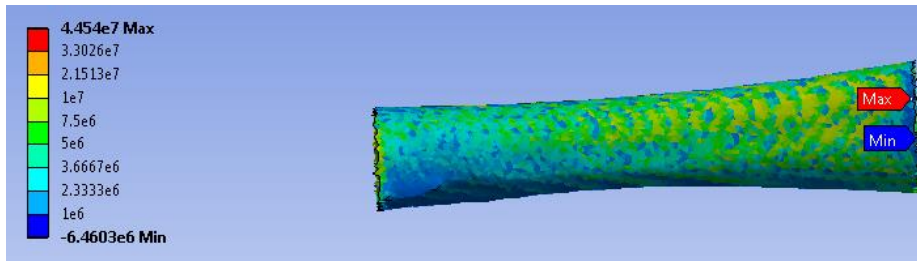

FIGURE 123. Distribution of the peak maximum principal stress (Pa) across the diaphysis of the femur for a bed fall onto linoleum (ATD experiment trial 10). Posterior-medial view.

FIGURE 124. Distribution of the peak maximum principal strain across the diaphysis of the femur for a bed fall onto linoleum (ATD experiment trial 10). Posterior-medial view. (a) shows the distribution without a threshold and (b) displays the elements with strains greater than 0.73% (yield strain threshold).

FIGURE 125. Distribution of the maximum von Mises stress (Pa) across the diaphysis of the femur for a bed fall onto linoleum (ATD experiment trial 10). Posterior-medial view.

FIGURE 126. Distribution of the peak maximum principal stress (Pa) across the diaphysis of the femur for a bed fall onto linoleum (ATD experiment trial 11). Posterior view.
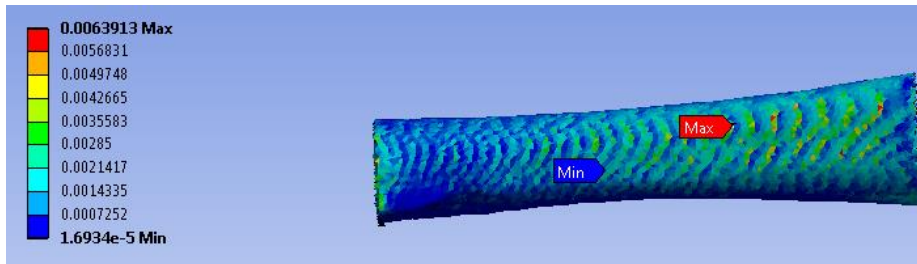
FIGURE 127. Distribution of the peak maximum principal strain across the diaphysis of the femur for a bed fall onto linoleum (ATD experiment trial 11). Posterior view.
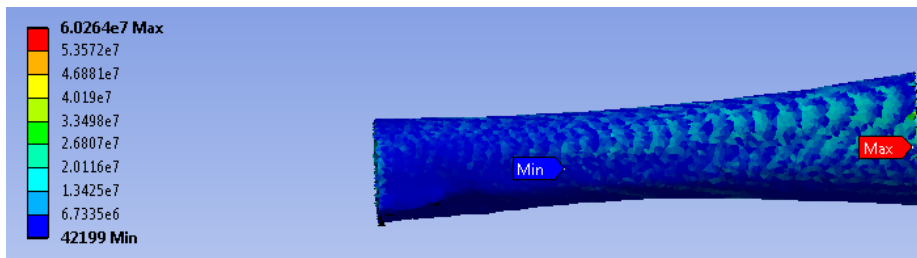

FIGURE 128. Distribution of the maximum von Mises stress (Pa) across the diaphysis of the femur for a bed fall onto linoleum (ATD experiment trial 11). Posterior view.
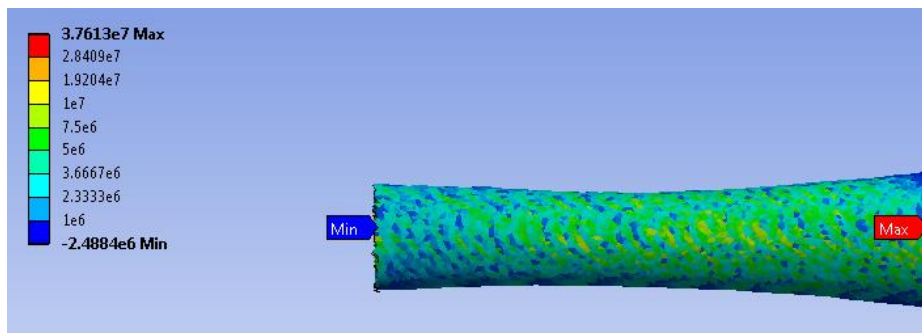

FIGURE 129. Distribution of the peak maximum principal stress (Pa) across the diaphysis of the femur for a bed fall onto linoleum (ATD experiment trial 12). Anterior view.

FIGURE 130. Distribution of the peak maximum principal strain across the diaphysis of the femur for a bed fall onto linoleum (ATD experiment trial 12). Anterior view. (a) shows the distribution without a threshold and (b) displays the elements with strains greater than 0.73% (yield strain threshold).

FIGURE 131. Distribution of the maximum von Mises stress (Pa) across the diaphysis of the femur for a bed fall onto linoleum (ATD experiment trial 12). Anterior view.

B. Feet-First Falls

1. 69cm Falls onto Carpet

FIGURE 132. Distribution of the peak maximum principal stress (Pa) across the diaphysis of the femur for a 69cm feet-first fall onto carpet (ATD experiment trial 2). Anterior view.
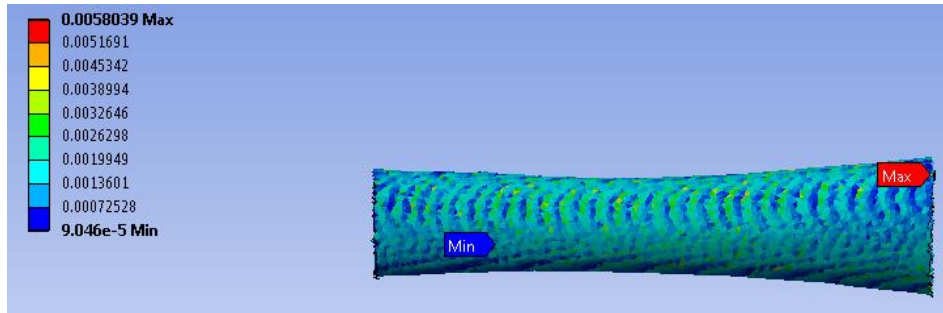

FIGURE 133. Distribution of the peak maximum principal strain across the diaphysis of the femur for a 69cm feet-first fall onto carpet (ATD experiment trial 2). Anterior view.
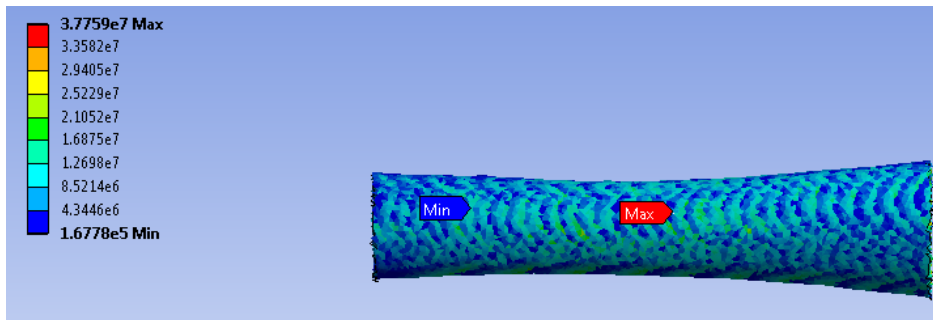

FIGURE 134. Distribution of the maximum von Mises stress (Pa) across the diaphysis of the femur for a 69cm feet-first fall onto carpet (ATD experiment trial 2). Anterior view.
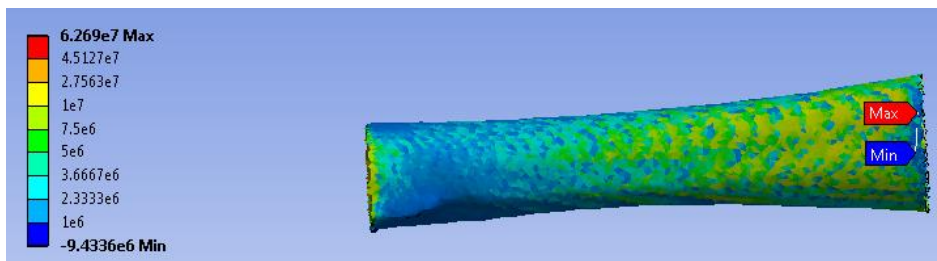
FIGURE 135. Distribution of the peak maximum principal stress (Pa) across the diaphysis of the femur for a 69cm feet-first fall onto carpet (ATD experiment trial 3). Posterior view.
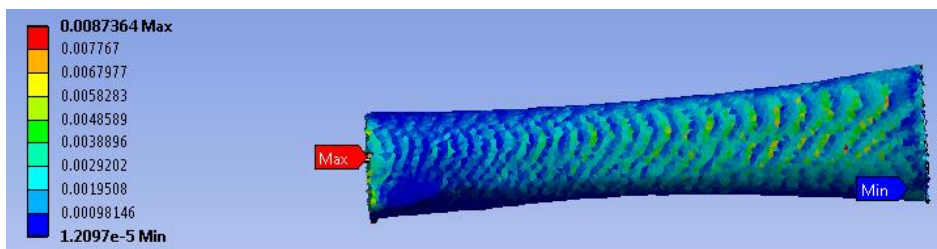

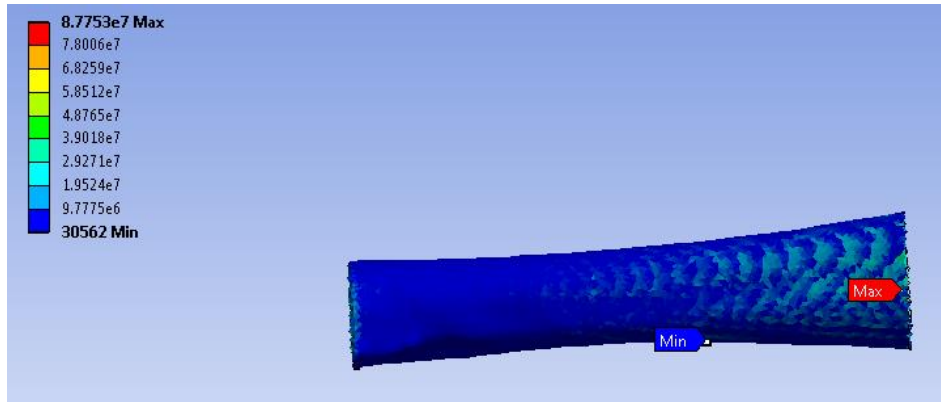FIGURE 136. Distribution of the peak maximum principal strain across the diaphysis of the femur for a 69cm feet-first fall onto carpet (ATD experiment trial 3). Posterior view. (a) shows the distribution without a threshold and (b) displays the elements with strains greater than 0.73% (yield strain threshold).

FIGURE 137. Distribution of the maximum von Mises stress (Pa) across the diaphysis of the femur for a 69cm feet-first fall onto carpet (ATD experiment trial 3). Posterior view.
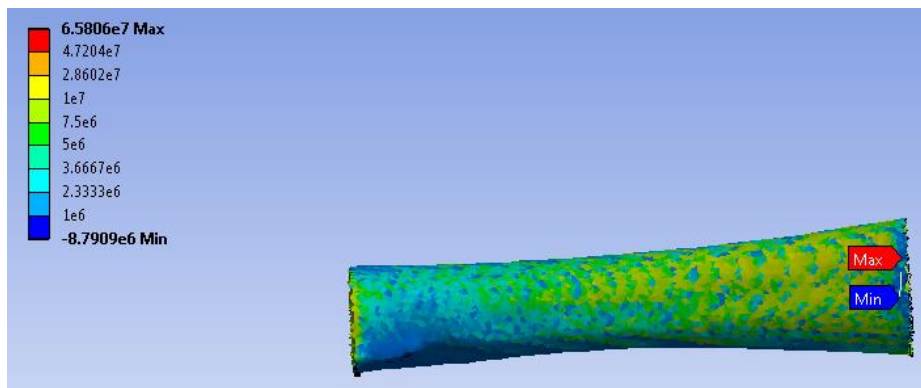
207

FIGURE 138. Distribution of the peak maximum principal stress (Pa) across the diaphysis of the femur for a 69cm feet-first fall onto carpet (ATD experiment trial 5). Posterior view.

FIGURE 139. Distribution of the peak maximum principal strain across the diaphysis of the femur for a 69cm feet-first fall onto carpet (ATD experiment trial 5). Posterior view.

FIGURE 140. Distribution of the maximum von Mises stress (Pa) across the diaphysis of the femur for a 69cm feet-first fall onto carpet (ATD experiment trial 5). Posterior view.

2. 69cm Falls onto Linoleum

FIGURE 141. Distribution of the peak maximum principal stress (Pa) across the diaphysis of the femur for a 69cm feet-first fall onto linoleum (ATD experiment trial 3). Anterior view.
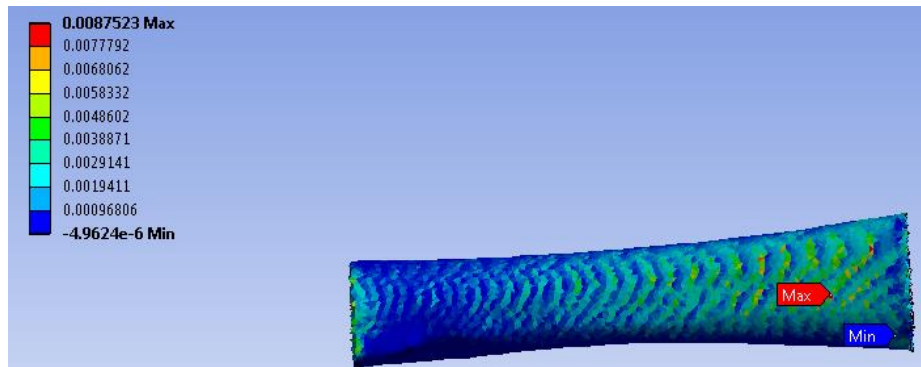
FIGURE 142. Distribution of the peak maximum principal strain across the diaphysis of the femur for a 69cm feet-first fall onto linoleum (ATD experiment trial 3). Anterior view.
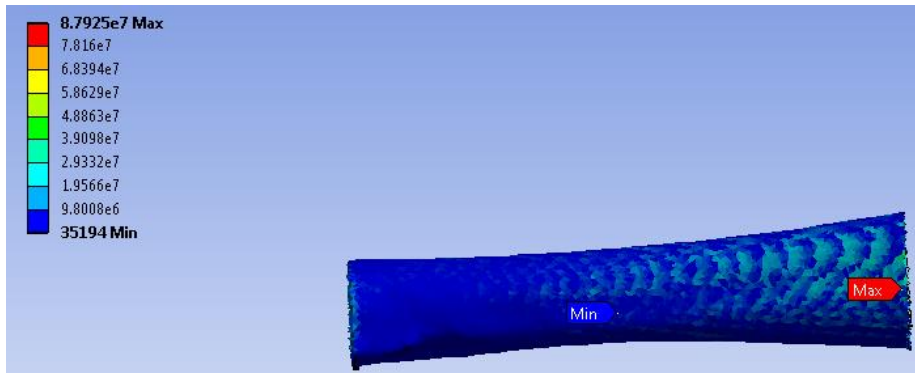

FIGURE 143. Distribution of the maximum von Mises stress (Pa) across the diaphysis of the femur for a 69cm feet-first fall onto linoleum (ATD experiment trial 3). Anterior view.
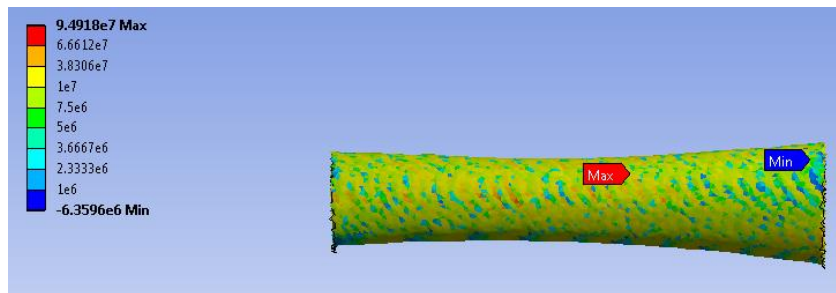

FIGURE 144. Distribution of the peak maximum principal stress (Pa) across the diaphysis of the femur for a 69cm feet-first fall onto linoleum (ATD experiment trial 8). Posterior view.
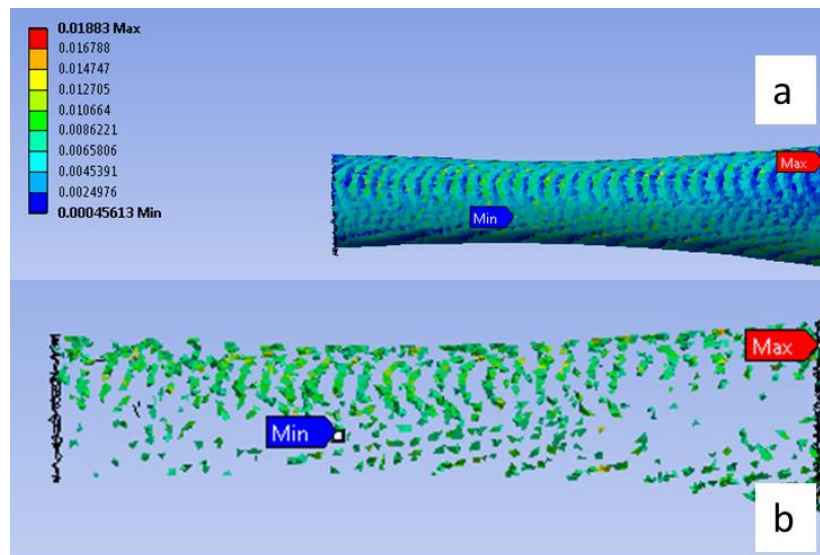

FIGURE 145. Distribution of the peak maximum principal strain across the diaphysis of the femur for a 69cm feet-first fall onto linoleum (ATD experiment trial 8). Posterior view.
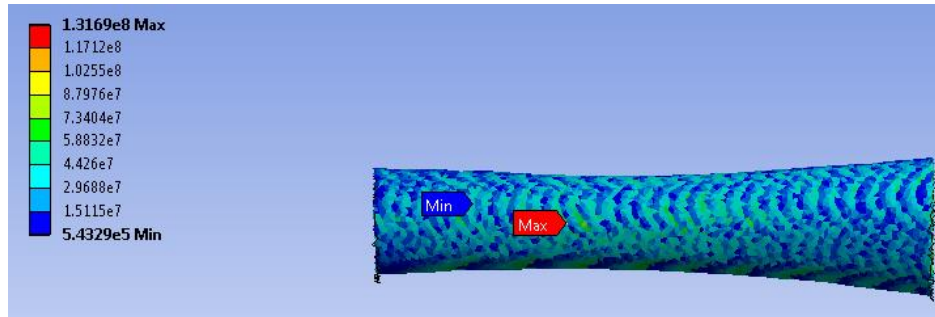
209

FIGURE 146. Distribution of the maximum von Mises stress (Pa) across the diaphysis of the femur for a 69cm feet-first fall onto linoleum (ATD experiment trial 8). Posterior view.

FIGURE 147. Distribution of the peak maximum principal stress (Pa) across the diaphysis of the femur for a 69cm feet-first fall onto linoleum (ATD experiment trial 9). Posterior view.

FIGURE 148. Distribution of the peak maximum principal strain across the diaphysis of the femur for a 69cm feet-first fall onto linoleum (ATD experiment trial 9). Posterior view.

FIGURE 149. Distribution of the maximum von Mises stress (Pa) across the diaphysis of the femur for a 69cm feet-first fall onto linoleum (ATD experiment trial 9). Posterior view.
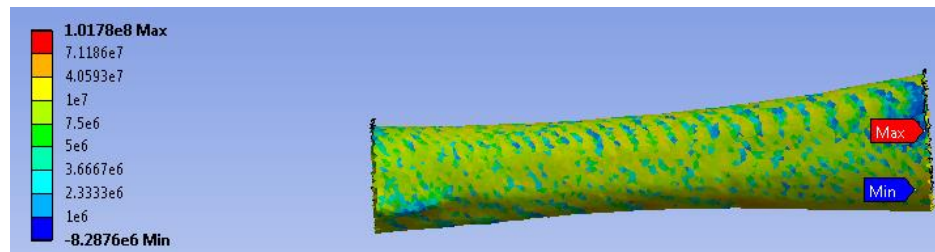
3. 119cm Falls onto Carpet

FIGURE 150. Distribution of the peak maximum principal stress (Pa) across the diaphysis of the femur for a 119cm feet-first fall onto carpet (ATD experiment trial 3). Anterior view.
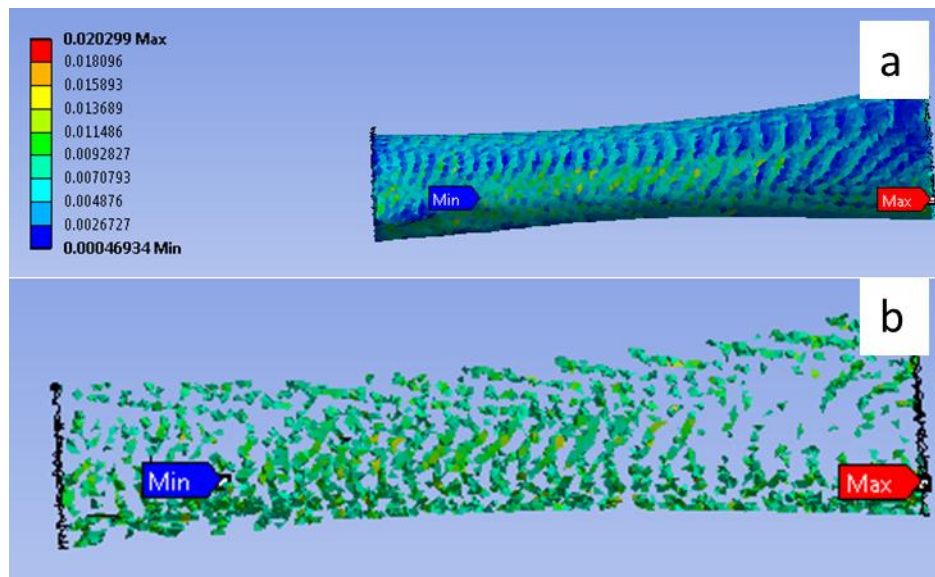

FIGURE 151. Distribution of the peak maximum principal strain across the diaphysis of the femur for a 119cm feet-first fall onto carpet (ATD experiment trial 3). Anterior view. (a) shows the distribution without a threshold and (b) displays the elements with strains greater than 0.73% (yield strain threshold).
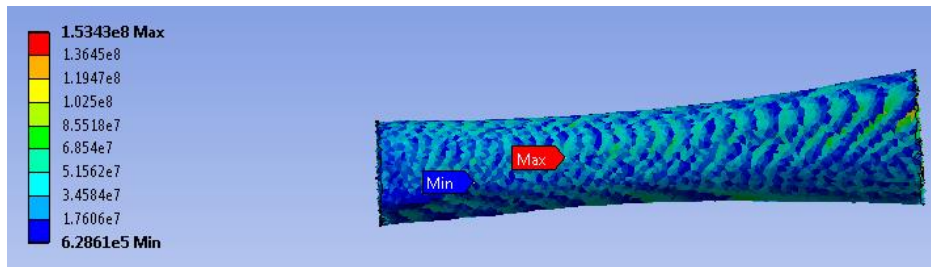
FIGURE 152. Distribution of the maximum von Mises stress (Pa) across the diaphysis of the femur for a 119cm feet-first fall onto carpet (ATD experiment trial 3). Anterior view.
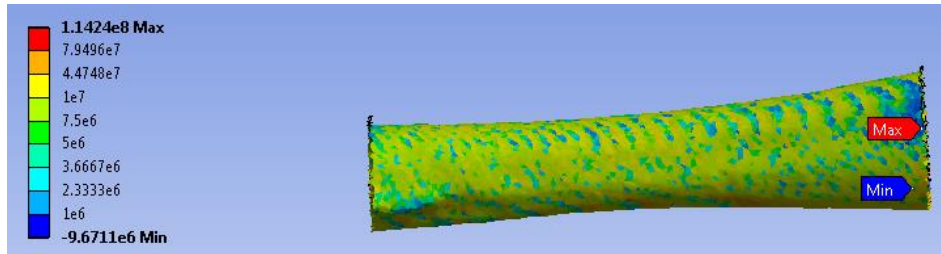

FIGURE 153. Distribution of the peak maximum principal stress (Pa) across the diaphysis of the femur for a 119cm feet-first fall onto carpet (ATD experiment trial 7). Posterior view.

FIGURE 154. Distribution of the peak maximum principal strain across the diaphysis of the femur for a 119cm feet-first fall onto carpet (ATD experiment trial 7). Posterior view. (a) shows the distribution without a threshold and (b) displays the elements with strains greater than 0.73% (yield strain threshold).

212

FIGURE 155. Distribution of the maximum von Mises stress (Pa) across the diaphysis of the femur for a 119cm feet-first fall onto carpet (ATD experiment trial 7). Posterior view.

FIGURE 156. Distribution of the peak maximum principal stress (Pa) across the diaphysis of the femur for a 119cm feet-first fall onto carpet (ATD experiment trial 9). Posterior view.
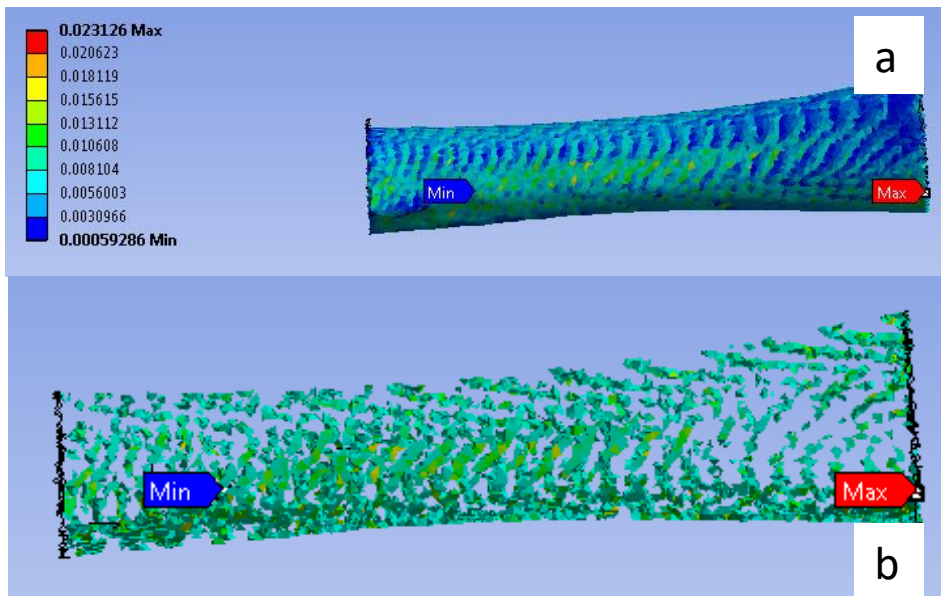

FIGURE 157. Distribution of the peak maximum principal strain across the diaphysis of the femur for a 119cm feet-first fall onto carpet (ATD experiment trial 9). Posterior view. (a) shows the distribution without a threshold and (b) displays the elements with strains greater than 0.73% (yield strain threshold).
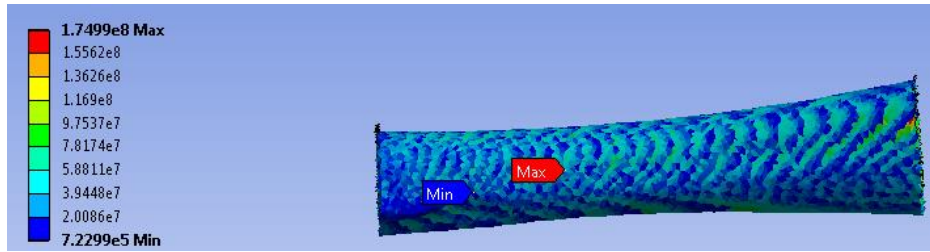
FIGURE 158. Distribution of the maximum von Mises stress (Pa) across the diaphysis of the femur for a 119cm feet-first fall onto carpet (ATD experiment trial 9). Posterior view.

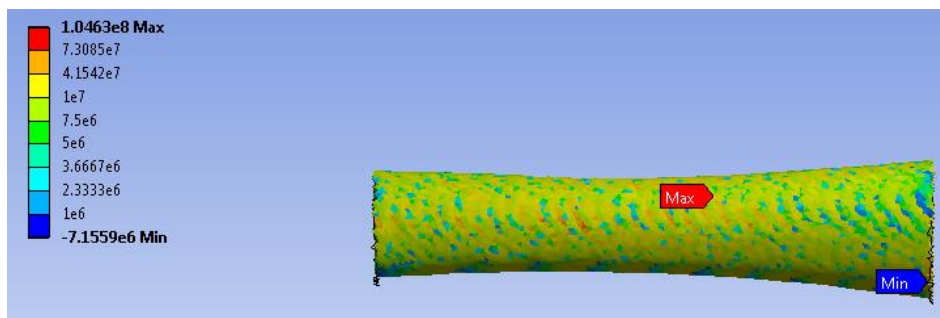## 4. 119cm Falls onto Linoleum

FIGURE 159. Distribution of the peak maximum principal stress (Pa) across the diaphysis of the femur for a 119cm feet-first fall onto linoleum (ATD experiment trial 3). Anterior view.
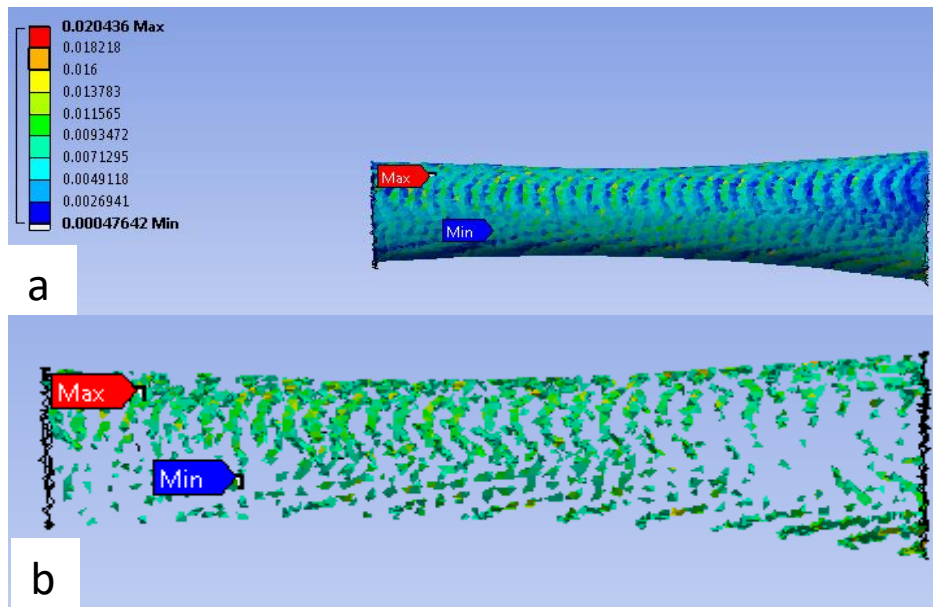

FIGURE 160. Distribution of the peak maximum principal strain across the diaphysis of the femur for a 119cm feet-first fall onto linoleum (ATD experiment trial 3). Anterior view. (a) shows the distribution without a threshold and (b) displays the elements with strains greater than 0.73% (yield strain threshold).
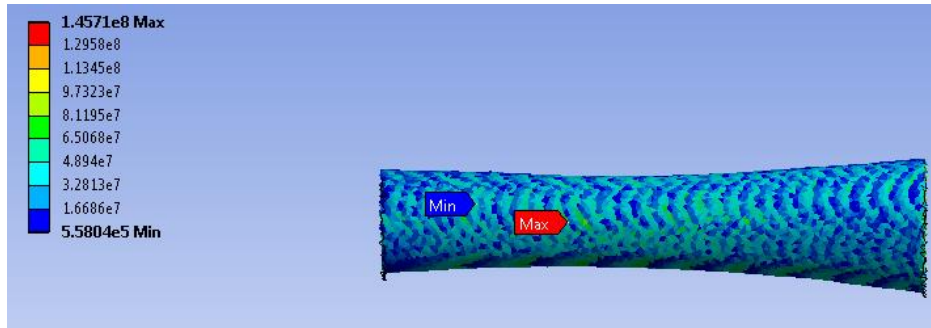
FIGURE 161. Distribution of the maximum von Mises stress (Pa) across the diaphysis of the femur for a 119cm feet-first fall onto linoleum (ATD experiment trial 3). Anterior view.
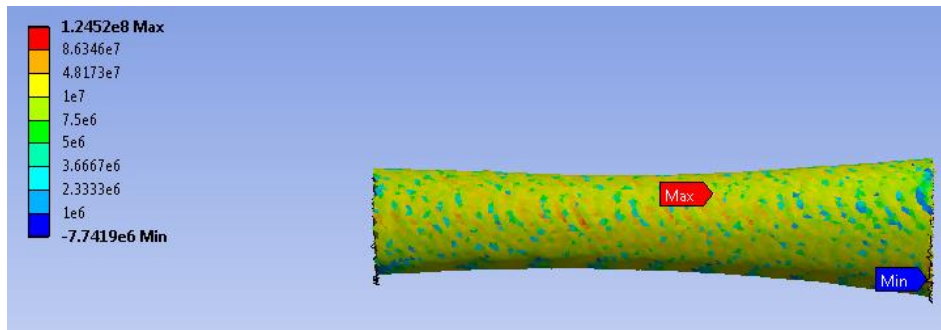

FIGURE 162. Distribution of the peak maximum principal stress (Pa) across the diaphysis of the femur for a 119cm feet-first fall onto linoleum (ATD experiment trial 4). Anterior view.
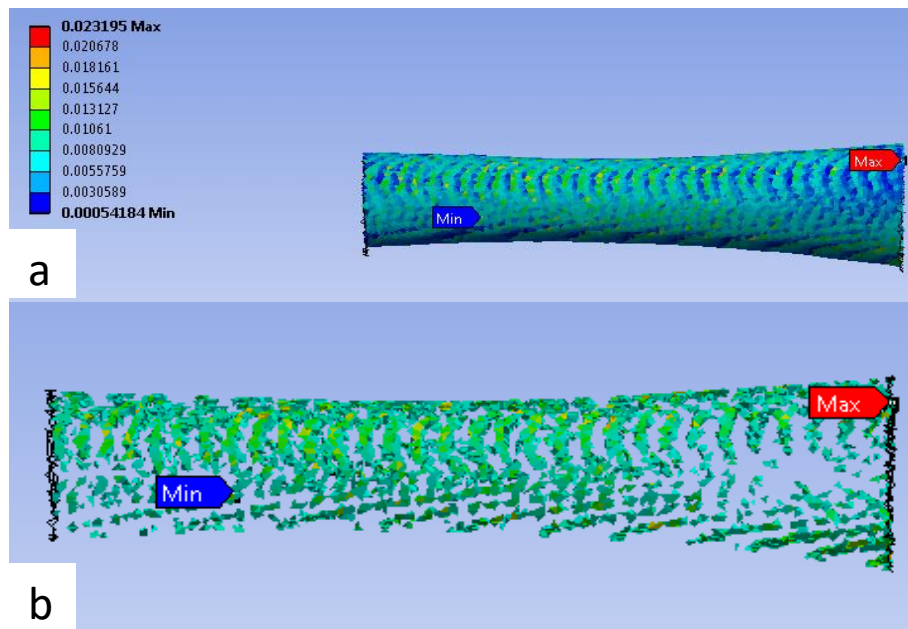

FIGURE 163. Distribution of the peak maximum principal strain across the diaphysis of the femur for a 119cm feet-first fall onto linoleum (ATD experiment trial 4). Anterior view. (a) shows the distribution without a threshold and (b) displays the elements with strains greater than 0.73% (yield strain threshold).

215

FIGURE 164. Distribution of the maximum von Mises stress (Pa) across the diaphysis of the femur for a 119cm feet-first fall onto linoleum (ATD experiment trial 4). Anterior view.

FIGURE 165. Distribution of the peak maximum principal stress (Pa) across the diaphysis of the femur for a 119cm feet-first fall onto linoleum (ATD experiment trial 9). Posterior view.

FIGURE 166. Distribution of the peak maximum principal strain across the diaphysis of the femur for a 119cm feet-first fall onto linoleum (ATD experiment trial 9). Posterior view. (a) shows the distribution without a threshold and (b) displays the elements with strains greater than 0.73% (yield strain threshold).
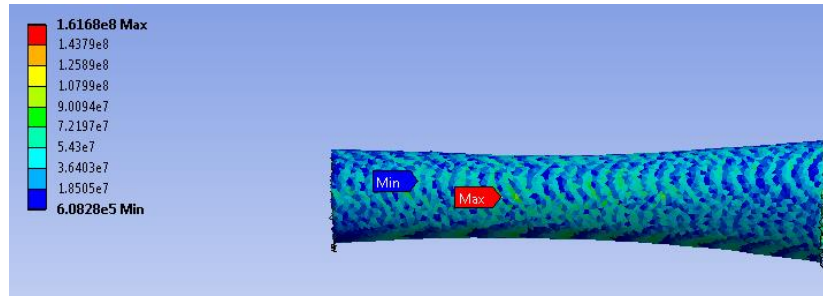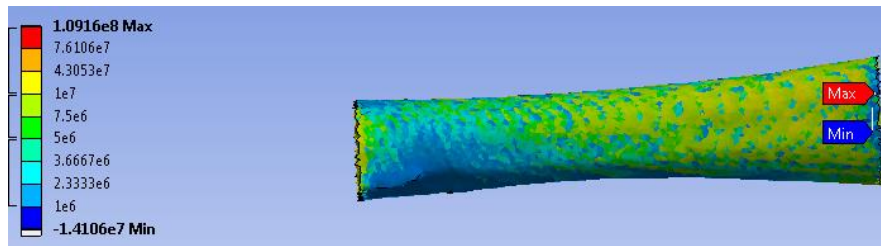

FIGURE 167. Distribution of the maximum von Mises stress (Pa) across the diaphysis of the femur for a 119cm feet-first fall onto linoleum (ATD experiment trial 9). Posterior view.
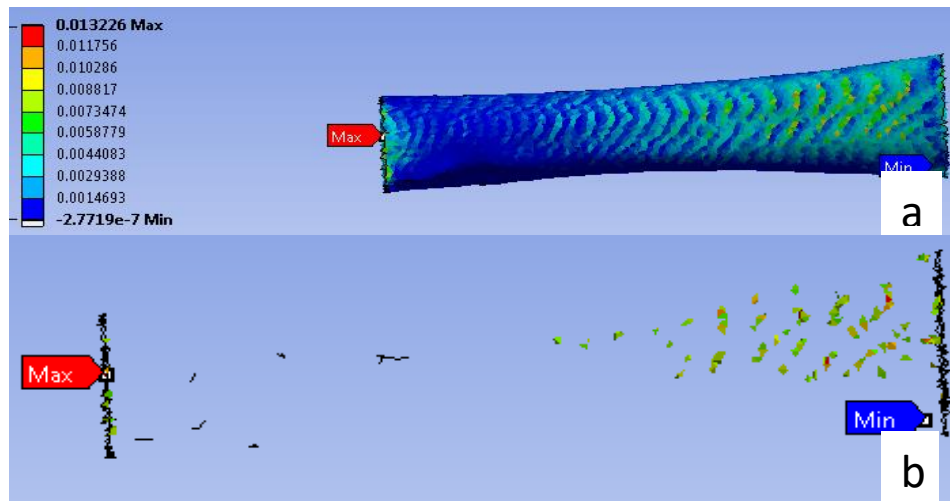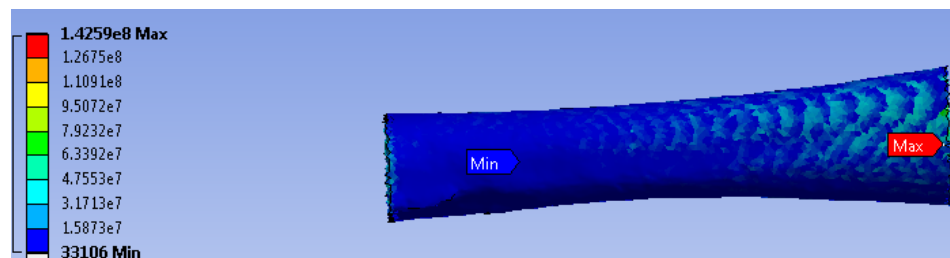
216

APPENDIX V. EVALUATION OF BONE SURROGATES FOR USE AS A PEDIATRIC

BONE SURROGATE

The purpose of this section is to evaluate how all the specimens compare to pediatric

bone and whether it could be a suitable surrogate to represent pediatric bone in future work. To

address the purpose a comparison of the other specimens (reduced metaphyses and solid) were

compared to the outcomes of the hollow specimens and all were compared to pediatric bone data

in the literature. The methodology outlined in the methods for hollow specimens (Methods

section C.2. Mechanical Testing of Bone Models) were used to evaluate the additional specimens

considered. Solid specimens refer to those where the entirety of the femur was sintered or had no

medullary cavity. Reduced metaphyses specimens refer to those with a reduced infill (or reduced

sintered portion) at the metaphyseal region of the bone in addition to having a medullary cavity

like the hollow specimens. The reduced infill in the reduced metaphyses specimens was done to

correspond to the reduced density of the metaphyseal region compared to the hollow specimens.

A. Results of Mechanical Testing of Bone Models

1. Three-point Bending Testing

In addition to the hollow specimens evaluated, three solid specimens were also evaluated using three-point bending where one was tested with a strain rosette. A representation of the fracture pattern due to this loading can be viewed in Figure 168.

FIGURE 168. Sample fracture patterns of a hollow (labeled H7) and solid specimen (labeled S6) as a result of three-point bending loads. Posterior view (left) and transverse plane view (right).

The force-displacement curve for the solid specimens tested can be found in Figure 169. The fracture load and stiffness for each solid specimen can be found in Table XXX. The mean fracture load was 689.5N ± 28.41N. The mean stiffness was 188.2N/mm ± 11.99N/mm. The mean AUC was 1397Nmm ± 87Nmm. The mean flexural modulus was 2811 MPa ± 196MPa.
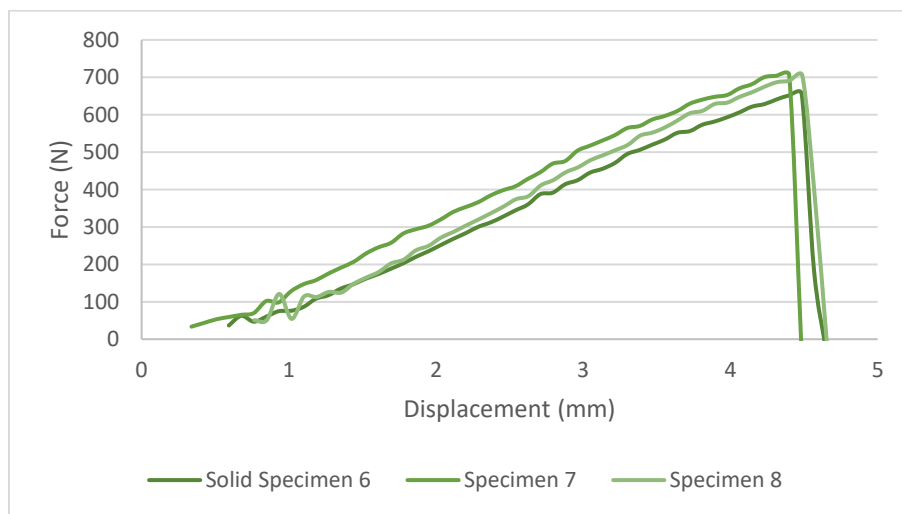

FIGURE 169. Force-displacement curves of the solid specimens tested under bending loading conditions. Note: The curves have not been adjusted to accommodate the toe-region.

218

TABLE XXX.

OUTCOMES FOR SOLID SPECIMENS IN THREE-POINT BENDINGS

Solid Specimen ID	Fracture Load (N)	Stiffness (N/mm)	Area Under the Curve (Nmm)	Modulus (MPa)
6	657	177	1323	2639
7	706	187	1493	2770
8	706	201	1376	3024
Mean	690	188	1397	2811
Standard Deviation	28	12	87	196

The minimum principal strain time history for solid specimen 7, which was tested with a strain rosette is displayed in Figure 170. The peak minimum principal strain of (-0.95%) is greater than that observed in the evaluation of the hollow specimens (-0.76%).
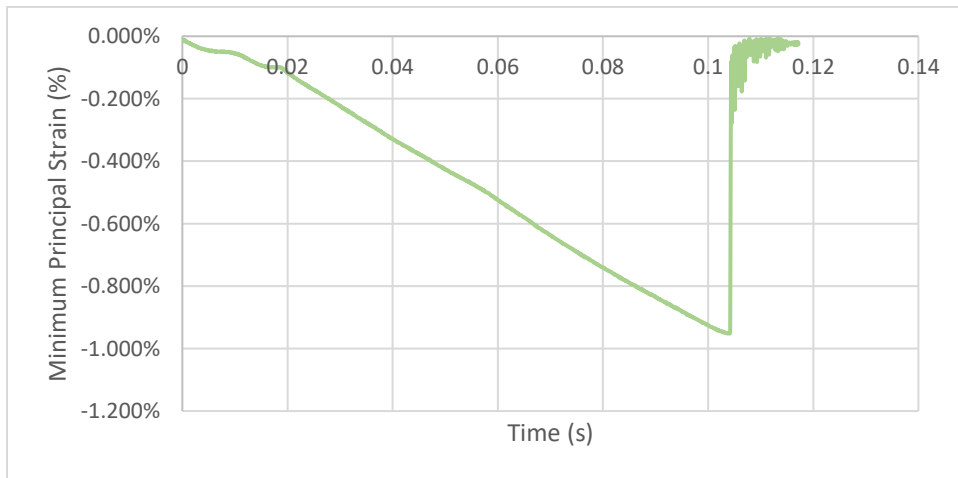

FIGURE 170. Minimum principal strain time history for three-point bending loading condition of solid specimen 7.

a. Comparison to FE Prediction and Hollow Specimens. The FE model predicted outcomes (fracture load, stiffness, and AUC) were generally higher than the mean of the hollow specimens but were more similar to that of the solid specimens. These outcomes were typically higher for both the FE model predicted outcomes and those for the solid specimens compared to that of the hollow specimens. A comparison of the FE model predicted values to the different types of specimens tested using three-point bending can be seen in Figure 171.
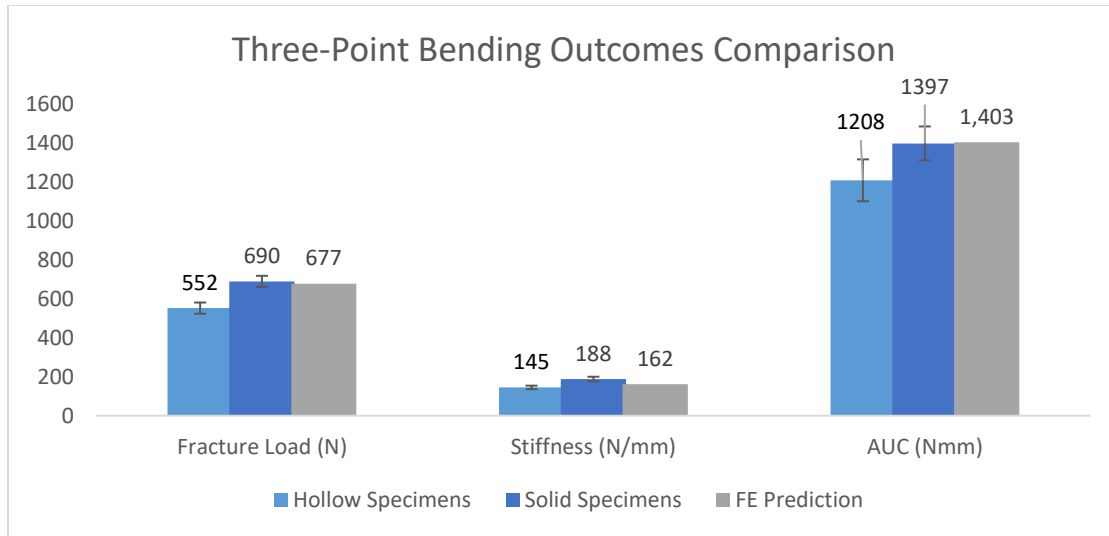
FIGURE 171. Comparison of the outcomes of three-point bending for the hollow and solid specimens along with the FE predicted outcomes. The outcomes considered are fracture load, stiffness, and area under the curve (AUC). Experimental values are mean ± standard deviation.

2. Compression Testing

The compression tests resulted in a range of fracture patterns. The occurrence of these patterns in each specimen type can be seen in Figure 46 and a representative view of each fracture type can be found in Figure 47. Grouping of fracture types was done with the location of positive or distal wedges produced and the degree to which the plane of the fracture deviated from being parallel to the transverse plane. A total of 3 reduced metaphyses specimens, 5 hollow specimens whose results can be found in the main body of the paper, and 3 solid specimens were tested for the compression loading condition.

The force-displacement curve for the reduced metaphyses specimens tested can be found in Figure 172. The fracture load and stiffness for each specimen can be found in Table XXXI. Specimen 3 was plastically loaded during the setup and was excluded from analysis. The mean fracture load was 3025 N ± 44 N. The mean stiffness was 1004.7N/mm ± 77.3N/mm. The mean AUC was 6952 Nmm ± 484 Nmm.
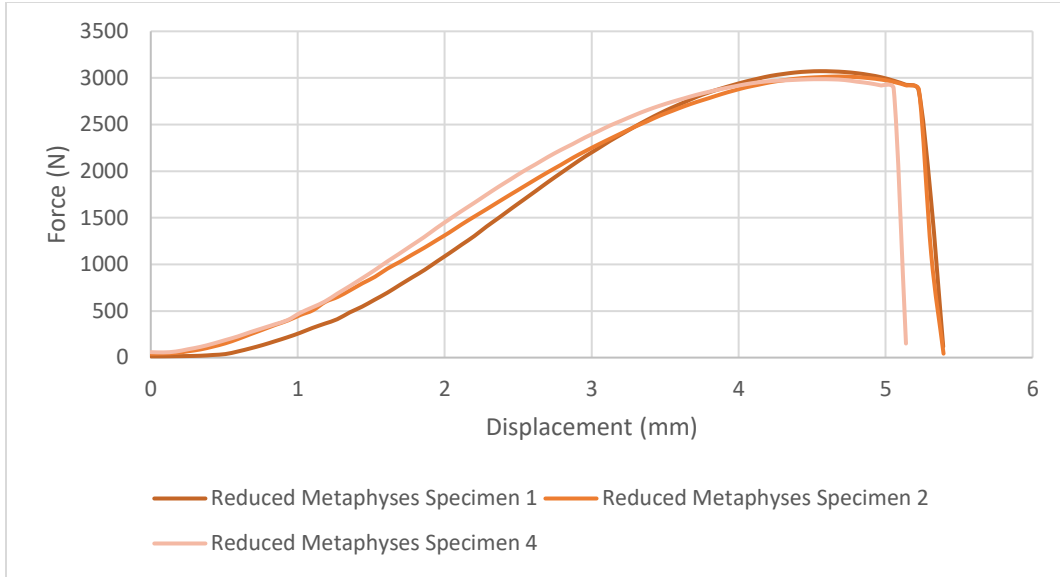
FIGURE 172. Force-displacement curve for the reduced metaphyses specimens tested under the compressive loading conditions. Note: The curves have not been adjusted to accommodate the toe-region.

TABLE XXXI.

OUTCOMES FOR REDUCED METAPHYSES SPECIMENS IN COMPRESSION

Specimen ID	Fracture Load (N)	Stiffness (N/mm)	Area Under the Curve (Nmm)
1	3073	1076.3	6398.7
2	3015	922.8	7295.4
4	2986	1015.1	7160.5
Mean	3025	1004.7	6951.5
Standard Deviation	44	77.3	483.5

The force-displacement curve for the solid specimens tested can be found in Figure 173. The fracture load and stiffness for each specimen can be found in Table XXXII. The mean fracture load was 3815N ± 151N. The mean stiffness was 1388.7N/mm ± 37.7N/mm. The mean AUC was 6459 Nmm ± 345 Nmm.
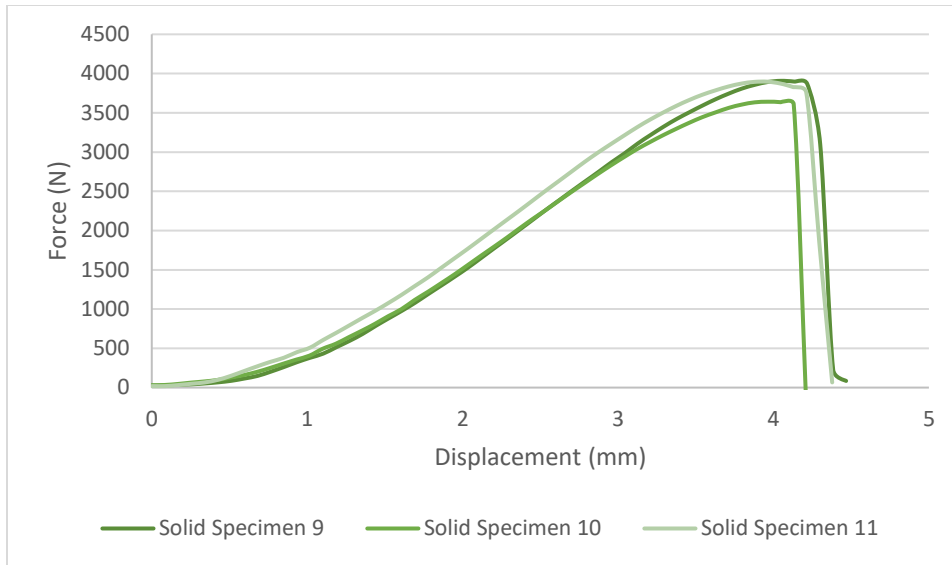
FIGURE 173. Force-displacement curve of the solid specimens tested under the compressive loading conditions. Note: The curves have not been adjusted to accommodate the toe-region.

TABLE XXXII.

OUTCOMES FOR SOLID SPECIMENS IN COMPRESSION

Solid Specimen ID	Fracture Load (N)	Stiffness (N/mm)	Area Under the Curve (Nmm)
9	3908	1403.1	6524.5
10	3642	1345.9	6086.8
11	3897	1417.1	6766.6
Mean	3815	1388.7	6459.3
Standard Deviation	151	37.7	344.5

The strain gauge time histories of the resulting minimum principal strain can be found in Figure 174. It is important to note that the strain gauge used was only capable of recording a range of ±3% strain. Hollow specimen 17 had reached this maximum limit of the strain gauge. The mean peak minimum principal strain was -1.42% ± 1.23% for the hollow specimens. The reduced metaphyses specimen had a peak strain of -2.31%. The solid specimen had a peak strain of -1.74% which was lower than that of the reduced metaphyseal specimens and within one standard deviation of the mean of the hollow specimens. Due to the different fracture patterns

222

(Figure 47) observed in testing of the hollow specimens, differing time histories of the minimum principal strain were expected.
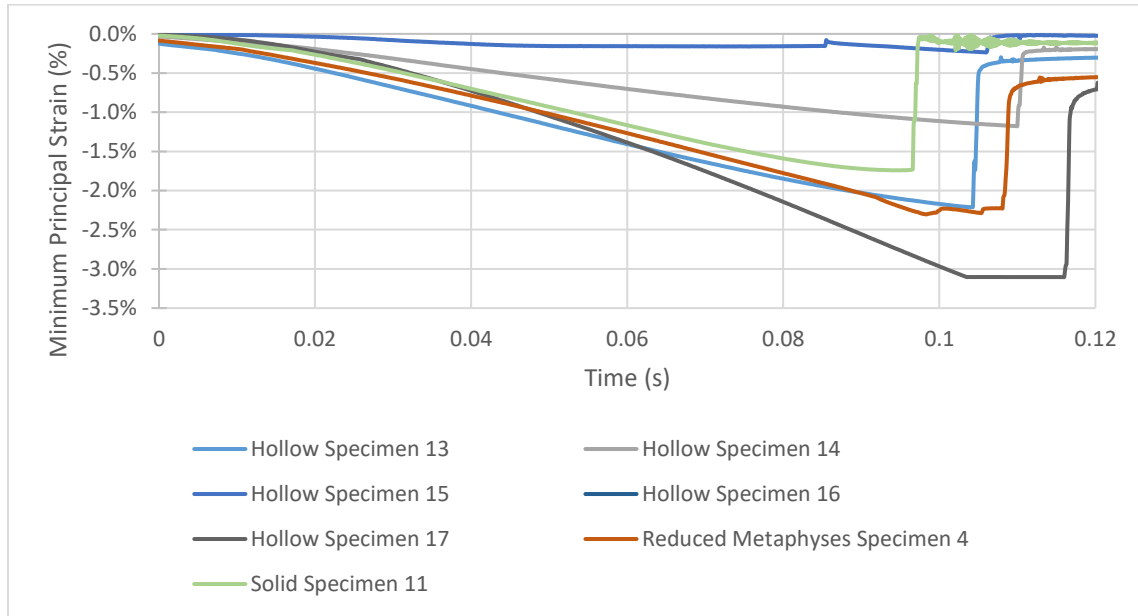

FIGURE 174. Minimum principal strain time histories for all specimens tested with a strain gauge under the compression loading conditions. Note: The curves have not been adjusted to accommodate the toe-region.

a. Compression Outcomes Comparison. The FE prediction was consistently lower than all bone surrogate specimen types tested for the means of the fracture load, stiffness, and area under the curve outcomes (Figure 175). The mean fracture load and mean stiffness were the lowest for the hollow specimens and highest for the solid specimens. For the area under the curve outcome, the hollow and solid specimens were similar while the mean of the reduced metaphyses specimens was higher.
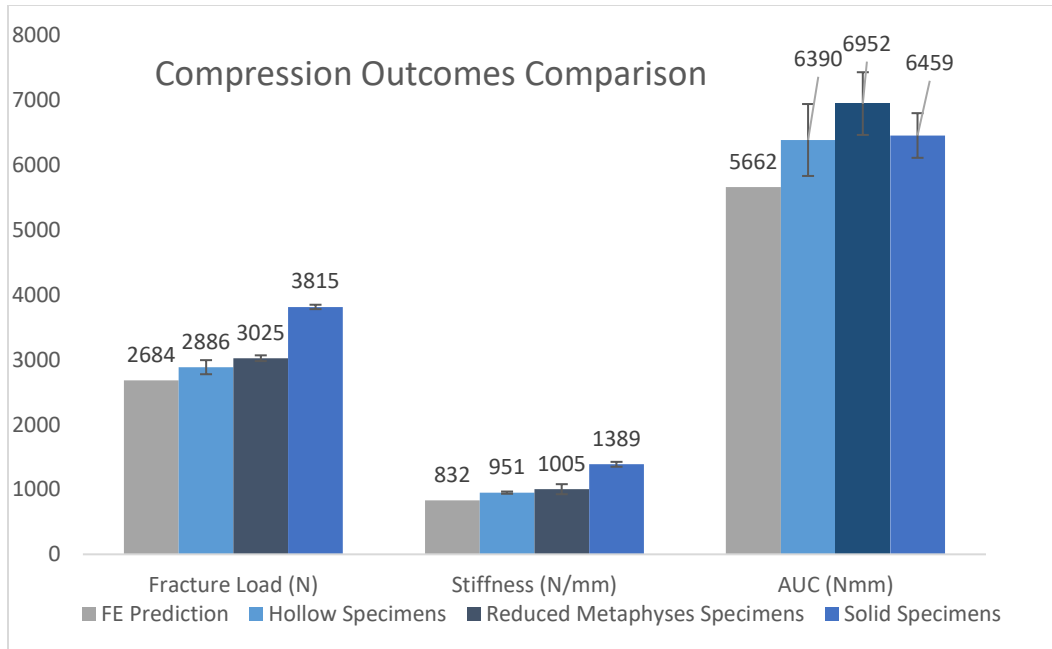
223

FIGURE 175. Comparison of the outcomes for the validation compression testing of the surrogate bones including the hollow, reduced metaphyses, and solid specimens to the FE predicted values. Experimental values are mean ± standard deviation.

B. Bone Surrogate Evaluation Discussion

For use as a bone surrogate, the glass fiber and polyamide (PA) 650 blend used in SLS to create the bone surrogate resulted in a surrogate that was brittle when compared to bone. When comparing the validation testing to whole bone mechanical property studies in the literature, it was typically much more brittle and had a lower strength than the behavior of immature animal or human tissue. Whole bone mechanical property testing typically focuses on evaluating bending or torsion loading conditions. Compared to the pediatric whole bone testing of a three-point bending setup conducted by Miltner et al. (1989), the mean moment to failure in the bone surrogate testing was 12Nm compared to the 80-100Nm moments observed in the specimens from seven to fifteen months old. The surrogate bone is less stiff with a mean stiffness of

145N/mm compared to a stiffness of 373N/mm of infant porcine bone (Bertocci, 2017) and a minimum stiffness of 800N/mm in adult human femurs (Cristofolini et al., 2010).

Using specimens with reduced infill at the metaphyses was an attempt to incorporate a less-dense structure which would correspond to the trabecular and less ossified regions of the bone. Since the reduced infill region would be beyond the supports in the bending testing, it was only used to test in compression. Since there are no known studies that have evaluated the whole bone in compression, no comparison to the literature can be made. When comparing the means of each specimen type for the compression loading condition, the hollow specimens resulted in a lower peak force (2886N vs 3025N) as well as a lower stiffness (951N/mm vs 1004N/mm). Due to the limited sample size of both types of specimens, reducing the infill appeared to create a stiffer specimen which may be in part due to the packed powder of the nylon and glass fiber which was still in the interstitial spaces of the bone surrogate. With an increased sample size, the difference in behaviors between the reduced infill and hollow specimens may be better explained.

Further improvements and modifications to either the materials or manufacturing process used is necessary in order to recreate properties more representative of pediatric bone. The surrogate evaluated her was more brittle than mechanical properties of bone in the literature suggesting that this is not a suitable surrogate to use for pediatric bone.

Education

J.B. Speed School of Engineering,
University of Louisville, Louisville, KY
B.s. – Bioengineering – May 2015, GPA – 3.83/4.00;
- Tau Beta pi
- Mickey R. Wilhelm Achievement Award

M.eng – Bioengineering – May, 2018
- Mickey R. Wilhelm Achievement Award

Thesis

"INVESTIGATING THE LIKELIHOOD OF PEDIATRIC FEMUR FRACTURE DUE TO FALLS THROUGH FINITE ELEMENT ANALYSIS"
- Developed finite element femur model from a CT scan
- Evaluated loading conditions from previously conducted fall scenarios simulated using an anthropomorphic test dummy representative of a 12-month-old child using finite element analysis

Publications

Mckinsey, K., Bertocci, G., Thompson, A. (2017). Development of In Silico Pediatric Femur Model to Evaluate Bed Falls [abstract]. In: Injury Biomechanics Symposium 2017; 2017 May 22-23. Ohio State University, Columbus, OH.

Mckinsey, K., Bertocci, G., Thompson, A. (2018). Investigating the Likelihood of Pediatric Femur Fracture due to Falls Through Finite Element Analysis [abstract]. In: Injury Biomechanics Symposium 2018; 2018 May 20-22. Ohio State University, Columbus, OH.

Presentations

Mckinsey, K. (2017, May). *Development of In Silico Pediatric Femur Model to Evaluate Bed Falls.* Poster session presented at the Injury Biomechanics Symposium at the Ohio State University, Columbus, OH.

Experience

R&D Co-op Ethicon, Inc.
August 19, 2013 – December 12, 2013; May 12, 2014 – August 15, 2014; January 12, 2015 – May 8, 2015
Third Co-op Rotation: Endo-mechanical, Powered Endoscopic Stapler

- Designed and developed the test method and setup for determining the parameters to be set for magnet and Hall Effect sensor configurations within the endocutter.
  - The method was designed to be able to be used in future configurations of the sensor and magnets in the current or future devices.
- Developed computational tables in Excel to determine the inertia of the motor-gearbox to be used to determine the output load of the handle onto the shaft to be able to use in parameterizing the handle of the device.
- Lead and managed the co-op volunteering committee. Co-op committee leader responsibilities included organizing and leading meetings to designate events to the members of the team and assisting the members when issues had arisen with their events.

Second Co-op Rotation: ENSEAL, Open Surgery Bipolar Tissue Sealing Device

- Primary responsibilities were to build and to maintain prototypes throughout the term.
- Other responsibilities include assisting with testing and conducting data analysis.
- Determined ongoing quality issues during assembly of the prototypes which caused malfunctioning of the devices during testing. This would lead to changes that would be put into effect in future prototype builds.

First Co-op Rotation: Endo-mechanical, Powered Endoscopic Stapler

- Primary project focused on determining the potential for generating marketing claims that dealt with tissue flow and thick tissue hemostasis.
  - Responsibilities included test method development, testing, and conducting data analysis.
  - Generated results demonstrating that the product potentially has less tissue flow compared to Covidien's Tri-Staple. This would allow for a marketing claim that the product produces less tissue tags than the competitor. This test was continued and used as part of the marketing material for the device.

Primes Undergraduate Teaching Assistant University of Louisville, Bioengineering Department
January 6, 2014 – April 29, 2014
Teaching Assistant for Biotransport Phenomena:

- Provided supplemental instruction to students outside of the regularly scheduled class time which included reviewing questions either seen on a homework, test, or quiz.

<div align="center">Skills & Abilities</div>

Programs: NXCad, SolidWorks, Matlab, Minitab, Labview, ANSYS, and Materialise Mimics